NASA/TM—2005–212786

Solar Probe: Report of the Science and Technology Definition Team

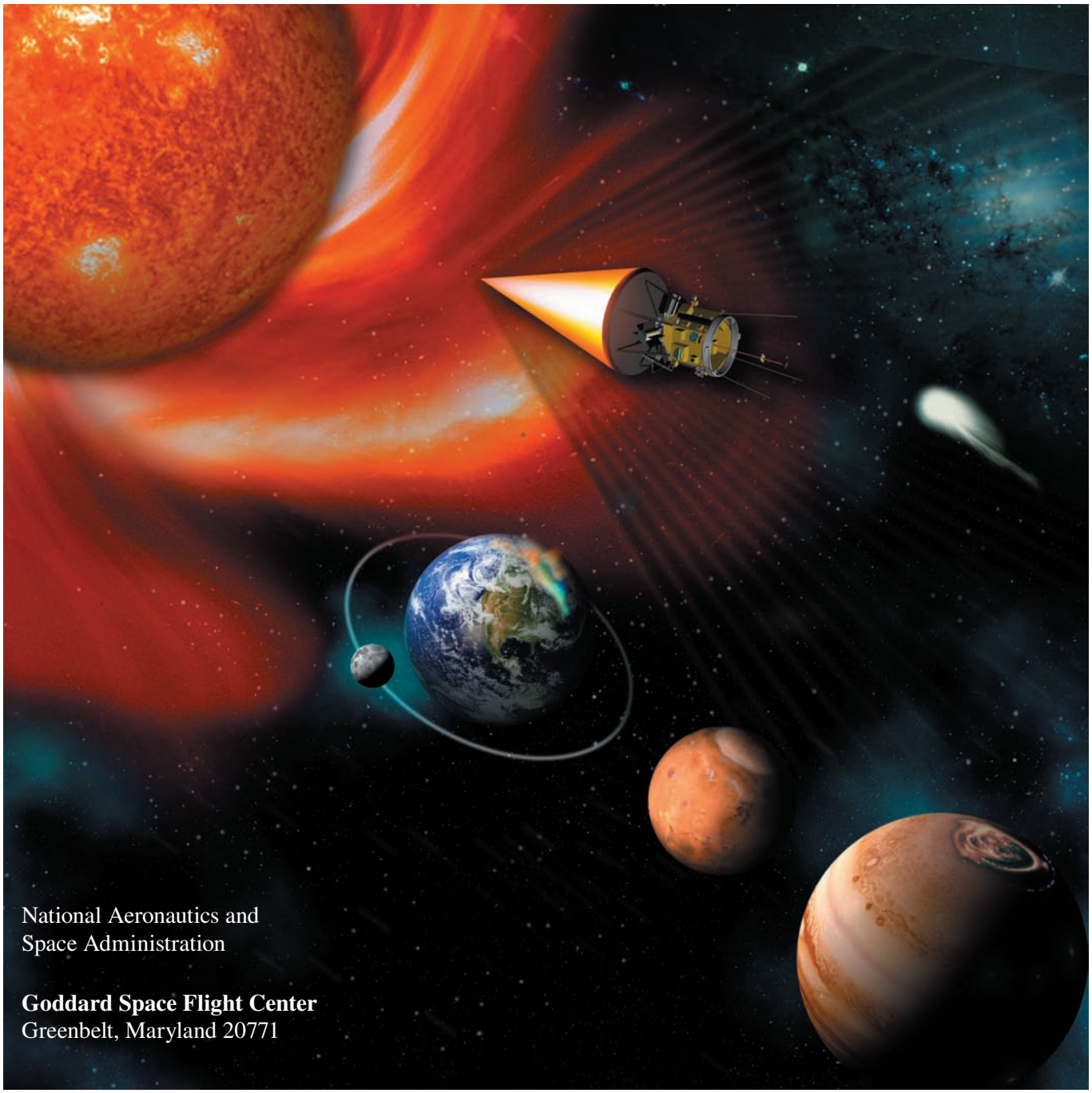

National Aeronautics and
Space Administration

Goddard Space Flight Center
Greenbelt, Maryland 20771

September 2005

The NASA STI Program Office … in Profile

Since its founding, NASA has been dedicated to the advancement of aeronautics and space science. The NASA Scientific and Technical Information (STI) Program Office plays a key part in helping NASA maintain this important role.

The NASA STI Program Office is operated by Langley Research Center, the lead center for NASA's scientific and technical information. The NASA STI Program Office provides access to the NASA STI Database, the largest collection of aeronautical and space science STI in the world. The Program Office is also NASA's institutional mechanism for disseminating the results of its research and development activities. These results are published by NASA in the NASA STI Report Series, which includes the following report types:

- TECHNICAL PUBLICATION. Reports of completed research or a major significant phase of research that present the results of NASA programs and include extensive data or theoretical analysis. Includes compilations of significant scientific and technical data and information deemed to be of continuing reference value. NASA's counterpart of peer-reviewed formal professional papers but has less stringent limitations on manuscript length and extent of graphic presentations.
- TECHNICAL MEMORANDUM. Scientific and technical findings that are preliminary or of specialized interest, e.g., quick release reports, working papers, and bibliographies that contain minimal annotation. Does not contain extensive analysis.
- CONTRACTOR REPORT. Scientific and technical findings by NASA-sponsored contractors and grantees.
- CONFERENCE PUBLICATION. Collected papers from scientific and technical conferences, symposia, seminars, or other meetings sponsored or cosponsored by NASA.
- SPECIAL PUBLICATION. Scientific, technical, or historical information from NASA programs, projects, and mission, often concerned with subjects having substantial public interest.
- TECHNICAL TRANSLATION. English-language translations of foreign scientific and technical material pertinent to NASA's mission.

Specialized services that complement the STI Program Office's diverse offerings include creating custom thesauri, building customized databases, organizing and publishing research results . . . even providing videos.

For more information about the NASA STI Program Office, see the following:

- Access the NASA STI Program Home Page at http://www.sti.nasa.gov/STI-homepage.html
- E-mail your question via the Internet to help@sti.nasa.gov
- Fax your question to the NASA Access Help Desk at (301) 621-0134
- Telephone the NASA Access Help Desk at (301) 621-0390
- Write to:
  NASA Access Help Desk
  NASA Center for AeroSpace Information
  7121 Standard Drive
  Hanover, MD 21076-1320

NASA/TM—2005–212786

Solar Probe: Report of the Science and Technology Definition Team

National Aeronautics and
Space Administration

Goddard Space Flight Center
Greenbelt, Maryland 20771

September 2005

Acknowledgments

Individuals from a number of institutions have helped with this study, and the members of the STDT gratefully acknowledge their contributions. The engineering team at JHU/APL, led by Doug Eng, included Doug Mehoke, Ted Hartka, Melissa Wirzburger, Yanping Guo, Barry LaBonte, Richard Conde, Dave Drewry, Don King, Robin Vaughan, Dave Persons, Brian Sequeira, Jennifer Sample, Jeff Lees, Barbara Leary, and Carl Engelbrecht. Cesar Carrasco (University of Texas at El Paso) modeled the effects of the near-Solar dust environment on the spacecraft. Justin Edmondson (University of Michigan), Stuart Bale (University of California at Berkeley), and Bill Kurth (University of Iowa) helped with the definition of the instrument specifications and requirements for the Fast Plasma and the Plasma Wave instruments. Scott Weidner (Southwest Research Institute) worked closely with the instrument team members to develop the requirements for the common Data Processing Unit. Celeste Satter (Jet Propulsion Laboratory) shared her expertise on antenna materials. Gil Colon and Mary DiJoseph, both of Goddard Space Flight Center, along with Andy Santo and Matt Jones (JHU/APL) and Regan Howard (Orbital Sciences Corporation), provided valuable project management support. Margaret Morris and the JHU/APL Technical Communications Group provided editorial and production support.

Available from:

NASA Center for AeroSpace Information
7121 Standard Drive
Hanover, MD 21076-1320
Price Code: A17

National Technical Information Service
5285 Port Royal Road
Springfield, VA 22161
Price Code: A10

Table of Contents

Solar Probe Science and Technology Definition Team

D. J. McComas, Chair
Southwest Research Institute
San Antonio, Texas, 78228-0510, U.S.A

L. W. Acton
Montana State University
Bozeman, Montana 59717-3840, U.S.A

M. Balat-Pichelin
PROMES-CNRS
B.P. 5 Odeillo
66125 Font Romeu Cedex, France

V. Bothmer
Institut für Astrophysik
Georg-August-Universität Göttingen,
37077 Göttingen, Germany

R. B. Dirling, Jr.
SAIC
Fountain Valley, California, 92708, U.S.A.

W. C. Feldman
Los Alamos National Laboratory
Los Alamos, New Mexico, 87545, U.S.A.

G. Gloeckler
University of Maryland
College Park, Maryland, 20742, U.S.A.

S. R. Habbal
Institute for Astronomy
University of Hawaii
Honolulu, 96822, U.S.A.

D. M. Hassler
Southwest Research Institute
Boulder, Colorado, 80302, U.S.A

I. Mann
Institut für Planetologie
Westfälische Wilhelms-Universität Münster
48149 Münster, Germany

W. H. Matthaeus
Bartol Research Institute
University of Delaware
Newark, Delaware, 19716, U.S.A.

R. L. McNutt, Jr., *APL Study Scientist*
The Johns Hopkins University
Applied Physics Laboratory
Laurel, Maryland, 20723, U.S.A.

R. A. Mewaldt
California Institute of Technology
Pasadena, California, 91125, U.S.A.

N. Murphy
Jet Propulsion Laboratory
Pasadena, California, 91109, U.S.A.

L. Ofman
California Institute of Technology
Pasadena, California, 91125, U.S.A.

E. C. Sittler, Jr., *GSFC Study Scientist*
NASA Goddard Space Flight Center
Greenbelt, Maryland, 20771, U.S.A.

C. W. Smith
University of New Hampshire
Durham, New Hampshire, 03824, U.S.A.

M. Velli
Dipartimento di Astronomia e Scienza del Spazio
Università degli Studi di Firenze
50125 Firenze, Italy[1]

T. H. Zurbuchen
University of Michigan
Ann Arbor, Michigan, 48109, U.S.A.

Support Staff and Ex Officio Members

K. A. Potocki, *APL LWS Program Manager*
The Johns Hopkins University
Applied Physics Laboratory
Laurel, Maryland, 20723, U.S.A.

D. A. Eng, *APL Engineering Team Lead*
The Johns Hopkins University
Applied Physics Laboratory
Laurel, Maryland, 20723, U.S.A.

H. M. Maldonado, *Study Lead*
NASA Goddard Space Flight Center
Greenbelt, Maryland, 20771, U.S.A.

Mary DiJoseph, *Project Support*
NASA Goddard Space Flight Center
Greenbelt, Maryland, 20771, U.S.A.

M. Guhathakurta, *LWS Program Scientist*
NASA Headquarters
Washington D.C., 20546-0001, U.S.A.

C. St. Cyr, *LWS Senior Scientist*
NASA Goddard Space Flight Center
Greenbelt, Maryland, 20771, U.S.A.

W. S. Lewis, *Technical Writing Support*
Southwest Research Institute
San Antonio, Texas, 78228-0510, U.S.A.

[1]Also at the Jet Propulsion Laboratory

Blank Page

Solar Probe: Executive Summary

Solar Probe will be a historic mission, flying into one of the last unexplored regions of the solar system, the Sun's atmosphere or corona, for the first time. Approaching as close as 3 R_S above the Sun's surface, Solar Probe will employ a combination of in-situ measurements and imaging to achieve the mission's primary scientific goal: to understand how the Sun's corona is heated and how the solar wind is accelerated. Solar Probe will revolutionize our knowledge of the physics of the origin and evolution of the solar wind. Moreover, by making the only direct, in-situ measurements of the region where some of the deadliest solar energetic particles are energized, Solar Probe will make unique and fundamental contributions to our ability to characterize and forecast the radiation environment in which future space explorers will work and live.

Our First Visit to a Star

Two of the transformative advances in our understanding of the Sun and its influence on the solar system were the discovery that the corona is several hundreds of times hotter than the visible solar surface (the photosphere) and the development—and observational confirmation—of the theory of the corona's supersonic expansion into interplanetary space as a "solar wind."

In the decades that have followed these important milestones in solar and space physics, the composition, properties, and structure of the solar wind have been extensively measured, at high heliolatitudes as well as in the ecliptic and at distances far beyond the orbit of Pluto. The corona and the transition region above the photosphere have been imaged with unprecedentedly high resolution, revealing a complex architecture of loops and arcades, while photospheric magnetography has uncovered the "magnetic carpet" of fine-scale flux bundles that underlies the corona. Observational advances have been accompanied by advances in theory and modeling, with a broad range of models offering plausible scenarios to explain coronal heating and solar wind acceleration.

We now know more about the corona and the solar wind than ever before. And yet the two fundamental questions, raised in the 1940s by the discovery of the corona's million-degree temperature and in the early 1960s by the proof of the supersonic solar wind's existence, remain unanswered: ***why is the solar corona so much hotter than the photosphere? And how is the solar wind accelerated?***

The answers to these questions can be obtained only through in-situ measurements of the solar wind down in the corona. A mission to provide these measurements, to probe the near-Sun particles-and-fields environment, was first recommended in 1958, at the dawn of the space age, by the National Academy of Science's "Simpson Committee." Since then, NASA has conducted several studies of possible implementations of a Solar Probe mission, and Solar Probe has remained at the top of various National Academy and NASA science priority lists. Most recently, the National Research Council's "decadal survey" in solar and space physics recommended implementation of a Solar Probe mission "as soon as possible" (*NRC*, 2003), while NASA's Sun-Solar System Connection Roadmap identifies Solar Probe as a "Flagship" mission that "is ready to fly and is our highest priority for new resources" (*NASA*, 2005).

To date, however, nearly 50 years after the Simpson Committee report and despite strong and repeated endorsements of a Solar Probe by the National Academy, NASA, and the solar and space physics community, the closest any spacecraft has come to the Sun is 65 R_S, far outside the region

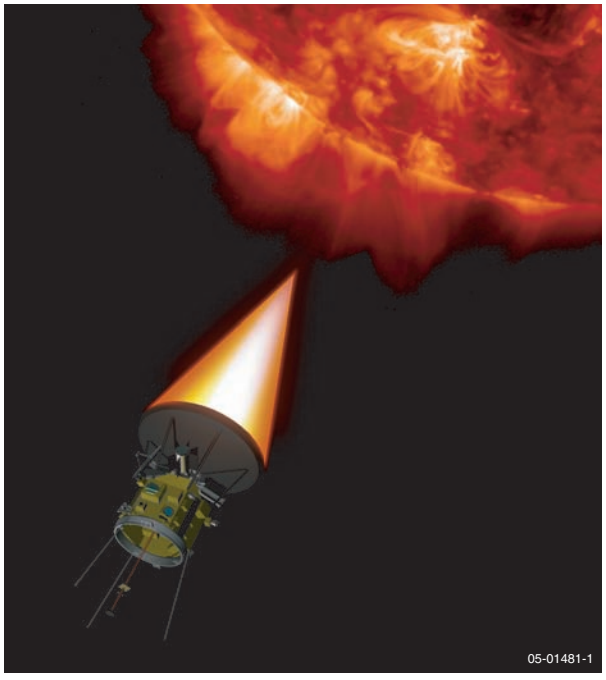

Artist's concept of the Solar Probe, with the glowing cone of the Thermal Protection System pointed toward the Sun inside 0.8 AU.

where the acceleration of the solar wind occurs. ***Thus the need for a Solar Probe remains.***

This report describes the results of an intensive year-and-a-half study by the Solar Probe Science and Technology Definition Team which demonstrates that Solar Probe is fully ready to move forward as a cost-effective and acceptably low risk mission. ***Solar Probe will be the first spacecraft to venture into the unexplored inner reaches of the heliosphere where the solar wind is born. Through high-cadence in-situ measurements of the solar wind plasma, energetic particles, and fields as close to the Sun as 3 R_S, supplemented by coronal and photospheric imaging, Solar Probe will provide the data needed to solve, finally, the twin mysteries of coronal heating and solar wind acceleration.*** This historic mission will transform our understanding both of our Sun and of other stars with hot, x-ray-emitting coronas and supersonic winds as well.

Solar Probe Science Objectives

Present observation, theory, and modeling provide the following general picture of the corona and solar wind. At times of lower solar activity, the solar wind is bimodal, consisting of a dominant quasi-steady high-speed wind that originates in open-field polar coronal holes and a variable, low-speed wind that originates around the equatorial streamer belt. With increasing activity, this orderly bimodal configuration of the corona and the solar wind breaks down, as the polar holes shrink and streamers appear at higher and higher heliographic latitudes. At these times, the bimodal wind structure is replaced by a complex mixture of fast flows from smaller coronal holes and transients, embedded in a slow-to-moderate speed wind from all latitudes. The energy that heats the corona and drives the wind derives from photospheric motions and is channeled, stored, and dissipated by the magnetic fields that emerge from the photosphere and structure the coronal plasma. Several fundamental plasma physical processes—waves and instabilities, magnetic reconnection, turbulence—operating on a vast range of spatial and temporal scales are believed to play a role in coronal heating and solar wind acceleration.

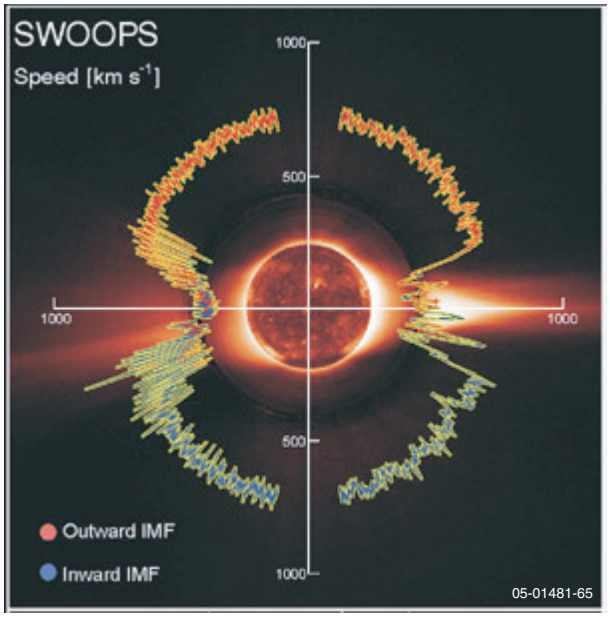

At solar minimum the solar wind is dominated by a high-speed flow from polar coronal holes, with a slower, variable flow emanating from the equatorial streamer belt.

Thus we have the general picture. But the devil—and the physics—is, as always, in the details. For example, the association of the fast and slow components of the solar wind with large-scale magnetic structures (coronal holes, streamers) in the corona is well established. However, to understand coronal heating and solar wind acceleration in coronal holes, it is necessary to know the geometry and dynamics of the expanding magnetic field and to determine the role of fine-scale structures (such as polar plumes and macrospicules) in coronal heating. In the case of the slow wind, a critical unknown is the morphology of the magnetic field in the regions where the wind forms. Similarly, the morphology of the magnetic field in active regions, which contribute to the solar wind at least during solar maximum, is also unknown. Thus a major science objective of the Solar Probe mission is ***to determine the structure and dynamics of the magnetic fields at the sources of the fast and slow solar wind.***

The precise mechanisms by which energy is transferred from the photosphere and subsequently dissipated to heat the corona and accelerate the solar wind are not known. For example, low-frequency Alfvén waves are thought to be launched into the corona by photospheric motions. What is the energy flux in these waves close to the Sun? How is the energy of the waves dissipated? Through phase mixing? Through resonant absorption by coronal loops? Through nonlinear cascade processes? Observations suggest that ion cyclotron waves play an important role in heating the corona

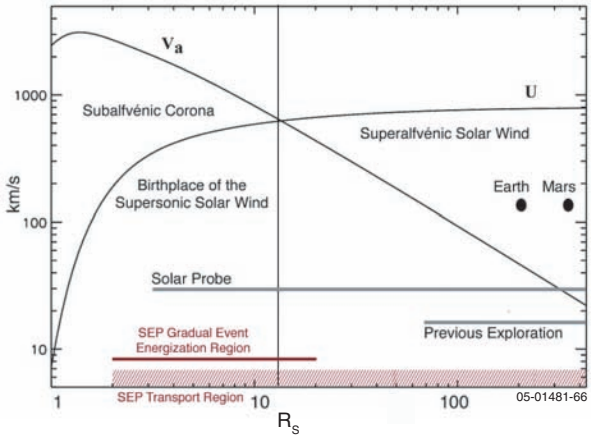

Model profiles of the solar wind speed (U) and the Alfvén wave speed (V_a) with distance from the Sun. The vertical bar separates the source, or sub-Alfvénic, region of the wind from the supersonic solar wind flow. Solar Probe is the first mission to fly inside the solar wind source region.

and fast wind. But how and where are these waves generated? Are they produced locally by plasma instabilities, through turbulent cascade from lower-frequency waves, or in the lower corona by reconnection? And generally, what is the role of reconnection (e.g., in nanoflares) relative to that of wave dissipation in coronal heating? To answer these and similar questions, Solar Probe will, as a second main objective, ***trace the flow of energy that heats the corona and accelerates the solar wind.***

Solar Probe's third major science objective is ***to determine what mechanisms accelerate and transport energetic particles*** at the Sun and in the inner heliosphere. Two kinds of solar energetic particle (SEP) events occur during active periods, often both together: gradual events, in which particles are accelerated in the corona by shocks driven by fast coronal mass ejections (CMEs), and impulsive events, in which particles are accelerated by solar flares. In addition, even at the quietest times there is a continuous outflow from the Sun of particles of intermediate energies (suprathermal to >10 MeV). The mechanism responsible for this outflow is not known. Further questions concern the relative contributions of reconnection, shocks, and turbulence to particle acceleration in impulsive events, the identity and source of seed populations for gradual events, and the means by which energetic particles are transported to high latitudes. Accomplishment of this objective will not only advance our understanding of a fundamental plasma process, energetic particle acceleration, but will also significantly contribute to efforts to predict SEPs, which present one of the most serious threats to astronaut health and safety.

The inner heliosphere is populated with dust grains originating from comets and asteroids. This inner heliospheric dust cloud, the source of the zodiacal light and the Sun's F-corona, has not been well characterized. Solar Probe's unique path near the Sun will make it possible to answer questions about the size and mass distribution of the dust, about its

Solar Probe Science Objectives

Determine the structure and dynamics of the magnetic fields at the sources of the solar wind

a. How does the magnetic field in the solar wind source regions connect to the photosphere and the heliosphere?
b. How do the observed structures in the corona evolve into the solar wind?
c. Is the source of the solar wind steady or intermittent?

Trace the flow of the energy that heats the solar corona and accelerates the solar wind

a. How is energy from the lower solar atmosphere transferred to and dissipated in the corona?
b. What coronal processes shape the non-equilibrium velocity distributions observed throughout the heliosphere?
c. How do the processes in the corona affect the properties of the solar wind in the heliosphere?

Determine what mechanisms accelerate and transport energetic particles

a. What are the roles of shocks, reconnection, waves, and turbulence in the acceleration of energetic particles?
b. What are the seed populations and physical conditions necessary for energetic particle acceleration?
c. How are energetic particles transported radially and across latitudes from the corona to the heliosphere?

Explore dusty plasma phenomena and their influence on the solar wind and energetic particle formation

a. What is the dust environment of the inner heliosphere?
b. What is the origin and composition of dust in the inner heliosphere?
c. What is the nature of dust–plasma interactions and how does dust modify the spacecraft environment close to the Sun?
d. What are the physical and chemical properties of dust-generated species?

composition and origin, and about its interaction with the near-Sun plasma and gas environment. Of particular interest is the contribution of the dust to the "inner source" of energetic particles. As its fourth objective, Solar Probe will ***explore dusty plasma phenomena in the near-Sun environment and their influence on the solar wind and energetic particle formation.***

To address these objectives, Solar Probe will **explore** a region of the solar system never before visited by a spacecraft. With the data it transmits back to Earth, solar and space physicists will answer questions that cannot be answered by any other means and will attain a **deep understanding** of phenomena and processes in this fascinating and critical region. And as with any great voyage into uncharted realms, Solar Probe's journey to the Sun holds the promise of many more unanticipated **discoveries**—new mysteries to challenge humankind's ever-expanding knowledge of our home in the universe.

Science Implementation

Solar Probe will address the four science objectives through a combination of in-situ and remote-sensing observations performed from a polar orbit about the Sun. Inside a distance of 0.3 AU on both sides of perihelion, Solar Probe will make in-situ measurements of plasma, suprathermals, energetic particles, magnetic fields, waves, and dust in the near-Sun environment. Extreme ultraviolet and magnetic imaging of solar wind source regions and white-light imaging of coronal structures will be performed on both inbound and outbound legs of the solar pass. The remote-sensing observations will allow in-situ measurements to be related to magnetic and plasma structures at the Sun. Closest approach will occur at a perihelion altitude of 3 R_S above the surface. Supporting remote-sensing observations from ground-based, sub-orbital, and space-based assets will be coordinated with the perihelion pass to provide context for Solar Probe's in-situ measurements. A large and dedicated theory and modeling program will be an integral part of the Solar Probe mission, starting 3 years before the first perihelion pass.

Solar Probe's baseline payload is a single, integrated package consisting of both in-situ and remote-sensing instruments serviced by a common Data Processing Unit (DPU) and Low-Voltage Power Supply (LVPS). The in-situ

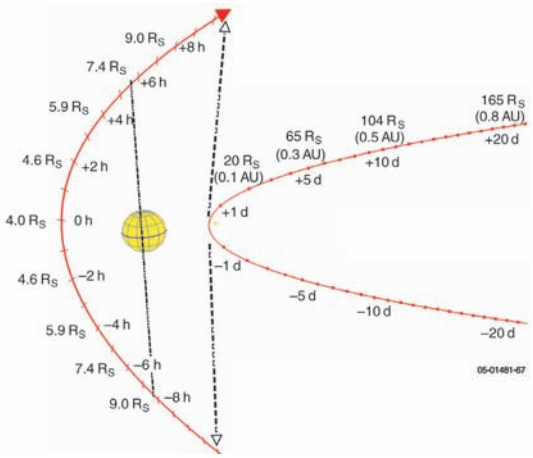

The Solar Probe trajectory. Encounter science begins at 0.3 AU, 5 days before closest approach, and lasts until 5 days after closest approach.

instrumentation includes a Fast Ion Analyzer (FIA), two Fast Electron Analyzers (FEAs), an Ion Composition Analyzer (ICA), an Energetic Particle Instrument (EPI), a Magnetometer (MAG), a Plasma Wave Instrument (PWI), a Neutron/Gamma-ray Spectrometer (NGS), and a Coronal Dust Detector (CD). The remote-sensing instrumentation comprises a Polar Source Region Imager (PSRI), for EUV and magnetographic imaging of the solar wind source regions, and a white-light Hemispheric Imager (HI), for imaging coronal structures. An integrated payload developed by a single combined investigator team was baselined in the study as a means of achieving the maximum science return for the minimum mission costs and of reducing payload mass and power while providing added functional redundancy.

Baseline Mission

The baseline mission provides for two flybys of the Sun, separated by ~4.6 years, thus allowing Solar Probe to measure the solar wind and corona at different phases of the 11-year solar cycle, independent of launch date. For a launch in 2014, the first flyby will take place in 2018, around the projected activity minimum of solar cycle 24. The second solar flyby will occur in 2023, at a time of increasing solar activity.

Solar Probe will use a Jupiter gravity assist flyby (closest approach ~12 R_J, minimizing exposure to the jovian radiation belts) to achieve a polar orbit about the Sun with a perihelion of 4 R_S (3 R_S above the surface). The spacecraft will arrive at the Sun

~4.1 years after launch, approaching from the south with a maximum velocity of 308 km/s at perihelion. For the first encounter, the perihelion pass is designed to take place with Earth 15° off quadrature, allowing for a high data rate (at least 25 kbps) for real-time science telemetry and for simultaneous supporting remote-sensing observations from Earth. Because of coronal scintillation effects, the Ka band will be used for the real-time data transmission. Pole-to-pole passage occurs entirely within 9 R_S and lasts ~14 hours.

The Earth–Sun geometry for the second encounter (34° off quadrature) will again allow for simultaneous remote-sensing observations from Earth. However, the high-gain antenna will point away from Earth so that only low-data-rate real-time telemetry using the low-gain antennas will be possible. Extensive recorded data will be downlinked after both encounters to provide the complete detailed observations.

The Atlas 551 is baselined as the Solar Probe launch vehicle, although the mission design allows for dual-launch compatibility with a Delta IV Heavy.

Solar Probe Spacecraft

The baseline Solar Probe is a 3-axis stabilized spacecraft designed to survive and operate successfully in the intense thermal environment that it will encounter during its voyage around the Sun. The spacecraft's most prominent feature is the Thermal Protection System (TPS), comprising a large 2.7-m diameter carbon–carbon conical primary shield with a low-conductivity, low-density secondary shield attached to its base. The TPS protects the spacecraft bus and instruments within its umbra during the solar encounter. The bus consists of a hexagonal equipment module and a cylindrical adapter. It provides an efficient mechanical structure that accommodates the instruments and spacecraft subsystems and handles the loads from the TPS and the launch loads. Solar Probe will be powered by three multi-mission radioisotope thermoelectric generators (MMRTGs). Simple monopropellant will be used for ΔV maneuvers and attitude control. The Guidance and Control System consists of two redundant star trackers, an inertial measurement unit, digital Sun sensors, 4 reaction wheels, and 12 thrusters. The spacecraft is equipped with one high-gain antenna for data downlink during the first solar encounter; a medium-gain antenna, the primary antenna during the cruise phase of the mission; and two low-gain antennas for emergencies or periods when the pointing of the medium and high-gain antennas is precluded. The X band will be used for both data downlink and command uplink; the Ka band will be used only for data downlink.

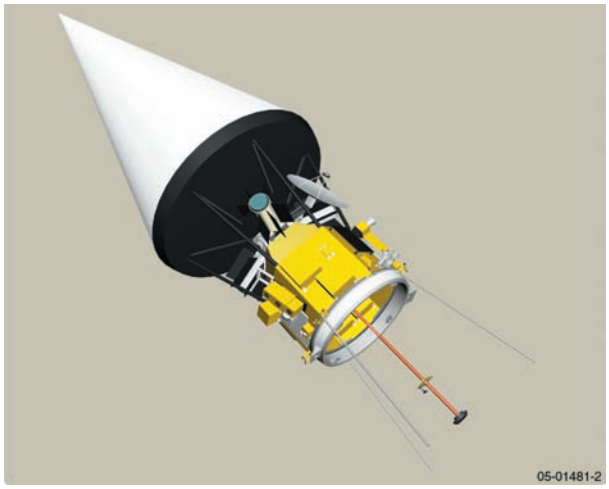

The design of the Solar Probe spacecraft is based on rigorous engineering studies that demonstrate the technical feasibility and affordability of the mission.

The imagers, CD, EPI, NGS, and one FEA are mounted on the Solar Probe bus. The FIA, the second FEA, and the ICA are mounted on a movable ram-looking arm, which will be gradually retracted as the spacecraft approaches the Sun. This arrangement provides viewing to near (2° inside of) the edge of the TPS umbra. To enable imaging of the solar wind source regions, a retractable, thermally robust periscope will be used to extend the PSRI optics beyond the TPS umbra. Both the side-looking arm and the periscope are designed to be fail-safe. The MAG is mounted to the 2-m axial boom that extends from the bottom deck of the spacecraft and that also accommodates a solar horizon sensor used for attitude safing during the solar encounter. The PWI consists of three actuator-controlled 1.75-m antennas mounted to the bottom deck.

Solar Probe and Human Exploration

Solar energetic particle (SEP) events present a serious radiation threat to human explorers living and working outside low-Earth orbit. Development of an SEP forecasting capability is critical to space radiation risk mitigation and management. By making the first direct measurements of the

near-Sun regions through which all SEPs must travel, by directly sampling the regions where gradual SEPs are energized, and by identifying the seed populations for these dangerous particles, ***Solar Probe will provide critical ground-truth data needed for the development of the predictive models that, combined with solar and heliospheric monitoring, will enable forecasting of the space radiation environment in support of human exploration.***

Summary

Solar Probe is an exciting mission of exploration, discovery, and deep understanding. It will journey to one of the last unexplored regions of the solar system and reveal how the corona is heated and the solar wind accelerated, solving two fundamental mysteries that have been top-priority science goals for many decades. The mission described in this report is based on an exhaustive and rigorous engineering study directed by the present Science and Technology Definition Team. Of paramount importance in the engineering study were trades concerning mission safety and cost, with the recommendation of a single integrated payload and the baselining of the Atlas 551 as the launch vehicle being key factors in achieving an affordable mission. ***The rigor and thoroughness of this study ensures that the described mission is technically feasible, can be accomplished within realistic resources, and can fully achieve its four science objectives, thus transforming our understanding of the Sun and its sister Sun-like stars and enabling exploration.***

> To understand the genesis of the heliospheric system, it is necessary to determine the mechanisms by which the solar corona is heated and the solar wind is accelerated and to understand how the solar wind evolves in the innermost heliosphere. These objectives will be addressed by a Solar Probe mission. Because of the importance of these objectives for the overall understanding of the solar-heliosphere system, as well as of other stellar systems, a Solar Probe mission should be implemented as soon as possible within the coming decade.
>
> NRC, *The Sun to the Earth—and Beyond, a Decadal Research Strategy in Solar and Space Physics* (2003)

1. Solar Probe and Human Exploration

NASA's new "Vision for Space Exploration" calls for an "extended human expedition to the Moon" some time between 2015 and 2020 and for the eventual human exploration of Mars. One of the problems that must be solved for this vision to become reality is the problem of space radiation, which presents a serious threat to the health and safety of future human explorers. A number of major research initiatives are now under way to improve our understanding of the biological effects of radiation and to develop effective shielding material. ***Another important aspect of space radiation risk reduction and management is the development of the capability to forecast the radiation environment, and here Solar Probe has a unique and significant contribution to make to human exploration.***

The two principal sources of space radiation with which astronauts traveling outside Earth's magnetosphere will have to contend are ***galactic cosmic rays*** and ***solar energetic particles***. Galactic cosmic rays (GCRs) are very energetic particles that are accelerated by a variety of processes within the galactic environment and then propagate into the solar system. Most of the GCR flux is filtered by the outer heliosphere; the remaining GCRs enter the solar system, providing a radiation background whose levels are modulated by the heliospheric magnetic field, with the smallest fluxes observed around solar maximum. The variability in the continuous GCR background over the solar cycle is generally well documented. The most pressing practical challenge in reducing the GCR risk is the development of adequate and cost-effective shielding for spacecraft and shelters where astronauts can spend the majority of their time.

In contrast to the relatively steady fluxes of GCRs, solar energetic particle (SEP) events are episodic and thus unpredictable, and can expose astronauts and spacecraft systems to intense fluxes of particles with energies >100 MeV for periods of hours to days.[1] The effects of an SEP event on the health of human explorers can be quite serious, depending on such factors as the total absorbed dose and the dose rate, which in turn depend both on physiological factors and on the characteristics of the SEP event (energy spectra, flux, duration). Acute effects from exposure to SEPs range from dizziness, nausea, and headaches to radiation sickness and, in principle, even death.

SEP events are divided into two types: short-lived ***impulsive*** events, in which the particles are accelerated in solar flares, and ***gradual*** events, in which the particles are accelerated at shocks driven by fast coronal mass ejections (CMEs) in the near-Sun coronal environment. Both processes operate together in some events, but generally speaking the gradual events produce the largest fluences of particles and most dangerous radiation environments for astronauts. SEP events occur most frequently from solar maximum to several years beyond maximum.

One the largest SEP events recorded occurred in August 1972, during the Apollo program, but fortunately not during a mission. A recent study of the health effects of SEP exposure based on data from this event concludes that "the combination of high doses and high dose rates delivered to crews by solar particle events of the magnitude and duration of the August 1972 event is likely to produce significant acute effects, which could be mission- or even life-threatening unless a heavily shielded space is provided for use by the crew" (*Parsons and Townsend*, 2000). An extraordinarily intense event occurred recently, on January 20, 2005, with a very hard proton energy spectrum extending up to 400 MeV. An astronaut, exposed during this event on the surface of the Moon and protected only by a space suit, would have received an estimated radiation dose of ~300 cSr, which would have been enough to cause radiation sickness (http://www.srl.caltech.edu/ACE/ACENews/ACENews87.html).

In contrast to GCRs, solar energetic particle radiation presents a problem of monitoring and forecasting rather than shielding: "It is not too difficult a task to provide appropriate shielding or storm shelters to protect against exposure during SPEs, but surveillance methods to predict and detect solar particle events from both sides of the sun relative to a spacecraft must be improved" (*NRC*, 1996). The risk to future astronauts will come from SEP events that catch them unawares as they are engaged in exploration activities away from the shielded living quarters, laboratories, or storm shelters of their lunar or martian bases. In such cases, monitoring

[1]An SEP event in April 2002 led to the loss of Japan's Mars mission, Nozomi; another SEP event in October 2003 rendered the MARIE instrument on the Mars Odyssey spacecraft inoperative. The loss of the MARIE instrument is ironic, as it was designed to measure the radiation environment at Mars.

and real-time forecasting are vitally important if astronauts are to receive the advance warning they need in order to have enough time to find shelter.

Models that can provide real-time forecasting of SEP spectra and fluxes are currently being developed and refined (e.g., the Space Weather Modeling Framework at the University of Michigan). At present, however, the accuracy of such models is limited by their dependence upon assumptions about the physical conditions in the corona and inner heliosphere, between 2 and 20 solar radii (R_S), where gradual SEP events originate. ***Solar Probe will explore this critical region for the first time*** **(Figure 1-1**). It will directly address how SEPs can be accelerated and transported in this region, identify their seed populations, and establish the physical conditions (e.g., magnetic field structure, turbulence levels, and Alfvén speed) under which these critically dangerous particles are generated (cf. Section 2.3 below). ***Solar Probe will thereby provide the "ground truth" for models that eventually will be run in real time to make global predictions, and it will thus play a truly enabling role in the human exploration of the Moon and Mars.***

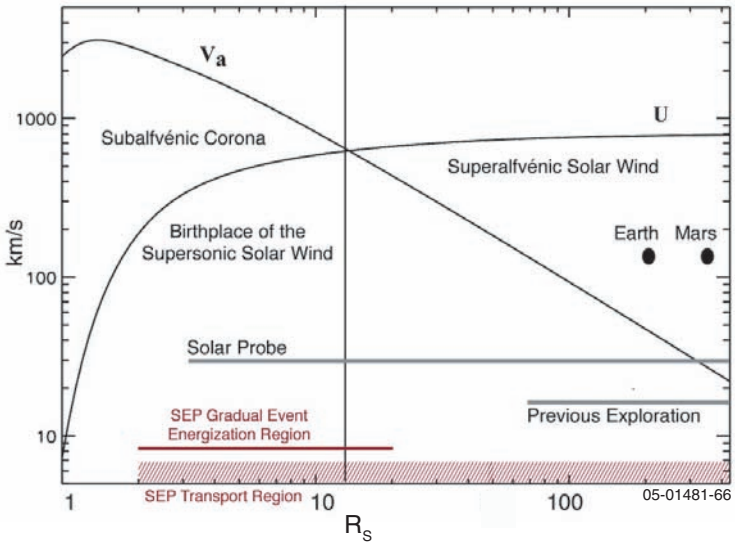

Figure 1-1. Model profiles of solar wind speed and Alfvén wave speed with distance from the Sun. The vertical bar separates the source, or sub-Alfvénic, region of the wind from the supersonic solar wind flow. Solar Probe is the first mission to fly inside the solar wind source region and to sample directly the critical region of the outer corona where solar energetic particles (SEPs) are generated.

2. Solar Probe Science Objectives and Measurement Requirements

Remote-sensing observations from space-based platforms such as Yohkoh, SOHO, and TRACE, as well as from ground-based observatories, together with in-situ measurements by Helios, IMP, Ulysses, Wind, and ACE, have led to changing perspectives in our understanding of coronal heating and solar wind acceleration. As the time and space resolution of instrumentation has increased, the fundamental role played by the Sun's magnetic field in shaping dynamical processes on all scales in the three-dimensional heliosphere throughout the solar activity cycle has become more apparent. Significant progress has been made in our knowledge of coronal structures, particularly of fine-scale structures such as polar plumes, coronal bright points, and the Sun's "magnetic carpet"; and we have witnessed fundamental advances in our understanding of the nature of the solar wind, the association of its fast and slow components with specific coronal structures, and its variability with changing solar activity.

Important early clues about the bimodal structure of the solar wind came from the Helios mission, the only mission to explore the inner heliosphere as close to the Sun as 0.3–0.7 AU. Helios demonstrated that properties such as solar wind speed, ion temperatures, and turbulence amplitude increase with distance from the heliospheric current sheet or as a function of heliomagnetic latitude. In its two orbits about the Sun's poles, Ulysses has explored the three-dimensional structure of the solar wind as it changes over the course of a solar activity cycle (**Figure 2-1**). Ulysses has shown that the fast solar wind, with a speed around 750 km/s, is the basic, quasi-steady outflow from the high-latitude solar corona during the minimum phase of the solar cycle and demonstrated that the fast wind originates from regions where the coronal electron temperature is

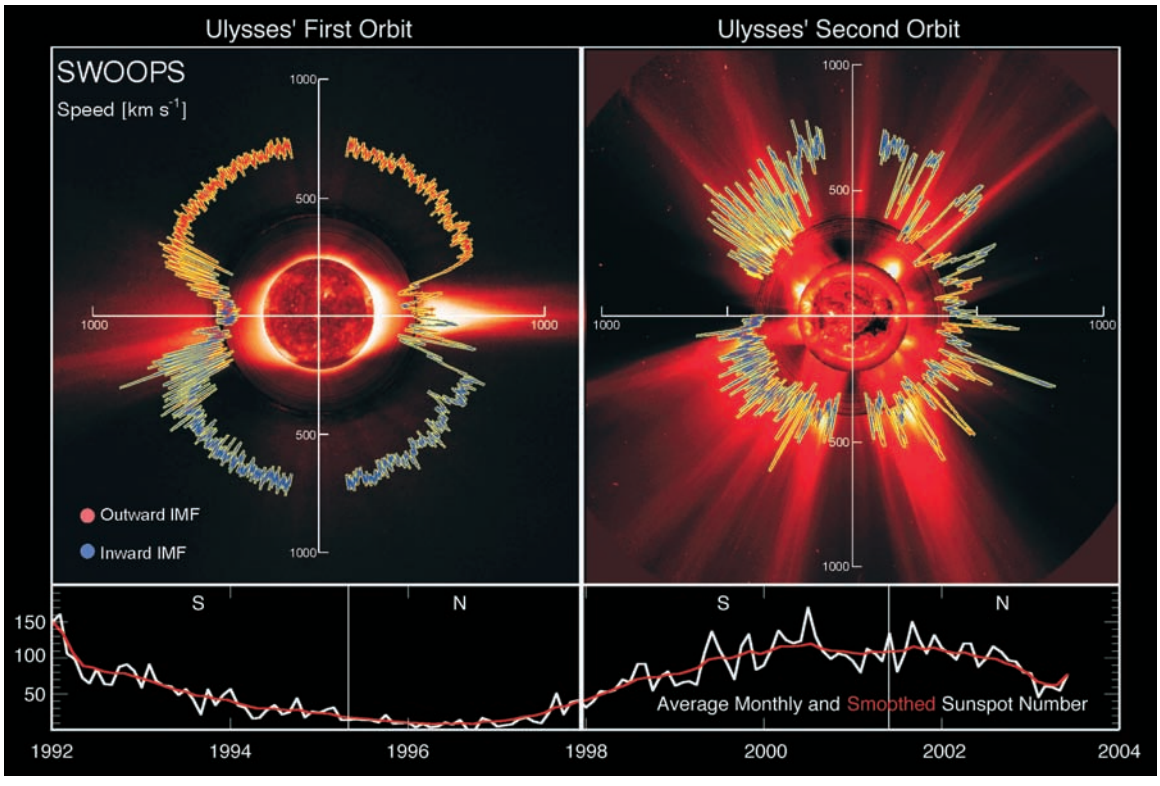

05-01481-68

Figure 2-1. Plots of solar wind speed as a function of heliographic latitude, illustrating the relation between the structure of the solar wind and coronal structure at solar minimum (left) and solar maximum (right). The baseline Solar Probe mission provides for two solar flybys, each at a different part of the solar cycle, so that measurements can be obtained at both the quiet and active phases of the cycle. (Ulysses SWOOPS solar wind data are superposed on composite solar images obtained with the SOHO EIT and LASCO C2 instruments and with the Mauna Loa K-coronameter [*McComas et al.*, 2003]).

relatively cool (**Figure 2-2**). This inverse correlation between flow speed and coronal electron temperature poses a fundamental challenge to one of the basic tenets of the original theory of the solar wind, which assumes high coronal electron temperatures and heat conduction. A further challenge to the original theory comes from SOHO measurements, which suggest that the open corona expands principally because of the very high, anisotropic temperatures of the coronal ions, with the minor species reaching temperatures of 10 MK at a few solar radii.

Unlike the fast wind, which originates in coronal holes, the slow solar wind is confined to regions emanating from the magnetic activity belt. SOHO observations suggest that the slow wind flows in a bursty, intermittent fashion from the top of helmet streamers, which were first seen to expand continuously, in x-rays, by Yohkoh. The organization into fast and slow components characterizes the solar wind around solar minimum. As the solar activity cycle progresses, however, Ulysses has shown that the simple bimodal structure gives way to a much more variable, but typically slower, solar wind at activity maximum, apparently originating not only from the much more sparse coronal hole regions and quiet Sun, but also from coronal active regions. To whatever degree the various models of solar wind acceleration have succeeded in reproducing observations of the fast wind, still less success has been obtained in efforts to understand the acceleration of the slow wind.

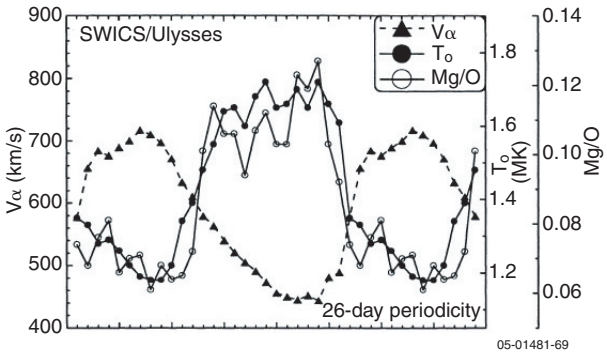

Figure 2-2. Solar wind speed, freezing-in temperatures determined from O^{7+}-to-O^{6+} abundances, and magnesium-to-oxygen ratios as a function of time measured by Ulysses during a low-latitude crossing of alternating high- and low-speed streams. The anti-correlation of wind speed with electron temperature as determined from the freezing-in temperature is dramatic, calling into question the role of thermal electrons in driving the solar wind (*Geiss, Gloeckler, and v. Steiger*, 1995).

A third type of flow arises from large eruptions of coronal magnetic structures, known as coronal mass ejections (CMEs). Their initiation requires an entirely distinct mechanism from the slow and fast wind. One of the important developments in solar and heliospheric physics during the last 25 years is the recognition that shock waves driven by fast CMEs can relatively often accelerate particles to energies exceeding 1 GeV and that such shock-driven "gradual" energetic particle events are distinct from "impulsive" events associated with solar flares. However, the identity of the seed particles and the physical conditions necessary for the acceleration of particles in gradual events are not known.

Although there are many models for various aspects of magnetic activity, coronal heating, and solar wind acceleration, the lack of magnetic field and detailed plasma measurements in the region inside 65 R_s does not allow their validation or falsification. Basic unanswered questions concern the dynamics of photospheric and coronal magnetic fields in the source regions of the solar wind; the storage, transport, and release of the mechanical energy required for coronal heating; the specific mechanism(s) for the conversion of energy between the magnetic field and thermal particles; and the sources of high-energy particles and the mechanisms by which they are accelerated. These questions motivate three broadly distinct but interlinked top-level Solar Probe objectives. A fourth top-level objective of an exploratory nature concerns the source, composition, and dynamics of dust in the inner solar system. In the following sections, these four main objectives are translated into specific scientific questions and basic measurement requirements.

2.1 Determine the structure and dynamics of the magnetic fields at the sources of the fast and slow solar wind

In-situ measurements of the solar wind by Ulysses and other spacecraft have confirmed the origin of fast wind streams in coronal holes and demonstrated the overall association of wind speed and coronal structure throughout the solar activity cycle (cf. **Figure 2-1**) (*McComas et al.*, 2003). However, while the properties of the fast and slow wind in interplanetary space are well-established, their source regions have been explored only via remote

sensing observations, which have revealed that the solar corona, even at solar minimum, displays a rich variety of dynamic magnetized structures over a wide range of temporal and spatial scales. Solar Probe will combine remote sensing observations (e.g., of the polar photospheric magnetic fields) with in situ particles and fields measurements to determine how these dynamic structures merge, in time and space, to yield the wind measured in interplanetary space.

2.1.1 How does the magnetic field in the solar wind source regions connect to the photosphere and the heliosphere? The geometry of the magnetic field expansion in the inner corona, from the photosphere out to a few solar radii, plays a fundamental role in determining density distribution and solar wind speeds in solar wind models, as the field lines define the flow tubes along which mass and energy flux are conserved. Close to the Sun, SUMER and MDI observations from SOHO suggest that the source of the fast solar wind is associated with the strong supergranular network magnetic fields in coronal holes (*Hassler et al.,* 1999, **Figure 2-3**), which rapidly fan out to fill the corona. Ulysses observations have shown that the radial magnetic field component measured in the fast wind is largely independent of latitude, so that any latitudinal gradient in the average field at the coronal base must be washed out by transverse non-radial expansion closer to the Sun. This non-radial divergence of the magnetic field is a fundamental property of the corona (e.g., *Feldman et al.*, 1996) as it determines the areal expansion along flux tubes, which has been shown to be inversely correlated with the asymptotic solar wind speed. It is thought that flux tube expansion is caused by the excess high-latitude magnetic pressure, and models suggest that it occurs out to radial distances $> 10\ R_S$. Based on Ulysses data, the magnitude of the average polar magnetic field has been estimated to be 6 G at solar minimum, though values up to 15 G in the photosphere may not be excluded. At present, there are no direct measurements of the polar magnetic field below 1.5 AU (*Sittler and Guhathakurta*, 1999; 2002). ***By measuring the radial magnetic field in situ along its trajectory, and remotely sensing the polar photospheric field at the same time, Solar Probe will allow a complete description of magnetic field and solar wind expansion free from unknown parameters. These measurements will provide both a test of existing models of coronal structure and rigorous constraints on future coronal models.***

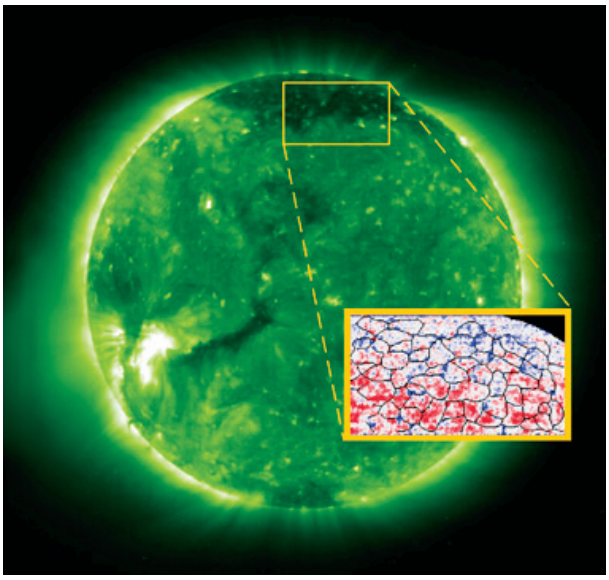

95-01481-70

Figure 2-3. Polar coronal holes, such as that seen in this SOHO/EIT image, are the source of the fast solar wind. SUMER measurements of Doppler-shifted coronal emission lines superposed on the magnetic network (inset) suggest that the high-speed outflow from coronal holes is associated with the chromospheric network (*Hassler et al.*, 1999). Solar Probe will make the first in-situ measurements of such outflows and will test the hypothesis that the primary source region for the fast solar wind is in the magnetic network.

The magnetic network in the quiet Sun looks remarkably similar to the network in coronal holes in spectral lines formed at lower, transition region temperatures, while it is harder to distinguish in lines formed at 10^6 K. If a similar coronal heating mechanism is at work in both the quiet Sun and coronal holes, any difference in their appearance is presumably related to the magnetic field topology, including, perhaps, its time dependence. The larger densities, apparently higher electron temperature, and different chemical composition of the quiet Sun would then be the result of a larger filling factor of closed magnetic field lines compared with that in coronal holes. While the imprint of coronal holes and equatorial helmet streamers is manifest in the solar wind in the form of fast and slow streams and embedded plasma sheets, the fate of the quiet Sun corona is unknown. Is the plasma in the quiet Sun confined by closed magnetic field lines, so that the fast wind is entirely of coronal hole origin? Or is there a mass loss from the quiet Sun as well, and if

so, what is its speed and how does it merge with the surrounding solar wind?

The magnetic field in active regions above sunspots provides the strongest confinement of hot plasma in the corona and is seen as bright x-ray loops, which often end in cusp-like shapes at their summit. At greater heights, these develop into streamers, which at solar minimum are large and elongated and form a belt around the solar magnetic equator. Remote sensing observations by SOHO/UVCS of the EUV emission lines of minor ions, combined with multi-fluid models, provide some clues about the source regions of the slow solar wind in coronal streamers, but the magnetic field topology in these regions and the role it plays in plasma outflow are unknown.

The complexity of the coronal magnetic field structure increases with increasing activity during the solar cycle. At activity maximum, disk observations show the existence of very complicated loop structures, and images of the extended corona show streamers protruding from the solar surface not only in the equatorial regions but at all latitudes around the disk as well (**Figure 2-4**). ***Solar Probe will determine where the slow solar wind forms in and around streamers and whether specific magnetic signatures, such as embedded current-sheets, are associated with its formation. Further, studies of solar wind sources during periods of solar maximum indicate a contribution to the wind from inside active regions as well.*** Solar Probe will determine the topology of magnetic field lines within active regions that give rise to solar wind flow.

Solar Probe will travel over coronal holes, the quiet Sun, and the active solar corona at distances between 9 and 4 R_S and under both quiet and active conditions. It will trace the origin of the fast and slow wind and correlate the flow speed with closed/open magnetic field line topologies, as measured by photospheric field measurements and determined indirectly through the in-situ measurement of such parameters as electron and energetic particle bi-directional streaming. Relating the in-situ coronal observations with surface structures will require remote sensing: ecliptic viewing of the white-light corona to trace field lines in the plane of the Solar Probe orbit, tomographic images from the all-sky coronagraph to identify coronal structures in the local spacecraft environment, and a polar view of the photosphere and photospheric magnetic fields from the spacecraft perspective to identify and locate the source region structures.

At present, relating the solar wind to the coronal magnetic structures in which it originates involves mapping the measured photospheric field out to some radius and extrapolating the solar wind flow radially backward to this same radius, where a boundary condition—typically that the magnetic field be radial—is imposed. The radius where the connection between solar wind backwards extrapolation and solar magnetic field forward extrapolation are matched is typically located at ~2–3 R_S. ***In-situ magnetic field measurements by Solar Probe during the fast latitude scan around perihelion will provide definitive ground truth for such mapping, and data from the polar passages will allow a better reconstruction of the magnetic field from the Sun into interplanetary space.***

In-situ measurements of the heliospheric magnetic field suggest a global structure that is generally similar to that predicted by *Parker* (1958), with

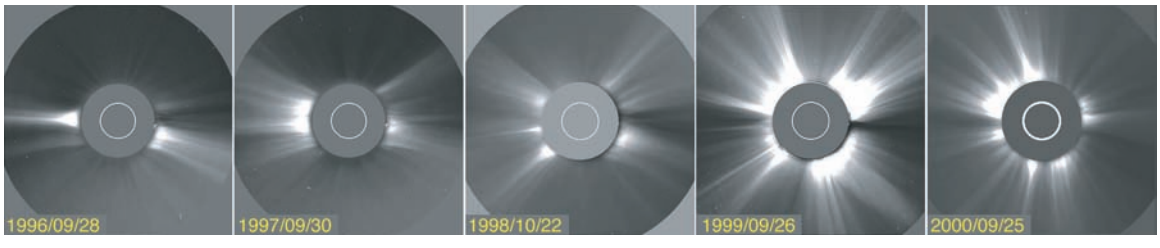

05-01481-71

Figure 2-4. SOHO/LASCO C2 images showing the evolution of the streamer belt during the rising phase of solar cycle 23. With increasing activity, polar coronal holes shrink and streamers appear at higher and higher heliolatitudes. The solar wind loses its orderly bimodal character and becomes a complicated mixture of fast flows from small coronal holes and transients embedded in a moderate-to-slow wind from all latitudes. Solar Probe will relate the flow speed measured in situ with the magnetic field structures in the coronal and photospheric source regions.

a spiral structure caused by the combination of solar wind expansion and solar rotation and a warped current sheet separating the northern and southern polarities. However, it has been proposed (*Jokipii and Kota*, 1989)—but not confirmed observationally inside 1.9 AU—that photospheric motions of magnetic field lines at low frequencies over the poles produce strong and variable deviations from the Parker's prediction for the global field structure at high latitudes. The resulting large-amplitude interplanetary fluctuations would be responsible for large changes in the predicted drift of galactic cosmic rays into the heliosphere. Ulysses observations of the magnetic field orientation in corotating rarefaction regions also show large deviations from Parker's model (*Murphy et al.*, 2002; *Schwadron*, 2002). Further evidence that the field deviates from the Parker model at large distances from the Sun came from the surprising detection by Ulysses of solar energetic particles at higher latitudes caused by shocks associated with cororating interaction regions (CIRs) formed at lower latitudes (*McKibben et al.*, 2001). It has been suggested that the observed departures from the Parker spiral result in part from the rigid rotation of coronal holes, which implies efficient reconnection between the open coronal hole field lines and the quiet Sun and the resulting diffusion of open field lines across coronal hole boundaries (*Fisk*, 1996; *Fisk and Schwadron*, 2001). In-situ measurements by Solar Probe of the magnetic field along a polar orbit spanning from a few AU down to 4 R_S will help test such theories of the heliospheric magnetic field.

Measurement Requirements

- In-situ magnetic field and plasma velocity measured continuously inside 0.3 AU
- Solar wind density, temperature, and composition as a proxy for individual flow tubes
- Electron distribution function (bidirectional streaming as evidence of closed magnetic field topology), correlated with solar wind composition and velocity and magnetic field data
- Photospheric magnetic field at high latitudes and line-of-sight velocity fields
- All-sky coronagraph imaging of the polar regions

2.1.2 How do the observed structures in the corona evolve into the solar wind? The outer solar atmosphere is structured by the magnetic field over a wide range of scales. Active regions and the quiet Sun display extended arcades and loops with thicknesses down to present observational resolution limits of a 1000 km or less, merging into the helmet streamers observed over the activity belt in coronagraph images. White light and UV coronograph-spectroscopic observations show coronal holes to be far from featureless as well. Bright striations, or plumes, can be traced all the way from the solar surface out to 30 R_S (**Figure 2-5**).

The relationship of plumes to the fast wind is poorly understood. They appear above x-ray bright points in the coronal holes, and are denser by factors of 2 or more than the surrounding regions. UV lines in the plumes appear to be narrower (i.e., the plumes are cooler) than in the darker lanes separating them, while measurements of outflows suggest that the dark lanes are preferential outflow regions (*Teriaca et al.*, 2003). Earlier measurements also revealed an apparent large first ionization potential (FIP) effect in plumes, thus excluding the possibility that they could be the source of the fast wind. However, more recent analyses using SOHO/CDS data have shown that plumes do not have a significant FIP effect, contradicting the earlier observations (*Del Zanna, Chiuderi, and Parenti*, 2004). Moreover, the scale height temperature in plumes seems to be too high to allow them to remain in static equilibrium (*Wilhelm et al.*, 1998), and dynamic wave activity, suggestive of acceleration mechanisms, has been observed in plumes by SOHO/EIT (*DeForest and Gurman*, 1998; *Ofman, Nakariakov, and DeForest*, 1999) and SOHO/UVCS (*Ofman et al.*, 1997; 2000). Finally, Doppler dimming measurements using SOHO/SUMER in the height range 1.05–1.35 R_S have found outflow velocities in plumes of order 60 km/s, exceeding those in the interplume regions (*Gabriel et al.*, 2003).

Fine-scale structures are observed in the fast wind as well as in coronal holes, including the so-called microstreams and pressure-balanced structures. These are fluctuations in radial velocity that last about 16 hours in the spacecraft frame and have a magnitude on the order of 50 km/s. Such structures may be a remnant of the original acceleration process (see Section 2.1.3), or perhaps are the final result of the merging of plume and interplume regions. ***By flying through the polar coronal holes over a range of distances from 30 to 8 R_S, Solar***

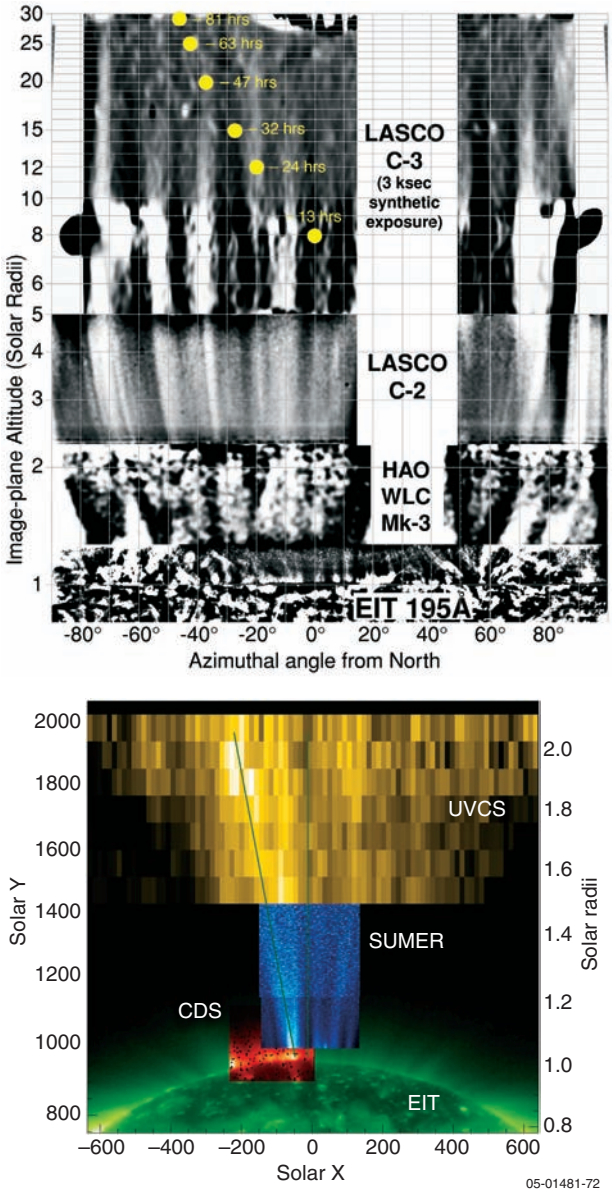

Figure 2-5. Top: The Solar Probe orbit (yellow dots) superposed on a composite image showing the polar plumes and interplume regions from the surface out to a distance of 30 R_S (*DeForest et al.*, 2001). Bottom: Composite showing detailed plume structure in the lower corona (*Teriaca et al.*, 2004). It is unknown how polar coronal plumes are formed, how their density structures are maintained in the solar wind, and what their fate in the more distant heliosphere is, as in-situ measurements from 1 AU are unable to identify them. Coronal plumes may or may not be a primary source of solar wind, a question which Solar Probe will answer.

Probe will observe and cross coronal plumes or their remnants, estimate their filling factor and contribution to the overall solar wind flow, and assess the expansion factors of the flow tubes carrying the solar wind flow. These observations will make it possible to clarify how microstreams form and evolve and to determine what their relationship to coronal fine-scale structures is. Achieving this objective will require both in-situ measurement of the magnetic field and plasma velocity and full distribution function (density temperature and composition of solar wind) to identify individual flow tubes and use of the tomographic reconstruction technique of the all-sky white-light coronagraph, which will provide information on the filling factor and geometrical distribution of plumes.

The LASCO and UVCS telescopes on the SOHO mission have made important contributions to our knowledge of the origins of the slow solar wind streams around helmet streamers (**Figure 2-6**). Sequences of LASCO difference images obtained

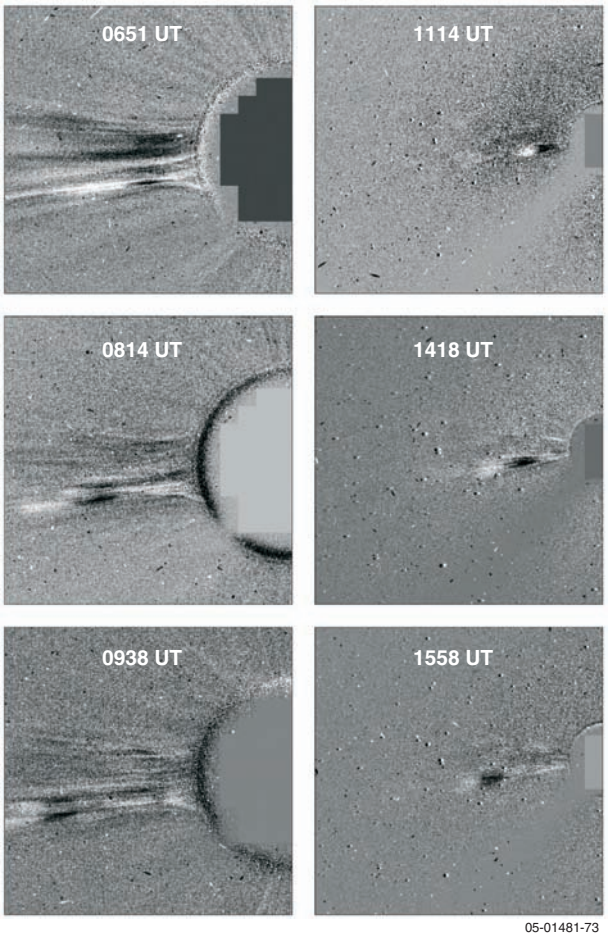

Figure 2-6. Difference images from the SOHO/LASCO coronagraphs showing the expulsion of material from the streamer belt (*Sheeley et al.*, 1997). These images show how dynamic the release of mass from the magnetically confined corona may be. Solar Probe will cross structures such as these at perihelion and will give detailed measurements of magnetic field, density, and velocities.

Relating Coronal and Solar Wind Structures

Plasma measurements in the solar wind have revealed a multitude of structures, from pressure-balanced structures to magnetic holes to micro-streams. It is not known if and how such structures are related to the coronal plumes observed in the corona via remote sensing. Our ability to determine the geometrical structure of coronal plumes and rays, as well as of equatorial streamers, suffers from the line-of-sight integration effects typical of an optically thin plasma. In-situ measurements of basic plasma properties and composition and the magnetic field as a function of distance from the Sun will not suffer from this limitation, however, and can be compared with the coronal structure as it is observed by both ground-based coronagraphs and Solar Probe's Hemispheric Imager itself. Sequences of images acquired as Solar Probe approaches and crosses coronal plumes will be used to determine the dimension and filling factor of the plumes. In-situ measurements will identify structures in the plumes such as entropy jumps and tangential discontinuities and will be compared with remote-sensing observations. Such structures can confidently be identified as spatial owing to the long lifetime of a plume relative to the time required for the spacecraft to pass through it. (Remote-sensing observations have shown that plumes are relatively stable structures with a lifetime of several hours. Solar Probe will cross a plume in a matter of minutes. For example, the spacecraft will traverse a plume that is 10,000 km in diameter at the Sun and ~120,000 km across at 8 R_S in 10 minutes.)

in 1996 (sunspot minimum) give the impression of a quasi-continuous outflow of material in "puffs" from the streamer belt (*Sheeley et al*., 1997). A quantitative analysis of moving features shows that they originate above the cusp of helmet streamers and move radially outward, with a typical speed of 150 km/s near 5 R_S, increasing to 300 km/s at 25 R_S (**Figure 2-7**). The average speed profile is consistent with an isothermal corona at the temperature $T \approx 1.1 \times 10^6$ K (SOHO/UVCS measurements indicating a temperature 1.6×10^6 K in the streamer core, at activity minimum) and a critical point near 5 R_S. The ejection of material may be caused by loss of confinement due to pressure-driven instabilities as the heated plasma accumulates or to current-driven instabilities (tearing and or kink-type instabilities) in the sheared field of the streamer. *Sheeley et al.* (1997) conclude that the features they observe trace the wind motion like "leaves in the wind." ***Solar Probe will cross the paths of these ejecta from streamers and will ascertain whether the ejection of coronal material occurs in a continuous flow or whether the puffs are in fact disconnecting plasmoids. If the latter, Solar Probe will determine the magnetic field configuration of the plasmoid as well as the magnetic morphology at the point of disconnection in the corona.***

Comparison of Galileo radio data with SOHO/UVCS images clearly shows the association of the slow wind with streamer stalks, that is, with the regions above the cusps of helmet streamers that include the current sheet (*Habbal et al*., 1997). It is not known, however, whether there is a single current sheet that runs along the nearly equatorial strip of maximum brightness in the white corona, i.e., along the streamer belt (as surmised by *Wang et al.,* 1997), or whether there are a number of stalk/sheet structures of finite longitudinal extent. Nor is the structure of current sheets in streamer stalks known. Do they have a simple structure, or are they made up of multiple sheets in a more complex magnetic field morphology, as is suggested in part by SOHO/UVCS measurements (*Noci et al*., 1997) and multiple current sheet crossings in situ (*Smith*, 2001)?

During periods of maximum activity the solar wind flow is much more variable and structured than the simple bimodal case found at solar minimum. The solar wind speed is typically lower, with the exception of very high speed CME-driven flows, and the source regions of the wind are more uncertain. The quasi-stationary (non-CME driven) flows appear to originate not only from coronal holes and their boundaries, but also from active regions, which are associated with both the slower and moderately fast winds. The solar wind from active regions seems to be structured into substreams separated by distinctive structures such as magnetic holes, plasma sheets, or lower entropy regions (*Neugebauer et al*., 2002).

White-light all-sky coronagraph images by Solar Probe from a polar perspective above 20 R_S will reveal the geometrical distribution of plumes in coronal holes, the plasma structures enveloping

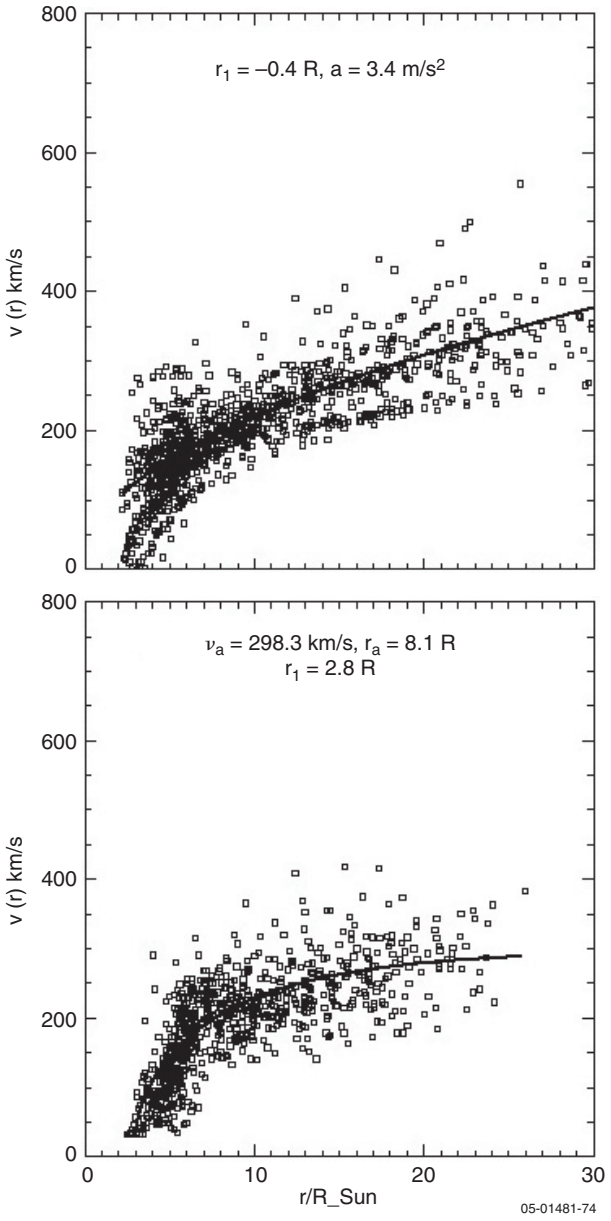

Figure 2-7. Scatter plots of the speed of density perturbations, or plasma puffs, as determined from difference images from the SOHO/LASCO instrument, as a function of distance from the Sun, together with a best fit for the radial velocity profile (*Sheeley et al.*, 1997). The plasma puffs serve as tracers of the slow solar wind, which experiences acceleration over a more (top panel) or less (bottom panel) extended radial distance from the Sun. Solar Probe will directly measure densities and speeds within this full distance range, determining the contribution of plasmoids to the overall mass flux from the Sun.

active regions and helmet streamers, and their filling factors, while in-situ measurements of plasma and magnetic field properties will clarify magnetic field morphology, the nature of plasma/current sheets, and the source regions of solar wind.

Measurement Requirements

- In-situ magnetic field and plasma velocity and full distribution functions (solar wind density, temperature, and composition as a proxy for individual flow tubes)
- Electron distribution function (bidirectional streaming as evidence of closed magnetic field topology), correlated with solar wind composition and velocity and magnetic field data
- Photospheric magnetic field at high latitude and line-of-sight velocity fields
- All-sky coronagraph imaging of coronal structures

2.1.3 Is the source of the solar wind steady or intermittent? As observed in situ at large distances from the Sun, the solar wind appears as a continuous, if structured, plasma outflow. Its quasi-steady character may be a property of the outflow at the solar source. However, the apparently quasi-stationary wind may also result from a number of spatially limited, impulsive events that are distributed over smaller scales (*Neugebauer*, 1991; *Feldman et al.*, 1997).

There is abundant evidence for the intermittent or "pulsed" (*Feldman et al.*, 1997) character of the high-speed wind: observations of microstreams and persistent beam-like features in the fast wind (**Figure 2-8**); interplanetary scintillation measurements of field-aligned density structures having a 10:1 radially-aligned axial ratio and apparent field-aligned speeds ranging from ~400 to ~1280 km/s (*Coles et al.*, 1991; *Grall et al.*, 1996); and remote sensing observations of the chromosphere, transition region, and corona revealing explosive, bursty phenomena (microflares) associated with magnetic activity over an extremely wide range of energy and time scales. *Feldman et al.* (1996, 1997) have interpreted the fine-scale structures observed in the fast wind as remnants of spicules, macrospicules, x-ray jets, and H-alpha surges and hypothesize that the fast wind results from the superposition of transient reconnection-generated jets. ***If this hypothesis is correct, then the heating of the corona leading to its time-dependent acceleration to form an ensemble of outward-going jets should be accompanied by the annihilation of oppositely-directed magnetic flux bundles clustered near the magnetic network, in turn leading to transient hard x-ray***

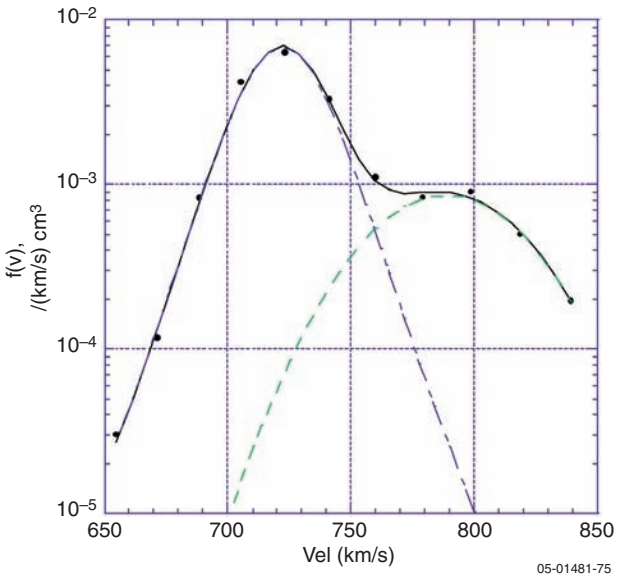

Figure 2-8. Two-beam model fit to the logarithm of phase space density for the Ulysses proton spectrum in the high-speed solar wind (*Goldstein et al.*, 2000). A proton beam with a drift speed of about 50 km/s, i.e., the Alfvén speed, gives the best fit. By measuring the plasma continuously within 65 R_S, Solar Probe will determine where this beam forms and whether it is the direct remnant of the acceleration mechanism or is produced in situ by wave–particle interactions.

and gamma-ray bursts, along with neutron production in the 1 to 10 MeV energy range, which could be detected by Solar Probe.

For the slow solar wind, evidence in favor of an intermittent origin is even more abundant. As mentioned above, blobs of plasma appear to be lost by helmet streamer structures overlying active regions, and various mechanisms have been proposed for this process. At solar maximum, an important and definitely intermittent solar wind component is present in the form of CMEs, and the fine-scale structure of the solar wind from active regions suggests at least a spatially structured origin for the various flow streams. More generally, smaller CME-like events at all scales could contribute significantly to the solar wind throughout the activity cycle.

Recent models of the solar wind (e.g., *Feldman et al.*, 1996; 1997; *Fisk*, 2003; *Schwadron and McComas*, 2003) require an intermittent, bursty origin for the solar wind, as the mass flux is lost by the reconnection of closed loops to open field lines. Loops may act as plasma storage deposits, accumulating energy and matter that will be injected in the solar wind. For a given energy flux, hotter loops contribute a larger mass flux, and therefore the asymptotic wind speed is lower. The inverse correlation of electron temperature and solar wind speed inferred from in-situ observations (*Gloeckler et al.*, 2003) may thus be an intrinsic signature of the loops that are the source of solar wind. In this view, all solar wind material comes from plasma that was once confined in coronal loops and has therefore been injected into the wind via magnetic reconnection with open field lines (*McKenzie and Mullan*, 1997). This view is also supported by in-situ measurements of the abundance of elements with a low first ionization potential (FIP bias), whose coronal accumulation can only occur in loops. FIP bias is close to 2 in the fast wind or high-latitude region and greater than 3 everywhere else (*Zurbuchen et al.*, 2002), evidence that the fast wind comes from small, short-lived loops, while slower wind may come from larger, longer-lived structures.

Direct, in-situ measurements of the structure of the solar wind, of the ion and electron distribution functions, and of elemental abundance variations close to the Sun will provide the data required to test these models. Solar Probe will directly measure both the electron distribution function and flow speeds of minor ions in the coronal hole, and, at perihelion, may directly sample composition differences on closed and open fields. By continuous direct sampling the plasma flow as the spacecraft approaches the Sun, Solar Probe will be able to assess the spatial and temporal character of the filling factor of the fast solar wind, while imaging the coronal structures that it will cross above 10 R_S. It will measure how microstreams in the fast wind change and whether they merge with pressure-balanced or other density-enhanced plume-like structures. The time-dependent variability observed in the wind might also increase close to the Sun, revealing signatures of multiple sources such as bursty events or micro-CME's.

Measurement Requirements

- In-situ magnetic field and plasma velocity at high cadence in inner heliospheric regions (below 20 R_S)
- Solar wind density, temperature, and composition
- Electron distribution function (bidirectional streaming as evidence of closed magnetic field line topology), correlated with solar wind composition and velocity and magnetic field;

strahl; high-energy tails of proton and helium distribution functions at high cadence
- Neutron and gamma-ray emissions
- Energetic electrons and ions

2.2 Trace the flow of the energy that heats the solar corona and accelerates the solar wind

The solar corona loses energy in the form of radiation, heat conduction, waves, and the kinetic energy of the solar wind flow. It is estimated that the energy flux required to balance such losses from the corona varies from $\varepsilon = 10^7$ erg/cm^2/s for active regions to $\varepsilon = 5–8 \times 10^5$ erg/cm^2/s for coronal holes and streamer belt cusps (*Withbroe and Noyes*, 1977). This energy must come from mechanical energy residing in photospheric convection, the solar magnetic field acting both to channel and store this energy in the outer atmospheric layers. However, the mechanisms by which the energy is transferred and dissipated to generate the hot corona, solar wind, and heliosphere throughout the Sun's activity cycle remain one of the fundamental unanswered questions in solar and heliospheric physics.

Remote-sensing measurements of the solar corona and in-situ measurement of particle distribution functions in the fast and slow solar wind streams have shown that the heating process is correlated with magnetic structure, and at solar minimum, with the basic bimodal nature of the solar wind. SOHO/UVCS observations using the Doppler dimming technique (*Li et al.*, 1998; *Kohl et al.*, 1998) (**Figure 2-9**) and interplanetary scintillation measurements (*Grall et al.*, 1996) indicate that the high-speed solar wind is rapidly accelerated near the Sun, reaching speeds of the order of 600 km/s within 10 R_S (*Grall et al.*, 1996; **Figure 2-10**). Observations of comet C/1996Y1 confirm a most probable speed of about 720 km/s for the solar wind at 6.8 R_S (*Raymond et al.*, 1998). Such rapid acceleration appears to result from the extremely large and anisotropic effective temperatures in the lower corona that have been deduced from measurements by SOHO/UVCS. These temperatures are much higher perpendicular to the magnetic field. The fast solar wind measured in situ shows what may be a relic of this anisotropy, which is smaller than that inferred from coronal observations, but persists in the distance range from 0.3 to 5 AU. Proton, alpha-particle, and minor ion distribution functions in the fast wind also present a non-thermal beam-like component whose speed is comparable to the local Alfvén speed. All these properties suggest that Alfvén or ion–cyclotron waves play a major role in coronal heating and solar wind acceleration. It is difficult, however, to separate remnant signatures of solar wind acceleration from in-situ processes. Measurements close to the Sun are required to distinguish the effects of in-situ processes and

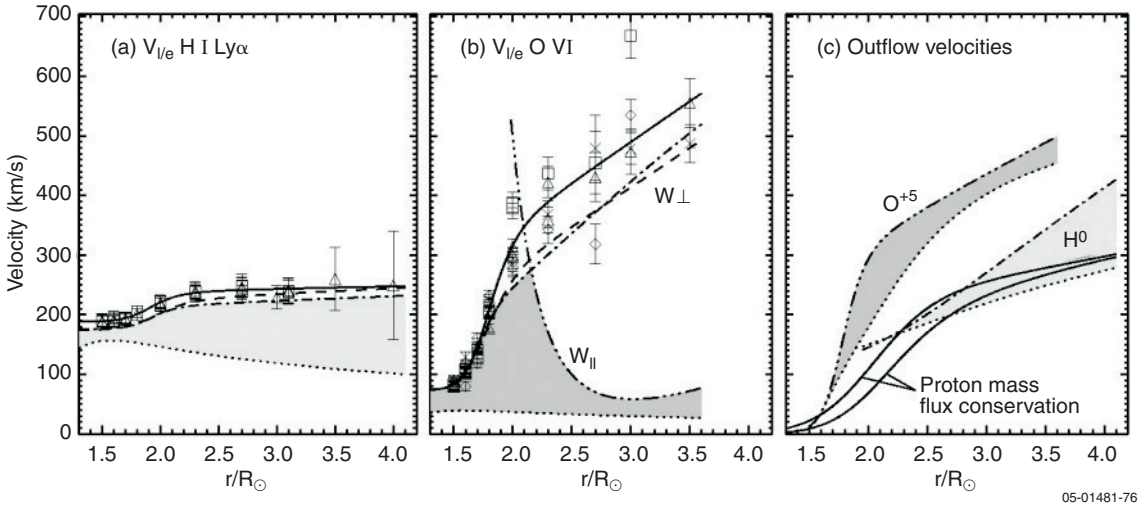

Figure 2-9. SOHO/UVCS emission line width observations show anisotropic velocity distributions of neutral hydrogen (a proxy for protons) and O^{5+} and preferential acceleration of minor ions relative to the hydrogen atoms. Shaded areas indicate uncertainties due to thermal broadening. Preferential acceleration of the minor ions may result from ion-cyclotron resonance or from wave-particle interactions involving nonlinear Alfvén waves. Solar Probe will establish the role of various wave-particle interactions in heating the corona and accelerating the solar wind (*Kohl et al.*, 1998).

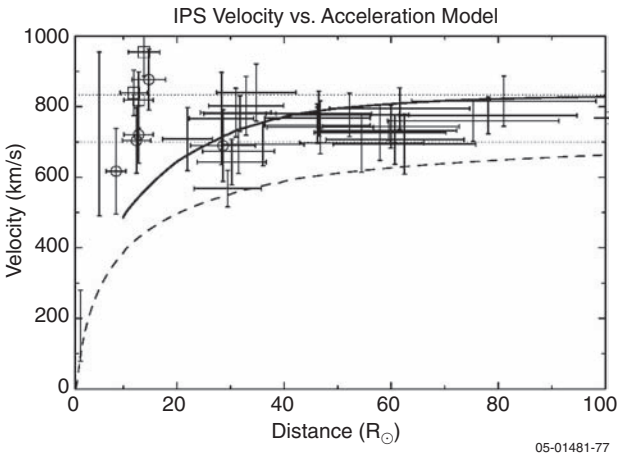

Figure 2-10. Apparent flow speed of the fast wind vs. distance determined from radio scintillation measurements by EISCAT, VLBA, and Spartan 201-01, showing rapid acceleration of the solar wind at distances ≤ 10 R_S (*Grall et al.* 1996). These measurements rely on the phase shifts in radio signals caused by the movement of density structures across the line of sight, and therefore contain the effects of compressive waves. Solar Probe will provide continuous direct measurements of the solar wind inside 65 R_S, with significantly smaller error bars down to 5–10 R_S.

obtain a more direct measure of the acceleration mechanism(s).

The different properties of the turbulence observed in the fast and slow solar wind are further evidence of the role played by turbulence and wave–particle interactions in coronal heating. Fast streams contain stronger fluctuations in transverse velocity and magnetic fields, and display a higher degree of correlation between the velocity and magnetic fluctuations (often described as a well-developed spectrum of quasi-incompressible Alfvén waves propagating away from the Sun). In the slow wind, this correlation occurs at a much lower level, while larger fluctuations in density and in the magnitude of the magnetic field are present, indicating a more evolved magnetohydrodynamic (MHD) turbulent state there. This difference in turbulence state between fast and slow wind streams, together with the fact that slow wind distribution functions are much closer to equilibrium, suggests that the outward propagating wave flux contributes to the heating of the steady fast wind, while the slow wind is heated much more variably. It is not known, however, how the turbulent flux increases toward the Sun, whether it is sufficient to power coronal heating and solar wind acceleration, and how it is driven by time-dependent events in the photosphere, chromosphere, transition region, and lower corona.

By providing the first in-situ measurements of the distribution functions, waves, turbulence, and electromagnetic fields from 0.3 AU to 4 R_S, and by correlating them with plasma and magnetic field structures, Solar Probe will be able to answer the basic questions of how the solar corona is powered, how the energy is channeled into the kinetics of particle distribution functions in the solar corona and wind, and how such processes relate to the turbulence and wave–particle dynamics observed in the heliosphere.

2.2.1 How is energy from the lower solar atmosphere transferred to, and dissipated in, the corona? An abundant amount of mechanical energy is available in photospheric motions. The question is: How is this energy transmitted upwards and dissipated in the right place, within a few solar radii of the surface, to heat the corona? The coincidence of magnetic and thermal structures suggests that the magnetic field plays a fundamental role in channeling, storing, and dissipating the energy, both via the emergence of photospheric flux tubes and through their continuous distortion and convection by the photospheric velocity fields. Photospheric motions on different timescales have different effects, which may be broadly divided into two categories: power at periods below a few minutes propagates in the form of MHD waves (AC), while power at lower frequencies is stored by currents or gradients in the coronal magnetic field (DC) (*Hollweg*, 1974; 1978).

Because of the high coronal temperatures, the resistivity of the coronal plasma is weak (i.e., magnetic Reynolds numbers are of order $S \sim 10^{12}$ based on collisional resistivity). Weak resistivity implies that the dissipation of MHD waves must occur via the development of steep gradients and small scales—through nonlinear steepening or a turbulent cascade, for example, or through phase-mixing and resonant absorption. In the case of energy stored in DC currents, dissipation occurs by means of current sheet collapse and magnetic reconnection. Ultimately, both mechanisms require large electric fields, so that particle acceleration occurs, resulting in non-thermal particle distributions.

Whether the solar corona is heated by low-frequency waves resulting from motions naturally arising in the photosphere or whether the

Tracing the Flow of Energy in the Corona

As the Solar Probe approaches the Sun, it will carry out the first direct measurements of local particle distribution functions, density and velocity field fluctuations, and electromagnetic fields. Cross-correlations between density, velocity, and magnetic and electric field fluctuations will be used to distinguish energy in dynamic fluctuations from thermal broadening. The amount of energy in the electrons will be determined directly, thus placing quantitative limits on the role of electron heat-flux in coronal energy transport. In the fluctuations, temporal and spatial wave-vectors perpendicular and parallel to the magnetic field directions will be convolved and Doppler-shifted in the spacecraft frame. The Doppler shift for transverse scales of order 10^5 km at the polar transit (corresponding to supergranule scales at the surface) is of the order of magnitude of 10^{-3} Hz, which is close to frequencies of the characteristic 5-minute oscillations. Again, cross-correlation of velocity, density, and electromagnetic fluctuations will allow a partial separation of spatial and temporal effects. Measurements of the minor ions, in particular alpha particles, will also allow filtering of some of the dominant Alfvénic wave-modes so that the relative role of the so-called Alfvénic turbulence can be quantitatively determined. Identifying smaller-scale structures, both propagating (shocks from the steepening of compressible modes) and non-propagating (current sheets), will also require use of the complete distribution functions and electromagnetic fluctuations at the highest resolutions. In the latter case, multi-instrument coordination will be achieved using pattern recognition from in-situ and simulated data.

dominant energy source resides in the currents stored via slower field line motions has been the subject of strong debate. Among the MHD waves, only Alfvén waves would appear to survive the strong gradients in the chromosphere and transition region, because slow modes steepen into shocks while fast modes suffer total reflection. Transmitted waves propagate at large angles to the radial direction, since a 100-s wave with an Alfvén speed of 2000 km/s has a wavelength along the direction of the field of 2×10^5 km, while the perpendicular coherence will be at most 10^4 km. Longer-period waves must have an even larger ion anisotropy. Waves reaching the lower corona must therefore be shear Alfvén waves, although discrete coronal structures such as loops and plumes might channel surface waves and propagate energy as global oscillations as well.

Several mechanisms for the dissipation of waves have been proposed, among which phase-mixing (*Heyvaerts and Priest*, 1983) and resonant absorption (*Ionson*, 1978) are the most widely invoked. Both processes rely on gradients in coronal structures or, more generally, on the presence of non-uniform phase speeds, resulting in the corrugation of wave-fronts and the development of small scales as the waves propagate. It is not clear, however, that wave dissipation by either process could occur within the distance required to produce the high-speed wind (i.e., 1.5 R_S from the coronal base in open field regions) (*Hansteen et al.*, 1997). Phase mixing and resonant absorption might play a specific role in coronal structures such as plumes, where guided surface and slow-mode waves have been remotely observed and modeled (*Ofman et al.*, 2000). Alternatively, the upward-transported waves may drive low-frequency turbulence and a quasi-perpendicular cascade involving counter-propagating waves (*Matthaeus et al.*, 1999) to provide the source for extended heating at smaller scales needed to drive the fast wind from coronal holes. In any of these scenarios, the details of the kinetic processes that convert small-scale fluid motions into thermodynamic internal energy remain to be discovered.

Parker (1988) argued that most of the energy reaching the corona must come from the slow displacement of closed field lines in low-lying loops, which are tangled until they spontaneously develop current sheets and then reconnect, resulting in elementary dissipation events known as nanoflares. In this scenario, the energy for coronal heating is stored in presently unmeasured coronal magnetic field fluctuations. On the basis of coronal heating energy requirements, Parker estimated that 10^{24} ergs must be released per elementary event. MHD numerical experiments have shown how power-law distributions in energy release are a natural outcome of the Parker scenario, with indices not far from those observed in x-ray flaring events (*Georgoulis et al.*, 1998). The original nanoflare heating scenario has been strongly debated, observational work having focused mostly on the power-law index characterizing the distribution of the panoply of small-scale energetic events observed in the corona, transition region, and network. However, extrapolating the data

to lower energies and inferring the total contribution of such events to coronal losses is subject to strong uncertainties (*Cargill and Klimchuk*, 2004). The direct detection of nanoflares is beyond the scope of the Solar Probe mission. However, ***the detection of energetic particles and their spectra, as well as the measurement of the coronal magnetic field and its fluctuations at perihelion, where confined coronal plasma may be traversed, will provide important indirect evidence for the lower energy scales to which bursty events extend.***

Recently the role of low-lying loops and reconnection at transition region heights due to photospheric dragging of network and intra-network fields (magnetic carpet vs. canopy) has been stressed as a potential source of energy, in the form both of direct heat and of waves launched by reconnection (*Axford and McKenzie*, 1992; *Schrijver*, 1997; *Longcope et al.*, 2003; *Fisk*, 2003). High-frequency modes of this type (e.g., ion–cyclotron waves) (*Marsch and Tu.*, 2001) can propagate into the corona, where they can drive the heating of both protons and minor ions (see Section 2.2.2 below). Similar phenomena may be involved in the polar radial magnetic field inversions observed by the Ulysses spacecraft (*Yamauchi et al.*, 2004). Reconnection, buffeting of field lines associated with photospheric oscillations, and direct field line dragging by photospheric velocity fields have also been invoked to account for the formation of chromospheric and coronal features such as spicules and macrospicules (*Sterling*, 2000), although no theory has yet been able to completely describe such phenomena.

With a comprehensive measurement of plasma and electromagnetic fluctuations in the inner solar wind (<20 R_S), ***Solar Probe will determine how the energy that powers the corona and wind is dissipated and what the dominant dissipative structures are, as well as the frequency spectrum of electromagnetic fluctuations.*** Small-scale magnetic reconnection, of both the "anti-parallel" and "component" types, occupies an important place in the closed field line Parker mechanism and in open field line cascade and phase mixing models. ***An important set of investigations on Solar Probe will therefore be the multi-instrument detection of signatures of small-scale reconnection, such as bidirectional plasma jets, accelerated particles, magnetic field, and velocity gradient correlations along the trajectory.***

Energy transport and dissipation mechanisms strongly depend on the mean free path of particles in the coronal plasma, which varies drastically both with distance from the Sun (from the base of the corona to the supersonic solar wind), as well as across coronal structures (coronal holes to helmet streamers). This dependence has led to the suggestion that coronal heating arises from energy stored in non-thermal wings of particle distribution functions generated between the chromosphere and transition region or, more generally, in the region where the solar atmospheric plasma changes from collisional to collisionless. The higher temperatures and subsequent outflows would then arise naturally through velocity filtration by the Sun's gravitational potential (*Scudder*, 1994).

By measuring electron and ion distribution functions up to large energies as a function of distance from the Sun in the inner heliosphere, ***Solar Probe will be able to assess the contribution of the velocity filtration mechanism to shaping coronal distribution functions. Solar Probe will clarify the relative role of reconnection compared to other heating mechanisms and will for the first time identify the coronal regions above which Coulomb collisions are negligible.***

Measurement Requirements

- Magnetic field, velocity field, and density fluctuations and their spectra
- Particle distribution functions of protons, electrons, alpha particles, and possibly minor ion species; suprathermal populations
- High-cadence 3-axis electric and magnetic field plasma wave measurements
- Plasma wave electric and magnetic field wave form for coherent structure identification

2.2.2. What coronal processes shape the non-equilibrium velocity distributions observed throughout the heliosphere? The significant broadening of minor ion emission lines observed in coronal holes with Spartan and UVCS on SOHO results from unresolved ion motions and is indicative of high-temperature anisotropies in the coronal holes, with preferred heating in a direction perpendicular to the radial and preferential acceleration of minor ions over neutral hydrogen, which in the lower corona should be strongly coupled to protons (*Li et al.*, 1998; *Kohl et al.*, 1998). Preferential heating of

minor ions with respect to protons and temperature anisotropies is also observed in the fast solar wind, where in-situ measurements have shown that the perpendicular temperature in the thermal core component of the proton velocity distribution is higher than the parallel temperature. In-situ measurements have also shown that the magnetic moment is not conserved, implying that plasma turbulence heats the ions significantly in directions perpendicular to the magnetic field from 0.3 out to 1 AU and beyond. Whether this turbulent heating is the primary energy source closer to the Sun, however, is unclear; also, because the temperatures determined from remote-sensing techniques are indirect and are dependent on empirical modeling, discriminating turbulent bulk perpendicular and parallel motions from real temperatures requires direct measurement. ***By carrying out such measurements inside 0.3 AU for protons, helium, and minor ions, Solar Probe will clarify the role of turbulence and wave–particle interactions in shaping the particle distribution functions. Solar Probe temperature data will also provide a yardstick for future remote sensing temperature observations.*** We emphasize that remote sensing measurements of the Lyman-alpha line determine properties of the neutral hydrogen distribution, whose coupling to protons depends crucially on the density profiles; semi-empirical models of the solar wind require an average mean proton temperature of at least 3 MK between 2 and 4 R_S, but only ***Solar Probe will for the first time measure the proton temperatures in the corona directly (perhaps approaching or passing beyond the temperature maximum at low latitudes), leading to an understanding of the energetically dominant wave–particle interaction properties.***

In addition to the core component, the proton distribution in the fast solar wind has an accelerated beam component whose drift speed is comparable to the Alfvén speed, which is close to the alpha particle drift speed with respect to the protons (*Feldman et al.*, 1974; *Marsch et al.*, 1982; *Tu et al.*, 2004). (The two principal explanations put forward for the presence of such beams are direct generation in the jet superposition picture of solar wind formation (Section 2.1.3) and wave–particle interactions in the solar wind acceleration region. The relative drift of protons and alpha particles is observed beyond 0.3 AU in the solar wind, and should reach enormous values if it remains close to the Alfvén speed approaching the Alfvénic point. Solar Probe measurements of the shape of the proton and alpha-particle distribution functions will describe this phenomenon below 0.3 AU and determine how this drift originates, yielding clues about the responsible mechanisms.

In-situ measurements of the solar wind and remote sensing observations of coronal holes (Section 2.2.1) strongly implicate resonant interaction with ion–cyclotron waves as the mechanism responsible for heating and accelerating coronal hole ions to generate the fast solar wind. The evidence pointing to this mechanism includes observations of extended proton heating, minor ion heating, equal thermal ion velocities, and greater-than-mass-proportional ion temperatures. A natural process that might lead to these effects is "cyclotron sweeping" (*Hollweg and Isenberg*, 2002), which relies on the gradual decrease with distance from the Sun of the ion–cyclotron frequency relative to the Alfvén wave frequency. Minor ions, with resonance at lower frequency, would therefore come into resonance closer in the corona, and naturally tap higher-energy regions of the turbulent spectrum, assuming a standard, decreasing shape for energy as a function of frequency. Although this process may work for minor ions, its efficiency is dramatically reduced for protons (*Isenberg*, 2004), calling its relevance into question as a whole. ***Solar Probe measurements of the high-frequency wave spectra and wave-mode analysis, together with proton and alpha-particle distribution functions, will determine the relevance of ion–cyclotron waves in regulating solar wind acceleration processes.***

Other possibilities exist for converting collective plasma energy into thermal energy, thereby shaping plasma distribution functions: in addition to the cyclotron mechanisms discussed above, which feed on fluctuations that vary along the magnetic field, there are also a variety of processes that are powered by cross-field perpendicular fluctuations. Among these are oblique wave damping or Landau damping, weakly collisional and/or compressive damping, and mechanisms involving nonlinear dynamics of current sheets that might be formed by small-scale shears or reconnection activity. The last-mentioned include kinetic (lower hybrid) plasma turbulence, electron solitary structures, mode conversion, and nonlinear beam instabilities. As an example, in the solar wind, there is evidence

that the dissipation of kinetic Alfvén waves at large perpendicular wavenumbers, due at least in part to Landau damping and gyroresonant effects, contributes significantly to plasma heating (*Leamon et al*., 1998).

Solar Probe data will allow identification of the heating mechanisms that operate in the corona and of their relative contributions to coronal heating. Do these same processes occur inside 20 R_S? What are the properties of both high- and low-frequency fluctuations responsible for wave–particle interactions and turbulence? ***Solar Probe will measure the proton and alpha particle distribution functions and the temperatures of minor ion species and their anisotropies and will determine their relationship to fluctuations in the magnetic field and the bulk velocity field. Solar Probe will thereby identify the basic interactions shaping the distribution functions in the solar wind acceleration region, providing the ground truth knowledge needed to answer the most basic questions about energy dissipation and heating in the corona.***

Measurement Requirements

- Particle distribution functions of protons, electrons, alphas, and possibly minor ion species
- Magnetic, velocity, density, and temperature fluctuations in the MHD range (below the proton cyclotron frequency)
- Plasma wave measurements at high cadence; electric field measurements

2.2.3. How do the processes in the corona affect the properties of the solar wind in the heliosphere? The fast wind displays Alfvénic turbulence, i.e., fluctuations sharing many properties of large-amplitude Alfvén waves propagating away from the Sun (including nearly vanishing magnetic pressure fluctuations), but with a flat frequency (f) spectrum, $E_f \sim 1/f$. The origin of the shape of this "flicker noise" spectrum is not understood, although it is suggestive of the presence of scale-invariant processes, such as reconnection, in the lower corona (*Matthaeus et al*., 1986). At higher frequencies the spectrum gradually steepens, which is presumably associated with an active turbulent cascade. The break point between the two spectral forms is, roughly, at the measured correlation scale of the fluctuations, which gradually evolves towards lower frequency with increasing heliocentric distance.

Is the lower-frequency $1/f$ spectrum a remnant of the wave flux that contributes to plasma heating in the lower corona? The existence of a broad spectrum is evidence in itself of significant dynamic evolution, for otherwise significant traces of transmission through the coronal cavity should be found, in the form of preferred frequencies or broad "lines" in the spectrum (*Velli*, 1993). But if the very-low-frequency solar wind fluctuations are remnants of coronal heating, then Solar Probe will encounter and detect additional required factors, such as a flux of "inward" type Alfvénic fluctuations, a possible component of compressive fluctuations, and signatures of an incompletely understood mechanism for containing the inward waves in the presence of the turbulence near the Alfvénic critical point. ***There has been some debate as to whether signatures of the global solar oscillations, such as the 5-minute photospheric p-modes, survive in the solar wind, as measurements are very close to the noise level as measured in situ (*Thomson et al., *1995). Solar Probe measurements will also determine whether such oscillations are present in the corona, before there is time for nonlinear dynamics to smooth them out.***

Simple extrapolation, along with interplanetary scintillation observations (*Canals et al*., 2002), suggests that Solar Probe will observe rms velocity field fluctuations of about 200 km/s at the Alfvénic critical point, while at the base of the corona limits obtained from spectral line-widths indicate a turbulent velocity near the transition region of 30 km/s (*Chae et al*., 1998, **Figure 2-11a**). Observations of fluctuation amplitudes from the Sun out to 1 AU are summarized in **Figure 2-11b** (*Cranmer and van Ballegooijen*, 2005). Such measurements appear to be broadly consistent with an Alfvén wave propagation that is modified very little by nonlinear effects, in which case there would be little or no contribution from these waves to coronal heating. ***Solar probe will unequivocally determine whether the currently observed fluctuations are in fact one of the principal agents in the coronal heating and wind acceleration process.***

By measuring the fluctuations of velocity, density, temperature, and magnetic fields from 0.3 AU down to 4 R_S, Solar Probe will determine how the Alfvénic turbulence observed in high-speed solar wind streams is generated and how it evolves, how much energy is available, how it is distributed in space and

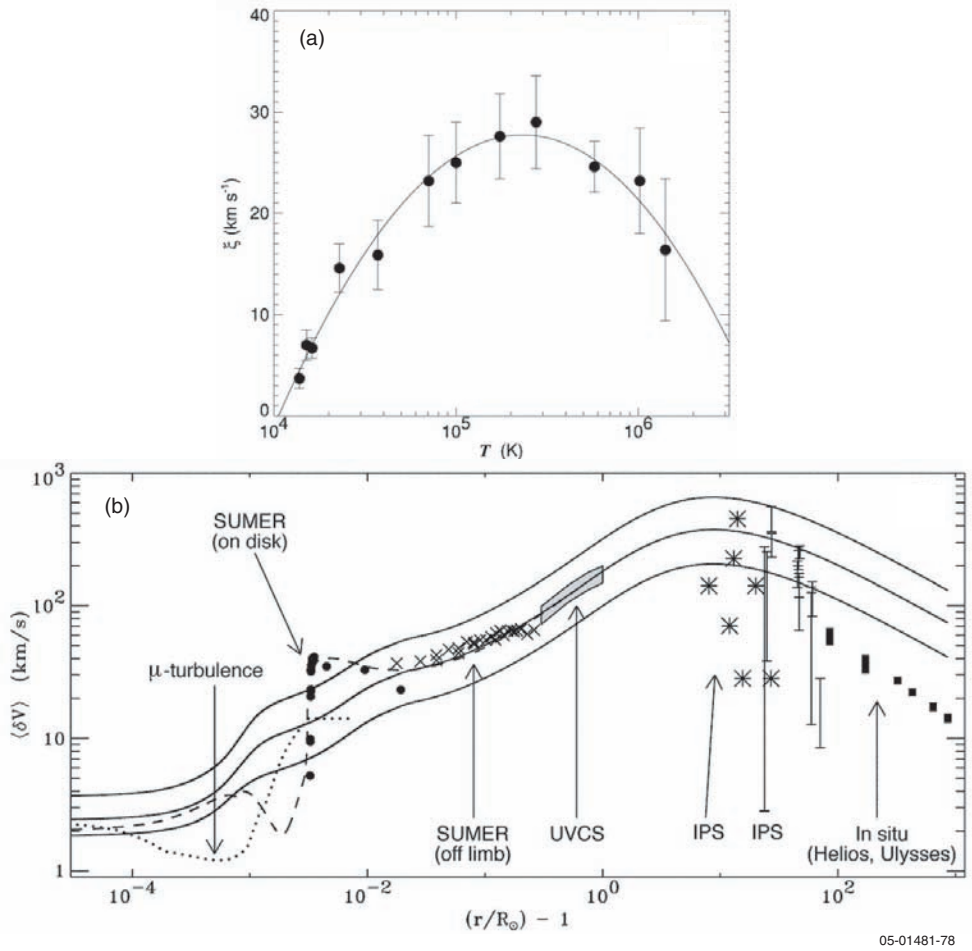

Figure 2-11. (a) Non-thermal component to line model broadening in the solar atmosphere as a function of temperature showing a maximum around 30 km/s at transition region heights (*Chae et al.*, 1998). (b) Composite of observations of magnetic field and velocity field fluctuation amplitude with height in the solar atmosphere (*Cranmer and van Ballegooijen*, 2005). Solar Probe will fill the gap between the data labeled UVCS and IPS by directly measuring velocity and magnetic field fluctuations with continuous coverage between 65 and 4 R_S. It will also obtain the spectral distribution of the fluctuations and clarify their role in coronal heating and solar wind acceleration.

time, and what wave-modes and/or structures are excited. Solar Probe will also ascertain whether the observed in-situ fluctuations are indeed the remnant of the coronal heating process and will determine how their evolution is coupled to the evolution of the thermodynamic properties of the plasma itself, principally temperature, density, velocity, and average magnetic field. Moreover, beyond their importance for addressing fundamental questions in solar physics, ***Solar Probe's measurements of the properties of turbulence and nonlinear plasma dynamics in the corona and solar wind will be a watershed for all of astrophysics, where these phenomena are invoked over widely different contexts, from accretion disks to the collisionless shocks occurring in galaxy-cluster formation.***

Apart from determining the initial conditions for the origin the solar wind turbulent spectra, coronal processes have a large impact on other solar wind properties. For example, the composition of the solar wind and its variation with wind speed, which also follows a bimodal pattern, show that the slow wind is enhanced in low first ionization potential (FIP) elements with respect to photospheric values (*Zurbuchen et al.*, 2002). This most probably results from the longer confinement time, in or around closed coronal loop type structures, of the slow solar wind plasma (Section 2.1.3). Solar Probe will measure the abundances of heavy ions in the slow and fast wind close to the Sun, ions that to date have been observed only remotely or far from the Sun in situ. Solar Probe may also be able to detect

light FIP elements, such as Na, which, due to their low abundance, have not been observed so far. The measurement of the FIP effects in these elements can provide strong constraints on the mechanism responsible for the FIP effect and yield clues to the ionization processes in slow and fast solar wind plasma.

The outer solar corona between 5 and 20 R_S plays a fundamental role in determining large-scale properties such as solar wind angular momentum loss and global heliospheric structure. This is because the Alfvénic critical surface, where the solar-wind speed overtakes the Alfvén speed, defines the point where the plasma ceases to corotate with the Sun, i.e., where the magnetic field loses its rigidity to the plasma. This is also the region where the velocity gradients between the fast and slow speed streams develop, determining the initial conditions for the development, further out, of corotating interaction regions (CIRs). ***In crossing this critical distance range for the first time, Solar Probe will obtain precise measurements of the plasma flow, magnetic field, and their gradients. These measurements will make it possible to determine the initial conditions for the development of heliospheric structure, enabling a predictive approach to mean global heliospheric structure based on actual coronal measurements.***

Measurement Requirements

- Basic plasma (proton, alpha particles, minor ions) and magnetic field measurements
- Plasma wave electric field measurements to above the plasma frequency for quasi-thermal noise spectroscopy and high-resolution electric and magnetic field wave-form data for electromagnetic fields
- Plasma wave electric and magnetic field measurements up to the proton cyclotron frequency
- Electron temperature gradient, density gradient, electric field/interplanetary potential
- Remote sensing of underlying photospheric magnetic structure for correlation with in-situ data

2.3. What mechanisms accelerate and transport energetic charged particles?

The current paradigm (e.g., *Reames*, 1999) defines two classes of solar energetic particle (SEP) events. Gradual events are accelerated by CME-driven shocks and are characterized by roughly coronal abundances and charge states. Impulsive events are generally much smaller events associated with impulsive x-ray flares and are characterized by enrichments in ^{3}He, heavy ions such as Fe, and electrons, with charge states characteristic of temperatures ranging from ~5 to 10 MK. This paradigm distinguishes between two separate acceleration processes and acceleration sites, both driven by eruptive events on the Sun: (1) CME-driven shock acceleration starting in the high corona and continuing into interplanetary space and (2) acceleration at the flare site, presumably driven by magnetic reconnection. Both processes are known to operate in larger SEP events, and studies at 1 AU during Solar Cycle 23 present a complex picture of events that often exhibit characteristics of both gradual and impulsive SEP events (e.g., *Cohen et al.*, 1999; *Cane et al.*, 2002; *Tylka et al.*, 2004). In addition to such transient energetic events, observations at 1 AU show a continual outflow of intermediate-energy particles from the Sun extending from suprathermal energies to >10 MeV/nucleon. The mechanisms responsible for the acceleration of these particles are not known.

Distinguishing the various acceleration processes occurring at the Sun on the basis of data acquired at 1 AU is difficult. Transport through the interplanetary medium washes out the time structure, reduces the intensities by orders of magnitude, and leads to mixing of particles from different acceleration sites. Solar Probe measurements, made at distances as close to the Sun as 4 R_S, will not suffer from transport effects, because the Probe will sample energetic particles close to their acceleration sites on the Sun and will explore, in situ, acceleration sites in the corona and inner heliosphere. In particular, recent results from ACE, SOHO, and WIND point to the increasing importance of the high corona (2 $R_S < r < 20\ R_S$) as an acceleration site for energetic ions and electrons—a region that Solar Probe will sample directly. These measurements will address key questions important for understanding solar energetic particle acceleration and transport. The following discussion presents examples of how Solar Probe can address these questions.

2.3.1 What are the roles of shocks, reconnection, waves, and turbulence in the acceleration of energetic particles? In ^{3}He-rich SEP events,

abundance ratios of ^{3}He/^{4}He commonly exceed those in the solar wind (~5×10^{-4}) by 3 orders of magnitude or more. In addition, heavy nuclei abundances (relative to coronal values) tend to increase with increasing mass, resulting in roughly tenfold enhancements of Fe/O of and in enhancements of "ultraheavy" (Z > 30) elements by factors as large as 10^2 to 10^3 (*Mason et al.*, 2004; *Reames*, 2004; see **Figure 2-12**). Explanations of this highly selective fractionation have generally focused on plasma processes that heat and/or accelerate ions in a certain range of charge/mass ratio, including models based on electromagnetic ion–cyclotron waves (see, e.g., the review by *Miller*, 1998). However, *Mason et al.* (2004) have suggested that these processes fail to account for the overall composition pattern and suggested that coronal shocks may be the accelerating agent in impulsive SEP events.

About 1000 impulsive SEP events per year are estimated to occur on the Sun during solar maximum, but the number may be much larger because many small events undoubtedly go undetected at 1 AU. **Figure 2-13** shows a series of ~10 events observed at 1 AU during a period of several days. Observations of the same ^{3}He-rich SEP event by IMP-8 at 1 AU and by Helios at 0.32 AU show that the event is ~100 times more intense at 0.32 AU and much more localized in time (**Figure 2-14**). Observed even closer to the Sun, these events will appear as intense bursts of only minutes in duration. ***With simultaneous solar observations from***

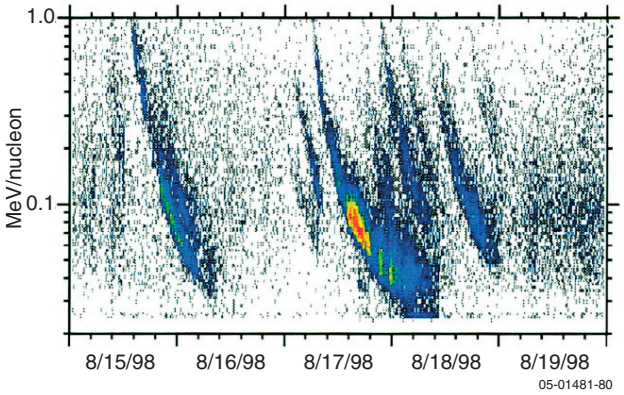

Figure 2-13. Energy vs. time plot showing a series of impulsive events observed by ACE in 1998 (Mason et al., 1999). Because of velocity dispersion, the highest-energy particles arrive first.

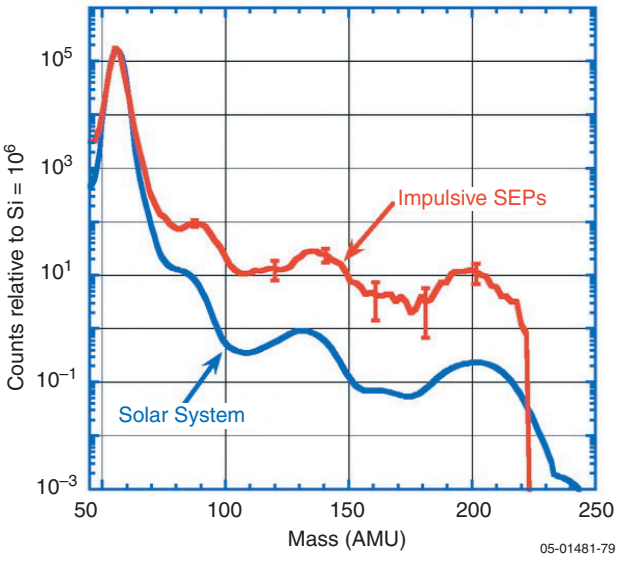

Figure 2-12. Nuclei with mass >90 (Z > 40) are overabundant in impulsive solar energetic particle events (compared to solar material) by factors ranging from ~10 to ~50 when normalized to Fe. Since Fe is itself overabundant by a factor of ~10, the Z > 40 overabundance is even greater when normalized to He or oxygen (observations by *Mason et al.*, 2004). The origin of these overabundances is not understood.

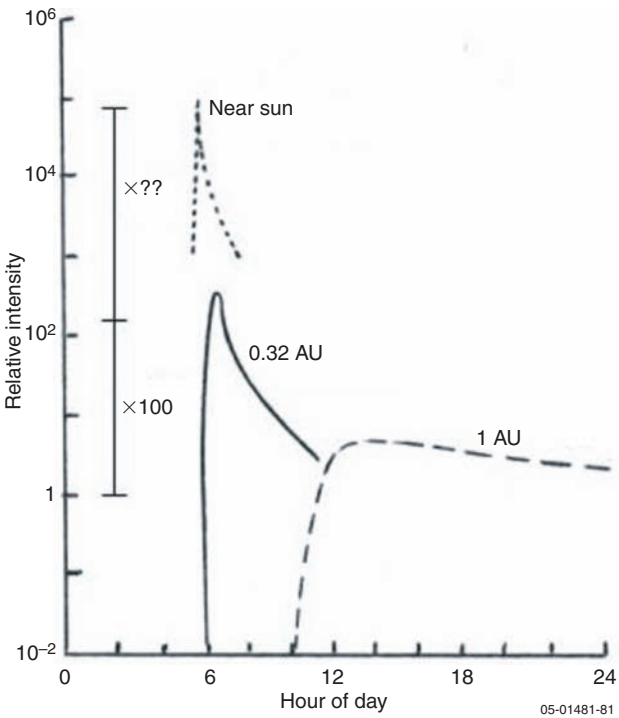

Figure 2-14. Time profiles of an impulsive ^{3}He-rich event observed at 1 AU on May 17, 1979 by ISEE-3 and at 0.32 AU by Helios-1 (based on data in *Mason et al.*, 1989). Both spacecraft were magnetically well connected to the flare site. Note that the peak intensity is ~100 times greater at 0.32 AU. Closer to the Sun the event will be even more localized in time.

1 AU it should be possible to trace events observed by Solar Probe to the flare site, to measure the flare properties, and to obtain the underlying magnetic field configuration. In addition to composition measurements, Solar Probe will measure near-relativistic (V > 0.1 c) electrons from these events within a fraction of a minute of their release. These electrons are particularly important for untangling acceleration processes because their acceleration sites can be sensed remotely by microwave radio emission or hard x-rays. Analogously for energetic ions, ***Solar Probe may also observe gamma rays and neutrons from these solar flare events, providing information on the accelerated particle components on closed field lines in the solar atmosphere.***

Although the occurrence rate of SEP events is greatly reduced at solar minimum, strong evidence suggests that particle acceleration occurs continuously on the Sun or in the inner heliosphere, even at solar minimum. All solar wind species that have been measured (H^+, He^+, and He^{++}) exhibit suprathermal tails that extend up from several times the solar wind speed (~10 keV/nucleon (**Figure 2-15**). These tails are more prominent in the ecliptic than over the poles, and they are continuously present, even in the absence of solar activity or interplanetary shocks (e.g., *Gloeckler et al.*, 2000). The

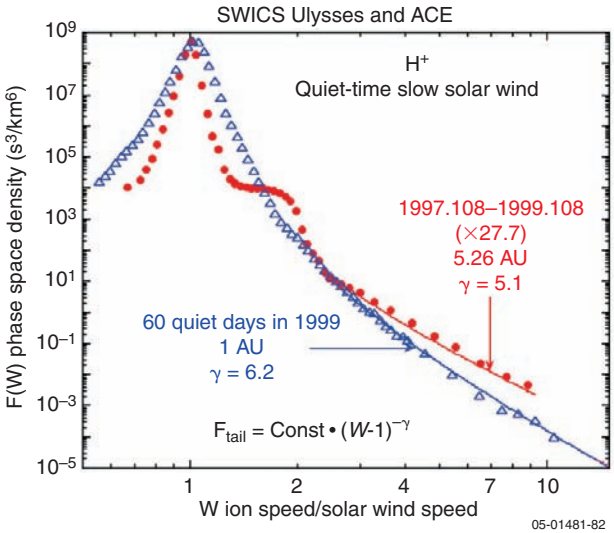

Figure 2-15. All solar wind species somehow develop suprathermal tails extending to >100 keV/nuc somewhere between the Sun and 1 AU, as illustrated in these data from Ulysses and ACE (*Gloeckler et al.*, 2000). The mechanism for creating these tails is not known. Note that 10 times the solar wind speed is close to ~100 keV/nucleon.

fact that even interstellar pickup He^+ exhibits a suprathermal tail suggests that the acceleration occurs (by some unknown process) in the inner heliosphere (e.g., *LeRoux et al.*, 2002). However, evidence also indicates that ^3He is continuously accelerated at the Sun, even during the quietest periods, suggesting that more or less continuous acceleration may be occurring in microflares such as those reported by RHESSI (*Krucker et al.*, 2002). ***Solar Probe will investigate these acceleration processes by exploring the inner heliosphere to distances where no spacecraft has ventured before, and by searching for particle acceleration associated with microflares and other processes at distances where the particle intensities will be orders of magnitude larger than at 1 AU.*** The small-scale, randomly occurring "component" reconnection that typifies microflares may be an indicator of a scale-invariant dissipation process that not only heats coronal plasma (see Section 2.2.1), but also produces a stochastic component of the electric field that contributes to particle acceleration. The production of these dissipative structures may be related to the small-scale termination of the cascade of plasma turbulence that connects large with small scales and may be distributed throughout the heliosphere (*Matthaeus and Lamkin*, 1986; *Ambrosiano et al.,* 1988). ***Solar Probe plasma, field, and energetic particle instruments will examine these processes, including the geometrical properties of the plasma fluctuations (see Section 2.3.3) in critical, previously unexplored regions.***

Hard x-ray, gamma-ray, and neutron observations by Solar Probe can also reveal the occurrence of sporadic and/or continuous particle acceleration on the Sun. Solar neutron observations on Solar Probe are of special interest because low-energy neutrons that do not survive to 1 AU can only be observed close to the Sun. (~1 MeV (10 MeV) neutron intensities at 5 R_S are ~1.5×10^{10} (3.7×10^6) times greater than at 1 AU.) Neutron observations close to the Sun may reveal evidence of small nanoflares, which have been suggested as a principal source of energy for heating the corona (see Section 2.1.3).

Measurement Requirements

- Composition and energy spectra of energetic ions and electrons
- Suprathermal ions and electrons
- Neutron and gamma-ray emissions

- In-situ magnetic field and solar wind properties
- Photospheric EUV and magnetic field measurements

2.3.2 What are the seed populations and physical conditions necessary for energetic particle acceleration? SOHO has observed more than 8000 CMEs since 1996, but has measured only about 100 large SEP events during this same time period (particle intensities >10 particles/cm^{2}sr-s with E > 10 MeV). The acceleration mechanism (first-order Fermi acceleration) in gradual SEP events is generally well understood. Moreover, it is known that faster CMEs can form shocks more easily and that shocks driven by fast, wide CMEs accelerate particles more efficiently. It remains a mystery, however, why, for a given CME speed, the peak intensity of >10 MeV protons can vary by a factor of ~10^4 (*Kahler*, 2001).

To forecast large SEP events reliably, it is necessary to determine why some CMEs accelerate particles more efficiently than others. The suggested possibilities include: (1) the presence or absence of a pre-existing population of suprathermal ions, left over either from a previous gradual event (e.g., *Kahler* 2001) or from small impulsive flares (*Mason et al*., 1999); (2) the presence or absence of successive, interacting CMEs (*Gopalswamy et al*., 2002); (3) pre-conditioning and production of seed particles by a previous CME (*Kahler*, 2001; *Gopalswamy et al*., 2004); (4) improved injection efficiency and acceleration rate at quasi-perpendicular (as opposed to quasi-parallel) shocks (*Tylka et al*., 2005); (5) variable contributions from flare and shock-accelerated particles (*Cane et al*., 2003), including acceleration of associated flare particles by the shock (*Li and Zank*, 2004; *Cliver et al*., 2004); and (6) production of SEPs in polar plumes, where shock formation may be easier (*Kahler and Reames*, 2003).

Timing studies have shown that gradual SEP events are first accelerated at distances between ~3 and 12 R_S (*Kahler*, 1994; *Mewaldt et al*., 2003). Formation of the CME-driven shock requires that $V_{cme} > V_{sw} + V_{fast}$, where $V_{fast} \approx (V_A^2 + c_s^2)^{1/2}$, V_A is the Alfvén speed, and c_s is the sound speed (see e.g., *Kahler and Reames*, 2003). It has therefore been suggested that SEPs originate beyond ~3 R_S because there is a peak in the Alfvén velocity at ~3 R_S, such that it is only beyond this radius that shocks can be easily formed and sustained for typical CME speeds (e.g., *Gopalswamy et al*., 2001; **Figure 2-16**). In MHD simulations of SEP events driven by coronal shocks (e.g., *Zank et al*., 2000; *Sokolov et al*., 2004) it is necessary to assume or model a variety of conditions in the region where gradual SEP events originate, including the magnetic field and density profiles, the solar wind and Alfvén speeds, the density of seed particles, and turbulence levels that determine the particle diffusion coefficient**.** ***Solar Probe will measure the solar wind and magnetic field close to the Sun, the density and energy spectrum of suprathermal seed particles, and the spectrum of magnetic turbulence directly, thus providing needed constraints on simulations of SEP events.***

The probability that Solar Probe will encounter particle intensity levels characteristic of large SEP events at 1 AU (e.g., >100 particles/cm^{2}sr-s with E > 10 MeV) is about 80% during solar maximum conditions (*Feynman et al*., 2000). It is much less

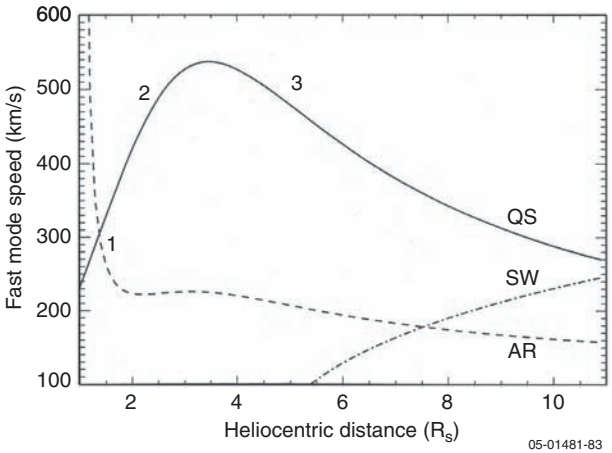

Figure 2-16. Estimated speed profile of the fast magnetosonic mode (V_{fast}) in the quiet Sun (QS) and in the active region (AR) coronas (from *Gopalswamy et al*., 2001). Conditions for shock formation differ in the three regions marked 1, 2, and 3. A coronal mass ejection (CME) can form a shock if the CME speed exceeds the sum of V_{fast} plus the solar wind speed (SW), one estimate for which is shown above. Shocks formed inside ~3 R_S will not propagate into the quiet corona beyond ~3 R_S unless they have speeds greater than ~540 km/s; however, the CME driver could form a new shock once beyond the peak. The height of the peak in the V_{fast} curve depends on the actual density and magnetic field values in a given location, but the shape of the curve will be the same. Solar Probe will directly measure these quantities into 4 R_S, and determine how they vary. By measuring where and how easily shocks can form, Solar Probe will provide ground truth for models of solar energetic particle acceleration by fast CMEs.

Probing the Near-Sun Energetic Particle Acceleration Region

Solar energetic particle acceleration occurs within an extended region between 2 and 20 R_S. Correlated Solar Probe measurements of energetic particle spectra and solar wind properties inside 20 R_S will be used to understand and characterize the nature of SEP acceleration near the Sun. From Solar Probe data it will be possible to establish, for example, the average profile of the Alfvén and sound speeds in the corona. With this information, the effectiveness of CMEs in creating shocks and the strength and number of the resulting shocks can be assessed. Further, Solar Probe may detect the presence of smaller and perhaps more frequent CMEs and shocks that are blended into the background and thus indistinguishable at 1 AU but that are suspected to play perhaps a quite important role in solar energetic particle acceleration. The basic information needed to understand how efficiently shocks accelerate particles will be obtained from measurements of turbulence upstream and downstream of shocks in the corona. Other observations—e.g., of small-scale bursts or the absence thereof or the appearance of distinct features in what is a power-law tail in the ion and electron particle distribution functions at 1 AU—will clarify the nature of the acceleration processes and can be used to test ideas about the scale invariance of energy release events. The postulated role of wave–particle interactions would be confirmed, for example, by the observation of bump-on-tail distributions for the electrons, which are capable of creating ion–cyclotron waves that could then accelerate and energize minor ions.

likely, however, (~10–20% probability) that the Solar Probe flyby will take place while a CME-driven shock is accelerating >10 MeV particles inside 100 R_S. Nonetheless, Solar Probe measurements of the ambient conditions that exist prior to such events will be of enormous value to our efforts to understand SEP acceleration and transport.

In addition, Solar Probe will almost certainly observe a significant level of the particle acceleration activity that must be going on continually on the dynamic Sun because the intensity of events too small to be detected at 1 AU will be orders of magnitude greater in the near-Sun region. Capturing a large SEP event would yield fascinating data, but measurements of even the expected low-level activity would provide definitive information on the unknown details of near-Sun SEP acceleration and transport.

Measurement Requirements

- Basic plasma (proton, alpha particle) and magnetic field measurements, and their gradients
- Major and minor ion distribution functions extending to high-energy tails
- Composition and spectra of ions extending from energies through ~100 MeV/nuc, including ^{3}He
- Plasma wave electric field measurements to above the plasma frequency for quasi-thermal noise spectroscopy
- Plasma wave electric and magnetic field fluctuation spectra
- Remote sensing of underlying photospheric magnetic structure for correlation with in-situ data
- Remote sensing of active regions, flares, and CMEs

2.3.3 How are energetic particles transported radially and across latitudes from the corona to the heliosphere? Ulysses measurements have shown that SEPs can reach high latitudes (*McKibben et al.*, 2001). Three explanations for these observations have been proposed: (1) the CME shocks accelerating the particles extended to high latitudes and crossed the interplanetary magnetic field lines connecting to Ulysses; (2) significant particle cross-field diffusion took place; and (3) magnetic field lines connecting high latitudes with low-latitude active regions existed in the solar corona, allowing particles to reach high latitudes close to the Sun. On the basis of a comparison of onset times at Ulysses with onset times in the ecliptic for events with the same solar origin, *Dalla et al.* (2002) conclude that high-latitude events are not compatible with direct scatter-free propagation along a magnetic field line, but rather the large path lengths and late release times suggest that propagation to high latitudes requires scattering. By approaching the Sun along a polar trajectory ***Solar Probe will encounter energetic particles at all latitudes and determine how scattering properties from the corona into the solar wind vary with magnetic field and turbulence intensities. These measurements, together with magnetic field measurements, will also help to identify large-scale deviations from the Parker spiral configuration (Section 2.1.1) and***

determine their role in energetic particle scattering.

Energetic electrons are observed in both impulsive and gradual SEP events. Because of the electrons' near-relativistic velocities, the onset times of electron events at 1 AU are often used to deduce SEP release times near the Sun for comparison with their associated electromagnetic signatures. Surprisingly, the deduced release times almost always appear to be delayed by ~10 minutes with respect to electromagnetic signatures such as soft x-ray and optical emissions from flares and associated radio emissions (e.g., *Krucker and Lin*, 2000; *Haggerty and Roelof*, 2002). This discrepancy has resulted in considerable debate concerning its cause—whether storage and subsequent release of the electrons, longitudinal propagation of the acceleration mechanism from the flare site to the injection site, or radial transport of the acceleration mechanism in the form of a CME-driven shock (*Haggerty and Roelof*, 2002). ***Close to the Sun propagation delays will be minimized, and energetic electron measurements combined with interplanetary magnetic field observations will reveal where and how particles are released from the Sun and/or accelerated in interplanetary space.***

Measurement Requirements

- High-energy ions and electrons
- In-situ vector magnetic field
- Photospheric EUV and magnetic field measurements
- Remote sensing of active regions, flares, solar radio bursts, and CMEs

2.4 Explore dusty plasma phenomena and their influence on the solar wind and energetic particle formation

The origin of dust in the inner solar system is not well understood. The ultimate sources of the dust population are thought to be the release of dust from comets and asteroids and the breakup of meteoroids (**Figure 2-17**). Subsequent dust–dust collisions lower the average mass of the dust particles. Dust orbital motion combines with Poynting–Robertson deceleration to increase the dust number densities towards the Sun (*Burns et al.*, 1979). Inward from 1 AU, the fragmentation of cometary meteoroids locally is believed to produce a majority of dust particles (*Grün et al.*, 1985; *Ishimoto*, 2000; *Mann et al.*, 2004). Dust particles attain electric surface charge through photo-ionization, electron emission, and interaction with the solar wind. While larger (>1 μm) particles move primarily in Keplerian orbits, smaller charged grains are deflected by the interplanetary magnetic field. The degree of deflection depends on the surface charge, which has not yet been directly measured for dust particles in space, and on the magnetic field magnitude and direction and their variation in time (*Mann et al.*, 2000). In addition, dust dynamics is likely to be influenced by events such as coronal mass ejections, which may even lead to dust destruction (*Misconi*, 1993, *Ragot and Kahler*, 2003).

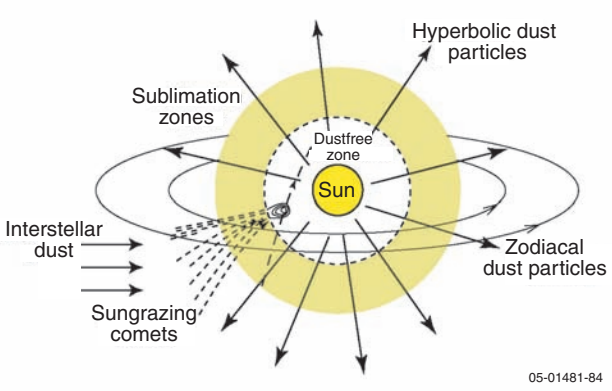

Figure 2-17. Sketch illustrating the dust environment near the Sun. Most of the dust near the Sun is bound in Keplerian, roughly circular orbits near the ecliptic, although some dust particles are ejected by radiation pressure on hyperbolic trajectories as β-meteoroids. Comets and asteroids are the principal sources of the solar dust cloud, with smaller contributions from sungrazing comets and interstellar dust. Solar Probe will make the first-ever in-situ measurements of the near-Sun dust environment (*Mann et al.*, 2004).

The interaction of dust in the inner heliosphere and the solar-wind plasma influences not only the dust population but the local plasma and gas environment as well. Notably, dust grains in the inner heliosphere are important as a source of pickup ions, protons as well as heavier species, which differ from the solar wind in their charge state and velocity distribution. These "inner source" pickup ions are potential candidates for subsequent acceleration and may contribute to the anomalous cosmic ray population (*Cummings et al.*, 2002). The interaction of the solar wind with dust particles also generates energetic neutral atoms (ENAs), which can be detected from Earth orbit (*Collier et al.*, 2001); smaller variations in this ENA flux may be due to

structures in the dust population (*Collier et al.*, 2003).

Although the dust supply from the frequently observed sungrazing comets is negligible, they provide an impressive example of the fate of solar system objects in the inner solar system and in the vicinity of the Sun. They also illustrate how the presence of small bodies can influence the local environment. For example, SOHO/UVCS observations of the sungrazing comet C/2001 C2, at heliocentric distances of 4.98 and 3.60 R_S, revealed sequential fragmentation events along the comet's path and provided evidence for the creation of a population of neutral hydrogen through the exchange of charge between coronal protons and material sublimated from pyroxene dust grains as well as between coronal protons and atoms created from the photodissociation of water (*Bemporad*, 2005).

Despite some valuable observations (e.g., from Helios and Ulysses), much of our understanding of dust in the inner heliosphere is theoretical and model-based, and many basic questions remain open, awaiting detailed measurement of the near-Sun dust population. What, for example, are the mass distributions and fluxes of dust particles as a function of distance from the Sun? How are dust fluxes correlated with fluxes and velocity distributions of pickup ions? What are the major elemental compositions and bulk density of the dust and how do they vary with distance from the Sun? In-situ observations with Solar Probe will be crucial in resolving many of the present uncertainties regarding dust origin, its composition, and spatial distribution. Since dust is a common component of interstellar material as well as most likely of other stellar systems, Solar Probe results will have a direct bearing on certain astrophysical problems, with the near-Sun dust cloud serving as an analogue for circumstellar dust clouds, for example.

2.4.1 What is the dust environment in the inner heliosphere? Because of current observational limitations, there are great uncertainties in our knowledge and models of the spatial distribution of dust in the inner heliosphere and even at 1 AU. Brightness observations of dust are limited by line-of-sight geometry and biased by large dust grains. Thus they do not reveal the complex dynamics of small dust particles nor do they allow their size distribution and composition to be derived. Given these and other observational limitations, the mass distribution of dust at 1 AU is described by the interplanetary flux model (IFM) (*Grün et al.*, 1985). It is assumed that the IFM can be extrapolated inward to give an estimate of the mass distribution in the near-Sun environment. The radial dependence consistent with 1 AU observations is flat inside 10 R_S with an inner cutoff at 2 R_S and an approximate r^{-1} decrease beyond 10 R_S. Most (~90% at 1 AU) of the dust is believed to be concentrated near the ecliptic plane (which takes 23% of the volume of the sphere). At high latitudes, a second, spherically symmetric component with a steeper increase toward the Sun is assumed. This picture is consistent with zodiacal light observations and based on the hypothesis that comets and asteroids and meteoroids from comets and asteroids are the main sources of the dust cloud (*Mann et al.*, 2004).

One recent study suggests that the density at 1 AU may be enhanced by up to a factor of 3 in the middle mass range (*Love and Brownlee*, 1993) compared with that given by the interplanetary flux model. In addition, mutual collisions may increase dust densities for masses smaller than 10^{-7} g compared with the distribution extrapolated from 1 AU (*Mann et al.*, 2004). Number densities near the Sun may thus exceed those given by the present model by an order of magnitude. Moreover, since part of the collisional evolution takes place in meteoroid trails, the dust distribution in the inner solar system may not be homogeneous within the cloud (*Mann and Czechowski*, 2005).

Coronal observations show that the dust number density is influenced by sublimation inward from 10 R_S, but there is no feature that indicates the beginning of the dust-free zone outside 2 R_S. This implies that some species survive to this distance or even closer (see Section 2.4.2 below). Although Solar Probe will not reach distances where the dust-free zone is expected, it will cross regions where volatiles and significant amounts of the other dust compounds sublimate.

Solar Probe will characterize the near-Sun dust environment by determining how the mass distribution of dust and impact directions vary along the spacecraft trajectory and how the observed impact signals vary with the mass and impact parameters of the dust particles. Solar Probe dust measurements will likely require substantial

Determining the Distribution of Cosmic Dust near the Sun

Solar Probe will make in-situ measurements of the dust flux along the spacecraft trajectory. While it will not be possible to distinguish spatial variations in the flux from temporal variations directly, it should be possible to distinguish between temporal and spatial effects indirectly by comparing the dust measurements with the particles and fields measurements. That is, variations in the flux of small grains that are correlated with magnetic field variations are likely due to Lorentz forces, while fluxes of dust particles varying over a broad size spectrum and correlated with field data are more likely to result from local dust sources. Measurements close to known meteoroid streams will be useful in determining the nature of the variability observed in the dust fluxes. Imaging with the Hemispheric Imager will permit deconvolution of the size distribution of the large-grain dust population in the environment of the spacecraft. Comparison of the "foreground" dust brightness pattern with brightness patterns determined from other space-based coronagraphs will help in characterizing the size distribution of the large particles and its variation within the inner heliosphere. Combining models of the diffraction pattern of large particles with the size distribution of small dust particles measured in situ will make it possible to trace the change in the size distribution over a large range of particle sizes. By determining the size distribution of the dust as a function of distance from the Sun, Solar Probe will trace the sublimation sequence of particles and therefore provide some basic data about the dust composition. Solar Probe dust measurements will be used with dust distribution models to fully describe the distribution of dust in the inner heliosphere.

revision of the paradigm of a homogeneously distributed dust cloud that is stable in space and time.

2.4.2 What is the origin and composition of dust in the inner heliosphere? While the sources of dust are thought to be mainly comets and asteroids, it is not clear how much each source contributes. Collision models suggest that the contribution of cometary dust to the inner heliospheric dust population is greater near the Sun than in the outer solar system beyond 1 AU. Little is known about the composition of dust. Laboratory studies, both past and ongoing, on dust samples (e.g., interplanetary dust collected in the stratosphere and dust currently collected during space missions) provide important information about the collected species, but the samples are limited to those dust particles that survive the collection process and, moreover, there are spatial biases. In-situ spacecraft measurements have so far not been successful in determining dust composition, but some relevant data on element abundances have been obtained during flybys at comet Halley (*Kissel et al.*, 1987). These Halley data suggest that cometary dust has a completely different composition from cometary material, namely a high abundance of the elements C, H, O, N, as well as an extremely low density, i.e., a porous structure (**Figure 2-18**). Even less is known about the composition of the dust material close to the Sun. If dust originates from comets, dust grains should be rich in the elements C, H, O, N, which according to some models form organic refractory compounds. In addition to C, H, O, N, the dust is expected to consist to a great extent of silicates and components such as sulfides and metal oxides. Solar wind and suprathermal solar particle material will also be implanted in the surface of grains, enriching the grains in noble gases such as He and Ne. (If the energy of the impinging ions significantly exceeds that of the solar wind, then they will simply pass through the grains). This

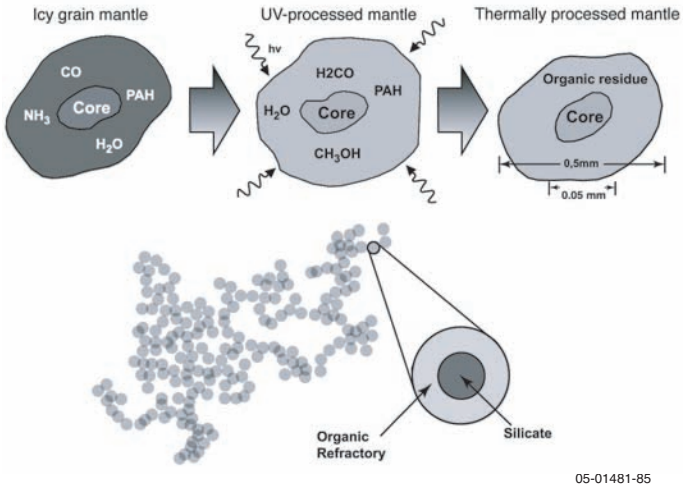

Figure 2-18. Sketch illustrating the evolution of a cometary dust grain. Cometary dust grains are produced by collisions in meteoroid streams inward from 1 AU. Solar Probe will cross the region where the organic refractory material and the silicate material from comets sublimates. By sampling pickup ions created from the sublimated material, Solar Probe will obtain clues to the composition the organic refractory materials in comets.

implantation process should lead to the production of molecules such as OH, H_2, NH, and other light molecular species near the surface of the grains. Ulysses observations of pickup ions at distances of several AU suggest that this is in fact the case. Finally, it has been proposed that an accumulation of silicon nano-dust forms near the Sun (*Wimmer-Schweingruber and Bochsler*, 2003; *Habbal et al.*, 2003),[1] a suggestion that is currently under critical debate (*Mann et al.*, 2004; *Mann and Czechowski*, 2005).

Sublimation releases material from the dust grains into the solar wind, where it is converted into pickup ions (see Section 2.4.4). The sublimation of meteoritic silicates produces highly refractory metal oxides that can survive at distances as close to the Sun as 2 R_S. It is not known at what distance from the Sun CHON materials sublimate. They are clearly not highly volatile, however, since otherwise they would sublimate in the vicinity of the comet.

Solar Probe measurements of pickup ions created from material released from the dust by sublimation will provide information about the composition of dust. This information, combined with measurements of spatial variations of dust fluxes, will help establish the relative contributions of the sources of the dust cloud as well as dust composition.

2.4.3 What is the nature of dust–plasma interactions and how does dust modify the spacecraft environment close to the Sun? As indicated in the preceding sections, the interaction of the dust with solar-wind plasma significantly affects the dynamics and distribution of the dust—e.g., through charging, the Lorentz force, the pseudo Poynting–Robertson effect, and ion drag. In addition to its interaction with the quasi-stationary wind, the near-Sun dust population also interacts with and is influenced by transient events such as CMEs (*Ragot and Kahler*, 2002). Collisional evaporation, particularly in cometary meteoroid trails, is expected to influence the solar wind parameters measured locally. For example, a recent study shows that dust collisions in the inner solar system can produce some of the heavy species in amounts comparable to the observed inner source fluxes (*Mann and Czechowski*, 2005). The material released in such collisions may be responsible for the enhancements of the interplanetary field measured by Ulysses in association with meteoroid trails (*Jones et al.*, 2003; **Figure 2-19)**. These enhancements—which last for minutes to hours, are clustered in space, and occur more frequently in the inner solar system—may be the result of mass loading of the solar-wind plasma induced by collisional vaporization in the dust trails (*Mann and Czechowski*, 2005). It is still an open question how noble gases observed in the inner source are produced, with the solar wind surface interactions being a distinct possibility.

Dust impacting the spacecraft will influence the plasma environment of the spacecraft and may

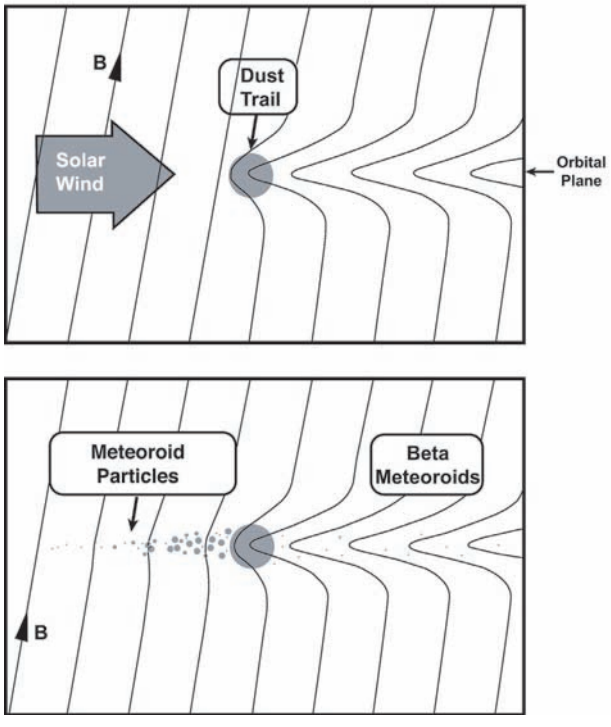

Figure 2-19. Cross-sectional sketch of cometary dust trail illustrating the formation of an interplanetary field enhancement (IFE). Such IFEs have been observed with Ulysses and correlated with meteoroid trails (cf. *Jones et al.*, 2003). Solar Probe will test the hypothesis that the IFEs result from mass loading of the solar wind by material produced by collisional vaporization in dust trails.

[1] Some solar eclipse observations have been interpreted as evidence for the existence of silicon nano-particles near the Sun (*Habbal et al.*, 2003). If true, this finding would be interesting for astrophysical studies, since it has been suggested that silicon nano-particles play a role in the extended red emission (ERE) observed in the diffuse interstellar medium (*Witt et al.*, 1998; *Zubko et al.*, 1999). More recent attempts to search for features of silicon nano-particles, on the other hand, were not able to detect their signature (*Singh et al.*, 2004). The majority of solids thought to be present in cosmic dust sublimate within 0.1 AU of the Sun, with some refractory compounds such as metal oxides (e.g., MgO) (*Mann and Murad*, 2005) surviving as close as a few solar radii to the Sun.

bias plasma and field measurements. Signals due to impact-generated ion cloudlets have been observed by plasma experiments on several spacecraft in the vicinity of planetary rings (*Gurnett et al.*, 1983; *Meyer-Vernet et al.*, 1986), in the interplanetary medium (*Gurnett et al.*, 1997), and during encounters with the comets Giacobini-Zinner, Halley, and P/Borrelly (*Neubauer et al.*, 1990; *Oberc and Parzydlo*, 1992; *Tsurutani et al.*, 2003).

Dust fluxes are expected to be especially high near the Sun. ***Solar Probe will measure these fluxes and characterize the near-Sun dust environment and its effects on in-situ plasma measurements.***

2.4.4 What are the physical and chemical characteristics of dust-generated species? Neutral and ionized material is released from dust grains by various mechanisms, including vaporization, sublimation, desorption, or direct collisions, and moves at speeds comparable to those of the dust grains (~50 km/s and higher). The neutral gas is quickly ionized by the solar wind and photons and, along with the ionized gas, is picked up by the solar wind to form part of the "inner source" pickup ion population (*Geiss et al.*, 1996; *Gloeckler and Geiss*, 1998; 2001). Inner source pickup ions, discovered with Ulysses, have provided limited knowledge concerning the composition of the gas released from dust and constraints on the spatial distribution and fluxes of dust grains. One of the surprising results has been the detection of noble gases and light elements in the inner source pickup ions having a composition remarkably similar to that of the slow solar wind. Molecular ions in the mass range up to ~40 amu have also been detected. These measurements imply that recycling of solar wind particles through adsorption and desorption constitutes an important mechanism for the origin of the inner source pickup ions. However, the fluxes of dust required to account for the amounts of observed pickup ions exceed by orders of magnitude the fluxes deduced from zodiacal light observations. Further progress in resolving the origin of inner source pickup ions will require in-situ measurements close to the Sun as well as better models of dust microphysics.

Solar Probe will measure both the dust fluxes and pickup ion densities and composition as a function of radial distance and latitude with sufficient resolution, sensitivity, and dynamic range to characterize the species generated from the dust grains near the Sun and to elucidate the mechanisms by which material is released from the dust.

Measurement Requirements

- Spatial variation of dust flux as a function of radial distance and latitude from 4 R_S to 5 AU
- Distribution functions and composition of inner source pickup ions
- Solar wind bulk parameters
- Solar wind ion composition
- Plasma wave electric field measurements
- Energetic particle spectra and composition
- Magnetic field orientation and strength

3. Science Implementation

The Solar Probe science objectives will be addressed through a combination of in-situ and remote-sensing observations performed from a 90°-inclination orbit about the Sun (**Figures 3-1 and 3-2**). (The baseline payload is described below, in Section 3.2). Beginning at a distance of 0.3 AU and for 5 days after perihelion, Solar Probe will make in-situ measurements of plasma, suprathermals, energetic particles, magnetic fields, waves, and dust in the near-Sun environment. EUV and magnetic imaging of solar wind source regions will be performed between 65 and 20 R_S on both the inbound and outbound legs; white-light imaging of the corona will be performed at a high cadence inside 20 R_S and at a lower cadence outside 20 R_S, both inbound and outbound. Closest approach will occur at a perihelion altitude of 3 R_S above the solar surface, with the Earth off-quadrature to allow for supporting remote-sensing observations of coronal structures and the sub-Probe disk from ground-based, sub-orbital, and space-based assets (see Section 3.3 below).

The Baseline Mission provides for two flybys of the Sun, each at a different phase of the solar cycle. With a launch in 2014, Solar Probe's first encounter will take place in 2018, around the projected activity minimum of solar cycle 24 (*Sello*, 2003), with the Earth 15° off-quadrature. The second encounter will occur ~4.6 years after the first, allowing Solar Probe to measure both the quiet and the active phases of the 11-year solar cycle, independent of the final launch date. The two encounters will yield four independent data sets, two from the northern hemisphere and two from the southern hemisphere, both approaching and receding. These data will be

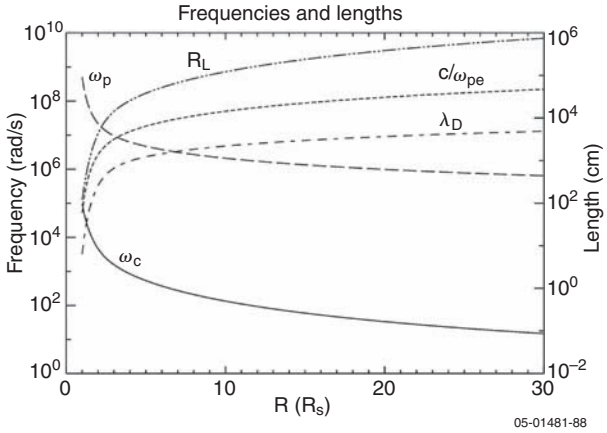

Figure 3-2. The variation in plasma parameters from 1 to 30 R_S, as determined for typical fast solar wind conditions. Scale lengths are the thermal Larmor radius, the electron skin depth, and Debye length. Frequencies are the electron plasma frequency and the proton cyclotron frequency. Values plotted are constrained by SOHO measurements of coronal density and temperature and Ulysses in-situ data from 1 AU.

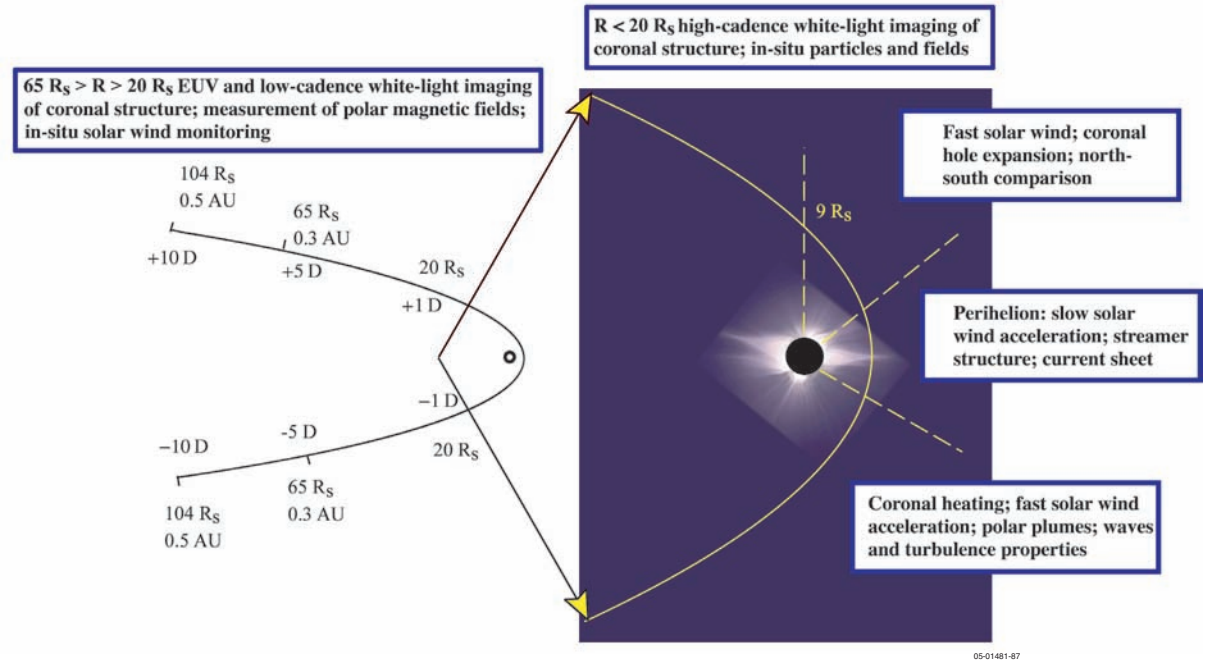

Figure 3-1. Solar Probe science measurements and objectives as function of orbital position.

used for comparative studies of coronal structure in the northern and southern hemispheres at two fixed epochs and of changes in the corona and solar wind as a function of the solar activity cycle. An additional benefit of the second encounter is that it will afford investigators an opportunity to optimize instrument operations and observing strategies based on the analysis of data acquired during the first flyby. Further, the second encounter's 34° off-quadrature geometry will expose a larger portion of the solar disk to viewing from Earth during the remote observing campaign conducted in support of the flyby.

The measurements required to address the four Solar Probe science objectives are listed in Section 2, at the end of the discussion of each subquestion. They are summarized in the Traceability Matrix (**Table 3-1**), which also briefly suggests investigative strategies that might be employed in answering the subquestions. The Science and Technology Definition Team (STDT) followed a strict traceability process to derive measurement requirements from the science objectives and subquestions and instrument specifications from the measurement requirements. Measurements that are *required* to address a specific question are identified in the Traceability Matrix by the letter "R," while "S" denotes *supporting* measurements. As can be seen from the Traceability Matrix, Solar Probe will address each science question with multiple kinds of measurements, thus ensuring comprehensiveness and providing redundancy and resiliency in the event that a particular instrument should fail.

3.1 Minimum Criterion for Success

Science objectives 2.1, 2.2, and 2.3 relate directly to Solar Probe's overall goal: to determine how the Sun's corona is heated and how the solar wind is accelerated. Thus the STDT recommends that the following requirement be established as the minimum success criterion for the Solar Probe mission: ***Solar Probe must address any two of the three questions under each of the first three science objectives (Sections 2.1, 2.2, and 2.3).*** Although the Baseline Mission (two passes with perihelion at 4 R_S) will provide the richest scientific yield, enabling comparative studies of the corona and solar wind at two different phases of the activity cycle, the STDT considers that the minimum success criterion can still be satisfied if resource constraints permit only one solar pass and/or require that perhelion be raised from 4 R_S to 5 R_S.

3.2 Baseline Payload

To meet the Solar Probe science objectives, the STDT recommends an integrated payload comprising in-situ and remote-sensing instruments serviced by a common data processing unit (CDPU) and low-voltage power supply (LVPS). The use of a common DPU/LVPS reduces mass, power, cost, and complexity through the sharing of resources among the instruments. As pointed out in the 1999 Solar Probe report (*Gloeckler et al.*, 1999), development of the payload as an integrated package under the direction of a single principal investigator would provide for streamlined, efficient project management and effective cost and schedule control. A single integrated payload has been assumed in the engineering study and cost estimate.

Solar Probe's **in-situ instrumentation** consists of a Fast Ion Analyzer, two Fast Electron Analyzers, an Ion Composition Analyzer, an Energetic Particle Instrument, a Magnetometer, Plasma Wave Instrument, a Neutron/Gamma ray Spectrometer,

Resolving Space–Time Ambiguities

Distinguishing between spatial structures and temporal variations is a well-known problem in the interpretation of in-situ data acquired from a single spacecraft. In the case of Solar Probe, this problem will be resolved by (1) imaging the local corona with an onboard wide-angle white-light coronagraph and (2) remotely observing the corona and underlying regions from Earth-based and near-Earth imagers, while simultaneously performing in-situ measurements of the coronal plasma and fields. At 30 R_S, Solar Probe will already be embedded in both large- and small-scale coronal structures such as polar plumes and streamers (cf. Figure 2-5). The Probe's white-light Heliospheric Imager (Section 3.2.8) will image these structures and the local environment through which the spacecraft is flying, and the resulting images can then be analyzed together with the simultaneous remote observations and in-situ data to distinguish spatial from temporal effects. In addition to this technique, it should be possible to perform limited statistical studies using the four data sets from the two solar flybys to establish which features in the in-situ data are indicative of spatial structures and which result from temporal variations.

Table 3-1 Traceability Matrix. All measurements/instruments are included in the Solar Probe Baseline Mission. "R" denotes measurements required to address the question in whose row they appear; "S" denotes supporting measurements.

KEY
R: Required
S: Supporting

CD: Coronal Dust Detector
EPI: Energetic Particle Instrument
FEA: Fast Electron Analyzer
FIA: Fast Ion Analyzer
ICA: Ion Composition Analyzer

HI: Hemispheric Imager
MAG: Magnetometer
NGS: Neutron/Gamma Ray Spectrometer
PSRI: Polar Source Region Imager
PWI: Plasma Wave Instrument

Science Objectives	Objective Questions	Strategy	Measurements/Instruments: PLASMA DISTRIBUTION; COMPOSITION; SUPRATHERMALS	ENERGETIC PARTICLES (EPI)	PLASMA WAVES (PWI)	VECTOR MAGNETIC FIELD (MAG)	NEUTRON/GAMMA-RAY EMISSIONS (NGS)	CORONAL DUST (CD)	SOURCE REGION IMAGING (PSRI)	WHITE LIGHT IMAGING (HI)
2.1 Determine the structure and dynamics of the magnetic fields at the sources of the fast and slow solar wind	a. How does the magnetic field in the solar wind source regions connect to the photosphere and the heliosphere?	Coordinate in-situ observations and remote-sensing of surface (65–20 R_S) and corona (high-cadence white-light imaging <20 R_S); intercompare in-situ measurements along the trajectory.	R	S	S	R			R	R
	b. How do the observed structures in the corona evolve into the solar wind?	Identify in-situ signatures of density and magnetic field structures or boundaries and compare with coronal structure as observed with remote sensing.	R	S	S	R			R	R
	c. Is the source of the solar wind steady or intermittent?	Perform statistical study of temporal, radial, and latitudinal variations of composition and plasma and field data; relate to filamentary structure and filling factors.	R	S	S	R	S			R
2.2 Trace the flow of the energy that heats the solar corona and accelerates the solar wind	a. How is energy from the lower solar atmosphere transferred to and dissipated in the corona?	Characterize the turbulence and energy budgets and their evolution along the trajectory; compare with sources at the Sun and along the trajectory; search for signatures of candidate dissipation mechanisms at kinetic scales.	R	S	R	R	R		S	S
	b. What coronal processes shape the non-equilibrium velocity distributions observed throughout the heliosphere?	Compare measured electromagnetic fields and distribution functions of protons, electrons,and heavy ions and their variability.	R	R	R	R				
	c. How do the processes in the corona affect the properties of the solar wind in the heliosphere?	Use measured amplitude and spectra of electromagnetic and plasma fluctuations to assess role of Alfvénic turbulence in coronal heating and solar wind acceleration; with modeling, determine origin of spectra (photospheric or coronal).	R	S	R	R				S
2.3 Determine what mechanisms accelerate and transport energetic charged particles	a. What are the roles of shocks, reconnection, waves, and turbulence in the acceleration of energetic particles?	Correlate energetic particle distributions and their temporal variations with shocks, signatures of reconnection, and properties of turbulence properties.	R	R	R	R	S		S	S
	b. What are the seed populations and physical conditions necessary for energetic particle acceleration?	Correlate suprathermal and energetic particle distribution functions with measured plasma and electromagnetic field properties.	R	R	R	R				
	c. How are energetic particles transported radially and across latitudes from the corona to the heliosphere?	Determine energetic article distribution functions and composition and turbulence properties along the trajectory, along with measured and modeled large-scale magnetic field.	R	R	R	R	S		R	S
2.4 Explore dusty plasma phenomena and their influence on the solar wind and energetic particle formation	a. What is the dust environment of the inner heliosphere?	Compare dust measurements with brightness patterns from coronagraph and models to characterize size distribution.			S	S		R		S
	b. What is the origin and composition of dust in the inner heliosphere?	Derive information about dust composition from measurements of dust-generated species and from sublimation sequence determined from size distribution as function of distance from the Sun.	R			S		R		
	c. What is the nature of dust-plasma interactions in the near-Sun environment?	Correlate plasma distribution functions, composition measurements, and dust properties.	R		S	S		R		S
	d. What are the physical and chemical characteristics of dust-generated species?	Measure composition of dust-generated species; correlate with dust, solar wind, and magnetic field data.	R			S		R		

Blank Page
(back of foldout)

and a Coronal Dust Detector. The **remote-sensing instrumentation** comprises a Hemispheric Imager for white-light imaging of coronal structures and a Polar Source Region Imager for EUV and magnetic imaging of the photosphere. The specifications for each instrument and their rationale are discussed in the sections that follow.

Tables 3-2 and **3-3** summarize, respectively, the instrument specifications and resource requirements for the baseline payload. To determine the instrument specifications, the STDT translated the Solar Probe science objectives into measurement requirements (cf. **Table 3-1**) and these into specific sensitivity, range, and resolution requirements. The mass, power, and data rate allocations shown in **Table 3-3** are based on those of past or existing instrumentation or components.

3.2.1 Fast Plasma Instrumentation. The Solar Probe Fast Plasma Instrumentation consists of a single Fast Ion Analyzer (FIA) and a pair of Fast Electron Analyzers (FEAs). The FIA and one of the FEAs are mounted, together with the Ion Composition Analyzer (ICA), on a movable arm on the ram side of the spacecraft; the arm is gradually retracted as the spacecraft approaches the Sun. This arrangement provides viewing to near (2° inside of) the edge of the heat shield umbra. The second FEA is mounted on the anti-ram side of the spacecraft body, pointing 180° away from the first. While the mission-unique aspects of Solar Probe will require new designs for the FIA and FEA instruments, the basic designs and subsystems can be drawn from a wide variety of previous heritage missions such as Ulysses, ACE, Helios, and Wind.

Fast Ion Analyzer (FIA). The FIA should be capable of measuring two- and three-dimensional distribution functions for protons and alphas over the energy/charge range of 50 eV/q to 20 keV/q. This energy range covers the lowest and highest expected speeds for 100 km/s protons and 1400 km/s alpha particles, respectively. The FIA's 3D temporal resolution of 3 seconds and 0.1 second for 2D distribution functions allows identification of boundaries in the solar wind down to ~1000 km near perihelion and wave modes (e.g., the gyrofrequency is ~30 Hz over the poles). The energy resolution ($\Delta E/E$) should be approximately 5%, which does a good job of resolving the supersonic solar wind beam out to beyond 1 AU. The sensitivity and dynamic range need to be adequate to measure 2D (energy and one angle) ion distributions in 0.1 s at 20 R_S without saturating the detectors all the way into perihelion. The FIA's field of view (FOV) needs to observe as much of the ram side of the viewing space as possible. For example, a top-hat analyzer with an ~330° fan in the X–Y plane (with some obscuration by the spacecraft) that deflects over 90° (±45°) in the X–Z plane, extending upward from the edge of the heat shield obscuration, provides adequate coverage. To resolve the ion distributions everywhere from 1 AU into perihelion, FIA's angular resolution needs to be ~5° around the solar wind beam and ~30° over the remainder of its FOV.

Fast Electron Analyzer (FEA). The FEAs should be capable of measuring two- and three-dimensional electron distribution functions over the energy range from ~1 eV to 5 keV. This energy range covers from the lowest energy photoelectrons, through the thermal core population and well up into the suprathermal halo population. The FEAs' 3D temporal resolution of 3 s (0.1 s for 2D distribution functions of energy and one angle) is matched to the FIA to help resolve plasma conditions and structures on the same scales. The energy resolution ($\Delta E/E$) should be approximately 10%, which does a good job of resolving the hot electron distributions. Like the FIA, the FEA requires a sensitivity and dynamic range adequate to measure the 2D distributions in 0.1 s at 20 R_S without saturating the detectors all the way into perihelion. Together the FEAs need to observe as much of 4π steradians as possible; all-sky imagers and deflecting top-hat analyzers are both appropriate approaches for achieving the needed FOVs. To resolve possibly very narrow halo electron beams (the strahl), the FEAs need angular resolutions that approach 3° in at least one dimension at higher energies around the magnetic field direction (this information is supplied real-time from the magnetometer via the payload DPU), while ~30° angular resolution is adequate to measure the remainder of the halo population and the core and photoelectron populations at lower energies.

3.2.2 Ion Composition Analyzer (ICA). The ICA is mounted, together with the FIA and one FEA, on the movable ram-looking arm referred to above. The ICA should be capable of measuring two- and three-dimensional distribution functions of He and heavy ions in the solar wind, over an energy range

Table 3.2 Solar Probe Baseline Instrument Payload

Instrument	Parameter(s) or Quantity(ies) Measured	Sensitivity *Dynamic Range*	Spectral Range *Resolution*	Angular Range *Resolution*	Time Integration *Cadence*
Fast Ion Analyzer (FIA)	H, He distribution functions	2D distributions in 0.1 s at 20 R_S	50 eV–20 keV *$\Delta E/E$ ~ 0.05*	330° × 90° (2 orthogonal) 10° × 10° 90° back from heat shield (phi) × centered on ram direction; 80° perp to symmetry axis; 5° toward beam to 20° away from beam	3 s for 3D; 0.1 s for 2D
Fast Electron Analyzer (FEA)	Electron distribution function	2D distributions in 0.1 s at 20 R_S	1 eV–5 keV *$\Delta E/E$ ~ 0.1*	As close to 4π less spacecraft obscuration ~3° (1D) near strahl 30° × 30° otherwise	3 s for 3D; 0.1 s for 2D
Ion Composition Analyzer (ICA)	Distribution functions of ^{3}He, ^{4}He, C, O, Mg, Si, Fe; composition of dust-related PUI from 2 to ~60 amu	Enable He/O in 10 s at 20 R_S	100 eV/q–60 keV/q *$\Delta E/E$ ~ 0.04–0.05*	120° × 120° 10° × 10°	10 s for He/O ratio at 20 R_S 60 s for heavy ions (e.g., Fe/O, charge states)
Magnetometer (MAG)	DC vector magnetic field	10 nT–8 G 3-axis *>10^4*	n/a	3° knowledge inside 20 Rs	20 samples/s
Plasma Wave Instrument (PWI)	3-axis AC E- and B-fields	2×10^{-17} V/m^2/Hz	**E**: 10 Hz–10 MHz **B**:10 Hz–80 kHz 40 samples/decade	n/a	0.1 s for spectral data; 60 s for waveform data
Energetic Particle Instrument (EPI)	Differential fluxes of H, ^{3}He, ^{4}He, C, O, Ne, Mg, Si, Fe, and e^-	10^7 protons/cm^2 s sr with 0.2–1 MeV 10^6 protons /cm^2 s sr with >1 MeV	0.02–100 MeV/nuc 0.03–3 MeV for e^- 6 energy bins/decade	Capability to measure pitch-angle distributions and anisotropies. Minimum coverage: 30° to 150° wrt nominal magnetic field at 4 R_S with	5 s for H; 30 s for Z ≥ 2; 1 s for e^-
Neutron/γ-ray Spectrometer	Neutron, hard x-ray, and γ-ray spectra	Factor of 10^4	0–20 MeV *<0.5 $\Delta E/E$* 0.02–10 MeV *(power-law spectrum)*	4π FOV for both energy ranges	10 s integration both ranges *10 s cadence both ranges*
Coronal Dust (CD)	Flux and mass spectrum; silicate vs. organic	m > 10–15 g for ΔV = 5 km/s (smaller particles detected for larger ΔV)	0.05–50 μm (1 fg–1 μg)	As close to 2π less spacecraft obscuration	10 s *30 s*
Hemispheric Imager (HI)	White light intensity	~10^{-9} erg/cm^2/deg/s	white light *n/a*	160° x 160° less spacecraft obscurations ~0.2°	1 - 10 s *90 s*
Polar Source Region Imager (PSRI)	Magnetic field EUV intensity	10 G 100 erg/cm^2/s/sr	Photospheric magnetic field ~10^6 K coronal emission	3° × 3° 24 arcsec 3° × 3° 24 arcsec	0.1 s exposure *10 min* 1 s exposure *10 min*

Table 3.3 Instrument Resource Requirements

Instrument	Mass (kg)	Power (W)	Peak Data Rate (kbps)
Fast Ion Analyzer (FIA)	2.8	3.7	10
Fast Electron Analyzer (FEA)	5.0	7.2	20
Ion Composition Analyzer (ICA)	7.0	6.0	10
Magnetometer (MAG)	2.5	2.5	1.1
Plasma Wave Instrument (PWI)	5.0	5.0	3.5
Energetic Particle Instrument, Low Energy (EPI-Lo)	1.4	2.3	5
Energetic Particle Instrument, High Energy (EPI-Hi)	2.7	1.7	3
Neutron/Gamma Ray Spectrometer (NGS)	2.0	3.0	0.5
Coronal Dust Detector (CD)	1.5	3.8	0.1
Hemispheric Imager (HI)	1.5	4.0	70
Polar Source Region Imager (PSRI)	3.5	4.0	70
Common DPU/LVPS	10.8	14.0	N/A
Total	45.7	57.2	123.2

from ~100 eV/q to ~60 keV/q and a mass range from 2 to > ~60 amu. The required energy range covers all major solar wind species that will be observed during the solar encounter. ICA's 3D temporal resolution of 10 s (at 20 R_S) permits temporal and spatial effects to be distinguished and allows comprehensive assessment of the non-thermal properties of the distribution functions that are generally expected from various solar wind acceleration and heating mechanisms. Furthermore, with the required mass range the ICA will measure species with low ionic charge states (i.e., He^+) and high masses (i.e., SiO_2), such as those produced from neutral sources in the inner heliosphere or created by the solar wind's interaction with dust near the Sun (e.g., inner source pickup ions). The energy resolution ($\Delta E/E$) should be 4–5%, sufficient to resolve the supersonic solar wind beam out to beyond 1 AU. The sensitivity should be sufficient to measure He/O ratios every 10 s at 20 R_S which can be achieved scaling from 1 AU observations of solar wind composition and charge states. The dynamic range should be ~10^4. The ICA FOV needs to observe as much of the ram side of the viewing space as possible due to the large amount of variability expected due to turbulence or waves in the outer corona. This can be achieved, for example, with a top-hat and swept FOV, or with an instrument with large instantaneous FOV as done on MESSENGER, provided that the edge of the FOV extends to close to the heat shield. To resolve the ion distributions everywhere from 1 AU to perihelion, ICA's angular resolution needs to be ~10° around the solar wind beam and ~20° over the remainder of its FOV.

3.2.3 Energetic Particle Instrument. The Solar Probe Energetic Particle Instrumentation (EPI) consists of a low-energy sensor (EPI-Lo) and a high-energy sensor (EPI-Hi). Both packages are to be mounted on the spacecraft body, where they view particles incident from both the sunward and anti-sunward hemispheres.

EPI Low-Energy Instrument (EPI-Lo). The EPI low-energy instrument is required to measure the composition and pitch-angle distributions of energetic particles. The composition includes hydrogen to iron as well as energetic electrons. As a minimum the detector should be able to make the ion measurements from ~20 keV/nucleon to ~1 MeV/nucleon and the electron measurements from ~25 keV to ~1 MeV. Composition measurements should discriminate protons, ^{3}He, ^{4}He, C, O, Ne, Mg and Si, and Fe. The measurements should have sufficient angular spread and resolution to enable pitch-angle measurements of the differential particle fluxes for a (nominal) radial magnetic field. A "slice" field of view of ~10° wide and >120° and at least 5 angular bins would suffice; at least 120° coverage and an angular resolution of no worse than 30° are required. The wider opening should be aligned with the spacecraft spin axis with the field of view just clearing the thermal protection

system. Larger solid-angle coverage and better species resolution are, of course, preferred. The preferential mounting is with the instrument field of view in the ram direction (or as close thereto as possible) to enhance the coverage of the particle population via the aberration due to the spacecraft velocity (at a 4-R_S perihelion, the spacecraft speed is ~300 km/s, and an energy of 20 keV/nucleon corresponds to a speed of ~2000 km/s). The sensitivity should be at least ~1 $(cm^2\ ster\ s\ keV)^{-1}$. Timing resolution should be no worse than 1 s for e^-, 5 s for protons, and 30 s for heavier nuclei. The capabilities described here can be achieved with energetic particle instruments of the type currently being flown on MESSENGER and included in the payloads of STEREO and New Horizons.

EPI High-Energy Instrument (EPI-Hi). The EPI high-energy instrument (EPI-Hi) is required to measure the composition and energy spectra of energetic nuclei with $1 \leq Z \leq 26$ from ~1 to 100 MeV/nucleon, as well as energetic electrons from ~0.3 to 3 MeV. The source of the energetic ions to be observed over the course of the Solar Probe mission range from quiet-time intensities of cosmic rays, to low-energy ions accelerated in CIRs and transient interplanetary shocks, to ions accelerated in small, impulsive events associated with solar flares, to solar energetic particles accelerated in large gradual events. As a minimum, the charge resolution should be sufficient to measure differential intensities of H, He, C, N, O, Ne, Mg, Si, and Fe, although minor species are also of interest. It would also be very useful (but is not required to satisfy the minimum science requirements), to extend composition measurements (of element groups) to include nuclei with $30 \leq Z \leq 83$ that are found to be enhanced in some SEP events associated with impulsive solar flares. It is required that ^{3}He and ^{4}He be separately identified whenever the ^{3}He/^{4}He ratio exceeds 1%. Assuming that onboard particle identification is used to sort species into a matrix of species versus energy bins, the energy resolution of these bins should be no worse than six intervals per decade.

Near the Sun it can be expected that energetic ions may be highly anisotropic and beamed along the interplanetary magnetic field, which is expected to be on average radial at closest approach, but could be highly variable. It is therefore desirable for the EPI-Hi instrument to sample as much of 4π steradians as possible, including, in particular, the forward hemisphere. As a minimum EPI-Hi should be able to observe particles with pitch angles ranging from 30° to 120° with respect to the spacecraft Z-axis with an angular resolution no worse than 30°. EPI-Hi should have sufficient directional information to be able to determine the magnitude and direction of 3D anisotropies.

Although not well known, it is expected that the intensity of SEP events will scale with distance from the Sun (R) approximately as R^{-3} (cf. *Reames and Ng*, 1998, and references therein). To observe particle populations that range from quiet-time levels near 1 AU to solar energetic particle (SEP) events near the Sun requires a dynamic range of ~10^7. The peak intensity of a typical impulsive event at 1 AU is ~1 to 10 protons/cm^2-sr-s >1 MeV. Scaling this to 4 R_S by R^{-3} suggests that intensities up to ~10^6 protons/cm^2sr-s >1 MeV should be measurable. Particle intensities should be measured with a timing resolution that is no worse than 1 s for electrons, 5 s for H, and 30 s for $Z \geq 2$ nuclei. There is considerable heritage for energetic particle instruments in the 1 to 100 MeV/nucleon energy range. Instrument designs that could be adapted to meet these requirements (assuming modern, low-power, low-mass electronics) have flown on Helios, Voyager, ISEE-3, Ulysses, Wind, and ACE, and will be flown on STEREO.

3.2.4 DC Magnetometer. The Solar Probe direct current Magnetometer (MAG) will provide context and definition of local magnetic structure and low-frequency (<10 Hz) magnetic fluctuations. MAG consists of one or more 3-axis sensors mounted close to the end of a deployable, non-retractable axial boom extending from the bottom deck of the spacecraft. (Owing to the size of the Thermal Protection System (TPS), MAG sensors can not be placed sufficiently far from the spacecraft body for a dual magnetometer configuration to be practical in removing spacecraft fields. A second MAG sensor could be used to provide low-power and low-mass redundancy.)

The MAG sensor will be located close to the search coil component of the Plasma Waves Instrument (PWI), making it necessary for both to work together to provide a suitable measurement environment. Close collaboration between the two teams

is critical to containing cross-contamination of the instruments and providing for the success of the mission. Signatures of plasma processes at the proton inertial scale, which result in the conversion of magnetic energy into heat, fall within the frequency range of the PWI, and only two suitably configured instruments will be able to provide the needed plasma diagnostics.

MAG Performance. Photospheric structures with scale sizes of tens of kilometers will have scale sizes of hundreds of kilometers if they are coherent out to the orbit of Solar Probe. A sample rate of 20 Hz gives a spatial resolution of approximately 30 km over the Sun's pole, which will provide minimal resolution of the magnetic structures. A burst or snapshot mode of higher time resolution is used for comparison with the PWI. Data telemetry compression to 16 bits/component (dynamic range 65536) will permit adequate retention of measurement resolution. Total telemetry dedication of 960 bps will permit adequate download of continuous 20-Hz vector measurement plus snapshot buffer.

Extrapolation of Helios data acquired at distances ≥0.3 AU yields an average interplenetary magnetic field (IMF) of approximately 260 nT at 20 R_S, the distance at which the primary mission begins. Various measurements and theories suggest that, within some regions and structures, the magnetic field might be as high as 1 to 6 G at 4 R_S. MAG should be capable of switching sensitivity ranges. At least four ranges are needed, with the most sensitive being $|B| < 0.1$ nT and the high-field range $|B| < 8.2$ G. With some adjustment to accommodate the upper range, this requirement could be met with magnetometers commonly flown on magnetospheric missions today.

Magnetic Cleanliness. For an expected field of ~250 nT, a DC cleanliness requirement at the magnetometer of 10 nT would be reasonable, with a low-frequency AC requirement of 1 nT. Given the small size of the spacecraft and short boom, cooperation between the instrument and spacecraft teams in controlling magnetic contamination is imperative and the spacecraft will need an enforced minimal magnetic cleanliness program. This program need not add cost, since magnetic contamination need only be contained to the level of the ACE spacecraft, but cleanliness must be addressed to achieve the core science goals of the mission.

3.2.5 Plasma Wave Instrument (PWI). The PWI sensors consist of a 3-axis search coil for detecting magnetic field fluctuations and a 3-element electric field antenna. The search coil sensor is mounted on the aft spacecraft boom, with the separation from the DC magnetometer and other instruments to minimize contamination of the search coil data to be determined. The electric field antenna is mounted on the base of the spacecraft, with the three antenna elements separated by ~120°. Each element is ~1.75 m long, with the last meter electrically isolated from the inner part of the antenna. The antenna inclination to the spacecraft axis is varied with distance from the Sun, so as to maintain the outer 1-m segment in sunlight, while minimizing heat input into the spacecraft. This arrangement allows the maximum separation between the outer antenna segments to facilitate quasi-thermal noise spectroscopy measurements inside 20 R_S. Having the end segments of the antenna elements sunlit inside of 20 R_S enables low frequency (< ~3 kHz) plasma waves to be sampled. Characterizing waves in this frequency range will provide insight into processes at and below the ion inertial scale.

Plasma wave instruments with the necessary capabilities have been implemented on numerous missions, including Cluster, Polar, FAST, and Geotail. Similar antenna concepts have been used on these missions; however, they were not designed to work in the thermal environment expected for Solar Probe. To be accommodated safely on the spacecraft, the PWI antenna will need to be made from a refractory material that will operate at temperatures up to 1400°C.

Search Coil Magnetic Field Measurements. The PWI magnetic field experiment should operate in the frequency range ~1 Hz to 80 kHz, allowing overlap with the DC magnetometer at low frequencies and to measure fluctuations beyond the ion cyclotron frequency at high frequencies (The sensitivities of the search coil and DC magnetometer are expected to be equivalent at approximately 10 Hz). The strawman instrument samples in frequency space at 40 channels per decade, with cross-spectral power between the field components at 20 channels per decade. Bursts of waveform data are also collected at a cadence of up to 60 s to allow detailed study of small-scale processes in the near-Sun plasma.

Electric Field Measurements. The PWI electric field experiment should measure fluctuations in the electric field from close to DC to above the plasma frequency (1 Hz to 10 MHz was chosen for the strawman instrument) so as to return information on low-frequency wave, turbulence, and small-scale structures and to diagnose plasma parameters (density and temperature) using the technique of quasi-thermal noise spectroscopy (QNS). QNS requires sampling total electric field fluctuations from low frequency to above the plasma frequency. The strawman instrument has a sampling density of 40 samples per decade and a temporal sampling period of 0.1 s to allow rapid sampling of plasma parameters local to the spacecraft. A sensitivity of 2×10^{-17} V/m^2/Hz at 10 MHz provides adequate signal to noise for QNS measurements. The strawman instrument returns 3-axis measurements sampled at 40 samples per decade, and as with the magnetic field, cross spectra between components are returned. In the low frequency regime (<10 kHz), cross spectra between E and B are measured to facilitate identification of wave modes. Waveform data that allow the study of small-scale phenomena are returned as burst mode data with a 60-s cadence.

3.2.6 Neutron/Gamma-Ray Spectrometer (NGS). The NGS detector should be capable of detecting and positively identifying neutrons and γ-rays from the Sun having energies that range up to 10 MeV. The neutron component should be capable of intrinsic energy resolution sufficient to separate neutrons having energies below and above 1 MeV, and better than 50% energy resolution for neutron energies between 1 and 10 MeV. This last requirement is needed to separate quasi-steady-state neutron emission from transient neutron emission. The NGS will measure the products of the acceleration of protons (via neutrons and γ-rays) and electrons (via γ-rays) as they interact with the dense low chromosphere and photosphere. If microflares or nanoflares play a significant role in coronal heating, these signatures of particle acceleration will be present. Their spectrum and time variation provide information on the acceleration process(es).

Upward-propagating protons and electrons may be directly detected by Solar Probe, although the probability of crossing the appropriate field lines at the critical time may be small. The neutron and γ-ray detection suffers no such restriction. Furthermore, Solar Probe's close passage to the Sun provides tremendous advantage for detection of low-energy neutrons because of their short lifetimes, as well as for spectroscopy of faint γ-ray bursts. These observations will, for the first time, provide solid statistical knowledge of frequency of energetic acceleration in small solar flares.

A detection of a burst of γ-rays would help refine the energy spectrum of transient neutrons through use of the measured time of flight between neutron arrival times and the time of the gamma burst. The detection sensitivity of the NGS should be sufficient to measure neutrons produced by flares that release greater than 10^{24} ergs.

A broad-band analysis of the γ-ray spectrum can provide a measure of the electron and ion components that will complement the detection of neutrons. The neutron measurements are most sensitive to the lowest-energy heavy-ion interactions, while the ion-induced gammas sample higher energies that may be present in the ion population. Bremsstrahlung from accelerated electrons will manifest themselves in a continuum spectrum that is distinguishable from that of the ion-induced gammas.

NGS Performance. The NGS is mounted behind the hydrazine tank. The presence of hydrazine onboard can be used as a separate detection channel via moderated neutrons. To adequately resolve the onset and duration of a γ-ray burst requires a sample period of 4 s in each of 64 energy bins, encompassing an energy band of 0.1 to 10 MeV. The neutron channel, because of the moderating influence of the hydrazine, will be detecting degraded neutrons with timing but less spectroscopic information. The neutron channel will require a sample period of 16 s over a neutron energy range of 0.05 to 20 MeV, also with 64-channel spectra. The detector must be able to distinguish statistically between fast neutrons and gammas and should possess an unambiguous neutron-detection channel. A spectral resolution better than 50% will allow broad-band analysis of the gammas and neutrons, sufficient to resolve the bremsstrahlung, nuclear, and neutron components. Both neutron and gamma spectrometer functions must efficiently reject charged particles.

Based upon extrapolation of measurements at 1 AU, an appropriate sensitive area for the γ-ray spectrometer is 40 cm^2 at 1 MeV, providing a sensitive

area of 10^5 cm^{-2} when scaled to 1 AU. The neutron spectrometer in the context of the spacecraft must have an effective area of 40 cm^2 at 1 MeV.

Heritage instruments for the Solar Probe NGS include those flown on Lunar Prospector, Mars Odyssey, and MESSENGER. (Like NGS, the MESSENGER instrument is located behind the propulsion-system hydrazine tank.)

3.2.7 Coronal Dust Detector (CD). The CD should be compact and lightweight and must be able to cope with the near-Sun thermal and particle environment. The CD assumed for this study is an impact ionization detector based on the Mars Dust Counter (*Igenbergs et al.*, 1998). Such devices measure ions and electrons produced by the impact of dust particles on the detector's target area to derive particle mass and have been successfully flown on Ulysses, Hiten, Galileo, and Nozomi (e.g., *Grün et al.*, 1992; *Sasaki et al.*, 2002). The CD is mounted on the +X (ram) face of the Solar Probe spacecraft, where it will be exposed to the maximum dust flux. For an aperture area of 140 cm^2, the dust model described in Appendix B predicts that 2×10^4 particles of masses larger than 10^{-17} g and up to 2×10^6 particles of masses larger than 10^{-19} g would be detected at the high-impact velocities that Solar Probe will experience. Independent pointing and special pointing accuracy are not required.

The CD will be operated continuously (except when in direct sunlight). Only modest telemetry allocation is required. The CD should have an external cover to be removed after launch. No special cleanliness is required, but purging with N_2 should be considered. Issues to be addressed for further development of the CD are the high voltage parts and the influence of the radiation environment and outgassing from the heat shield on the measurements. Measurement of particle mass is standard for impact ionization detectors but has not yet been demonstrated for the high impact speeds that the Solar Probe CD will experience.

Although a single sensor has been assumed in the payload design, we have conservatively included enough mass to accommodate a second sensor mounted at a different location on the spacecraft to provide a second look direction. The allocated power is adequate to two alternately operated sensors. Measurements from two sensors on different spacecraft locations can be used to distinguish between particles in prograde and retrograde motion as well as between particles in near-ecliptic and out-of ecliptic orbits. If resources permit, an alternative to two sensors would be a single detector with time-of-flight (TOF) capability. This would enable TOF measurement of the impact-produced ions, yielding mass spectra and allowing the elemental composition of the dust to be derived.

3.2.8 Hemispheric Imager (HI). HI is a broadband, very-wide-angle, white-light coronagraph with a ~160° FOV to image the local spacecraft environment and provide tomographic imaging of coronal structures (e.g., polar plumes) as Solar Probe flies through the corona. HI will also be able to observe coronal mass ejections (CMEs) and other dynamic structures as they evolve. Coronal tomography is a *fundamentally* new approach to coronal imaging (similar to a medical CAT scan) and is possible only because the imaging is performed from a moving platform close to the Sun, flying through coronal structures and imaging them as it flies by and through them. HI observations of the 3D coronal density structure are required to resolve ambiguities in the interpretation of spatial and temporal changes seen in the in-situ measurements. HI heritage stems from the all-sky coronagraph on SMEI, the HI wide-angle coronagraph on STEREO, and instrument prototypes developed as part of the 1995 Solar Probe Instrument Development Program (*Buffington et al.*, 1998).

The HI's FOV and resolution derive from the need to provide context for the in-situ instruments and to be able to reconstruct the 3D density structure of the corona tomographically. The 160° FOV is sufficiently large to view the corona from near the solar limb to beyond the zenith. A wide-angle view is particularly important for imaging faint coronal features, because the coronal intensity contrast is greatest *along* flux tubes and other magnetic structures near the zenith. The spatial resolution required to image small-scale coronal structures is of order 1°. The temporal cadence required to provide continuous observations and sufficient data for 3D tomographic reconstruction is ~90 s at perihelion.

3.2.9 Polar Source Region Imager (PSRI). PSRI uses an imaging periscope to view the Sun's poles above 60° latitude at distances beyond 20 R_S. The PSRI consists of two channels, a magnetograph channel to image the polar magnetic fields and an

EUV imaging channel to identify small-scale hot coronal plasma structures. These two channels will make it possible to relate the magnetic field structure to the heating of coronal structures at the poles and to establish the linkage between these source region(s) and the plasma flows measured at the spacecraft. PSRI magnetograph channel heritage stems from tunable etalon magnetographs flown on the Flare Genesis Balloon and instrument designs developed as part of the 1995 Solar Probe Instrument Development Program (*Title et al.*, 1999). PSRI EUV channel heritage stems from SOHO/EIT, TRACE, STEREO, GOES/SXI, and various rocket programs.

The imaging periscope uses two channels, each 1 inch in diameter, to view the solar surface at the Sun's poles. The periscope will be extended for 10 seconds (and then retracted) every 10 min while Solar Probe is beyond 20 R_S and above 50° heliolatitude. This operational sequence is based on a detailed thermal and mechanical analysis by the Solar Probe Engineering Team. During perihelion passage, inside 20 R_S, the periscope will be stowed behind the heat shield.

The FOV for the PSRI EUV channel is 3°. This requirement is driven by the need to view the entire polar region below the spacecraft from 20–65 R_S. The spatial resolution requirement is driven primarily by the need to resolve small-scale EUV structures at the coronal base of polar plumes. This spatial resolution can easily be achieved with the current EUV imaging channel baseline pixel size of 10 arcsec (two pixel resolution = 20 arcsec), corresponding to a 2-pixel resolution of ~2 Mm at 20 R_S (comparable to a spatial resolution of 2.5 arcsec at 1 AU). This single-pixel angular resolution is derived from the assumption of using a 1024×1024 format detector to image the full 3° FOV. A 1-s exposure in the EUV yields a single-pixel signal-to-noise ratio of ~10 for quiet Sun observations and ~30 for bright structures, which is adequate for the science requirements.

The PSRI magnetograph channel is designed both to probe the overall magnetic structure of the pole and to compare the presence of mixed-polarity magnetic structures to the solar wind conditions associated with polar plume footpoints. The magnetograph channel FOV requirements are identical to those of the EUV channel. The magnetograph channel spatial resolution is driven by the need to spatially resolve small-scale mixed polarity structures (~4 Mm). Because of the differential nature of magnetic flux measurements, the signal-to-noise ratio must be at least 100 in each pixel to achieve quantitative measurements of the magnetic field.

3.2.10 Common Data Processing Unit (CDPU). The CDPU integrates the data processing and low-voltage power conversion for all of the payload science instruments into a fully redundant system that eliminates replication, increases redundancy, and reduces overall payload resources. The CDPU consists of redundant sides (A and B), each of which contains a processor board, a low-voltage power supply board, a low-voltage distribution board, a serial instrument interface board, and a custom instrument interface board. The processor board employs a high-speed 32-bit processor and at least 2 Gbit of memory to service the instrument interface boards and perform all of the control and data processing that each instrument requires. This includes real-time control and servicing as well as processing of acquired data through fast-Fourier transform (FFT), compression, and custom algorithms that the instrument teams specify. The low-voltage power supply board and low-voltage distribution board efficiently convert the primary spacecraft power bus using DC–DC converters to the secondary voltage rails required by the instrument electronics and distribute those voltage rails to the science instruments. The serial instrument interface board is used for instruments whose front-end electronics produce results in digital form. This information will be transmitted serially from the instrument to the CDPU, buffered in memory on the interface board, and processed by the CDPU software. Other instruments require discrete control and analog conversion to process the data produced by their front-end electronics. The custom instrument interface board services these instruments, providing the control, processing, and data buffering required to integrate each instrument.

The CDPU provides a unified interface to the payload for the spacecraft. The spacecraft selects which side of the CDPU will be powered, leaving the redundant side off as a cold spare. The payload CDPU communicates with the spacecraft over a MIL-STD-1553 bus, accepting commands and producing CCSDS packets ready for final processing by the spacecraft for telemetry to the ground.

3.3 Supporting Scientific Activities

Solar Probe is analogous to a planetary flyby mission, in that the unique observations that justify the mission will be carried out in less than a day at perihelion. To obtain the maximum scientific return from this "burst" of observations, the Solar Probe mission needs to be supported by (1) theory and modeling and (2) a coordinated campaign of observations by relevant ground-based, suborbital, and space-based assets during the Probe's perihelion pass.

3.3.1 Theory and Modeling. Experience has shown that a broad involvement of the scientific community in targeted theoretical and computer modeling studies, both before and after the period of intense data gathering, multiplies by a significant factor the scientific return from exploratory space missions. To facilitate broad community participation in the Solar Probe mission, the Solar Probe STDT recommends that NASA establish a competitive Solar Probe Affiliated Scientist (SPAS) theory and modeling program. Affiliated Scientists should be fully involved early enough in the mission that their work can contribute to operational decisions (for example, concerning the design of burst-mode data collection during the perihelion pass). Affiliated Scientists should be selected 3 years prior to Solar Probe's first perihelion passage, with support through the first encounter plus 4 years. The SPAS program should provide for semi-annual meetings of Affiliated Scientists and Solar Probe investigators and, after perihelion passage, for several community workshops on specific aspects of Solar Probe science (e.g., magnetic reconnection and turbulence, plasma acceleration, etc.). We envision NASA support for 8 to 12 Affiliated Scientists and/or small subject teams, with an equivalent number supported by other national and international agencies.

3.3.2 Solar Probe Observation Campaign. Solar Probe's perihelion pass—the first passage of a spacecraft within 4 stellar radii of a star—will be so unique, exciting, and important a scientific opportunity for the solar and space physics and astrophysics communities that all relevant national and international scientific assets should be dedicated to providing supporting observations in a coordinated perihelion pass campaign. As part of its education and public outreach component, this campaign should also provide for the participation of amateur solar astronomers from around the world.

During its first flyby of the Sun, Solar Probe will pass 15° in front of the disk, inside the east limb as viewed from Earth. This orbit is designed to permit observation from Earth of the sub-Probe solar surface as well as to allow coronagraphic observations in the days and hours leading up to perihelion passage. A wide range of ground-based, sub-orbital, and space-based observations will thus be able provide unique and important contextual information for the Solar Probe measurements, substantially enhancing the science return from Solar Probe. Conversely, the remote observations will benefit from the unique ground-truth measurements provided by Solar Probe, which will allow benchmark calibrations of many observational techniques that rely on important but hitherto unverified assumptions about the near-Sun environment.

The planning and coordination of the Solar Probe perihelion pass campaign should be the responsibility of the Solar Probe team and Affiliated Scientists. (An example of how such a coordinated observational, data analysis, and theory campaign can be organized is provided by the RHESSI Max Millenium Program.) Funding for specific ground-based and/or suborbital solar observations should be provided by the Solar Probe project. We anticipate that support for other campaign activities will be provided by COSPAR, the International Astronomical Union, the National Science Foundation, and other national and international scientific agencies.

Blank Page

4.0 Mission Implementation

Throughout the present Solar Probe study, the STDT worked very closely with an engineering team from The Johns Hopkins University Applied Physics Laboratory (JHU/APL), with support from the Jet Propulsion Laboratory (JPL), the Goddard Space Flight Center, and STDT member and other institutions. This process led to the technical mission implementation described in this section, which clearly demonstrates that at least one detailed mission concept (1) is technically feasible, (2) fully addresses all four science objectives, and (3) minimizes risk and cost of implementation. During the five full STDT meetings, in several smaller subteam meetings, and in numerous teleconferences, STDT and engineering team members discussed and refined the science objectives, measurement requirements, instrument resource requirements and accommodation, orbit and encounter geometry, risks and risk reduction measures, and cost saving options. Ideas that emerged from these discussions were incorporated in rigorous mission design and engineering trade studies. The STDT encouraged the engineering team to draw on their own extensive internal experience with space missions, along with examining external ideas and solutions, in order to develop the most detailed and technically complete and accurate engineering study possible.

Among the various engineering challenges the team addressed, significant effort went into the design of the Probe's Thermal Protection System (TPS), accommodating instrument concepts defined by the STDT, and assessing the effects of the near-Sun dust environment on the spacecraft. Throughout the study we focused on minimizing both cost and technical risk as our prime considerations. Appreciable cost savings were achieved through the decision to configure the science payload as a single, integrated package, serviced by a common data processing unit, and through other design solutions that allow Solar Probe to be launched on an Atlas 551 in addition to being dual-compatible with the Delta IV Heavy to cover any launch vehicle uncertainty. ***The result is a technically feasible, acceptably low-risk and affordable mission that can survive in the unique thermal and dust environment near the Sun and that will fully achieve all of the Solar Probe science objectives.*** The sections that follow describe this baseline Solar Probe mission. Additional supporting material is presented in the appendices. Key requirements that flow down from the science objectives and drive the mission and spacecraft designs are summarized below:

Mission Requirements

- Perihelion distance of 4 R_S (3 R_S altitude)
- Solar approach trajectory approximately 90° out of the ecliptic
- A Sun-spacecraft-Earth geometry at encounter that allows simultaneous Earth-based observations to support Solar Probe observations.
- A Sun-spacecraft-Earth geometry that allows real-time science data return throughout the first encounter
- At least two solar encounters, preferably at different solar activity levels

Spacecraft Requirements

- Survive solar intensity at perihelion 3000 times that near Earth
- Survive intense radiation environment at Jupiter flyby
- Protect the instruments and spacecraft from the dust environment near the Sun
- Provide reliable power over the distance range 0.02–5.5 AU
- Provide significant real-time data throughout the first solar encounter
- Provide large total science data return for the solar encounter (~121 Gbits for first encounter)
- Accommodate significant payload mass (~52 kg) and average power (53 W)
- Provide science boom for magnetometer and Plasma Wave Instrument (PWI) search coils
- Provide required actuations of instruments and antennas for proper placement and FOV orientations during the encounters

4.1 Baseline Mission Design

The baseline mission design uses a direct Jupiter gravity assist (JGA) trajectory to place Solar Probe into a polar orbit about the Sun with a perihelion of 4 R_S (**Figure 4-1**). Venus and/or Earth gravity assists prior to the JGA were also considered as a means of reducing launch energy but were rejected because they would lengthen the time from launch to solar encounter and because of the perceived risks of an Earth flyby with a nuclear-powered spacecraft. A

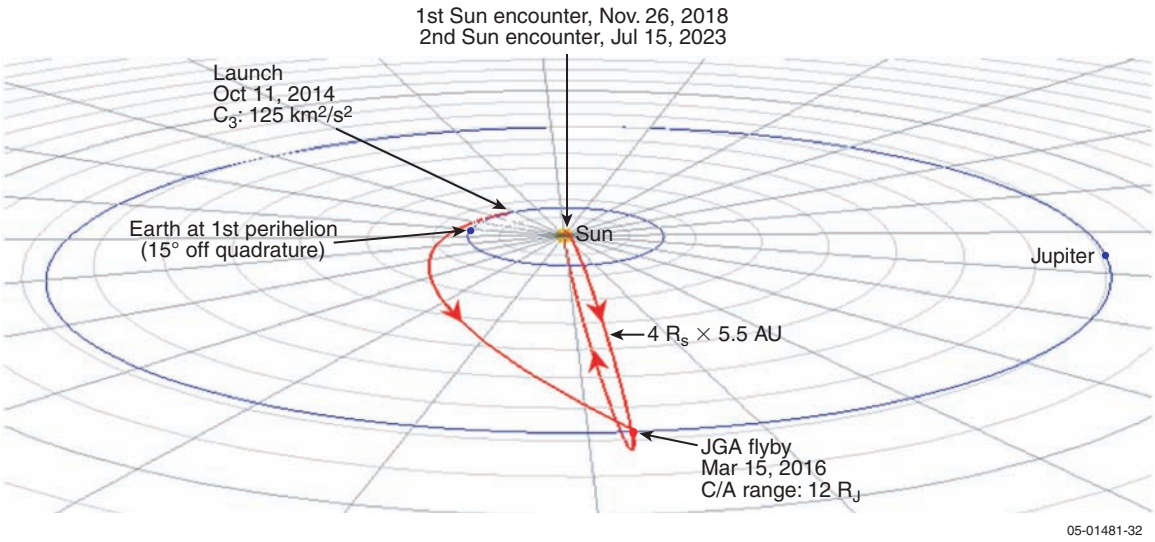

Figure 4-1. Solar Probe mission summary.

20-day launch window opens every 13 months to allow the desired trajectory and Sun–Earth geometry for the first encounter to be achieved. The current baseline mission assumes a launch in October 2014.

4.1.1 Launch and Launch Vehicle Selection. Solar Probe will be launched from the Eastern Test Range at Cape Canaveral Air Force Station, Florida. For a 2014 launch, the 20-day launch window opens on October 11. The maximum launch energy C_3 for this window is 125 km^2/s^2. For a 2015 launch, the maximum C_3 would be reduced to 122 km^2/s^2. Based on the current estimate of Solar Probe launch mass (including a 30% margin) and launch vehicle performance calculations provided by Kennedy Space Center (KSC), assuming the contracted performance for the New Horizons Pluto mission, either an Atlas 551 or a Delta IV Heavy, combined with a STAR 48B third stage, could provide the high launch energies required by Solar Probe. The Atlas 551 has been baselined as the Solar Probe launch vehicle for this study.

4.1.2 ΔV Requirement. Solar Probe's onboard ΔV requirement is fairly small because no deterministic burns are required and a free return trajectory will be used for the subsequent encounter. An estimated 150 m/s of ΔV is budgeted for:

- Maneuvers to correct launch vehicle dispersion errors
- Maneuvers to correct navigation errors prior to the JGA and solar encounters
- De-spin after third stage separation
- Momentum de-saturation

4.1.3 Jupiter Gravity Assist. For a 2014 launch, the JGA will occur in March 2016, with a closest approach distance of approximately 12 R_J. This target point was selected to achieve the desired solar encounter geometry with acceptable radiation doses at the Jupiter flyby. It results in a 4.1-year cruise from launch to the first solar encounter. A shorter 3.1-year flight time is possible but requires closest approach to Jupiter to occur at a distance less than 5 R_J, thus exposing the spacecraft to unacceptably high levels of radiation from Jupiter's radiation belts.

4.1.4 Solar Encounter. Solar Probe will approach the Sun from the south, reaching a maximum velocity of 308 km/s at perihelion. The pole-to-pole passage will take place within 9 R_S and will last roughly 14 hours. The encounter trajectory and timeline are shown in **Figure 4-2**. The first solar encounter will take place with the Earth 15° off quadrature as Solar Probe passes through perihelion (**Figure 4-3**). This geometry will allow the Probe to transmit data in real-time at a high data rate during the encounter and will enable simultaneous contextual imaging from Earth of the coronal structures through which the spacecraft is flying.

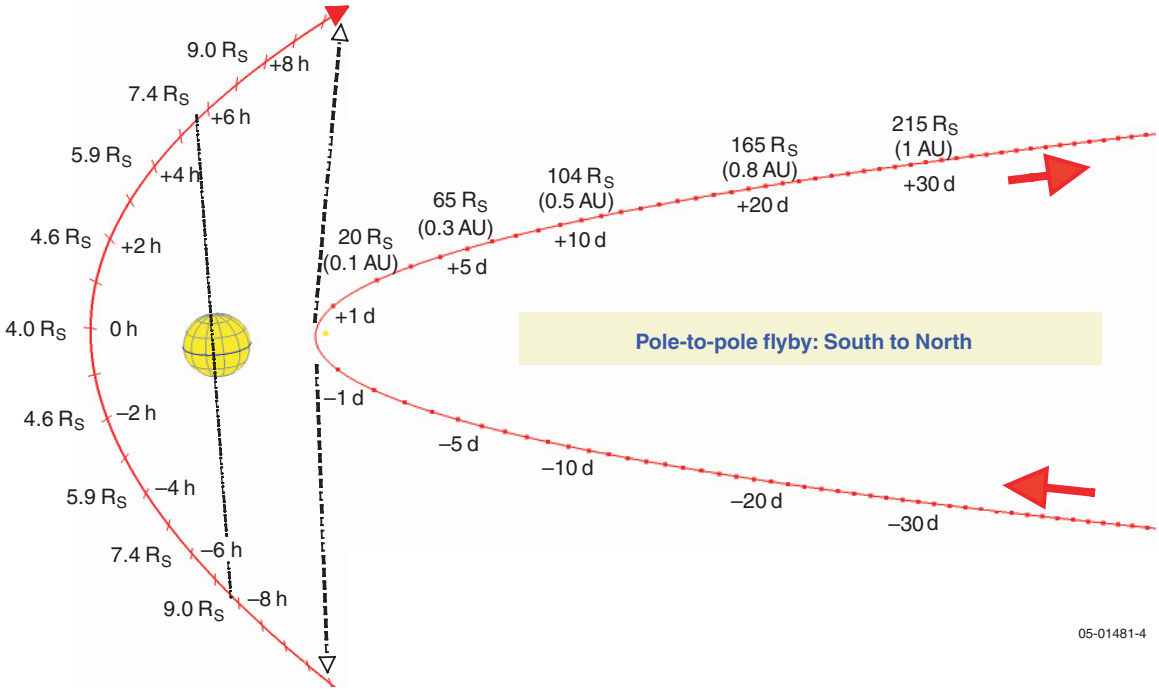

Figure 4-2. Solar encounter trajectory and timeline. Science operations begin at perihelion – 5 days (65 R_S) and continue until perihelion +5 days.

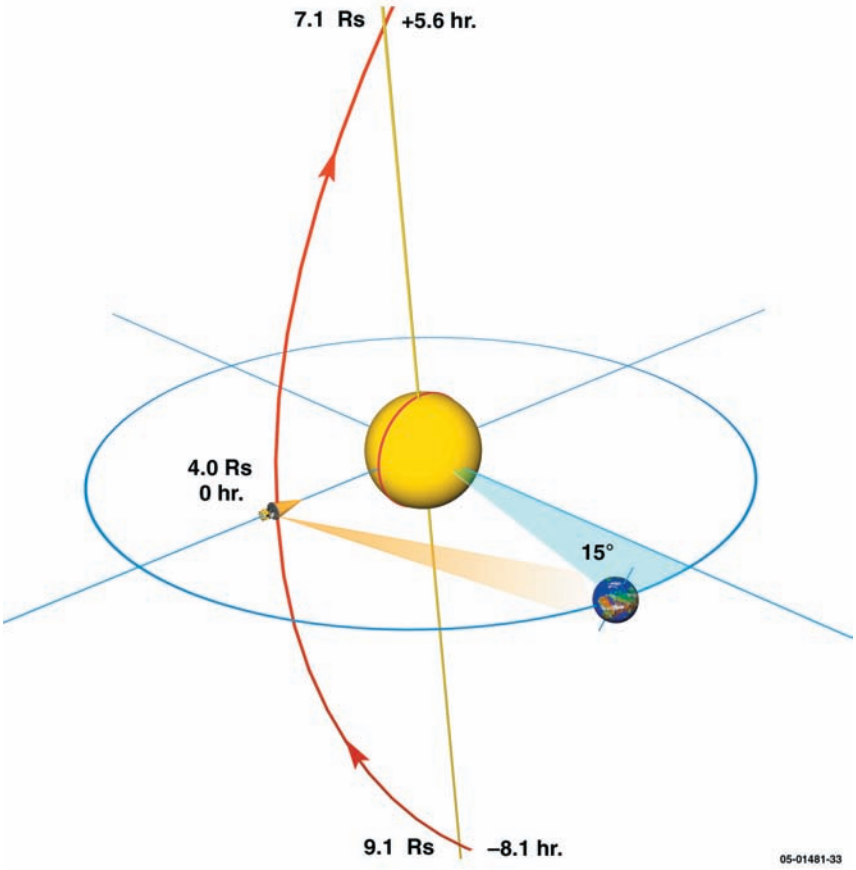

Figure 4-3. Geometry of the first solar encounter. Earth is positioned 15° off quadrature relative to the Sun–spacecraft line, allowing simultaneous observation from Earth of coronal features being sampled in situ by Solar Probe. The high-gain antenna points earthward, enabling real-time data transmission at a high data rate.

4.1.5 Subsequent Solar Encounters. Because of launch mass limits and potentially high ΔV requirements of retargeting, we decided to accept a free return trajectory for the second solar encounter. Depending on the launch year, the orbital period for a free return trajectory will vary with an average of around 4.5 years. For a 2014 launch, the orbit period will be 4.6 years, with a second solar encounter occurring on July 15, 2023 (8.8 years after launch). The encounter geometry will be 34° off quadrature (**Figure 4-4**), which will again permit simultaneous remote-sensing observations from Earth. High-data-rate real-time telemetry will not be possible during this encounter, however, because the high-gain antenna (HGA) will be pointed away from the Earth. For this encounter, the low-gain antenna (LGA) will provide the necessary communications for housekeeping and status, while the science data will be stored and sent after the second encounter is completed.

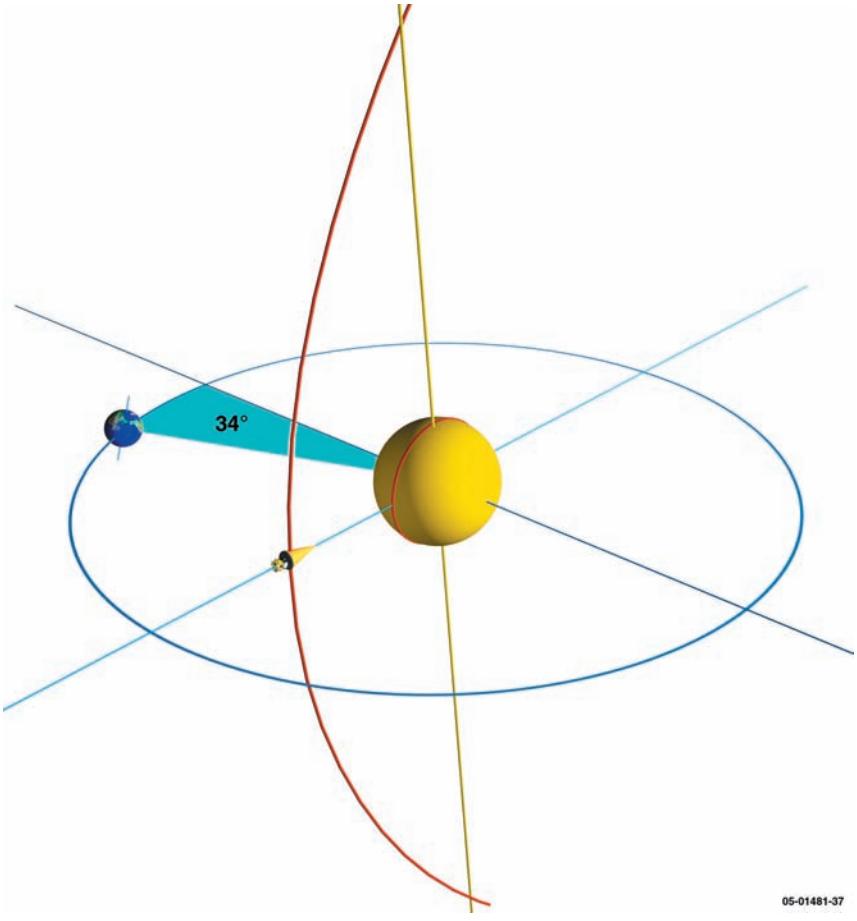

Figure 4-4. Second solar encounter geometry, with Earth 34° off quadrature.

4.2 Mission Concept of Operations

4.2.1 Launch and Early Operations. Solar Probe will be launched from Cape Canaveral within a 20-day launch window on an Atlas 551 with a STAR 48 third stage. As stated above, the nominal launch date is October 11, 2014. Except for propellant budgeted for launch vehicle dispersion and navigation corrections, the entire ΔV necessary for achieving the Jupiter flyby will be supplied by the launch vehicle. For the first and second-stage fly-out, the spacecraft will be 3-axis stabilized by the launch vehicle. For the third-stage fly-out, the stage will be spin-stabilized at approximately 60 rpm.

Upon separation from the third stage, Solar Probe will perform a de-spin maneuver and assume a 3-axis stabilized orientation with the medium-gain antenna (MGA) pointed toward the Earth. Communications will be established through the MGA. The MGA will be the primary antenna for communications until the HGA is released from its stowed position and checked out. The first 90 days after launch will be allocated to checkout of the spacecraft, which can easily be supported by 8-hour contact periods 3–4 times per week. During the first 7 days after launch, coverage will be continuous.

4.2.2 Outbound Cruise. After the initial checkout is completed, the number of contacts will be reduced to one 8-hour contact per week, which will be adequate for navigation updates as well for cruise science telemetry. All contacts will be initiated through the MGA and switched to the HGA if higher data rates are desired. Solar Probe will remain 3-axis stabilized, with the fixed MGA pointed toward Earth. During non-contact periods, a slow

rotation about the antenna axis (Y) may be introduced to minimize the cumulative angular momentum effects of solar pressure torque.

4.2.3 Jupiter Gravity Assist. Thirty days before the Jupiter encounter, the number of contacts with the spacecraft will increase to 3–4 per week to allow analysis, execution, and evaluation of a navigation burn planned for approximately 21 days prior to the flyby. This burn will provide corrections necessary to ensure that the gravity assist targets the spacecraft for the 4 R_S perihelion solar encounter. Additional corrections may be needed soon after the Jupiter encounter to correct any residual errors from the gravity assist maneuver.

4.2.4 Inbound Cruise. From 1 month after the JGA maneuver until 3 months before the solar encounter, the spacecraft will return to its cruise configuration and contacts will be reduced to one per week. Three months prior to the encounter, the number of contacts will again increase to 3–4 per week for instrument calibration, testing of spacecraft modes planned for the encounter, and instrument practice runs in preparation for the encounter. At ~0.8 AU, Solar Probe will point the TPS toward the Sun to protect the spacecraft and instruments from the intense solar flux. Because of the HGA gimbal limitation imposed by the TPS, the spacecraft may be required to off-point by as much as 13° from 0.8 to 0.3 AU in order to keep the HGA pointed towards the Earth. However, the spacecraft and instruments will remain safely within the protective umbra of the TPS at these distances.

4.2.5 Solar Encounter. At 0.3 AU, 5 days prior to perihelion, the primary science phase of the mission will begin, and telemetry will be continuous with Ka-band link, with a portion of the science and housekeeping data being sent in real time. A single-axis gimbal-and-arm mechanism that controls the rotation of the HGA about the X-axis, together with rotation of the spacecraft about the Z-axis, will enable the HGA to track the Earth while the TPS remains pointed at the Sun. During the encounter, the data rate will support at least 25 kbps. All science and housekeeping data will be recorded redundantly on two solid-state recorders (SSRs). All in-situ instruments will operate throughout the solar encounter, with the retractable arm maintaining the apertures of the fast plasma instrumentation near the edge of the umbra to maximize their field-of-view to the solar wind. The Polar Source Region Imager (PSRI) will begin solar surface imaging at about 65 R_S and will continue to operate until 20 R_S. The PSRI periscope will be retracted for a period of time after each image to allow it to cool after direct solar exposure. At 20 R_S inbound, the PSRI will cease taking data, and the Hemispheric Imager (HI) will increase its imaging cadence. At 20 R_S on the outbound leg, the HI cadence will decrease, and the PSRI will resume imaging of the solar surface until the Probe reaches 65 R_S. Throughout the encounter, the three Plasma Wave Instrument (PWI) electric field antennas will be actuator-controlled to extend ~1 m beyond the TPS umbra into direct sunlight. An extensive autonomous fault protection system will ensure that a safe spacecraft attitude is maintained in the event of any single hardware or software failure.

4.2.6 Post Encounter. The solar encounter phase will end 5 days after perihelion, and retrieval of non-real-time science data from the recorders will begin. During this time daily 8-hour contacts will be provided. The TPS will remain pointed toward the Sun until the spacecraft is beyond 0.8 AU. Contact will be maintained by pointing the HGA in the same manner as during the encounter. At 0.8 AU, the spacecraft can be re-oriented to provide continuous antenna coverage to the Earth. The planned 121 Gbits of recorded science and housekeeping data will be telemetered back to Earth in approximately 101 days assuming 8-hour contacts per day and an average data rate of 45 kbps.

4.2.7 Subsequent Encounters. A free return trajectory was selected for subsequent encounters to minimize the amount of propellant required and meet launch mass requirements. The free return period is dependent on the actual launch date but is approximately 4.6 years for a 2014 launch. The resulting west limb geometry relative to Earth for the second encounter will restrict HGA coverage, allowing only low-data-rate telemetry through the LGAs for real-time communications during the solar encounter. The recorded data will be sent after the encounter but additional contact time will be required because of the unfavorable relative geometries between Earth and the spacecraft.

Low-resolution in-situ science data will be collected and telemetered throughout the pre- and post-encounter cruise phases of the mission.

4.3 Mission Environment

Solar Probe must be able to operate and survive under extreme environmental conditions, which present significant challenges for the engineering design of the spacecraft. To achieve a polar orbit about the Sun, Solar Probe must perform a close Jupiter flyby, thereby exposing it to Jupiter's intense trapped radiation as well as to a thermal environment with very low solar flux. As the spacecraft approaches and flies past the Sun, it will be exposed to intense solar flux and bombardment by particles from the circumsolar dust cloud. In addition, the effects of coronal lighting and solar scintillation in the near-Sun environment must be accounted in the design of the attitude control and telecommunication systems.

4.3.1 Solar Flux. The most challenging spacecraft design driver is the intense solar flux to which Solar Probe will be exposed. At perihelion, the flux will be 400 W cm^{-2}, which is roughly 3000 times that at Earth orbit. As discussed in detail in Section 4.6 below, the TPS, consisting of primary and secondary shields, protects the instruments and spacecraft bus from direct exposure to this intense flux. Except for the PSRI periscope and PWI electric field antennas, the instruments and spacecraft components will reside within the umbra of the TPS at all times during the encounter. (The PSRI periscope will extend outside the umbra for multiple cycles lasting up to 30 seconds during the inbound and outbound legs while the spacecraft is beyond 20 R_S.)

As described above, Solar Probe will not turn the TPS toward the Sun until it is within 0.8 AU of the Sun. Thus the instruments and spacecraft components must be capable of accommodating a direct solar flux of up to 0.212 W cm^{-2} at 0.8 AU. In addition, during the JGA maneuver, Solar Probe will, at 5.5 AU, be in a region where the solar flux is ~30 times less than it is at Earth. Thus the spacecraft must be able to maintain the instruments and subsystems within allowable temperature limits over a rather dramatic range of thermal environments.

4.3.2 Radiation. Solar Probe will be exposed to three kinds of ionizing radiation: electrons and protons trapped in the jovian magnetosphere, solar energetic protons during solar maximum conditions, and gamma rays from the radioisotope thermoelectric generators (RTGs). **Table 4-1** gives the ionizing dose from each source received behind 100 mils of aluminum spacecraft shielding. The radiation dose near Jupiter was calculated for a closest approach distance of 12 R_J (*Divine and Garret*, 1983). The RTG gamma ray flux was derived from measurements of the Cassini RTGs. The JPL-91 solar proton flux model (*Xapsos et al*., 1996) was used at the 95% confidence level to estimate the solar energetic particle dose for solar maximum conditions. The relatively high total dose and the large initial dose during the Jupiter flyby influenced both the spacecraft design and mission operations concept. All electronics devices for this mission are selected to be radiation-tolerant to the total dose defined in **Table 4-1**. As a precaution, radiation-sensitive components not required for the JGA maneuver, including the redundant integrated electronics modules (IEMs) and star trackers, will be turned off while the spacecraft passes through Jupiter's radiation belts to minimize radiation effects.

4.3.3 Coronal Lighting. Coronal lighting near the Sun is an environmental factor that can have significant consequences for maintaining attitude control. Excessive coronal lighting can increase background noise and degrade the star tracker's ability to detect star constellations needed to determine spacecraft attitude. Although coronal lighting conditions can be estimated from data acquired by remote-sensing instruments in orbit at 1 AU, uncertainty about the actual lighting conditions will remain until a mission near the Sun is performed. Because of this uncertainty, the Solar Probe concept incorporates two star trackers, facing in approximately orthogonal directions, and a high-precision inertial measurement unit (IMU). Additionally, the spacecraft design concept incorporates a safing sensor

Table 4-1. Solar Probe total radiation dose

Component	Margin	Dose with Margin (krad Si)
Jupiter Pass	× 2	30
RTG gamma	× 1.5	4
Solar protons	× 3	10
Total		44

that detects the edge of the solar horizon if the star trackers are blinded for an extensive period.

4.3.4 Solar Scintillation. The effects of solar scintillation have been well characterized based on mission data from the Near Earth Asteroid Rendezvous (NEAR) mission as well as from the Magellan and Galileo missions. During the NEAR mission measurable telemetry losses in the X-band downlink were experienced around solar conjunction once the angle between the Sun, the Earth, and the spacecraft came within 2.3°. In the case of Solar Probe this angle will be less than 2.3° for ~14 hours during the spacecraft's pole-to-pole/perihelion pass. Based on the NEAR experience, an X-band downlink was not considered reliable to meet the real-time telemetry goals during this most critical period of the Solar Probe mission. Instead, the Ka-band has been baselined for the real-time data transmission during the first solar encounter because it is relatively unaffected by solar scintillation. The baseline telecommunications design provides at least 25 kbps of real-time telemetry throughout the solar encounter.

4.3.5 Micrometeoroids and Dust. Solar Probe will encounter several different dust environments and must be shielded against high-velocity impacts by particles of various sizes. During its journey in the ecliptic to Jupiter, the spacecraft will encounter a micrometeoroid and dust environment typical of that experienced by deep space missions that pass through the asteroid belt and near Jupiter. Once in polar orbit, and for most of its cruise, it will see mostly interstellar dust, similar to the dust environment experienced by Ulysses. As Solar Probe passes near the Sun, however, it may encounter significantly more dust, particularly within 30° of the ecliptic (*Mann et al.*, 2004) as it approaches perihelion. As discussed in Section 3.4, there is considerable uncertainty about the dust environment near the Sun, especially inside 10 R_S where observations are limited and dust destruction plays a significant role in the distribution of the dust population. In this region, it is expected that Solar Probe will encounter mostly small particles consisting of carbon and some refractory silicate material with a bulk density of ~2.5 g/cm^3. To define the shielding requirements for Solar Probe, a dust model was developed based primarily on the work of *Mann et al.* (2004). The model employs the following assumptions:

1. The number density of the dust in ecliptic orbits (within ±30° inclination) varies with distance as $1/r$ out to 10 R_S.
2. 5% of the dust within 30° of the ecliptic is in retrograde orbits.
3. Beyond 30° inclination, the flux is 10% that of item 1 for particles smaller than 5 μm and 5% that of item 1 for particles larger than 5 μm.
4. 50% of the flux at >30° inclination is in retrograde orbits.
5. All dust trajectories close to the Sun are circular.
6. As the distance from the Sun decreases to within 10 R_S, the number density of dust particles remains constant because of dust destruction.

Mann et al. (2004) estimate that significant dust particle collisions occur in the inner heliosphere that redistribute the particle flux greatly in favor of smaller particles, as illustrated in **Figure 4-5**. However, to account for uncertainties in the actual circumsolar dust environment, it was conservatively assumed that there are no collisions between particles. A quantitative comparison between the results of models with and without collisions is provided in Section 4.14 and demonstrates the level of conservatism in the estimates of critical particle size used in the engineering model. Specific equations and calculations used to model the near-Sun dust environment are presented in Appendix B. An analysis was also performed to verify that no known

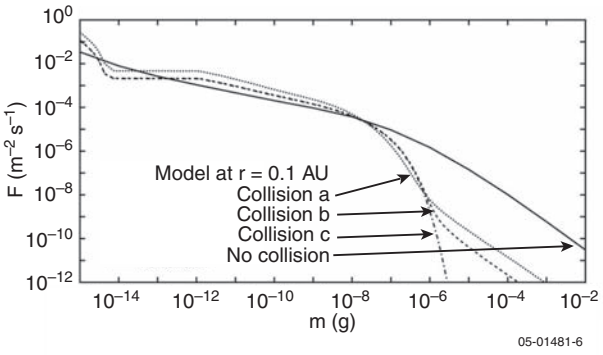

Figure 4-5. Predicted dust environment at 0.1 AU. The particle size distribution was calculated according to three different collision models (a, b, and c) as well as for a non-collision model. The models are described by *Ishimoto* (2000).

Sun-grazing comets, including the well-known Kreutz family, intersect the Solar Probe trajectory.

4.4 Spacecraft Overview

The Solar Probe spacecraft will operate in environments from 0.02 to 5.5 AU from the Sun and in close proximity to Jupiter (12 R_J) and will accommodate the science payload defined by the STDT. The spacecraft concept is illustrated in **Figure 4-6**. The major Solar Probe components are illustrated in the block diagram in **Figure 4-7**. This section provides an overview of the baseline design, discusses the fault protection approach, and summarizes the Solar Probe mass and power requirements. The individual subsystems and related design issues are described in subsequent sections.

4.4.1 Spacecraft Description. Solar Probe is 3-axis stabilized spacecraft. Its most prominent feature is the Thermal Protection System (TPS), a large conical carbon–carbon primary shield that is 2.7 m in diameter with a low-thermal-conductivity, low-density secondary shield attached at its base. The TPS protects the spacecraft bus and instruments within its umbra during the solar encounter and is attached to the bus with 12 struts. The science instruments are mounted either directly on the bus, on a retractable/extendable arm on the +X side of the spacecraft, or on the aft science boom. The science boom also carries a solar horizon sensor (SHS) for backup attitude safing during the solar encounter. Three deployable carbon–carbon plasma wave antennas are mounted 120° apart on the side of the bus. These antennas will penetrate beyond the umbra created by the TPS during the encounter. Instrument low-voltage power and data processing are provided by a common Data Processing Unit (DPU). The hexagonal bus carries the spacecraft subsystems and provides an efficient mechanical structure to handle the launch loads and integrate with the launch vehicle.

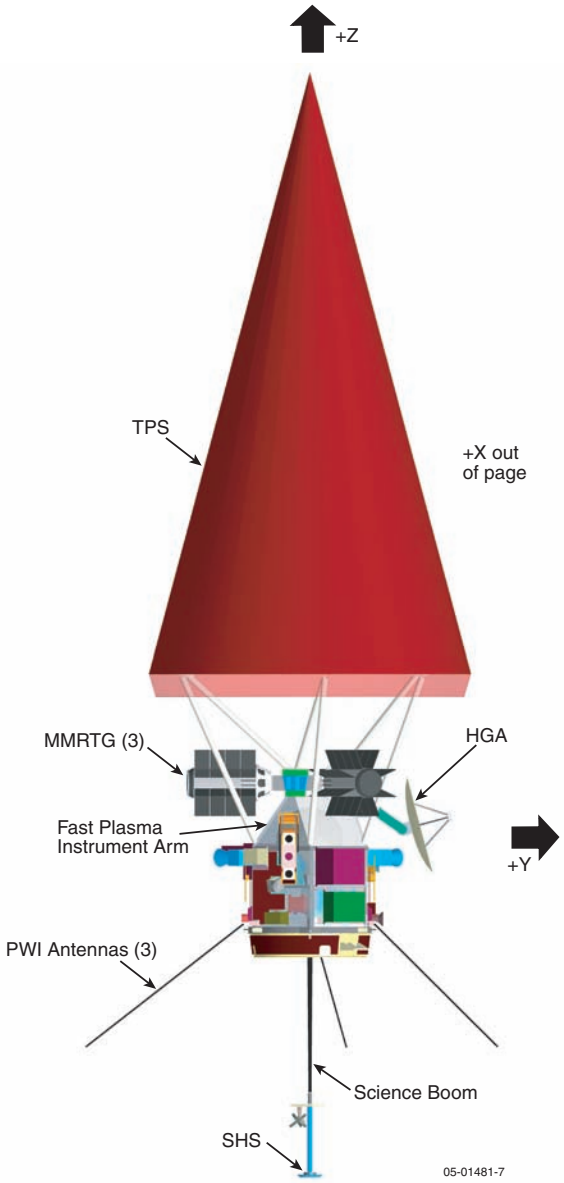

Figure 4-6. Solar Probe spacecraft.

Three Multi-Mission Radioisotope Thermoelectric Generators (MMRTGs) provide primary power to the spacecraft. They are mounted high on the bus to minimize the diameter of the TPS and are positioned to facilitate installation via access doors in the launch vehicle fairing. A lithium-ion battery is included as a secondary power source to handle transient peak loads (e.g., from thruster firings). A power system electronics (PSE) box uses shunt regulation to control spacecraft power. A power distribution unit (PDU) provides the relays to switch power loads as well as to provide pulsed loads to thrusters and single event actuators.

The command and data handling (C&DH) subsystem consists of dual integrated electronics modules (IEMs) and redundant attitude interface units (AIUs). The IEMs are a central feature of the Solar Probe avionics design and provide a packaging solution for the command and data handling hardware, central processor, and communications electronics

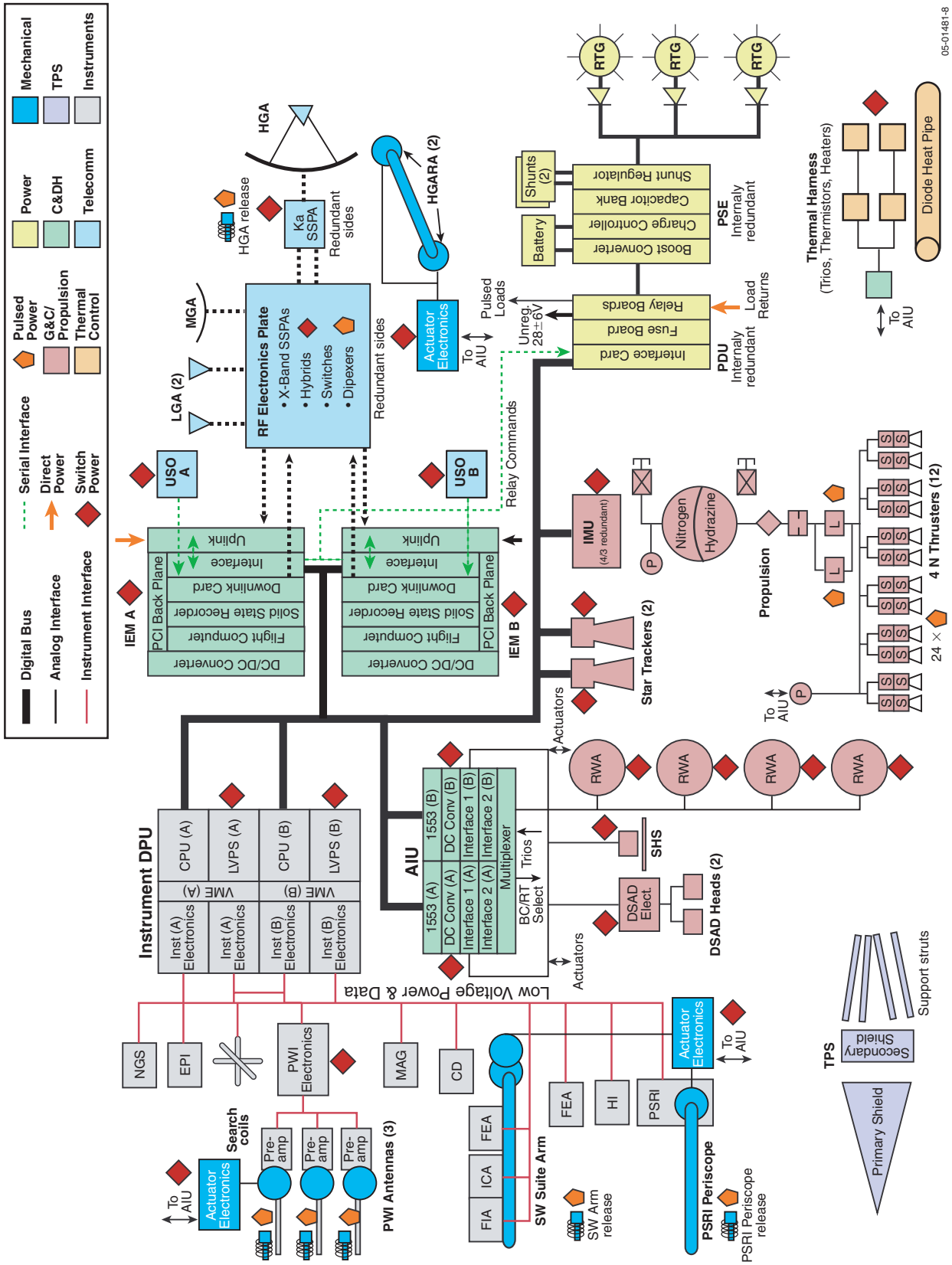

Figure 4-7. Solar Probe block diagram. Redundant hardware elements are used wherever possible to ensure reliability.

that is highly mass and volume efficient. Commands and data are routed throughout the spacecraft through a redundant digital 1553 bus. The AIUs provide the required interfaces between the digital bus and the attitude sensors. The baseline avionics architecture is based on that flown on previous JHU/APL missions, including NEAR, TIMED, MESSENGER, and New Horizons.

The guidance and control (G&C) subsystem consists of redundant star trackers and an internally redundant inertial measurement unit (IMU) as the primary attitude determination sensors, with digital solar aspect detectors (DSADs) and the SHS as back-up sensors for safing. The DSADs will be used outside of 0.8 AU, while the SHS will be especially designed for coarse near-Sun attitude determination. Four reaction wheels are used for attitude control.

The telecommunications subsystem consists of a gimbaled high-gain antenna (HGA), a medium-gain antenna (MGA), and two low-gain antennas (LGAs). Owing to its relative insensitivity to coronal scintillation, the Ka-band will be used for data downlink via the HGA during the first solar encounter. The X-band will be used for both command uplink and data downlink.

The propulsion subsystem consists of a single hydrazine tank with 12 4-N thrusters, which will be used for momentum control and trajectory correction maneuvers. The hydrazine propellant tank is central to the bus.

4.4.2 Spacecraft and Mission Reliability. Solar Probe employs both hardware and functional redundancy to reduce the risk of failure and ensure mission reliability. The fault protection approach adopted for the mission is based on several considerations. First, during a solar encounter attitude control must be precisely maintained to avoid exposing instruments and the spacecraft to direct solar flux. At the start of the solar encounter, control must be maintained within 15° to keep components safe within the umbra. At perihelion, the maximum off-pointing allowed is reduced to only 2°. Inability to recover very quickly from an attitude control fault could quickly result in a loss of the mission. Attitude control during the encounter is rendered even more challenging by uncertainties in the solar encounter environment such as coronal lighting, which could blind a star tracker, or torques induced by high-speed dust impacts. Second, the science data collection will occur over relatively short periods (~14 hours during the pole-to-pole pass), which means that the spacecraft must have significant onboard autonomy and hot backup systems during the solar encounters. In addition, the 9-year duration of the Solar Probe mission also influences hardware selection and redundancy decisions.

Hardware redundancy is incorporated in all spacecraft components and subsystems that can practically be made redundant (**Figure 4-7** and **Table 4-2**). However, years of space flight history have shown that classic hardware reliability models predict only a portion of mission failures. Many anomalies have common causes or stem from design or manufacturing flaws resulting in the failure of two identical units near or at the same time.

Table 4-2. Hardware redundancy

Functional Area	Hardware Redundancy	Comments
Spacecraft Central Processing	• 2 processors	• Hot spare during solar encounter • G&C processing on same processor
Instrument Data Processing	• 2 processors • 2 sets of instrument electronics • 2 LVPS	• Redundancy at board level in single DPU
Attitude Determination (cruise)	• 2 star trackers • redundant gyro in IMU • Multiple sun sensor heads	• One star tracker turned off during Jupiter flyby

Table 4-2. Hardware redundancy (continued)

Functional Area	Hardware Redundancy	Comments
Attitude Determination (solar encounter)	• 2 star trackers • redundant gyro in IMU	• Both star trackers on
Attitude Control	• 4 reaction wheels	• Three wheels needed for 3-axis control
Propulsion	• 12 thrusters	• Provides redundancy in each axis
Data Bus	• Redundant 1553 bus • Redundant AIU boards	• AIU redundancy at board level (1 box)
Data Storage	• 2 SSRs	• 1 recorder off during Jupiter flyby • All data recorded on both recorders simultaneously during solar encounter
Telecommunications	• 2 uplink cards • 2 downlink cards • 2 LGAs • 2 X-band SSPAs • 2 Ka-band SSPAs	• Both uplink cards always on (unswitched) • MGA or HGA can be used for cruise communications • X- and Ka-band downlink capability in HGA • Cross strapping allows multiple combinations in SSPAs and electronics
Thermal Control	• 2 thermistor harnesses • 2 heater harnesses	
Power	• Redundant relays • Redundant 1553 electronics • Redundant PSE electronics • 3 MMRTGs	• PSE & PDU redundancy at board level • All three MMRTGs needed to meet performance requirements. However loss of a single unit would result in a degraded mission capability rather than a mission failure

In addition, protection from software faults is also required. As a result, Solar Probe incorporates functional redundancy in many critical areas so that the spacecraft can fully or partially recover the mission even if redundant hardware units fail or a software fault occurs. Solar Probe functional redundancy is highlighted in **Table 4-3.**

The mechanisms that control the deployment of several of the instruments represent a potential source of failure that had to be addressed in the Solar Probe design. The Plasma Wave Instrument (PWI) electric-field (E-field) antennas and Fast Plasma Instrumentation (FPI) retractable arm use stepper motors to vary their position as a function of changing TPS umbra angle, and a stepper motor and worm gear drive are used to extend the Polar Source Region Imager periscope outside the umbra and then retract it. A failure to control these mechanisms correctly during a solar encounter could endanger the instrument as well as the spacecraft. These mechanisms must therefore incorporate fail-safe features to guarantee mission reliability. Possible fail-safe approaches are summarized in **Table 4-4,** and the mechanism concepts and fail-safe features are discussed below in the instrument accommodation section (Section 4.5). **Figure 4-8** illustrates how all the instrument mechanisms can be safed within the TPS umbra at the perihelion distance of 4 R_S. The development of more detailed concepts—and perhaps of alternative approaches—will depend on the design of the actual instruments that are selected.

Table 4-3. Solar Probe functional redundancy

Functional Area	Primary System Failure	Functional Redundancy	Mission Impact
C&DH Processing	C&DH software fault	2nd IEM operates in different safe mode	Software must be promoted back into operational mode.
G&C Processing	G&C software fault	2nd IEM operates in different safe mode	Software must be promoted back into operational mode.
Attitude Determination (cruise)	Star tracker	IMU–short duration Sun sensor	Communications through MGA rather than HGA.
	IMU	Star tracker–low rates	Degraded pointing performance.
Attitude Determination (solar encounter)	Star tracker	IMU (few hours) Sun horizon sensor	Eventual loss of HGA and loss of real-time science. Communications only through LGA.
	IMU	Star tracker–low rates	Degraded pointing performance.
Attitude Control	Reaction wheels	Thrusters	Increased propellant usage may shorten mission. Increased outgassing.
Data Storage	SSRs	Real-time telemetry	Significant reduction in total science data return.
Telecommunications	Ka-band downlink	X-band downlink	Loss of real-time data and all communications P ± 8 hours.
	HGA	MGA LGA	MGA available during cruise. Significant reduction in data rate. LGA available during encounter to 1.6 AU. Emergency data rate only. Loss of real-time data and all communications P ± 8 hours.
Power	Battery	MMRTG	All unnecessary power turned off during maneuvers. May need to power cycle instruments during encounter.

Table 4-4. Instrument actuator safing concepts

Instrument Actuator	Failure Detection	Contingency Approach(s)
Fast Plasma Instrument Arm	Position & temperature sensors	Redundant actuator windings and command paths Pull arm back to stowed position within umbra
PSRI Periscope	Position & temperature sensors	Redundant actuator windings and command paths Jettison end of persiscope
PWI Electric Field Antennas	Position & temperature sensors	Redundant actuator windings and command paths Actuator rotates antennas back within umbra (safe positions both directions)

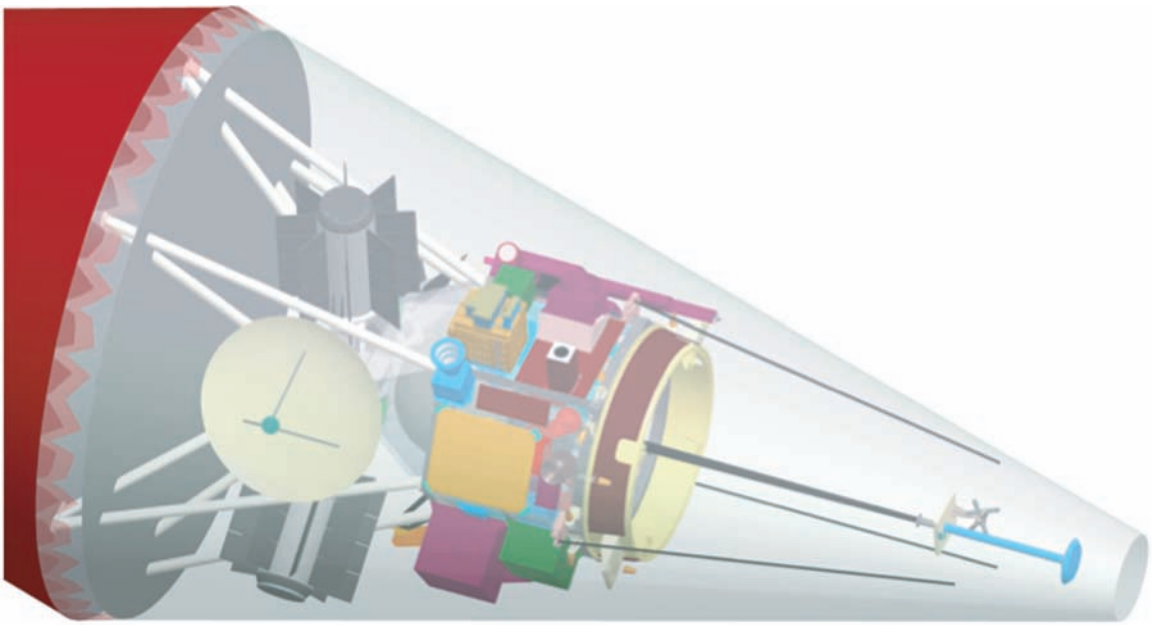

05-01481-34

Figure 4-8. In fail-safe mode the Fast Plasma Instrumentation arm, Polar Source Region Imager periscope, Plasma Wave Instrument antennas, and High-Gain Antenna are retracted to positions within the 4 R_S umbra.

4.4.3 Mass and Power Budget Summaries

Mass Budget. **Table 4-5** shows the mass summary for Solar Probe. Mass is summarized for the instruments, instrument support hardware such as the science boom, instrument mechanisms, and each spacecraft subsystem. Next to each category is the current best estimate (CBE). This represents the best current assessment of the mass for that subsystem/instrument at launch. In addition, a 30% margin is included to account for unanticipated growth as well as any launch reserves. Since specifics of the launch vehicle have not yet been set, propellant mass is based on that need to achieve the required ΔV after inclusion of the full 30% margin. A more detailed mass budget is provided in Appendix C.

Power Budget. Loads during the solar encounters determine the amount of power required for the mission. During this part of the mission, all subsystems and instruments are powered up and active. In addition, because of the large solar pressures and solar dust impacts, frequent momentum management maneuvers will be needed, requiring additional power for the thrusters. **Table 4-6** summarizes the average power required during the solar encounter based on current best estimates.

Figure 4-9 shows the predicted power vs. time curve for each of the three MMRTGs. As indicated in the plot, each MMRTG has a predicted beginning-of-life (BOL) power of 126 W. (The specified

Table 4-5. Solar Probe mass budget summary

Category	CBE Mass (kg)
Instrument Payload	51.7
Instrument Accommodation Hardware	18.6
Spacecraft	542.4
Telecommunications	21.6
Guidance & Control	38.1
Power	149.1
Thermal Protection System	133.8
Thermal Control	15.7
Command & Data Handling	20.4
Propulsion	26.2
Mechanical	108.3
Harness	29.3
Dry Total	612.8
Propellant	59.4
Estimated Launch Mass	672.2
Dry Mass Growth Margin	30%
Dry Mass with Margin	796.6
Launch Mass with Margin	856.0

Table 4-6. Solar Probe power budget summary

Subsystem	CBE Average Power (W)
Instruments	53
Instrument Accommodation Hardware	2
Spacecraft Total	176
Power	13
G&C	67
Propulsion	13
RF	25
C&DH	58
Thermal	0
Subtotal	231
Harness Loss	4
Total	235

Table 4-7. Available mission power for Solar Probe and resulting power margins at first and second encounters based on both predicted and specified power

Predicted Power Available (3 MMRTGs) First Solar Encounter	
Available Power 4.1 years	353 W
Total Margin from CBE	50%
Second Solar Encounter	
Available Power 8.7 years	328 W
Total Margin from CBE	40%
Specified Power Available (3 MMRTGs) First Solar Encounter	
Available Power 4.1 years	308 W
Total Margin from CBE	31%
Second Solar Encounter	
Available Power 4.1 years	283 W
Total Margin from CBE	21%

BOL power is greater than 110 W.) MMRTG power estimates are based on information from *Abelson et al.* (2005) and are consistent with recent data provided by the MMRTG contractor. **Table 4-7** compares the required power with the power available and indicates the available growth margin. For completeness, the power margin is given for both the specified and predicted MMRTG power levels. A more detailed breakdown of the power budget is provided in Appendix C.

4.5 Mechanical Design

The Solar Probe spacecraft bus carries the payload, the subsystems, and the TPS. The bus design was developed using proven design methodologies. It incorporates materials and attachments that have heritage from past and current programs and takes advantage of new technology that minimizes mass while maintaining low technical, cost, and schedule risk. The two main structural components of the bus are a hexagonal equipment module and a cylindrical adapter ring. The hexagon consists of 32-mm thick structural panels of 0.5- to 1.0-mm aluminum face sheets bonded to light-weight aluminum honeycomb core. This construction is typical of that used on recent spacecraft. The panels are removable to facilitate access to subsystem components inside the structure. The panels also provide good thermal conduction and electromagnetic compatibility grounding for the electronics and instruments. The adapter ring is a one-piece aluminum 7075-T73 machined ring forging. It is typical of most launch adapters and provides a very high strength factor of safety. The hydrazine propulsion tank is mounted on a deck in the center of the hexagonal module, where its loads are efficiently transferred into the adapter ring. The primary structure also has very efficient load paths to carry subsystems, instruments, and the TPS. The following sections describe the accommodation of the instruments (including deployables) and subsystems on or in the bus and the mechanical interface of the TPS with the bus. **Figure 4-10** (foldout) shows several spacecraft views and identifies the locations of the instruments and spacecraft components. The spacecraft dimensions are given in Appendix D.

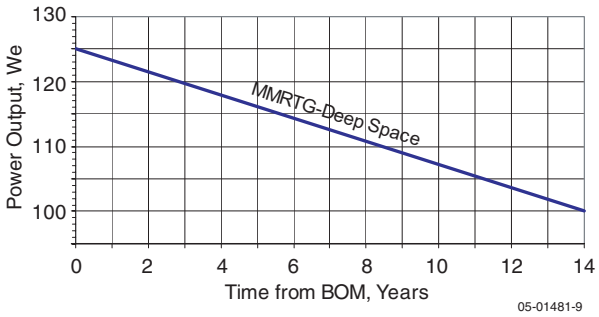

Figure 4-9. Predicted Multi-Mission Radioisotope Thermoelectric Generator power performance as a function of time from the beginning of the mission.

4.5.1 Instrument Accommodation. The configuration of the Solar Probe payload provides the optimum locations and fields of view (FOV) for the science instruments consistent with the requirement that the payload be maintained within the umbra of the TPS. (As discussed below, exceptions to this

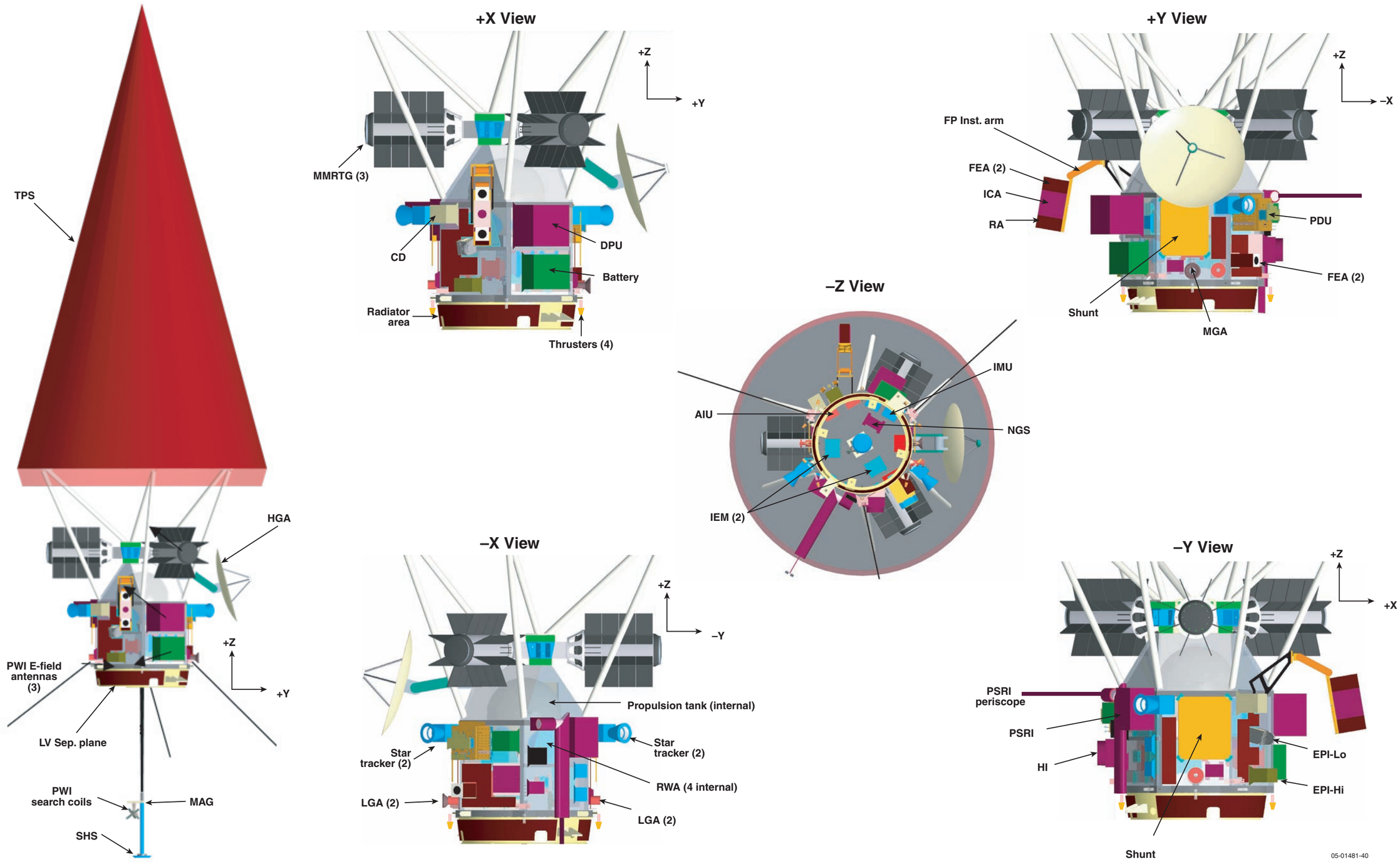

Figure 4-10. Solar Probe instrument and component locations.

Blank
(back of foldout)

requirement are the PSRI periscope and the PWI antennas.)

Fast Plasma Instrumentation. The Fast Plasma Instrumentation (FPI) consists of four sensors: a Fast Ion Analyzer (FIA), two Fast Electron Analyzers (FEA), and an Ion Composition Analyzer (ICA). The FIA, ICA, and one FEA are co-mounted on a retractable arm and face in the +X (ram) direction. The arm will be gradually retracted as the spacecraft approaches the Sun. This arrangement provides viewing to near (2° inside) the edge of the TPS umbra. The arm is actuated by two stepper motors. During launch, the arm will be held against the spacecraft by launch locks. After separation from the third stage, the launch locks will be released, allowing the stepper motors to drive the platform to the desired location. Various position and temperature sensors will monitor the health of the mechanism. The arm is designed to be fail safe. It will return permanently to the launch configuration in the event of failure. **Figure 4-11** shows the FPI on the arm and illustrates the FOV at two representative solar distances. The second FEA sensor is mounted directly on the –X (anti-ram) side of the spacecraft. An articulating arm on the –X side for the second FEA is unnecessary.

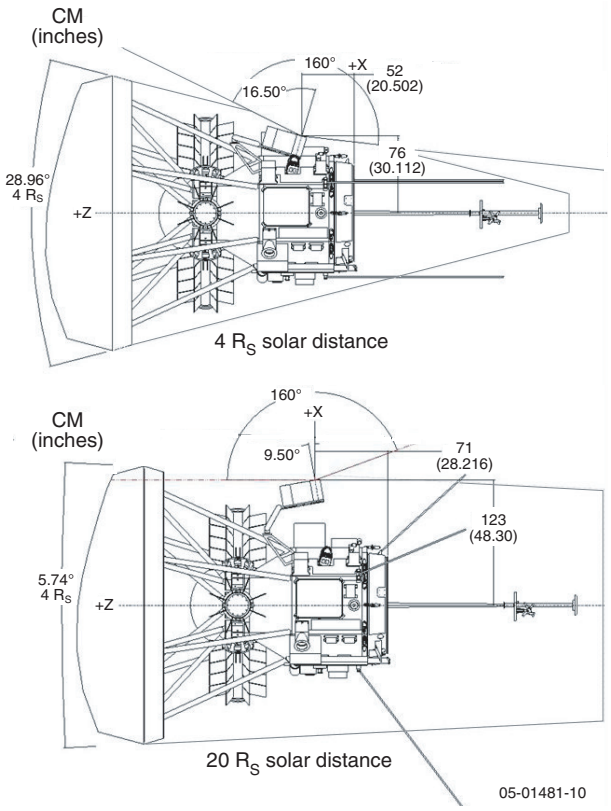

Figure 4-11. Position of the retractable arm for the Fast Plasma Instrumentation at two different distances from the Sun.

Energetic Particle Instrument (Low Energy). The EPI-Lo instrument is mounted 30° off the +X-axis on the +X/−Y panel. The 160° × 11.5° FOV is angled to the edge of the heat shield to maximize the FOV for the incoming energetic particles (**Figure 4-12**).

Energetic Particle Instrument (High Energy). The EPI-Hi instrument consists of two High Energy Telescope (HET) apertures and four Medium Energy Telescope (MET) apertures attached to the instrument box, which is mounted on the +X/−Y panel. The HET apertures are aligned with the spacecraft Z-axis so that they point sunward and anti-sunward during the encounter. The center of the 90° FOV of the four MET apertures is approximately orthogonal to the Z-axis; the apertures are angled 25° and 45° from the Y-axis toward the +X-axis (**Figure 4-13**).

Neutron and Gamma Ray Spectrometer. The Neutron and Gamma Ray Spectrometer (NGS) is located on the bottom of the equipment deck and centered as much as possible to allow the hydrazine tank to provide some shielding from the gamma

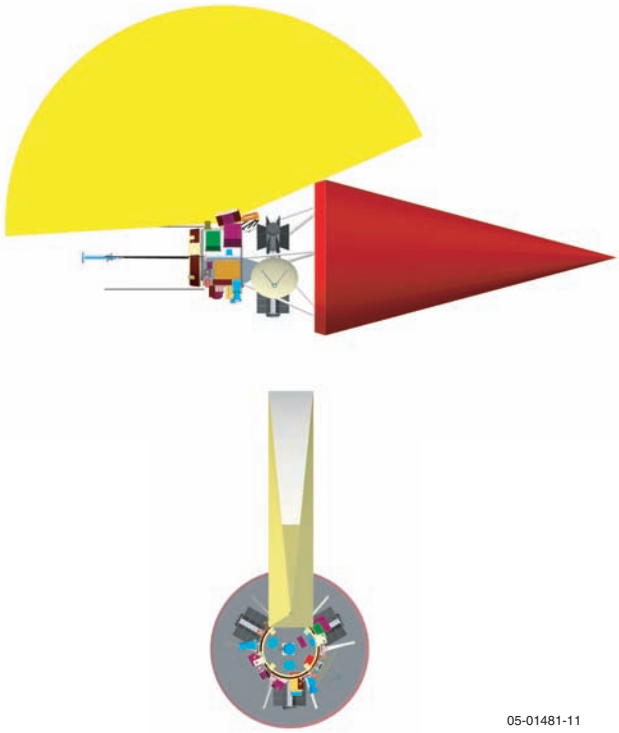

Figure 4-12. Field of view of the Energetic Particle Instrument (Low Energy).

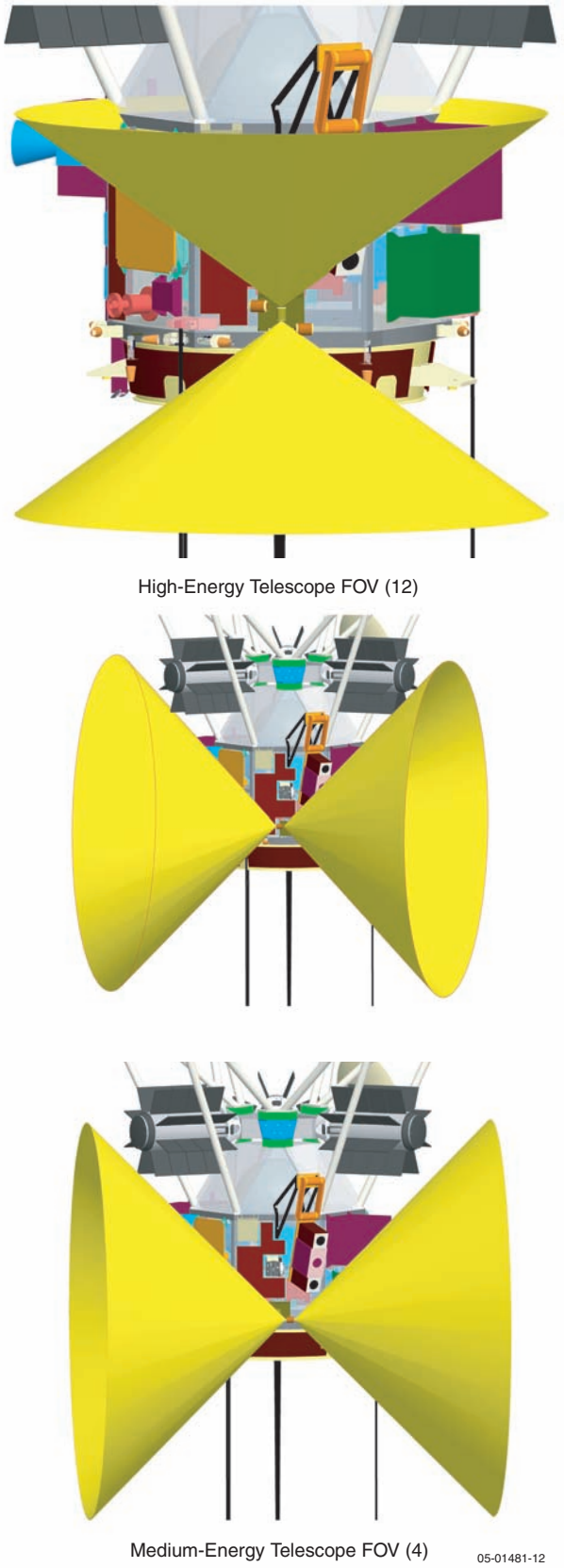

Figure 4-13. Fields of view of the Energetic Particle Instrument (High Energy).

radiation from the MMRTGs. The amount of shielding could vary significantly depending on the amount of hydrazine consumed during non-deterministic burns.

Coronal Dust Detector. The Coronal Dust Detector (CD) is mounted on the ram side (+X) of the spacecraft. This location exposes the CD to the maximum dust environment and provides for a clear FOV in the velocity direction.

Hemispheric Imager. The Hemispheric Imager (HI) is mounted low on the –X side of the spacecraft body. HI will provide coverage of the anti-ram direction during the solar encounter (**Figure 4-14**). (Coverage will be near-hemispheric rather than fully hemispheric owing to minor impingement on HI's large FOV by some of the spacecraft/payload elements, including the TPS, which effectively occults the Sun.) Because the HI is mounted on the anti-ram side of the spacecraft, the spacecraft body will help protect the imager from the coronal dust flux.

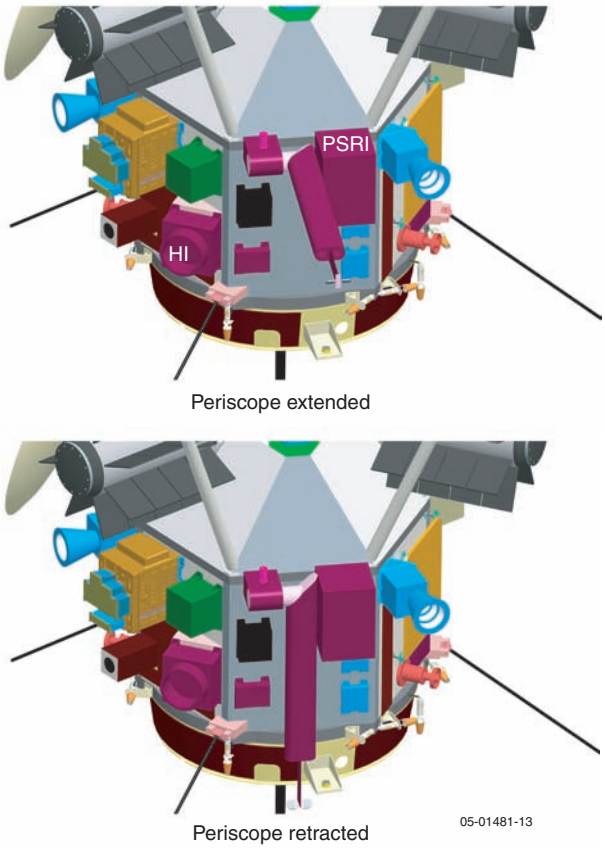

Figure 4-14. The locations of the Hemispheric Imager and the Polar Source Region Imager on the –X side of the spacecraft.

Polar Source Region Imager. The Polar Source Region Imager (PSRI) is mounted on the –X side of the spacecraft (see above, **Figure 4-14**). In order to view the Sun's polar regions, the PSRI uses a periscope to deploy two 25-mm^2 optical mirrors beyond the umbra. The mirrors will direct both UV and visible light to the instrument. Several materials may work as mirrors. Fused silica was assumed in the engineering study, since it can withstand rapid thermal changes. A carbon–carbon tube holds the mirrors in proper position to direct the two collimated beams back to the instrument. The periscope will be actuated by a stepper motor and worm gear drive. Several position sensors will be used to detect the nominal home, deployed, and safe positions, while temperature telemetry will provide information about the overall health of the mechanism. During launch the periscope will be locked flat against the spacecraft body. As a fail-safe measure, the periscope arm will be severed if it becomes stuck in the extended position and is not able to return to within the umbra.

Initial thermal analysis shows that the periscope can survive to distances of about 20 R_S from the Sun. This analysis assumes that the periscope will be exposed to the Sun for 30 seconds, including 10 seconds of imaging, and then retracted within the umbra for up to 10 minutes to allow the mirror to cool. The actual cadence will vary with solar distance and will depend on the final materials selected and limitations of the actual design.

Magnetometer. The Magnetometer (MAG) is mounted on a 2-m axial boom extending from the bottom deck of the spacecraft (–Z). The boom will be stowed at launch and will be deployed after separation from the third stage. The MAG is mounted on a bracket approximately 1.2 m aft of the spacecraft adapter ring.

Plasma Wave Instrument. The Plasma Wave Instrument (PWI) consists of three monopole electric field antennas, three magnetic field search coil antennas, three preamplifiers, and an electronics box. The electronics box is mounted on the –X/–Y panel of the spacecraft. The magnetic search coils will be mounted on the –Z axial boom inboard from the MAG by ~50 cm.

The PWI E-field antennas presented a design challenge from both a mechanical and a thermal perspective because for optimum science return they must extend 1 m beyond the TPS umbra, the angle of which will vary with distance from the Sun (**Figure 4-15**). Of the several concepts considered in the engineering study, the one finally adopted as the baseline design assumes three antennas independently mounted on the lower sides of the bus and separated by approximately 120° to provide 3-axis measurements. Each antenna will be a carbon–carbon tube with a diameter of approximately 1 cm.

The science objectives require that an electrically isolated 1-m section of each antenna be exposed to direct sunlight as the spacecraft travels inward from a distance of at least 20 R_S through perihelion. Stepper motors will be used to adjust the angles of the antennas relative to the spacecraft Z-axis as the umbra angle changes. The required range of motion during the mission ranges from 54° relative to the –Z-axis at 20 R_S to 0° at 4 R_S. The separation of the midpoint of the isolated section varies between 4.1 m at 20 R_S and 2.4 m at 4 R_S (**Table 4-8**). The

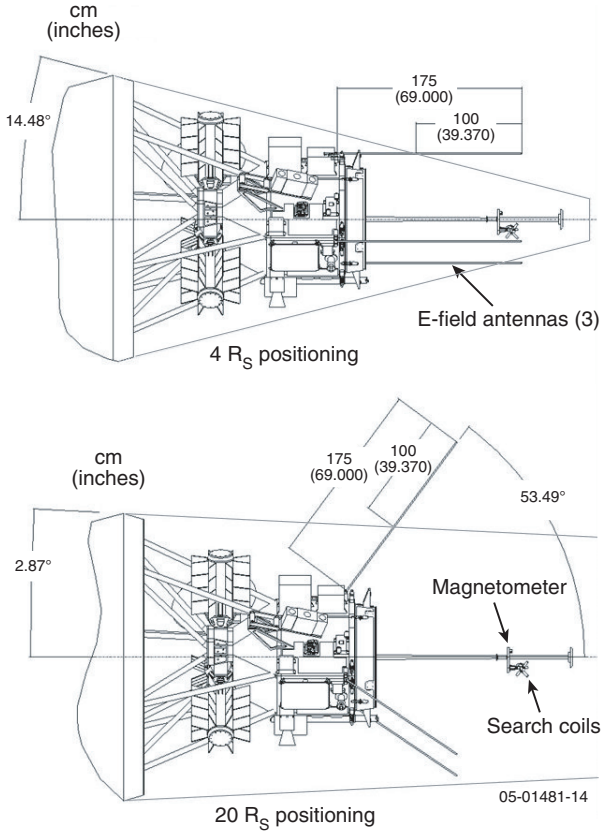

Figure 4-15. Position of the Plasma Wave Instrument electric-field antennas at two different distances from the Sun.

1.75-m antenna length allows 1 m to extend beyond the umbra at any range to the Sun that the TPS is pointed at nadir. For launch the antennas will be stowed against the spacecraft bus in the +Z direction and locked to the struts.

Since the antennas are exposed to direct sunlight, fail-safe devices are needed to ensure that the actuators do not fail with the antennas exposed at a large angle as the spacecraft approaches perihelion. The fail-safe devices rotate the antennas toward the –Z axis, as shown earlier (Figure 4-8), placing them safely within the umbra even at perihelion.

Thermal analysis of the baseline PWI design shows that the heat input from the PWI antennas to the spacecraft bus is less than 20 W over the range of antenna angles and solar distances of interest. As described below in Section 4.7 on thermal control, this heat input can be accommodated by the spacecraft. A bare carbon–carbon surface with a solar absorptivity of 0.9 and an IR emissivity of 0.9 was assumed in the analysis.

Data Processing Unit. The common Data Processing Unit (DPU) is mounted on the +X/+Y panel of the spacecraft.

4.5.2 Subsystem Accommodation. Most of the subsystem electronics are mounted on the internal or external surfaces of the hexagonal structure or inside the adapter. All subsystems fit within the 16.5° umbra provided by the TPS at perihelion. (The nominal umbra at perihelion is 14.5° with 2° allocated for misalignments and attitude control errors.)

Multi-Mission Radioisotope Thermoelectric Generators (MMRTGs). The MMRTGs are placed near the top of the spacecraft and positioned 120° apart. This location minimizes the diameter of the TPS (and thus its mass) and provides reasonable view factors to space for heat rejection. It also allows the RTGs to be installed through the fairing doors while the launch vehicle is on the launch pad. (A similar arrangement for the single RTG on the New Horizons Pluto mission has shown that this type of installation can be accomplished through the fairing doors.)

Propulsion System. Major components of the propulsion system are the hydrazine propulsion tank and 12 rocket engines. The tank is located at the center of the hexagonal structure, which helps minimize the center of gravity (CG) travel as propellant is expended. The propulsion system is integrally assembled with the structure so plumbing lines can be welded in place from the tanks to the thrusters, eliminating the need for field joints. Plumbing is routed inside the structure to allow removal of the side panels. The thrusters are placed to meet maneuver and control requirements discussed in Section 4.13 and are positioned so as to minimize impingement on the spacecraft and its components.

Telecommunications System. The placement of the antennas is determined by the orientation of the spacecraft with respect to the Earth. The High Gain Antenna (HGA), Medium Gain Antenna (MGA) and one Low Gain Antenna (LGA) point in the +Y direction towards Earth, while a second LGA is located on the −Y side to maximize antenna coverage for emergencies. The HGA is attached to the spacecraft bus with a dual-gimbaled mechanism that provides single-axis rotation in the Y–Z plane for Earth tracking; the other degree of freedom is provided by the rotation of the spacecraft about the Z-axis. The dual-gimbaled mechanism is required both to keep the antenna pointed at Earth and to keep it within the protective umbra of the TPS during the first solar encounter. The range of motion required by the HGA is from

Table 4-8. Articulation of the PWI electric field antennas as a function of solar distance

Solar Distance (Rs)	Umbra Angle (deg)	Antenna Angle (deg)	Ant. Midpoint Separation (m)
20	2.87	53.5	4.1
15	3.82	48.0	3.9
10	5.74	38.0	3.7
8	7.18	31.1	3.5
6	9.59	20.3	3.1
5	11.54	12.0	2.8
4.5	12.84	6.6	2.6
4	14.48	0.0	2.4

55° off the +Z-axis at 73 R_S inbound and 170 R_S outbound to 104° at perhelion (**Figure 4-16**). Off-the-shelf stepper motors can be used for the drive components of the antenna system. These motors have very accurate pointing capability, are highly reliable, and have heritage on many programs. The HGA assembly will be held to the spacecraft bus by a restraint mechanism before and during launch and released once the spacecraft is on orbit.

4.5.3 Launch Configuration. Figure 4-17 shows Solar Probe in its launch configuration, integrated with the STAR 48 third stage and enclosed within the 5-m short fairing of the Atlas 551. The STAR 48 third stage baselined for Solar Probe is the same third stage currently designed for New Horizons, but with a smaller payload attach fitting (PAF) (17 vs. 33 inches) to accommodate the taller Solar Probe spacecraft. In the launch configuration, the science boom is stowed, and the PWI antennas, FPI arm, PSRI periscope, and HGA are locked to the side of the bus. With this configuration, Solar Probe has approximately 0.9 m clearance in width and approximately 0.7 m clearance in height. This is relative to the static envelope defined in the *Atlas Launch Systems Mission Planners Guide*, which assumes the 5-m short fairing and a standard C-22 adapter ring. Three doors will have to be installed in the fairing for RTG installation.

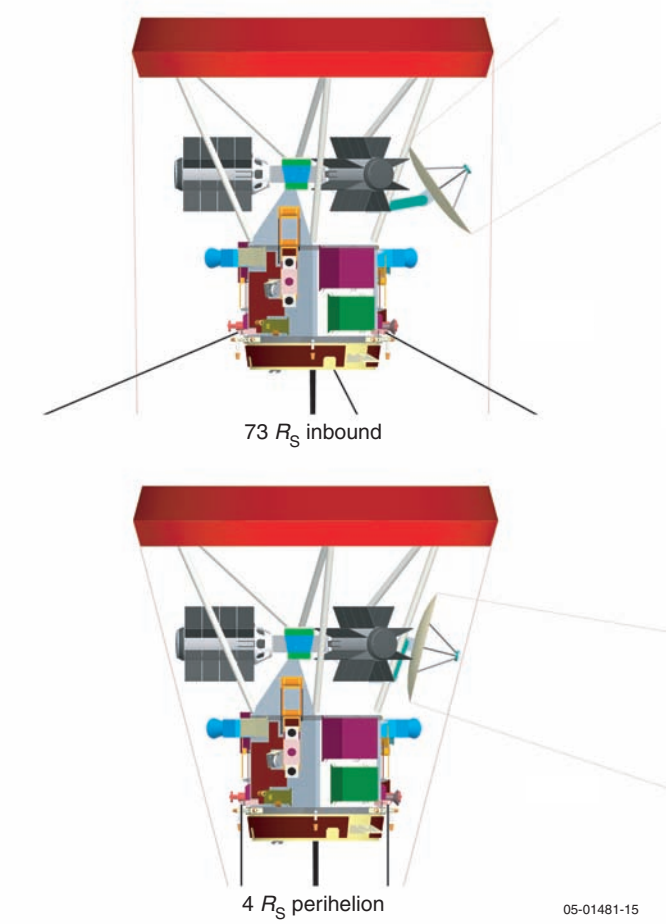

Figure 4-16. The range of motion of the high-gain antenna relative to the +Z axis is from 55° at 73 R_S (top) to 104° at perihelion (bottom).

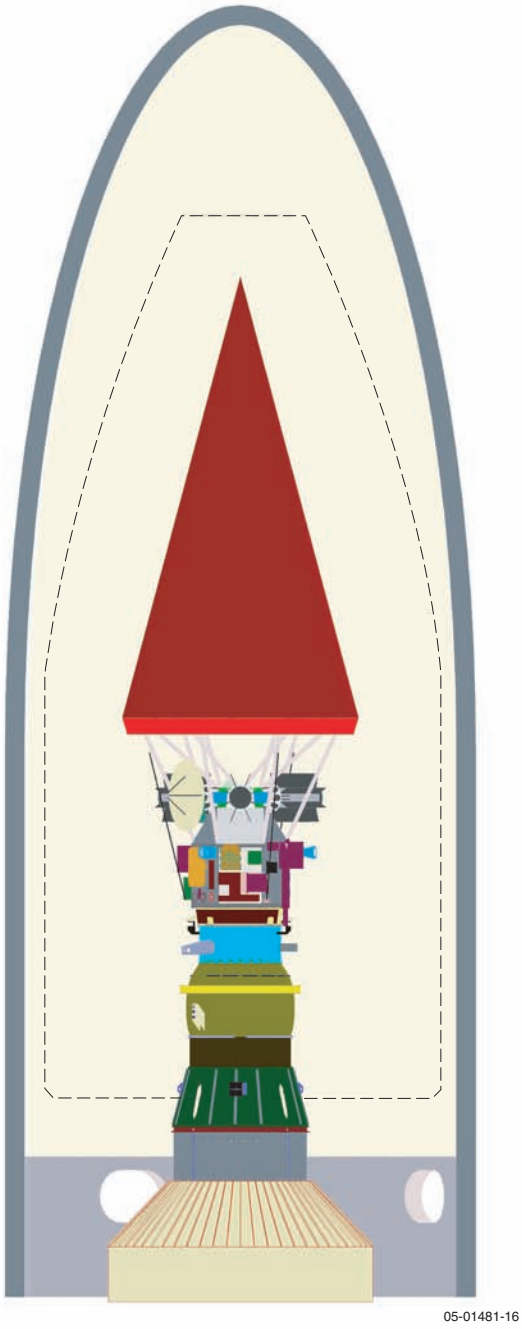

Figure 4-17. Solar Probe in launch configuration inside the Atlas 551 fairing.

4.5.4 Solar Probe Structural Analysis. A NASTRAN finite element model (FEM) consisting of 10429 nodes and 11124 elements was developed to investigate the distribution of the load and the natural frequencies of the spacecraft structure and the TPS and to better estimate the structural mass. The results of this analysis indicate that the design concept is sound and can meet launch load and stiffness requirements. Iteration of the TPS strut arrangement produced a first torsional frequency of the TPS of 16.8 Hz, which should not be a problem for either an Atlas or a Delta launch vehicle. The spacecraft first lateral mode is dominated by the vertical honeycomb panels. Calculated at 18.6 Hz, this mode is comfortably above the expected launch requirement of 15 Hz. The 45-Hz first thrust mode occurs in the RTG mounts, well above the expected 35-Hz requirement. The analysis also identified areas that will need to be tuned in future development to achieve additional frequency separation between some of the modes. Both the spacecraft lateral and TPS torsional frequency are greatly dependent on the positioning and attachment of the secondary shield to the bottom of the primary shield. Continued analysis will be conducted as a part of the risk reduction effort to converge on the final TPS structural design.

4.6 Thermal Protection System

The Solar Probe TPS shields the spacecraft bus and instruments from direct solar flux during the near-Sun mission phase, at distances closer than 0.8 AU. The TPS consists of three major components: the primary shield to limit the temperature and reject much of the heat to space, a secondary shield that slows heat transfer to the bus to manageable rates, and 12 struts to support the TPS structure at a safe distance from the spacecraft bus. Except for the PWI antennas and, for limited periods, the PSRI periscope, as described above, all components and subsystems will be shielded behind the TPS protective umbra during solar encounter.

4.6.1 Primary Shield. The primary shield consists of a carbon–carbon cone with a 15° half-angle. The steep angle minimizes its surface view factor directly to the Sun and maximizes it to space, reducing its maximum operating temperature. Although the steep angle is required to control the operating temperature, the shield does not necessarily need to be conical in shape. Options for multi-faceted pyramid-shaped primary shields can also be considered in future design trades if they appear to offer manufacturability advantages. However, for the purposes of this report, a conical shape was assumed.

The primary shield consists of six plies of carbon–carbon in a two dimensional quasi-isotropic lay-up (0°, +60°, −60°) with a thickness of 0.8 mm. An internal ring stiffener at the middle of the conical shield alleviates local modes in the primary shield while minimizing added mass. This stiffener is a 25 × 25 mm closed section, with a wall thickness of 0.5 mm. The material is a two-dimensional warp-aligned 5:1 carbon–carbon that achieves a high elastic modulus in the longitudinal direction and is the same material being used for the struts.

Primary Shield Surface Preparation. JPL and JHU/APL have conducted extensive studies of primary shield surface preparations that provide consistent optical properties for design and analysis and also offer favorable characteristics to reduce the primary shield temperature for a given solar flux. Preparation of the shield surface with a suitable material is strongly desired to reduce the mass and complexity of the TPS as well as to reduce potential outgassing of the carbon–carbon that could affect science experiments.

High-temperature measurements at APL have shown that several candidate materials have very good optical performance as compared with bare carbon–carbon (**Figure 4-18**), with absorptivity-to-emissivity ratios (α/ε) in the range of 0.2 to 0.6. Tested materials include aluminum oxide (Al_2O_3), PBN, and BaZP. In addition, JPL had previously carried out tests using pyrolytic graphite that yielded an α/ε ranging from 0.7 to 0.9. Bare carbon-carbon typically has α/ε values in the 1 to 1.1 range even with careful surface preparation.

Based on the available data, a ceramic surface with an α/ε of 0.6, which was considered a conservative estimate, was assumed for design calculations in this report. Use of a ceramic coating will reduce the equilibrium temperature of the primary shield from 2155 K (uncoated carbon–carbon, α/ε of 1) to 1850 K. Risk reduction activities will include additional testing, including testing of representative large-scale units, that may

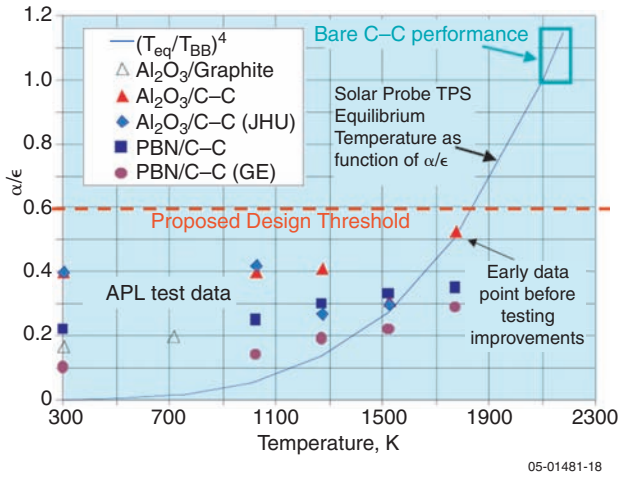

Figure 4-18. Optical performance of candidate Thermal Protection System surfaces.

demonstrate optical performance that is even better than predicted.

In addition to optical performance, several other test and analyses were conducted to address material suitability including environmental effects that could degrade optical performance, structural compatibility, outgassing, electrical charging, and micrometeorite/dust impact (**Figure 4-19**). Based on analysis and testing conducted to date, all candidate materials performed well, confirming that they may be suitable for the mission. In fact, Al_2O_3 is very mature technology and has been used for many previous applications. Additional details of the analyses and tests performed to support this effort are provided in Appendix E.

4.6.2 Secondary Shield. The secondary shield limits the flow of heat between the primary shield and the spacecraft bus and allows a significant portion of the heat to radiate into space. The secondary shield consists of a layer of low-density, low-conductivity material supported by upper and lower carbon–carbon face sheets. The top of the secondary shield will be exposed to the operating temperatures of the primary shield, and the insulation material must be able to accommodate these temperatures. Trade studies were conducted of several off-the-shelf candidate materials including ERG carbon foams or carbon felts or battes and silica-based insulation materials such as Microtherm G and silica aerogels. While the latter are significantly more efficient than carbon materials in terms of their conductivity versus density characteristics, and thus might help minimize the mass of the secondary shield, we decided that a single layer of carbon foam was adequate and presented the lowest risk. This insulation design will reduce the temperatures to approximately 500 K on the bottom side of the shield, which faces the spacecraft. A low-emissivity coating or high-temperature blanket on the bottom face sheet as well a high-temperature multilayer insulation (MLI) on the top surface of the spacecraft bus will provide the final thermal protection.

4.6.3 Attachment Struts. Twelve attachment struts support the TPS on the spacecraft during launch. Each strut is 5 cm in diameter and 0.5 mm thick,

Candidate material	Optical						Structural			Out-gassing			Charging				Particulate Impact	
	Baseline	Temperature effects	Radiation effects			Predicted PHS temperarure	Thermal cycling	Vibration	Cumulative/residual strengths	Temperature effects	Temperature/vac effects	Chemical interaction	Temperature effects	Radiation effects		Cumulative effects	Impact damage modeling	Effect on PHS performance
			EUV	Electron	Proton									Electron	Proton			
Al_2O_3	E,A	E,A	E	E	E	A	E	E		E		A	A	A	A	A	A	A
PBN	E,A	E,A	E	E	E	A				E		A	A					
BaZP	E,A	E,A	E	E	E	A				E		A						

E = Experiment A = Analysis

05-01481-19

Figure 4-19. Summary of the testing and analysis performed on candidate Thermal Protection System optical surfaces.

a geometry that balances thermal and structural requirements, and is made of carbon–carbon composite. The current concept assumes that the struts penetrate the secondary shield and attach to the TPS at the primary shield. In addition to supporting the TPS, the struts provide separation between the TPS and the spacecraft bus. The separation distance is currently set at 0.6 m to maximize the amount of heat that can be radiated into space from the secondary shield. The maximum separation is constrained by the size of the launch vehicle fairing as well as by the ability of the struts to support the TPS load. Since the struts are attached directly to the primary shield and the spacecraft bus, they can be a major source of heat input into the bus. Current analysis shows that the heat loads can be accommodated with the current strut configuration (see Section 4.7). Several options will be explored in the risk reduction effort to further reduce heat inputs by the struts by tailoring strut optical properties and introducing other strut materials such as polyimides to increase thermal resistance. If significant thermal issues are identified later in development, a contingency approach would be to thermally disconnect the struts through a pyro-actuated mechanism.

4.6.4 Risk Reduction Effort. Because the TPS involves a new design and no similar design has previously been flown in space, it is important that many of the technology risks be retired prior to Phase A. The risk reduction effort will focus on the following activities:

- Completing the analysis and testing on candidate optical surface preparations
- Completing the analysis and testing on candidate secondary shield materials
- Performing TPS design trades and selecting baseline shape, materials, and attachment approach
- Developing and fabricating both subscale and full-scale units for environmental testing

The current plan calls for the development and test of two full-scale TPS units. With sufficient funding, the first full-scale prototype could be built and tested within 2 years from the start of risk reduction.

4.7 Thermal Control

The unique environment in which Solar Probe will operate presents significant thermal design challenges. The spacecraft components and instruments must be kept between −20° and +50° C, and the propulsion system must be maintained at temperatures between +10° and +40° C. These temperatures must be maintained over extreme solar flux environments from 4 R_S to 5.5 AU. In addition to the intense solar flux on the TPS, the thermal system needs to reject excess heat from the three MMRTGs mounted on the bus structure, on average 285 W of internal thermal dissipation, and from three PWI antennas that are exposed directly to the solar flux and radiate and reflect heat back into the bus.

4.7.1 Analysis Approach. The Thermal Synthesis System (TSS) and SINDA were used to perform a thermal analysis, the results of which were used to determine the required radiator area and to size the thermal shield. The model was run for both a hot case (perihelion at 4 R_S) and a cold case (aphelion at 5.5 AU). It was also used for trade studies of the PWI antenna design and accommodation, RTG placement, and the thermal design of the TPS attachment struts. Results of this analysis (**Figure 4-20**) demonstrate that in both the hot and cold cases the payload and subsystems will remain within the allowable operating range.

4.7.2 Thermal Analysis Hot Case. The hot case analysis demonstrated that the heat flux into the spacecraft can be contained within manageable bounds and that, with a radiator area of 0.68 m^2 and a secondary shield thickness of 20 cm, normal spacecraft operating temperatures can be maintained throughout the encounter. The thermal balance for the hot case at 4 R_s is shown in **Figure 4-21**.

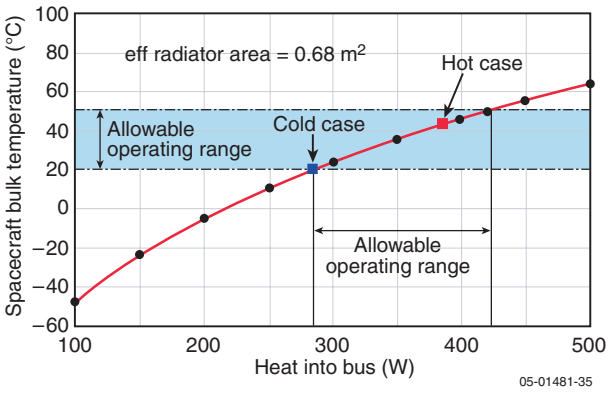

Figure 4-20. The bulk temperature of the spacecraft bus as a function of heat input into the bus, calculated for both perihelion (hot case, with and without the plasma wave antennas) and aphelion (cold case).

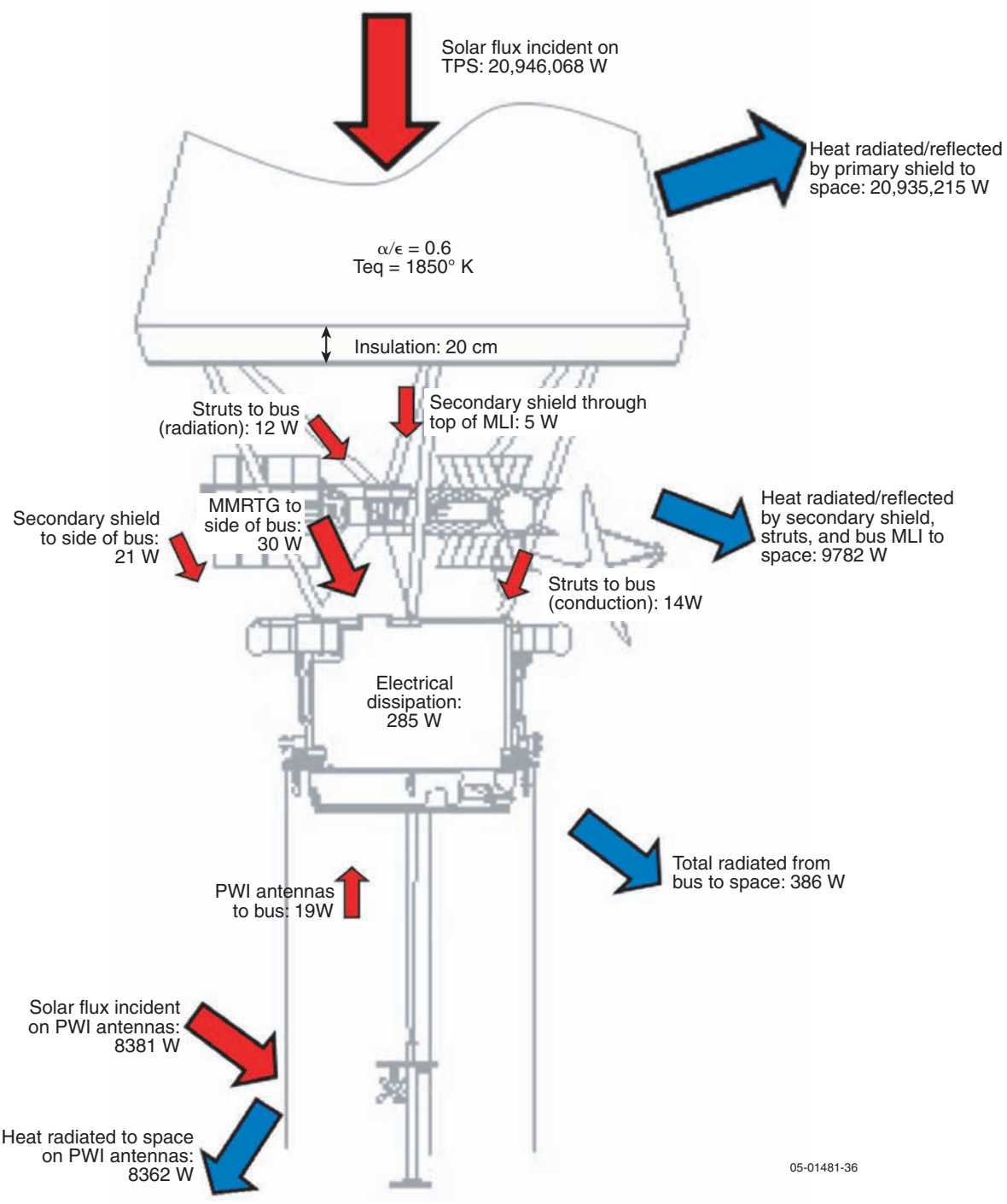

Figure 4-21. Thermal balance at 4 R_S (hot case) for the baseline Solar Probe configuration.

The results of the hot case analysis and sensitivity trades indicated that the heat inputs from all of the struts and the PWI electric field antennas can be accommodated if the baseline α/ε of 0.6 for the primary shield is achieved. As a fallback, if bare carbon–carbon is used for the primary shield (α/ε = 1.0), six of the struts would need to be thermally disconnected from the TPS after launch to keep the TPS mass within reasonable bounds. Thermally disconnecting the struts reduces the thickness of the secondary shield, and thus its mass (2.9 kg per centimeter of insulation thickness), but requires a

more complex design that would likely incorporate pyro-actuated strut separation mechanisms. Results of this sensitivity analysis are summarized in **Table 4-9**. Further trade studies will be conducted as part of the risk reduction effort to further optimize the design of the TPS and to minimize its mass.

4.7.3 Thermal Analysis Cold Case. Solar Probe's radiator surfaces are sized to balance the high flux environment experienced during a solar encounter with the low flux environment at 5.5 AU. Since Solar Probe is a very power-constrained mission, very little power will be available for heaters. However, the cold case analysis indicates that the RTGs will provide adequate heat to maintain the spacecraft and instruments within normal operating temperatures even for periods when there is no solar flux. As a contingency, mass and power budgets for heaters and diode heat pipes are provided if subsequent thermal studies show that they are necessary.

4.8 Power Subsystem

The Solar Probe power subsystem (cf. Figure 4-7) consists of three Multi-Mission Radioisotope Thermoelectric Generators (MMRTGs), a power system electronics box (PSE), two external shunts, a lithium-ion battery, and a power distribution unit (PDU). The PSE controls power to the spacecraft from the RTGs using resistive shunts to dissipate unneeded power and a small capacitor bank to provide an even flow of current to the spacecraft. It also controls battery charging and power. The PDU provides relays and switches controlling loads to various subsystems.

4.8.1 Primary Power Source. Three MMRTGs are the primary power source for Solar Probe. The RTG design that has been flown for the past 25 years is no longer produced and will not be available for Solar Probe. However, two radioisotope power sources are expected to be available for a 2014 launch: the MMRTG and the Stirling radioisotope generator.

The MMRTG is similar to previously flown RTGs and will be used on the Mars Science Laboratory (MSL). It is smaller than the older RTGs, however, and carries eight general-purpose heat sources (GPHSs) rather than 18. Transfer of the heat generated by the radioisotope units to electrical energy is expected to be approximately the same as in previous RTG designs. However, because of the smaller modular design and because the new MMRTG is designed to operate in the Martian atmosphere as well as in interplanetary space, the specific power has been reduced from over 5 W per kg BOL to 2.8 W per kg BOL. Each MMRTG is specified to provide at least 110 W BOL power per unit and is predicted to provide 126 W BOL. The mass of each MMRTG is specified to be less than 45 kg. The conceptual Solar Probe design assumes

Table 4-9. Perihelion thermal trades showing the sensitivity of the primary shield optical properties and Thermal Protection System strut configuration to the required secondary shield thickness and mass

Thermal Inputs to Bus	Baseline α/ε = 0.6 Struts Uncut	α/ε = 0.6 6 Struts Cut	α/ε = 1.0 6 Struts Cut	α/ε = 1.0 Struts Uncut
Electrical dissipation (W)	285	285	285	285
Strut conduction (W)	14	17	18	20
Strut radiation (W)	12	13	13	13
RTG (W)	30	31	29	30
Secondary shield to sides (W)	21	27	31	31
Secondary shield through top MLI (W)	5	3	7	9
PWI antennas (W)	19	19	19	19
Total (W)	386	395	402	407
Spacecraft bulk temperature (°C)	43	45	46	47
Required secondary shield thickness (cm)	20	15	21	29
Delta mass from baseline (secondary shield insulation & cutting devices) (kg)	n/a	−11.5	0	+23.1

that the cryogenic tubes used for additional cooling for the MSL mission would be removed, reducing the maximum mass to 43.5 kg.

The other option considered for Solar Probe was the Stirling Radioisotope Generator (SRG). SRGs offer the advantage of increased efficiency, resulting in a reduced unit mass compared with the MMRTG. SRGs are currently being developed at NASA Glenn Research Center. Although promising for future missions, SRG designs have no flight heritage and were considered a higher technical risk for Solar Probe than the MMRTGs. In addition, there are potential issues of electromagnetic and magnetic interference with the science measurements. Therefore, we selected the MMRTG as the baseline primary power source for Solar Probe.

Solar power has previously been studied as an option for Solar Probe and has been shown to be impractical because of the extreme range of solar flux experienced during the mission. A solar-powered mission would require enormous arrays to meet power requirements near the aphelion distance of 5.5 AU. These large arrays would not be stowable within the TPS umbra during the solar encounter and would have to be released, thus eliminating the possibility of a second solar encounter. Most importantly, however, experience with high-temperature solar arrays on previous missions and mission studies have shown that use of solar power is impractical at distances inside 0.25 AU, and such a system would not survive at perihelion distances of 4 R_S. Using battery power inside 0.3 AU would be very mass prohibitive and was not considered a viable alternative.

4.8.2 Secondary Power Source Selection. The study found that Solar Probe could experience potentially large transient peak power loads, primarily from reaction wheels, thrusters, and some of the instruments. Most of these peaks are expected to last less than 1 s, but during momentum management and ΔV maneuvers, significant power draws could last for several minutes. These potential peak power loads are likely to last too long to rely on a capacitor bank alone. We therefore decided to incorporate a small battery, on the order of 4.5 A-h, which is more than adequate to handle these transient peak power loads. A lithium-ion battery was chosen because of its high energy density and predicted availability in the next few years. Lithium-ion power sources have been under significant development in recent years and are considered to represent a low technical risk.

4.9 Command & Data Handling Subsystem

The Solar Probe C&DH subsystem (cf. **Figure 4-7**) is an integrated system that manages guidance and control (G&C), and spacecraft fault protection as well as command and data handling functions. The C&DH hardware consists of a primary and a backup integrated electronics module (IEM), two attitude interface units (AIUs), temperature I/O assemblies, and a data bus. The C&DH architecture and components have heritage in other spacecraft programs and/or are industry-standard designs, so that cost and technical risk are minimized.

4.9.1 Data Bus. The C&DH subsystem uses a 1553B data bus, which is a standard configuration with significant flight heritage. Its performance is more than adequate to handle spacecraft data traffic as well as the instrument peak data rates.

4.9.2 Integrated Electronics Modules (IEMs). Solar Probe uses an IEM architecture (**Figure 4-22**) for housing most of the C&DH hardware. This approach and a similar architecture have been employed in other spacecraft programs such as MESSENGER and New Horizons. The IEM architecture is a standard 6U compact PCI card architecture. Each IEM includes a flight processor, solid-state recorder (SSR), an interface card, telecommunications uplink and downlink cards, and a power conditioning card. The baseline flight processor is a RAD750-class (100+ MIPs) processor card. (The MESSENGER IEM flight processor implemented C&DH and G&C functionalities in a 25-MIPs processor.)

The two IEMs are fully cross-strapped to provide redundancy. The primary IEM processor will detect and correct spacecraft fault conditions, perform all G&C control functions, and serve as the spacecraft data bus controller. If a critical fault condition is detected in the primary IEM, data bus controller and G&C functions can be quickly switched to the backup IEM processor without rebooting that processor. The backup IEM will operate as a 1553B bus monitor and will receive the same G&C data as the primary IEM, enabling

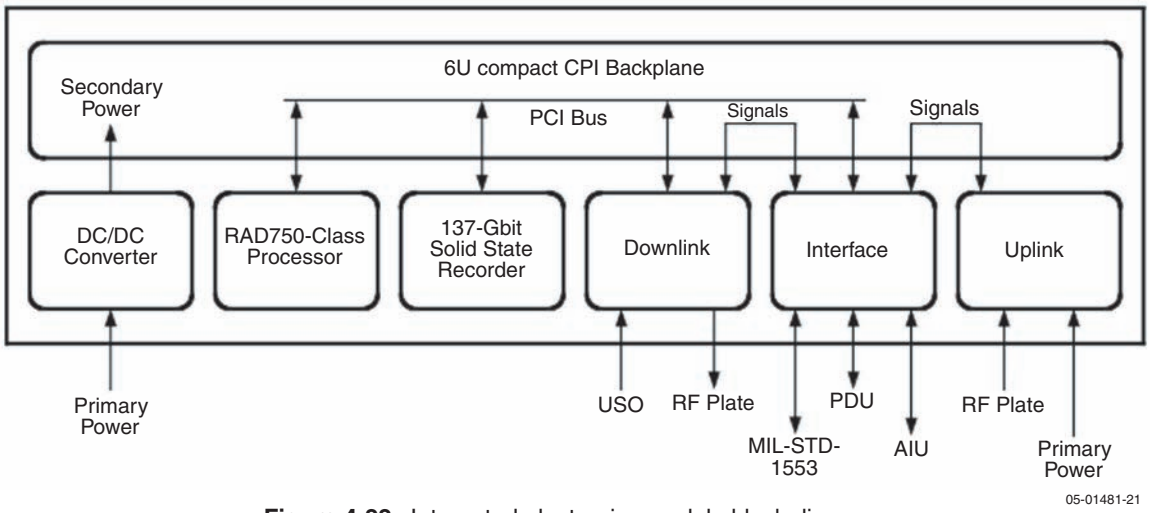

Figure 4-22. Integrated electronics module block diagram.

it to quickly take over G&C operations. The AIU will include hardware-based autonomy to switch control from the primary IEM to the backup IEM. During non-critical mission periods, the redundant IEM may be turned off to reduce spacecraft power bus loading.

During a solar encounter, both IEMs will be powered and each IEM will process uplink command messages and record all instrument science data, providing redundant recording of all science data. The backup IEM could receive the instrument data from either the common DPU (RT to RT transfer) or the primary IEM (BC to RT transfer), or it could utilize its bus monitor capability to acquire the data as they are transferred to the prime IEM.

Each IEM includes a 137-Gbit SSR board (which equates to 128-Gbit binary). The flash memory must perform properly at a total dose limit of 44 krad while operating at a 10% duty cycle. Studies undertaken as part of NASA's Living With a Star program have demonstrated that the radiation total dose hardness of flash memory devices is increased if the devices are not powered during exposure. Since the SSR board does not have to be powered during the Jupiter flyby, turning the SSR off near Jupiter is an option if additional (total dose) margin is required.

4.9.3 Attitude Interface Units (AIUs). Redundant AIUs housed in a single assembly provide all required interfaces between the 1553B data bus and the G&C system components: Sun horizon sensors (SHSs), digital solar aspect detectors (DSADs), reaction wheels, and temperature remote I/O (TRIO) units (**Figure 4-23**). While both AIUs can be powered at once, normally only the primary AIU will be powered.

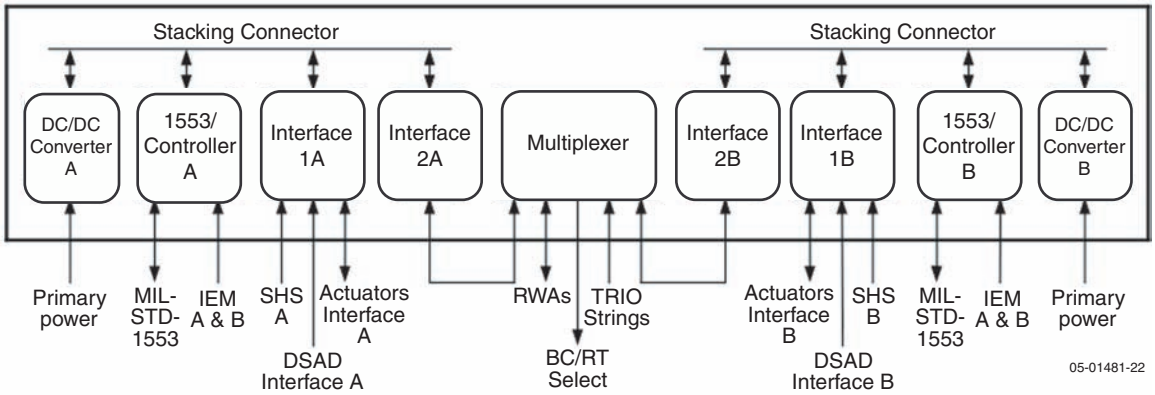

Figure 4-23. Attitude interface unit block diagram.

As noted above, the AIU includes a hardware autonomy circuit that will switch spacecraft control to the backup IEM if it detects a problem in the primary IEM. This switchover is accomplished by changing a signal that selects which IEM is the 1553B bus controller. By default, IEM software will execute a backup G&C algorithm when that IEM takes over as bus controller. The backup G&C mode is implemented in the IEM rather that in the AIU to prevent a failed AIU from switching control to itself. If an AIU does fail, the worst it could do is switch control from a working prime IEM to a working backup IEM.

The AIU design is based on 4 × 4 inch stackable slices. This design has been used in previous instruments. Each of the two AIUs in the stack is composed of four slices. A ninth slice is used to multiplex non-redundant components and signals to the prime AIU.

4.9.4 Temperature Remote I/O (TRIO) Assemblies. Spacecraft temperatures will be monitored by thermistors located around the spacecraft. The thermistors will be sampled by independent strings of TRIO assemblies (**Figure 4-24**), matchbook-sized units that monitor 15 thermistors each. Each TRIO assembly contains a single custom integrated circuit. Each TRIO assembly samples and stores the reading from the thermistors and transfers the data to the AIU over an I2C bus. The primary AIU is the I2C bus master and also provides power to the TRIO assemblies. The AIU multiplexer slice connects the TRIO I2C bus signals and power and ground lines to the primary AIU. Such TRIO assemblies have been used on several previous spacecraft.

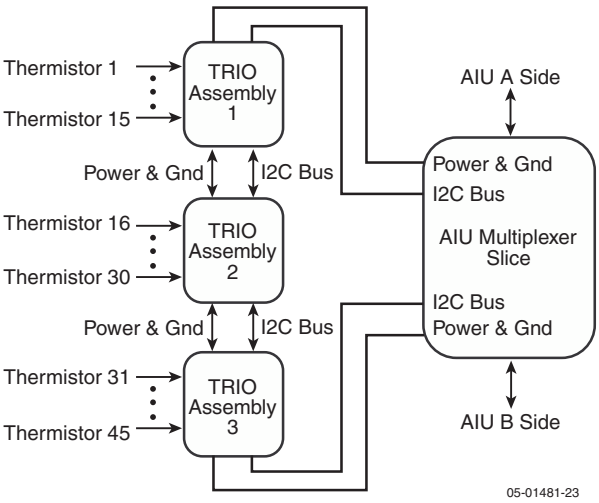

Figure 4-24. Block diagram of the temperature remote I/O assemblies.

4.9.5 C&DH Flight Software. The Solar Probe C&DH software has significant heritage from the MESSENGER flight software. The software is implemented in C code under the VxWorks real-time operating system. The G&C attitude estimation and attitude control algorithms are implemented as tasks that execute concurrently with other tasks that constitute the C&DH functionality. The primary flight processor, via hardware discrete, boots to a flight software application that becomes the 1553 bus controller and actively controls the spacecraft, performing all G&C and C&DH functions. The backup flight processor, when powered, boots to a flight software application that operates as a remote terminal on the 1553 bus and can record science data to the solid state recorder (SSR) in parallel with the primary flight processor.

The primary flight processor C&DH software manages the telecommunications uplink and downlink using CCSDS protocols for data handling. Commands are received in CCSDS telecommand packets that are either processed by the C&DH software or dispatched to the G&C tasks or to other subsystems on the 1553 bus, as indicated by an operation code contained in the packet header. The C&DH software supports storage of command sequences, or macros, which can be executed by a time-tagged command stored in flight processor memory.

The C&DH software collects engineering and science data from the instruments and manages the storage of those data on the SSR in the form of files. The current concept assumes that the common DPU compresses and packetizes the science data prior to their being sent to the SSR. The C&DH software can be configured to interleave CCSDS transfer frames of real-time telemetry packets with frames of SSR playback data. SSR playback is managed using the CCSDS File Delivery Protocol (CFDP) software that was successfully used on MESSENGER. CFDP provides a mechanism to downlink files from the SSR using a handshake with the CFDP client in the ground system software. This protocol automatically manages retransmission of any file fragments lost due to data dropouts without requiring retransmission of the entire file, and file transmissions may be suspended and resumed

between passes. No operator intervention is required to manage the retransmit process.

In addition to supporting standard command processing, data handling, macro storage and uplink/downlink functions, the C&DH software includes an autonomy evaluation engine that supports fault detection and protection. Data collected from all subsystems are stored in a memory buffer and can be referenced by uploaded autonomy rules. Each rule can monitor one or more telemetry points, perform computations, and execute a specified command if the premise of the rule evaluates "true" for a designated number of consecutive times. Typically the command is an instruction to execute a stored macro that performs a corrective action. This design allows for autonomy rules to be developed and uploaded without requiring software changes.

The C&DH software supports receipt of code, parameter, and rule uploads, and downlink of these items or flight software data structures. Additionally, the flight software maintains a number of history logs, event logs, and anomaly logs which may be downlinked to support anomaly investigation. The flight code implements a software watchdog that services a timer that forces a reset of the processor should any critical task fail to execute during the allotted time.

4.10 Telecommunications

The design of the Solar Probe telecommunications subsystem is determined by a number of factors. The need to provide real-time science data at a high rate during the first encounter requires a downlink frequency that will be minimally affected by coronal scintillation. Given the fixed amount of power available with the three MMRTGs, the power allocated to the telecommunications subsystem (~20 W CBE) must be sufficient to satisfy the requirements of that subsystem while ensuring that adequate power is available for the instruments and other subsystems. The baseline design achieves a significant savings in the power requirements of the telecommunications subsystem through the use of a noncoherent, transceiver-based navigation approach that eliminates the need for a transponder.

4.10.1 Downlink Frequency Selection. One of the most important considerations in selecting the telecommunications architecture was the need to provide a significant amount of real-time science during the encounter. Solar Probe will spend approximately 15 hours during the first solar encounter with the elongation or Sun-Earth-Probe (SEP) angle less that 2.3°. Conjunction experiments with other probes have shown that X-band and S-band communication links are adversely affected by coronal scintillation at small elongation angles. For example, a study of the NEAR-Shoemaker spacecraft as it underwent a superior conjunction in early 1997 showed significant degradation of command and telemetry links at X-band for elongation angles below 2.3° (*Bokulic and Moore*, 1999). Earlier studies of Magellan (*Webster,* 1994) and Galileo (*Beyer et al*., 1996) telecommunications performance yielded similar conclusions.

According to a model of radio wave propagation in turbulent media (*Armstrong and Woo*, 1980), scintillation loss varies inversely as the square of the frequency, and Ka-band links are significantly more resistant to coronal scintillation effects than X-band and S-band links. The frequency ratio of a Ka-band frequency to X-band frequency for a given Deep Space Mission System (DSMS) channel is 3.8:1, and consequently, the model predicts that Ka-band enjoys a 11.6-dB advantage over X-band with respect to scintillation loss. Improvements in link performance at Ka-band have been confirmed by simultaneous transmission of telemetry on X-band and Ka-band links during solar conjunctions with Mars Global Surveyor (*Morabito et al*., 2000), Deep Space 1 (*Morabito et al*., 2001), and Cassini (*Morabito et al*., 2002). Poor weather erodes some of the advantages of Ka-band, but even under 90% weather conditions, only a Ka-band system can provide significant telemetry. For this reason a Ka-band downlink has been selected as the baseline telemetry link for the first solar encounter. The telecommunications system will provide approximately 121 Gbits of recorded science and a real-time data rate of 25 kbps during this encounter.

An X-band system has several advantages over Ka-band when solar scintillation is absent, which will be the case for much of the mission. An X-band system, when taking advantage of the 70-m DSMS antennas, will actually outperform a Ka-band system, which is limited to the 34-m DSMS antennas for the foreseeable future. In addition, X-band is

relatively insensitive to weather as compared with Ka-band, offering additional flexibility. X-band also offers the benefit of greater technological maturity and flight heritage. And finally, an X-band system has a wider beam for a given antenna size than Ka-band, making pointing budgets more forgiving. In addition, since an X-band link was selected for the command uplink, adding an X-Band downlink is relatively straightforward. For these reasons, an X-band downlink has been incorporated in the Solar Probe design to provide redundancy and reduce mission risk.

4.10.2 Command Link Frequency Selection. The desire for simplicity and the extreme speed of the spacecraft at perihelion drive the choice of uplink frequency. The spacecraft reaches a top speed of 308 km/s, at which the angular separation between the transmitting and receiving lines of sight is nearly 3.5 beamwidths of a 34-m antenna if both the uplink and downlink are at Ka-band. However, the spacecraft speed is under 100 km/s for all but 2 days of the orbit, and the corresponding angular separation is approximately 1.3 beamwidths at Ka-band and one-half beamwidth at X-band. Consequently, an X-band command link was selected. The uplink allows a command rate of 500 bps with a link margin of 16 dB when spacecraft speed is 100 km/s. Alternatively, separate 34-m antennas could be used for Ka-band telemetry and commanding, but this option requires that the spacecraft carry a Ka-band receiver, which is less desirable because of technological immaturity and lack of heritage in interplanetary missions. Besides, the low data rate associated with commanding diminishes the need for Ka-band. The X-band configuration chosen uses receiver hardware with flight heritage from the TIMED and CONTOUR programs.

4.10.3 Telecommunications Subsystem Implementation. The Solar Probe telecommunications subsystem uses four antennas: a gimbaled high-gain antenna (HGA), a hard-mounted medium-gain antenna (MGA), and two hard-mounted low-gain antennas (LGAs). The HGA is used for Ka-band downlink, while X-band uplink and downlink capability is provided through all the antennas. The telecommunications architecture is shown in **Figure 4-25**.

The HGA is the preferred aperture for communications during the solar encounter and data retrieval phases of the mission, including all of the science telemetry. It is sized to remain within the shadow of the umbra during the perihelion pass. The main reflector is 0.8 m in diameter and utilizes a di-chroic subreflector to transmit a right-hand circularly polarized (RHCP) wave at Ka-band. A horn behind the subreflector provides bidirectional communications at X-band. A mechanically steered parabolic reflector dish was selected as the HGA because it provided the only practical solution to meet data rate, mass, and size requirements. A phased array antenna was considered and quickly discounted due to it complexity in number of elements for a Ka-band system, its mass inefficiency, and performance losses over the range of required elevation angles. Although the HGA affords the best link, it sets an upper bound for the total pointing error relative to the spacecraft-to-Earth line of sight at 0.2°.

The MGA and the LGAs are used for communication with the Earth during the cruise phase. The primary antenna used to establish communications during the cruise portion of the mission is the MGA. The MGA is hard-mounted to the spacecraft with its FOV centered in the +Y direction. The MGA has an angular coverage of 10° (±5°) and gain of 20.4 dBi at the X-band downlink frequency. Two LGAs were incorporated into the design for emergencies that could occur early in the mission or when mission events preclude pointing of the MGA and HGA. The LGAs are mounted 180° apart, each having a beamwidth of 45° (±22.5°) and peak gain of 10.75 dBi at the X-band downlink frequency. This LGA configuration allows low-rate telemetry and commanding at virtually any attitude at 1 AU. The MGA and LGA designs have prior flight heritage.

Figure 4-25 shows how the antennas connect to the spacecraft electronics. The spacecraft's transmitter section consists of a pair of downlink cards, each within its own IEM; four solid-state power amplifier (SSPA) modules, two at X-band and two at Ka-band; a pair of ultrastable oscillators (USOs); and a distribution network to couple signals between the SSPAs and any of the available antenna apertures. Primary power will be applied to only one of the four SSPAs to enable either X-band or Ka-band communications on the telemetry link. Both frequency bands are serviced by block-redundant SSPAs. The output from either of the X-band SSPAs may be steered to any of the

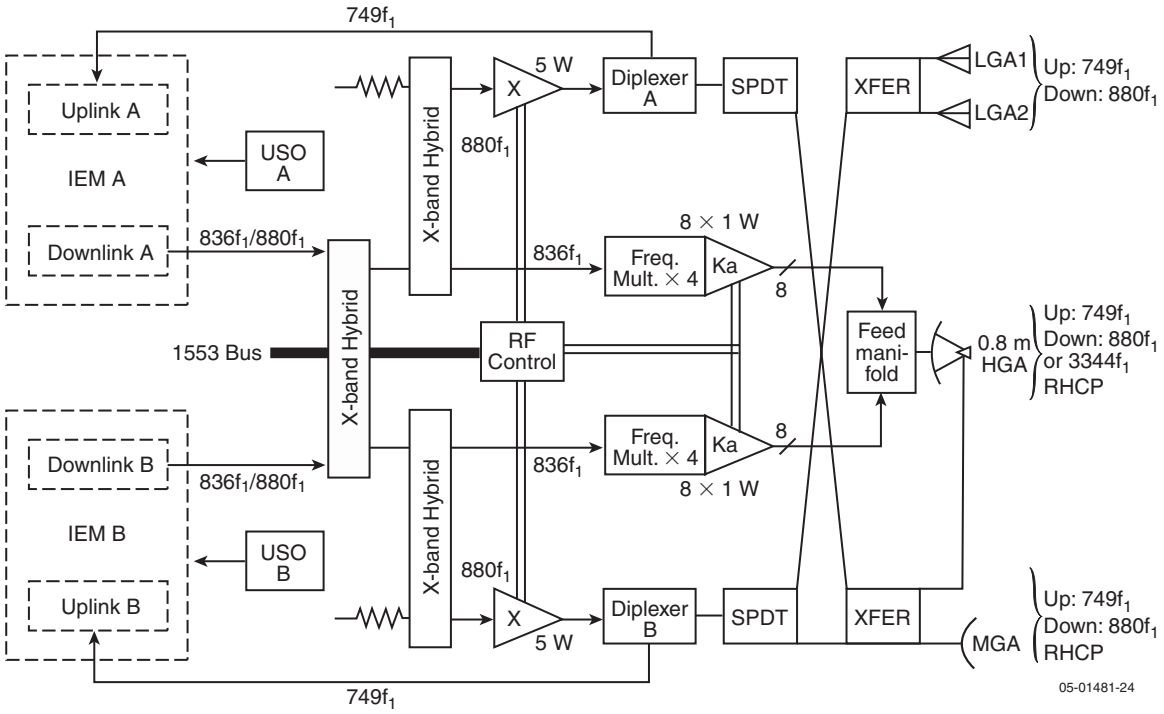

Figure 4-25. Telecommunications subsystem block diagram.

antennas through a network of single-pole-double-throw (SPDT) and transfer (XFER) switches, which are themselves configured for redundant operation. A frequency-quadrupling circuit drives the input of each bank of Ka-band SSPAs.

The downlink card assumed in the baseline design is based the one flown on TIMED and CONTOUR but is enhanced to support turbo-encoding to take advantage of the reduced signal-to-noise ratio (S/N) at which these DSMS links can operate. The baselined uplink card is identical to the one developed for the New Horizons mission. The USOs derive from designs used on CONTOUR and New Horizons, with enhancements to lower mass and primary power consumption and to improve immunity to radiation.

4.10.4 Telecommunications Subsystem Performance. The telecommunications subsystem performance varies over the mission as follows.

Real-Time Encounter Performance. Real-time telemetry at a high data rate will be available only during the first solar encounter because the HGA will not be pointed toward Earth during the second encounter. If Ka-band transmission is assumed, then real-time telemetry can be sent continuously at a rate of at least 25 kbps during the first encounter. With the HGA, a maximum command rate of 500 bps can be used except when the elongation angle is less than 2.3° . These rates accommodate both solar interference and the potential for unfavorable weather conditions (90% weather assumed) at the ground stations during the encounter.

Post-Encounter Telemetry Performance. During and after the first encounter the orientation and trajectory of the spacecraft relative to the Earth are very favorable for large telemetry rates and subsequent data return. Following the encounter, the Earth will be moving generally in the same direction as the spacecraft, so that the relative range between the spacecraft and the Earth will remain approximately 1 AU for the first 110 days after perihelion. After this time, the distance will increase at greater rates, and the telemetry rate will decrease.

The second solar encounter will occur with the HGA pointed away from the Earth and the spacecraft and the Earth moving in opposite directions after the flyby. The data rate will decrease rapidly as the range between the Earth and the spacecraft increases. In addition, owing to the encounter geometry, the HGA cannot be pointed towards

Earth until after the spacecraft is able to point the TPS away from the Sun, approximately 21 days after the encounter. These two factors together will result in significantly reduced data rates after the second encounter. **Figures 4-26 and 4-27** illustrate Solar Probe's expected telemetry performance after the first and second encounters, respectively.

Link Performance Summary. Link performance is determined primarily by the antenna used and by the relative distance from the spacecraft to the Earth. **Table 4-10** summarizes the estimated telemetry performance for the different antennas at varying distances. **Table 4-11** summarizes maximum command rates. Both tables assume post-encounter conditions (i.e., no significant solar interference) and, for all antennas except the LGA, the use of a 34-m DSMS antenna for the ground link. In the case of the LGA, a 70-m DSMS antenna is assumed along with a worst-case LGA orientation (random tumble), which is possible in an emergency situation.

Table 4-10. Estimated maximum telemetry rate as a function of spaceraft–Earth distance

Relative Earth–Spacecraft Distance (AU)	Estimated Maximum Telemetry Rate (bps)			
	HGA X-Band	HGA Ka-Band	MGA X-Band	LGA X-Band
1	8,000	45,000	180	5
2	2,000	7,000	40	0
3	900	5,000	40	0
4	500	2,800	8	0
5	320	1,800	8	0
6	220	1,250	8	0

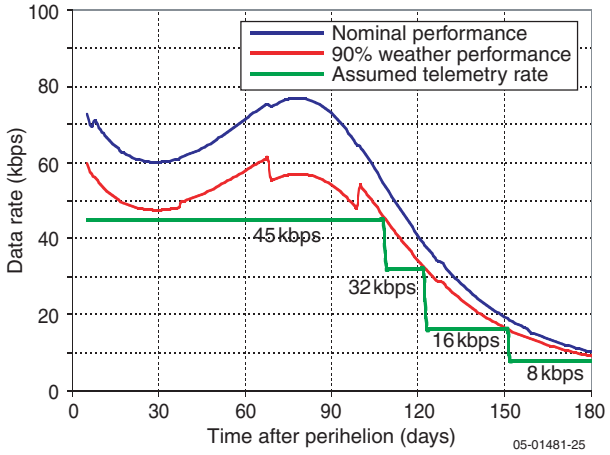

Figure 4-26. Telemetry rate as a function of time after first-encounter perihelion.

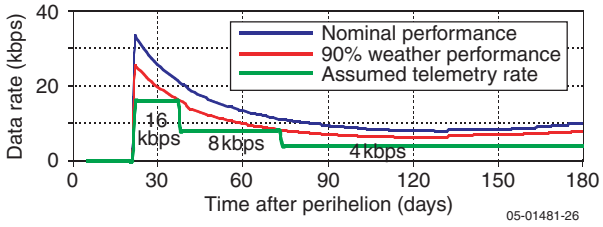

Figure 4-27. Telemetry rate as a function of time after second-encounter perihelion.

4.10.5 Noncoherent Navigation. Solar Probe's transceiver will be used to make accurate Doppler measurements, thus eliminating the need for a transponder and providing a significant and needed reduction in required spacecraft power. The Probe will measure the ground station's uplink carrier frequency and transmit the results to the ground station. The ground station will combine that information with measurements of the spacecraft's downlink carrier frequency to obtain a Doppler measurement that has the same precision as one obtained with a coherent transponder. A conceptual drawing of the approach is shown in **Figure 4-28**.

Extensive tests (*Jensen and Bokulic*, 2000) demonstrated that the noncoherent telemetry-assisted technique, which was developed for CONTOUR, makes velocity measurements with a precision of ≤0.1 mm/s for 1-min measurement intervals. The use of a lighter-weight, lower-power-consumption

Table 4-11. Estimated maximum command rate as a function of spacecraft-Earth distance

Relative Earth–Spacecraft Distance (AU)	Estimated Maximum Command Rate (bps)		
	HGA X-Band	MGA X-Band	LGA X-Band
1	2,000	500	8
2	2,000	125	8
3	500	125	0
4	500	31	0
5	500	31	0
6	125	31	0

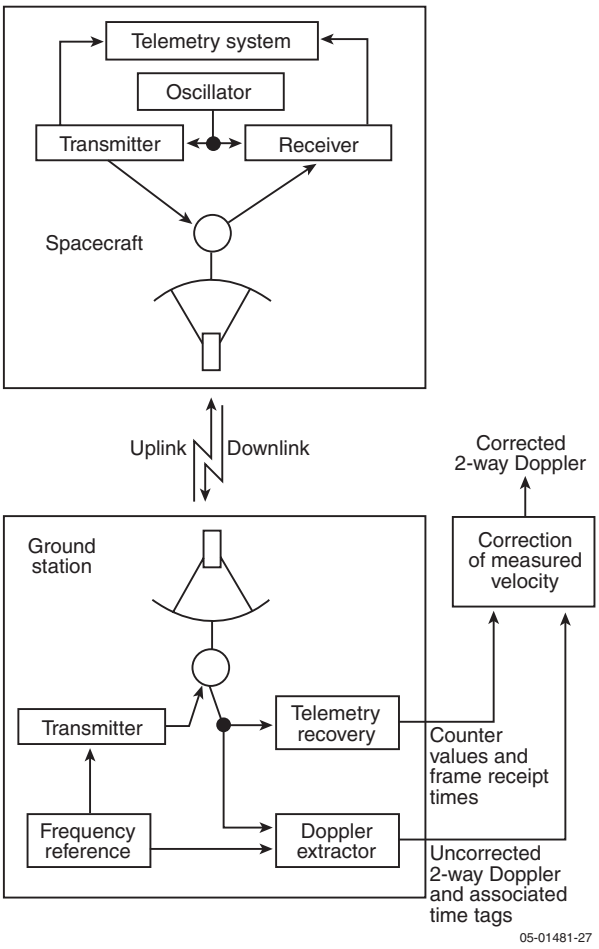

Figure 4-28. Schematic illustrating the noncoherent navigation concept.

transceiver on Solar Probe will thus yield results equivalent to those obtainable from a coherent technique with a transponder. The noncoherent tracking technique does not require any new equipment at the ground stations. However, the observed Doppler frequencies must be corrected by telemetry prior to their use in orbit determination.

4.11 Mission Data Management

The greatest amount of data will be returned during and after the first encounter, with real-time telemetry of 20 Gbits occurring during the encounter proper. Owing to the Sun-spacecraft-Earth geometry at the second encounter, the science data return will be reduced compared with that of the first encounter, but it will still be substantial. Cruise science can be telemetered at varying rates throughout the mission.

4.11.1 First Solar Encounter. In addition to the science data acquired during the solar encounter, Solar Probe will collect and store a significant amount of engineering data on the effects of the unique and challenging near-Sun environment on the spacecraft and subsystems. **Table 4-12** shows the breakdown of the required average instrument and housekeeping data rates allocated over the entire first solar encounter. The raw data rate represents the actual science data. The data rate to recorder columns includes a 30% margin and a 5% overhead for packetization of the data performed in the DPU and is used to estimate the maximum data bus bandwidth as well as to calculate the amount of data going to the SSR. Note that data rates for the HI and PSRI are combined as a single average data rate during the encounter to maintain consistent comparison with the other instruments shown on **Table 4-12**. In practice, the PSRI will only operate outside of 20 R_S and the HI will operate at a higher cadence inside of 20 R_S. Actual data rates for all instruments may vary some during the encounter, and a more detailed data schedule will be defined as the mission matures. 1800 bps of housekeeping data (e.g., spacecraft attitude data) are included with the science data because they are necessary to fully interpret the science data.

The resulting required data rate of 139.6 kbps will be achieved by using a standard 1553 data bus that transfers the instrument data packets from the DPU and the housekeeping data from various subsystems. Over the 10-day encounter, Solar Probe's two 137-Gbit SSRs will simultaneously record 121

Table 4-12. Instrument/housekeeping data rates during the first solar encounter

Instrument	Raw Data Rate (bps)	Data Rate to Recorder (bps)
FIA	10000	13650
FEA	20000	27300
ICA	10000	13650
EPI Low Energy	5000	6825
EPI High Energy	3000	4095
NGS	500	683
CD	100	137
Mag	1100	1502
PWS	10000	13650
HI/PSRI	40800	55692
Housekeeping	1800	2457
Total	102300	139640

Gbits of science data, including margin and packetization overhead. Two recorders are used to provide redundancy, which is important in view of the small window for primary science data collection. As a contingency, approximately 20 Gbits of data will be telemetered to the ground in real time using the Ka-band downlink at 25 kbps. This still allows a significant science return even if a catastrophic event should occur during the encounter.

After the first encounter is completed at perihelion plus 5 days, the primary role of the spacecraft is to telemeter the recorded science and housekeeping data. For approximately 110 days after the encounter, the data rate can be maintained 45 kbps using the Ka-band transmitter and the HGA. The number of days required to telemeter the recorded encounter data will depend on the amount of DSMS contact time available (**Table 4-13**).

The estimate of the number of days required to return the data assumes that CCSDS packets with 5% packetization and downlink overhead will be used and that 0.5% of the data packets will need to be resent to get 100% data return. It also assumes that 2 kbps of real-time housekeeping data are interleaved with the stored encounter data.

4.11.2 Second Solar Encounter The Sun-spacecraft-Earth geometry during the second encounter will not allow the same amount of science data to be returned as during the first encounter. The geometry prohibits real-time science telemetry since the HGA will be pointing away from the Earth. Moreover, contact will be made only starting 22 days after perihelion at a data rate of 16 kbps, and the downlink data rate rapidly declines after that since the distance from the Earth is greater and increasing at a faster rate.

In order to maximize the data return for the second encounter, it would be advantageous to increase DSMS contact time to continuous 24-hour coverage during this period. Using the same packetization, margin, CCSDS overhead, data loss, and a reduced real-time housekeeping assumption as described for the first encounter, the amount of data that can be returned vs. the number of days of continuous DSMS coverage is shown in **Table 4-14**.

4.11.3 Cruise Science. In addition to the primary science data returned during the solar encounters, Solar Probe will collect and telemeter science data during the cruise phase of the mission. As a part of normal operations and to maintain proper navigation, weekly 8-hour contacts will be conducted. During this time, a reasonable portion of the available bandwidth will be dedicated to additional science telemetry. The amount of available science data sent to the ground per week varies from 22 Mbits near aphelion to 1.2 Gbits when the spacecraft is able to operate at its maximum data rate of 45 kbps.

4.12 Guidance and Control

Solar Probe's guidance and control (G&C) subsystem is designed to maintain the spacecraft attitude required to protect the spacecraft bus from the harsh solar environment, point antennas for communications with Earth, provide desired viewing geometry for science instruments, and perform trajectory correction maneuvers. Redundant star trackers and a high-precision inertial measurement unit (IMU) provide attitude knowledge, while attitude control is provided by four reaction wheels and 12 4-N thrusters. The attitude determination and accuracy requirements derived from these different activities are summarized in **Table 4-15**. The pointing control requirement is driven by the need to point the HGA within 0.2° when downlinking using the Ka-band system. This will certainly be the case during the entire first encounter when a Ka-band downlink is needed to maintain a real-time

Table 4-13. Number of days needed to telemeter first encounter data

DSMS Contact Time per Day (h)	Days to Telemeter Encounter Data
24	34
16	51
8	101

Table 4-14. Number of days of Deep Space Mission System contact vs. returned second encounter data

Number of Days of DSMS Contact	Encounter 2 Data Downlinked (Gbits)
26	24.6
39	33.0
78	50.5
100	57.4

Table 4-15. Solar Probe pointing budget

Payload	Pointing Requirements (per axis)		
	Control degrees, 3σ	Knowledge degrees, 3σ	Jitter degrees, 3σ
Communication (HGA)	≤ 0.2 x, z	n/a	n/a
In situ instruments <0.3 AU	≤ 1 x, y, z	≤ 0.3 x, y, z	≤ 0.3 x, y, z over 10 s
Magnetometer <0.3 AU	≤ 1 x, y, z	≤ 1 x, y, z	≤ 1 x, y, z over 0.05 s
Plasma Wave Instrument <0.3 AU	≤ 1 x, y, z	≤ 1 x, y, z	n/a
Polar Source Region Imager 50 R_S to 20 R_S	≤ 0.5 x, y	≤ 0.5 x, y	≤ 0.03 x, y over 1 s
Hemispheric Imager < 20 R_S	≤ 1.0 y, z	≤ 1.0 y, z	≤ 0.03 y, z over 1 s

downlink in the presence of significant solar scintillation. Ka-band is also assumed as the baseline for HGA telemetry during most of the mission, although it may be supplemented by X-band transmission, which will reduce the pointing requirement somewhat. The pointing knowledge and jitter budget is driven by the two remote sensing instruments.

4.12.1 Attitude Determination. Spacecraft attitude will be determined by redundant star trackers and an internally redundant IMU. Using star trackers in the near-Sun corona presents a unique design challenge, which the Solar Probe design addresses by mounting the star trackers so that their fields of view are approximately orthogonal to the Sun as well as to each other. This configuration minimizes the chance that both units will be blinded by a localized coronal lighting event at the same time. Special care must be taken in the selection of the star trackers to ensure that they will perform properly with the elevated background noise of the near-Sun environment.

The IMU will provide the spacecraft rate and translational acceleration information necessary for maintaining attitude control as well as for closed-loop control during trajectory correction maneuvers. The IMU can also be used as a backup to the star trackers to propagate attitude for approximately 4 hours during a solar encounter if both star trackers are temporarily blinded. The IMU baselined for Solar Probe is a single integrated box with internal redundancy, although two separate units would also meet the needs of the mission.

The G&C subsystem includes two different kinds of Sun detection devices to provide coarse attitude determination for safing. During cruise, safing attitude determination will be performed by a set of digital solar aspect detectors (DSADs) that are mounted to provide wide-area coverage, allowing an attitude reference relative to the Sun if an attitude determination anomaly occurs. At distances beyond 3.0 AU, simply pointing the +Y-axis towards the Sun would allow contact with the Earth within the MGA beamwidth of 10°. Inside this distance, a small step search pattern would be performed to reestablish contact with the ground.

In the event of long-duration star tracker blinding, system resets, or other attitude control anomalies, a new sensor design, the solar horizon sensor (SHS), is proposed for attitude safing when the spacecraft needs to be protected behind the TPS umbra. The detector would be mounted at the end of the science boom and would consist of a conical ring of carbon-carbon material, a mirrored conical reflector, and a detector array with pinhole lens. The detector array resides in a small electronics box, which contains readout electronics for both the detector and a set of thermistors. If an attitude error that reaches a designated threshold should occur, the edge of the conical ring would become illuminated and projected onto the detector. The processed signal could be used to provide attitude control for safing during the solar encounter.

Most currently available attitude control hardware should meet the needs of Solar Probe with little or no custom modifications. Special care must be taken to select star trackers that will perform well in the intense coronal lighting environment. During the engineering study, one or more potentially suitable candidate star trackers were identified in existing product lines. The SHS will be the only

attitude determination device that will need to be developed for Solar Probe. Although new in design, the SHS would be developed based on existing Sun sensor technologies.

4.12.2 Attitude Control. Trade studies were performed to determine whether reaction wheels or thrusters should be used as the primary method of attitude control. Dead-band thruster control using small minimum impulse bit rocket engines such as are used on Cassini was considered because it appeared to offer a means of reducing mass and average power during the encounter. While the studies indicated that thruster control could reduce average power by approximately 20 W and might slightly reduce overall mass, they also revealed some disadvantages. Although the pointing requirement for the spacecraft is 0.2°, the required dead-band for the G&C system was budgeted to about 0.05° since much of the error budget will go to HGA misalignments and actuator setting errors. This small dead-band value would require frequent thruster firings, thus driving up the total propellant requirement and negating most of the mass savings. Overly frequent thruster firings were also a concern because of possible instrument contamination. In addition, it was feared that thrusters might interact structurally with the spacecraft more than reaction wheels would, although this effect has not yet been studied. Since several components such as the TPS, science boom, and plasma wave antennas could induce low-frequency modes, dead-band thruster control appeared less attractive.

Reaction wheels offer very tight pointing control and easily maintain spacecraft attitude at better than the budgeted 0.05°. Wheel control also interacts less with flexible modes and would be more likely to control them to meet the current jitter budget. Although power is tight on RTG missions, adequate power is available for reaction wheels. Therefore, reaction wheel control was selected as the baseline for Solar Probe. Thrusters will still be needed to control attitude when the wheels have to release their stored momentum and for controlling the spacecraft trajectory.

4.12.3 Pointing Strategy. For most of the mission, at distances outside 0.8 AU, the spacecraft will maintain 3-axis pointing control, with the +Y axis (nominal HGA/MGA boresight) pointed toward the Earth. While in cruise attitude mode, a slow rotation of about 0.5 rpm will be introduced to reduce angular momentum that builds up as a result of solar pressure torque. Occasionally enough momentum will build up that momentum dumping using the thrusters will need to be performed. Adequate pointing control should easily be maintained to keep the MGA pointed at the Earth to within 5° circular error 3σ.

Inside 0.8 AU, the Probe's attitude must change so that the TPS points towards the Sun, keeping the instruments and subsystems within its protective umbra. Some off-pointing from solar nadir may be allowed to keep the HGA and MGA pointed at the Earth as long as sensitive instruments and subsystems are not exposed to the Sun.

During the solar encounter (perihelion ± 5 days), spacecraft attitude will be maintained so that the Z-axis points toward solar nadir and the HGA and science pointing requirements are met. Momentum dumping will occur much more frequently during this period because of the intense solar radiation pressure. Each momentum management maneuver will be completed in less than 1 minute. For these short periods the thrusters will fire to remove angular momentum, and the control requirements for instrument pointing may not be maintained.

Solar pressure torques are often used as a means of passive momentum control. This option was considered as a possible augmentation of Solar Probe attitude control during the closest approach periods. This technique would require an intentional pointing offset of the heat shield that is adjusted automatically by the feedback control system. An advantage of passive dumping using solar pressure torques is that it could reduce the number of thruster momentum dumps needed. However, instrument pointing requirements might limit the range of offsets that could be used, reducing the overall contribution of a passive dumping mechanism. In addition, successful use of this method is also highly dependent on accurate modeling of the solar pressure effects. Given the uncertainties in models of the solar environment, Solar Probe's propulsion system is sized to allow all momentum control to be done with thrusters.

4.12.4 High Gain Antenna Control. When the spacecraft is operating within 0.8 AU and the +Z-axis is pointed toward solar nadir, the HGA

will be pointed by rotating the spacecraft about the Z-axis and rotating the antenna about the X-axis using a gimbal/arm mechanism. The spacecraft will be oriented such that the spacecraft–Earth line is located in the Y–Z plane. The G&C subsystem will compute the necessary positioning of the two gimbals for the HGA on the basis of onboard ephemeris models for the Earth, the Sun, and the spacecraft. The computation will essentially determine the rotation about the X-axis required to place the HGA boresight along the Earth line in the Y–Z plane. To keep the antenna in shadow, the X-axis rotation will require positioning two actuators based on knowledge of the Earth direction and of location of the edge of the umbra as derived from the spacecraft–Sun distance and TPS dimensions. The G&C system will translate the Earth–Sun geometry into the necessary low-level hardware commands to the gimballing mechanisms to achieve the correct HGA pointing. In the event of loss of onboard ephemeris knowledge or other fault conditions, the HGA will be commanded to its safe stowed position.

A simpler HGA pointing control will be used for periods in outer cruise where high-rate communication is desired. In this case, the TPS is not constrained to be Sun-pointed and the spacecraft +Y axis can be pointed directly at Earth. The HGA can remain at its nominal position with no gimbaling required.

4.12.5 Instrument Actuator Control. The G&C subsystem will interface with the PSRI periscope, PWI E-field antenna, and the FPI ram-looking arm mechanisms (cf. Section 4.5.1). At distances between 50 and 20 R_S, the PSRI periscope will be repeatedly extended beyond the umbra and then retracted in no faster than a ~10-min duty cycle. Periscope extension and retraction will be performed automatically on the inbound and outbound leg based on the distance from the Sun as derived from onboard ephemeris models. The position of the FPI arm will be adjusted to follow the edge of the umbra throughout the encounter. As in the case of HGA pointing control, the position of the arm will be determined based on the location of the edge of the umbra computed from the spacecraft–Sun distance and TPS dimensions. The G&C system will translate the umbra location into the necessary low-level hardware commands to the arm drive motor to maintain the desired instrument viewing geometry. As in the case of the HGA, the G&C system will command retraction of the PRSI and stowing of the side-looking arm if knowledge of Sun range is lost. The same approach will be used to drive actuators controlling the angle of the three PWI antennas, nominally maintaining an isolated 1-m section of the antenna exposed to sunlight outside the umbra.

4.13 Propulsion

Several types of propulsion systems were considered for Solar Probe, including both electrical and chemical systems. Electric propulsion systems were immediately discarded, however, because of the limited power available. Both a simple blow-down monopropellant system and a dual-mode system with bipropellant ΔV thrusters and monopropellant attitude control thrusters were considered. Although the latter might theoretically weigh less, the simple blow-down system was selected because of its lower cost, its reliability, and its packaging advantages.

The propulsion system architecture is shown in **Figure 4-29**. This design is similar in architecture to almost every hydrazine propulsion system flying today. Twelve 4-N thrusters provide forces in all required directions to control attitude and maneuver the spacecraft, and each thruster has series-redundant control valves to protect against leakage. Hydrazine propellant and nitrogen pressurant are stored in a single tank whose pressure decreases as propellant is depleted. Pressurant is separated from the propellant by an elastomeric

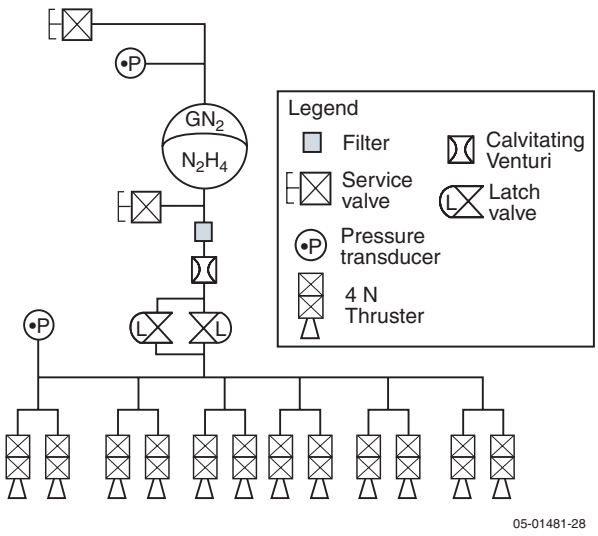

Figure 4-29. Propulsion subsystem architecture.

diaphragm within the tank. Latching valves isolate the thrusters from the tank for ground safety and system reliability (i.e., in case of a thruster leak), while manual service valves are used for testing and loading the system on the ground. The system's surge suppression orifices keep transient pressures within appropriate levels, and pressure transducers are used together with temperature telemetry to gauge propellant and monitor system performance in flight. Spacecraft ambient temperatures will be maintained such that the propulsion system requires no heaters except those on the thruster catalyst beds. Several flight-proven options exist for each component of the Solar Probe propulsion system. A representative set of heritage components was selected for preliminary performance evaluations, which demonstrated that system requirements can be met.

Because of the heat input from the secondary shield and MMRTGs, thrusters cannot be placed to provide coupled torques in all three axes. All twelve thrusters are therefore mounted around the bottom rim of the hexagonal bus (**Figure 4-30**). Four pairs of thrusters are located at vertices of the hexagon pointing in two opposite directions, each offset by 15° from the normal to the line connecting the vertices. These eight thrusters provide torque in both directions along each of the three axes of the spacecraft body. While redundant subsets of thrusters provide torque in each of the six directions (two pairs for each axis), perfect couples are obtained only for +Z- and −Z-axis. Because coupled pairs cannot be achieved in two rotation axes, some residual ΔV will be imparted to the spacecraft when using thrusters for attitude control. The other four thrusters are mounted on the bottom of the spacecraft, equally spaced along the +Y and −Y directions and along the +X and −X directions from the center line and pointing along the −Z axis. These four thrusters are primarily intended for imparting ΔV for spacecraft trajectory correction maneuvers. Any ΔV direction must be achieved by pointing the spacecraft +Z-axis in the ΔV direction. This approach is most efficient for propellant usage but presents complications for communications and/or collection of navigation tracking data during maneuver execution.

4.14 Micrometeoroid and Dust Protection

Initial analysis of the dust environment near the Sun (see Section 4.3) indicates that Solar Probe may encounter dust particles up to several hundred microns in diameter that are traveling at relative speeds as high as 500 km/s at perihelion. Such

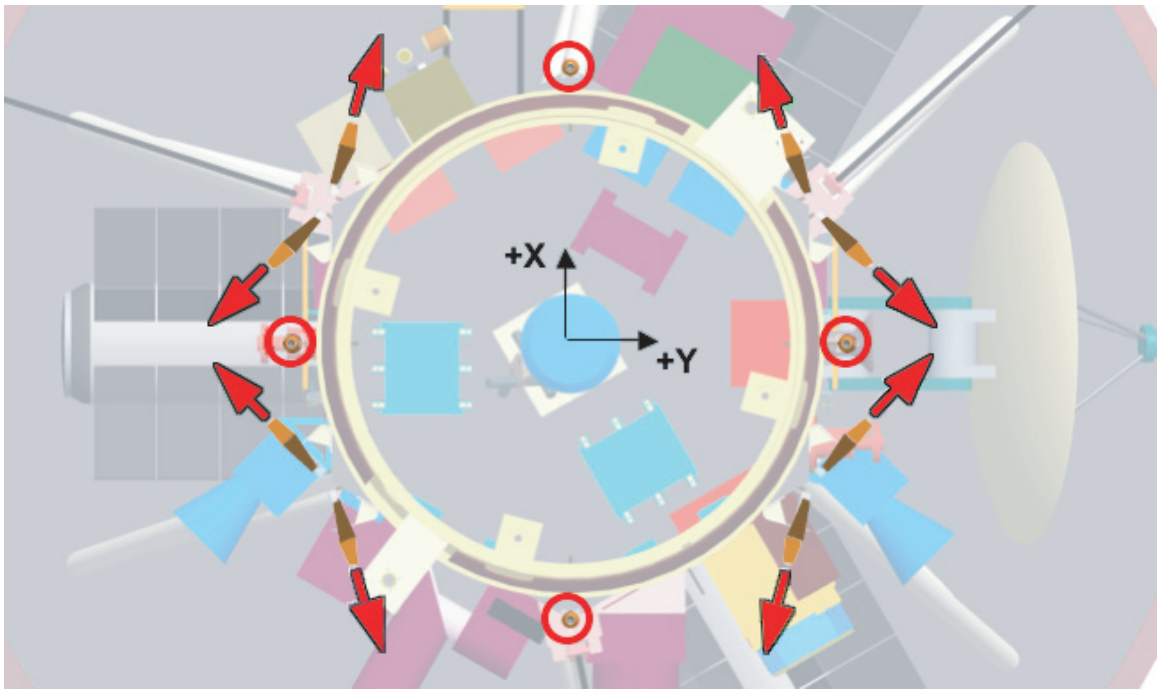

05-01481-29

Figure 4-30. Thruster layout.

impacts could damage instruments, spacecraft electronics, and propulsion hardware, while multiple impacts from smaller particles might degrade the performance of the TPS. In order to estimate the risk that the near-Sun dust environment[1] presents to the spacecraft and to develop a concept for a dust protection system, a study was performed using an analysis and prediction methodology employed for other NASA missions, both low-Earth orbit and deep space (*Elfer*, 1996; *Christiansen*, 1999). ***Using conservative, worst-case assumptions about particle size, velocity, and obliquity, the study demonstrated (1) that standard Whipple shielding consisting of spaced MLI blankets would be sufficient to protect the spacecraft bus and components in the near-Sun dust environment and (2) that the TPS would not be compromised either by multiple small-particle impacts or by the impact of an unusually large dust particle.***

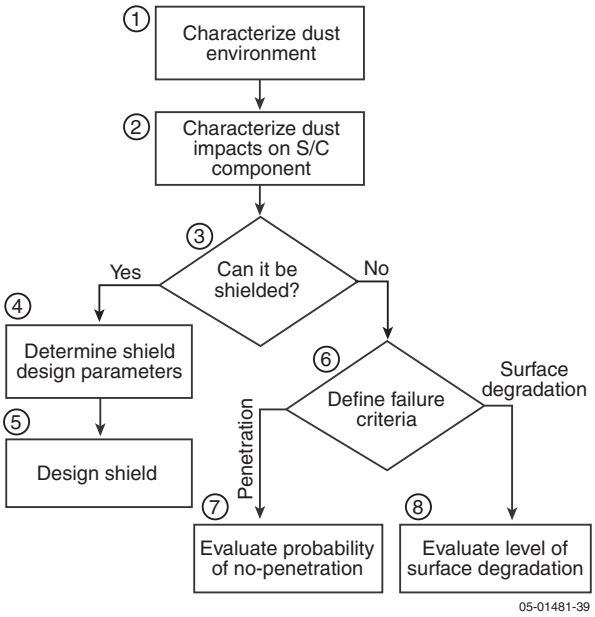

Figure 4-31. Chart illustrating the methodology employed in the dust risk/protection study.

4.14.1 Methodology. The methodology employed in the dust protection study is summarized in the paragraphs below and illustrated schematically in **Figure 4-31**. A complete description is provided in Appendix B.

The models of the near-Sun dust environment described in Section 4.3.5 were used to calculate dust flux as a function of solar distance, ecliptic latitude, and direction and to determine impact location, velocity, and obliquity angle. Impact probabilities for both the collision and the non-collision dust models (see Figure 4-5) were calculated for the following representative Solar Probe components: the Fast Ion Analyzer (FIA), Fast Electron Analyzer (FEA), Ion Composition Analyzer (ICA), Power Distribution Unit (PDU), spacecraft bus, and Thermal Protection System (TPS). These components are expected to be exposed to large dust fluxes, and the impact probabilities calculated for them thus represent upper bounds for impacts on other components not included in the study. (The vulnerability of instrument apertures to dust impacts was not analyzed because detailed instrument designs were not available. A detailed assessment cannot be performed until actual instrument designs are developed and aperture size and location can be specified. However, Appendix B provides information that instrument designers can use to calculate the critical particle size as a function of aperture area and thus to estimate the potential dust hazard for their instruments.)

For each of the selected components a 99% Probability of No Impact (PNI)[2] was calculated and the corresponding critical particle size was determined. Critical particle sizes were calculated for both the collision and the non-collision dust models. As can be seen from **Table 4-16**, when the non-collision model was used, the critical particle size increased by 30 to 140%.

The Coupled Thermodynamic and Hydrodynamic (CTH) hydrocode (*Boslough et al.*, 1993) was used to determine the shielding requirements for each of the selected components except the TPS (see Section 4.14.3 below). The largest critical particle size (i.e., that associated with the

[1]The study addressed only the dust environment inside 0.8 AU, which is considered to present the greatest potential risk.

[2]The Probability of No Impact is a metric used in the prediction and analysis of the damage to a component caused by a hypervelocity impact. It is the probability that, for a given particle flux, exposure area, number of impacts, and time, a particle of a given size (the "critical particle size") will not hit the component. For example, a PNI of 99% for a 56-μm particle means that there is a 99% chance that the component will not be hit by a particle of this size or larger or, alternatively, that there is a 1% chance of its being hit by a particle of that size.

Table 4-16. Critical particle diameters calculated for the collision A and non-collision dust models

Component	Critical Particle Diameter (μm)	
	Collision A Model	Non-Collision Model
FEA	56	132
FIA	56	132
ICA	62	148
PDU	206	266
Spacecraft Bus	246	437

non-collision model), a velocity[3] of 500 km/s, and zero obliquity were assumed in the CTH runs to demonstrate protection against the predicted worst-case environment. Shielding was considered adequate if no penetration or spalling occurred inside the box or structure of interest.

4.14.2 Dust Protection Concept. The CTH hydrocode simulations showed that the instruments, PDU, and bus can be protected against dust impacts by placing a multi-layer insulation (MLI) Whipple shield[4] at a standoff distance of 6 to 10 mm (**Table 4-17**) from the component in question. In all cases, the standoff distance was adequate to ensure that there was no spalling or penetration of the aluminum electronics box or structure. The hydrocode impact simulations were run for an 18-layer MLI blanket consisting of a 1-mil Kapton/vapor-deposited external surface and 18 layers of 0.3-mil embossed Kapton cloth. The aluminum housing of the instrument and PDU boxes was assumed to be 1 mm thick, and each face sheet on the honeycomb structural panels was assumed to be 0.5 mm thick. **Figure 4-32** shows a density plot from a CTH simulation of a particle impact on the MLI shielding protecting the PDU. The PDU is an ideal test case because it has both the largest surface area and the largest critical particle size.

4.14.3 Dust and the Thermal Protection System. The TPS, which will be fabricated of a 40-mil-thick carbon–carbon composite covered with a thin ceramic layer, cannot be shielded from dust impacts. The analysis of the TPS response to the near-Sun dust environment was thus focused on characterizing the effects of dust impacts on TPS performance. Impacts were modeled for dust particles ranging from a minimum particle size of 1 μm to a critical particle size of 670 μm. Empirical estimates for crater size as a function of particle size, impact velocity, obliquity angle, and material properties of the primary shield were used to predict the extent of damage to the primary shield resulting from dust impacts (*McDonnell*, 1999; *Hill*, 2004). A factor of 1.5 was incorporated to account for additional cracking that could occur in the surface beyond the crater. Two different impact scenarios were modeled, the first involving multiple impacts from smaller particles that degrade TPS optical properties, and the second involving a single impact by a very large particle.

Multiple Impact Scenario. A Monte Carlo simulation was run to assess the effect of multiple dust impacts on the TPS, which was modeled as 400 discretized flat panels to obtain a surface degradation profile. Relatively rare impacts by large particles as well as more frequent impacts by smaller particles were analyzed. The maximum area loss was found to be 0.024% on the panels facing in the +X direction (the ram direction at perihelion) (**Figure 4-33**). The area loss decreases to 0.001% toward the –X direction. The average area loss is 0.011% across the entire TPS. The majority of damage resulted from few impacts by large particles rather than from multiple small-particle impacts.

A thermal analysis performed to estimate the increase in the temperature of the primary shield as a function of surface area damage showed that the predicted damage would have a negligible effect on the overall thermal balance (**Figure 4-34**).

Table 4-17. Multilayer insulation standoff distance required to protect representative spacecraft components from dust impact

Component	Required MLI Standoff (mm)
Instruments	6
PDU	10
Spacecraft Bus	20

[3]No experimental data for such high velocity regimes are currently available.

[4] Whipple shielding is a standard method of dust protection and has been used on many missions, including Stardust, Cassini, and New Horizons.

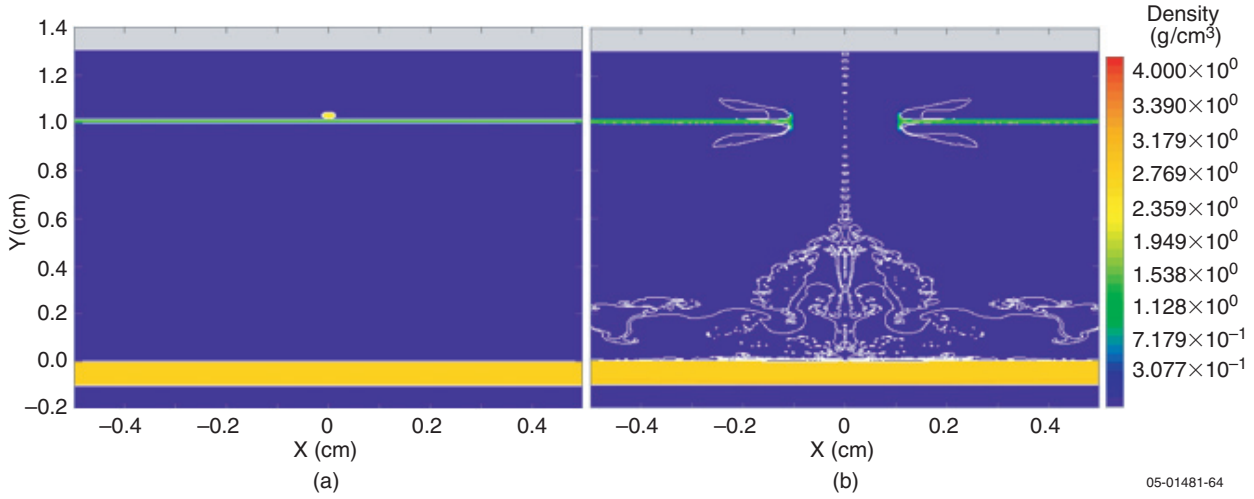

Figure 4-32. Density plots of a 270 micron particle impacting multilayer insulation at 500 km/s with a 10 mm standoff distance. (a) shows the initial state and (b) depicts the state at the end of the simulation.

According to this analysis, the TPS can tolerate almost 10% surface area damage and experience a net temperature increase of only about 50 K. Any small local hot spots are balanced out by the large surface area of the TPS cone and its internal view factor to itself.

Single Impact by Very Large Particle Scenario. A single impact by a very large particle is highly unlikely statistically. The critical particle size calculated for the TPS for a 99% PNI is 670 μm in diameter. In other words, there is only a 1% chance that the TPS could be hit by a particle of this size or larger. CTH simulations indicate such a particle—which is large for a dust particle—would be completely vaporized upon impact with the primary shield and thus would not penetrate the secondary shield. Thus even if the primary shield is penetrated, the energy from the remaining dust and primary shield vapor would be quickly dissipated within the cavernous TPS cone interior, and there would not be a direct light path from the Sun to the spacecraft bus.

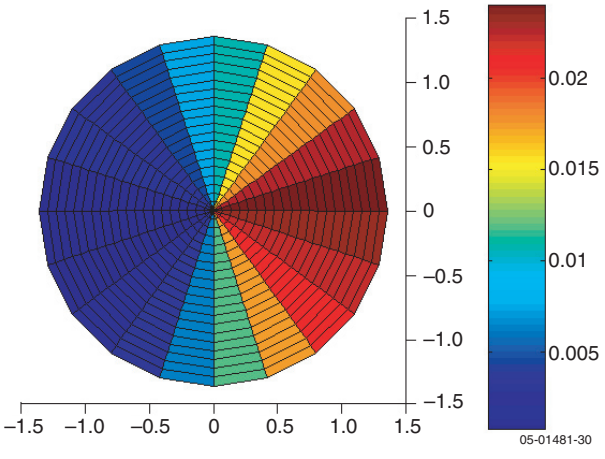

Figure 4-33. Area damage to the Thermal Protection System resulting from dust impacts.

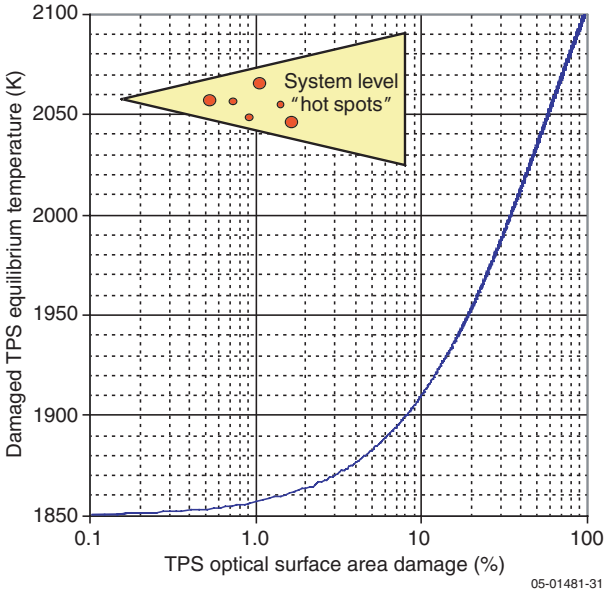

Figure 4-34. Change in the equilibrium temperature of the Thermal Protection System as a function of surface area damaged by dust impact.

The analysis demonstrates that even very large particle impacts would not result in the loss of the Solar Probe spacecraft. This result is in contrast to the Space Shuttle Columbia accident, where damage to that thermal protection system led to mission loss. In the case of the Columbia, once the leading edge of the Columbia's wing was significantly damaged, hot atmospheric gases under high dynamic pressure were forced into the interior of the wing, damaging vulnerable internal spacecraft structures. The situation is quite different for Solar Probe, which will operate in a hard vacuum. Should the TPS be penetrated by a large particle, there would be, in the rarefied plasma environment of the inner heliosphere, no dense, superheated gas to enlarge the hole or damage the spacecraft. As indicated above, even for much larger than predicted surface degradation, the overall temperature will not increase significantly. Solar Probe's TPS fully protects the spacecraft even if damaged by dust.

Blank

Appendix A: References

Abelson, R. D., et al., *Expanding Frontiers with Radioisotope Power Systems*, JPL D-28902, Jet Propulsion Laboratory, Pasadena, CA, Jan. 12, 2005.

Ambrosiano, J., et al., Test particle acceleration in turbulent reconnecting magnetic fields, *J. Geophys. Res.*, **93**, 14,383, 1988.

Armstrong, J. W., and R. Woo, *Contribution to Starprobe Report,* Inter-Office Memorandum no. 3331-80-070, Jet Propulsion Laboratory, Pasadena, CA, Dec. 15, 1980.

Axford, W. I., and McKenzie, J., The origin of high speed solar wind streams, in: *Solar Wind Seven*, ed. E. Marsch and R. Schwenn, p. 1, Pergamon, Tarrytown, N. Y., 1992.

Bemporad, A. et al., UVCS observation of sungrazer C/2001 C2: Possible comet fragmentation and plasma-dust interactions, *Astrophys. J.*, **620**, 523, 2005.

Beyer, P. E., D. J. Mudgway, and M. M. Andrews, The Galileo mission to Jupiter: Interplanetary cruise post-Earth-2 encounter through Jupiter orbit insertion, in *The Telecommunications and Data Acquisition Progress Report 42-125, 1996*, Jet Propulsion Laboratory, Pasadena, CA, p. 1, May 15, 1996.

Bokulic, R. S., and W. V. Moore, Near Earth Asteroid Rendezvous (NEAR) spacecraft solar conjunction experiment, *J. Spacecr. Rockets*, **36(1)**, 87, 1999.

Boslough, M. B., et al., Hypervelocity testing of advanced shielding concepts for spacecraft against impacts to 10 km/s, *Int. J. Impact Eng.,* **14**, 96, 1993.

Buffington, A., Very-wide-angle optical systems suitable for spaceborne photometric measurements, *Appl. Opt.*, **37**, 4284, 1998.

Burns, J. A., P. L. Lamy, and S. Soter, Radiation forces on small particles in the solar system, *Icarus*, **40**, 1, 1979.

Canals, A., et al., Estimating random transverse velocities in the fast solar wind from EISCAT interplanetary scintillation measurements, *Ann. Geophys.*, **20**, 1265, 2002.

Cane, H. V., et al., Two components in major solar particle events, *Geophys. Res. Lett.*, **30(12)**, 8017, DOI 10.1029/2002GL016580, 2003.

Cargill, P. J., and J. A. Klimchuk, Nanoflare heating of the corona revisited, *Astrophys. J.*, **605**, 911, 2004.

Chae, J., U. Schühle, and P. Lemaire, SUMER Measurements of nonthermal motions: Constraints on coronal heating mechanisms, *Astrophys. J.*, **505***,* 957, 1998.

Chae, J., A. I. Poland, and M. J. Aschwanden, Coronal loops heated by magnetohydrodynamic turbulence. I. A model of isobaric quiet Sun loops with constant cross-sections, *Astrophys. J.*, **581**, 726, 2002.

Christiansen, E. L., Design and performance equations for advanced meteoroid and debris shields, *Int. J. Impact Eng.,* **14**, 145, 1993.

Christiansen, E. L., Design practices for spacecraft meteoroid/debris (M/D) protection, *Hypervelocity Shielding Workshop Proceedings*, Institute of Advanced Technology, Catalog No. IAT.MG-0004, University of Texas, Austin, TX, 1999.

Cliver, E. W., et al., Coronal shocks and solar energetic proton events, *Astrophys. J.*, **605**, 902, 2004.

Cohen, C. M. S., et al., New observations of heavy-ion-rich solar particle events from ACE, *Geophys. Res. Lett.*, **26**, 2697, 1999.

Coles, W. A., et al., Comparison of solar wind velocity measurements with a theoretical acceleration model, *J. Geophys. Res.*, **96**, 13,849, 1991.

Collier, M.R., et al., Observations of neutral atoms from the solar wind, *J. Geophys. Res.*, **106**, 24,893, 2001.

Collier, M. R., et al., Dust in the wind: The dust geometric cross section at 1 AU based on neutral solar wind observations, in: *AIP Conference Proceedings 679: Solar Wind Ten*, Proc., Tenth Int. Solar Wind Conf., p. 790, American Institute of Physics, 2003.

Cranmer, S. R., and A. A. van Ballegooijen, On the generation, propagation, and reflection of Alfvén waves from the solar photosphere to the distant heliosphere, *Astrophys. J. Suppl.*, **156**, 265, 2005.

Cummings, A. C., E. C. Stone, and C. D. Steenberg, Composition of anomalous cosmic rays and other heliospheric ions, *Astrophys. J.*, **578**, 194, 2002.

Dalla, S., et al., Observation of decay phases of solar energetic particle events at 1 and 5 AU from the Sun, *J. Geophys. Res.*, **107**, 1370, 2002.

DeForest, C. E., and S. P. Plunkett, Observation of quasi-periodic compressive waves in solar polar plumes, *Astrophys. J.*, **501**, L217, 1998.

DeForest C. E. et al., Observation of polar plumes at high solar altitudes, *Astrophys. J.*, **546**, 569, 2001.

Del Zanna, G., D. Chiuderi, and S. Parenti, SOHO CDS and SUMER observations of quiescent filaments and their interpretation, *Astron. Astrophys.*, **420**, 307, 2004.

Divine, N., and H. Garrett, Charged particle distributions in Jupiter's magnetosphere, *J. Geophys. Res.*, **88**, 6689, 1983.

Elfer, N. C., *Structural Damage Predictions and Analysis for Hypervelocity Impacts – Handbook*, NASA CR-4706, NASA Marshal Space Flight Center, 1996.

Feldman, W. C., et al., Interpenetrating solar wind streams, *Rev. Geophys. Space Phys*, **12**, 715, 1974.

Feldman, W. C., et al., Constraints on high-speed solar wind structure near its coronal base: a ULYSSES perspective, *Astron. Astrophys.*, **316**, 355, 1996.

Feldman, W. C., et al., Experimental constraints on pulsed and steady state models of the solar wind near the Sun, *J. Geophys. Res.*, **102**, 26,905, 1997.

Feynman, J., and S. B. Gabriel, On space weather consequences and prediction, *J. Geophys. Res.*, **105**, 10,543, 2000.

Fisk, L. A., Motion of the footpoints of heliospheric magnetic field lines at the Sun: Implications for recurrent energetic particle events at high heliographic latitudes, *J. Geophys. Res.*, **101**, 15,547, 1996.

Fisk, L. A., Acceleration of the solar wind as a result of the reconnection of open magnetic flux with coronal loops, *J. Geophys. Res.*, **108 (A4)**, SSH 7-1, DOI 10.1029/2002JA009284, 2003.

Fisk, L. A., and N. A. Schwadron, Origin of the solar wind: Theory, *Space Sci. Rev.*, **97**, 221, 2001.

Gabriel, A. H., F. Bely-Dubau, and P. Lemaire, The Contribution of polar plumes to the fast solar wind, *Astrophys. J.*, **589**, 623, 2003.

Geiss. J., G. Gloeckler, and R. v. Steiger, Origin of the solar wind from composition data, *Space Sci. Rev.*, **72**, 49, 1995.

Geiss, J., G. Gloecker, and R. v. Steiger, Origin of C^+ ions in the heliosphere, *Space Sci. Rev.*, **78**, 43, 1996.

Georgoulis, M. K., M. Velli, and G. Einaudi, Statistical properties of magnetic activity in the solar corona, *Astrophys. J.*, **497**, 957, 1998.

Gloeckler, G., and J. Geiss, Interstellar and inner source pickup ions observed with SWICS on Ulysses, *Space Science Rev.*, **86**, 127, 1998.

Gloeckler, G., et al., Sources, injection, and acceleration of heliospheric ion populations, in: *Acceleration and Transport of Energetic Particles Observed in the Heliosphere*, AIP Conference Proceedings **528**, eds. R. A. Mewaldt et al., p. 221, 2000.

Gloeckler, G., and J. Geiss, Heliospheric and interstellar phenomena deduced from pickup ion observations, *Space Science Rev.*, **97**, 169, 2001.

Gloeckler, G., et al., *Solar Probe: First Mission to the Nearest Star, Report of the NASA Science Definition Team for the Solar Probe Mission*, The Johns Hopkins University Applied Physics Laboratory, Laurel, MD, 1999.

Gloeckler, G., T. H. Zurbuchen, and J. Geiss, Implications of the observed anticorrelation between solar wind speed and coronal electron temperature, *J. Geophys. Res.,* **108(A4)**, SSH 8-1, DOI 10.1029/2002JA009286, 2003.

Goldstein, B. E., et al., Observed constraint on proton-proton relative velocities in the solar wind, *Geophys. Res. Lett.*, **27**, 53, 2000.

Gopalswamy, N., et al., Near-Sun and near-Earth manifestations of solar eruptions, *J. Geophys. Res.*, **106**, 25,261, 2001.

Gopalswamy, N., et al., Interacting coronal mass ejections and solar energetic particles, *Astrophys. J.*, **572**, L103–L107, 2002.

Gopalswamy, N., et al., Intensity variation of large solar energetic particle events associated with coronal mass ejections, *J. Geophys. Res.*, **109**, A12105, 2004.

Grall, R. R., et al., Rapid acceleration of the polar solar wind, *Nature*, **379**, 429, 1996.

Grün, E., et al., Collisional balance of the meteoritic complex, *Icarus*, **62**, 244, 1985.

Grün, E., et al., Ulysses dust measurements near Jupiter, *Science,* **257**, 1550, 1992.

Gurnett, D. A., et al., Micron-sized particles detected near Saturn by the Voyager plasma wave instrument, *Icarus*, **53**, 236, 1983.

Gurnett, D. A., et al., Micron-sized particles detected in the outer solar system by the Voyager 1 and 2 plasma wave instruments, *Geophys. Res. Lett*., **24**, 3125, 1997.

Habbal, S. R., et al., Origins of the slow and the ubiquitous fast solar wind, *Astrophys. J.*, **489**, L103, 1997.

Habbal, S. R., et al., On the detection of the signature of silicon nanoparticle dust grains in coronal holes, *Astrophys. J.*, **592**, L87, 2003.

Haggerty, D. K., and E. C. Roelof, Impulsive near-relativistic solar electron events: Delayed injection with respect to solar electromagnetic emission, *Astrophys. J.*, **579**, 841, 2002.

Hansteen, V. H., E. Leer, and T. E. Holzer, The role of helium in the outer solar atmosphere, *Astrophys. J.*, **482**, 498, 1997.

Hassler, D. M., et al., Solar wind outflow and the chromospheric magnetic network, *Science*, **283**, 810, 1999.

Heyvaerts, J., and E. R. Priest, Coronal heating by phase-mixed shear Alfvén waves, *Astron. Astrophys.*, **117**, 220, 1983.

Hill, S. A, Determination of an empirical model for the prediction of penetration hole diameter in thin plates from hypervelocity impact, *Int. J. Impact Eng.,* **30**, 303–321, 2004.

Hollweg, J. V., Hydromagnetic waves in interplanetary space, *Astron. Soc. Pacific*, **86**, 561, 1974.

Hollweg, J. V., Alfvén waves in the solar atmosphere, *Solar Physics*, **56**, 305–333, 1978.

Hollweg, J. V., and P. A. Isenberg, Generation of the fast wind: A review with emphasis on the resonant cyclotron interaction, *J. Geophys. Res.*, **107(A7)**, SSH 12-1, DOI 10.1029/2001JA000270, 2002.

Igenbergs, E., et al., Mars dust counter, *Earth, Planets Space*, **50**, 241–245, 1998.

Ionson, J. A., Resonant absorption of Alfvénic surface waves and the heating of solar coronal loops, *Astrophys. J.*, **226**, 650, 1978.

Isenberg, P. A., The kinetic shell model of coronal heating and acceleration by ion cyclotron waves: 3. The proton halo and dispersive waves, *J. Geophys. Res.,* **109**, DOI:10.1029/2002JA009449, 2004.

Ishimoto, H., Modeling the number density distribution of interplanetary dust on the ecliptic plane within 5 AU of the Sun, *Astron. Astrophys.*, **362**, 1158, 2000.

Jensen, J. R., and R. S. Bokulic, Experimental verification of noncoherent Doppler tracking at the Deep Space Network, *IEEE Trans. Aerospace Electron. Sys,* **36(4)**, 2000.

Jokipii, J. R., and J. Kota, The polar heliospheric magnetic field, *Geophys. Res. Lett.*, **16**, 1, 1989.

Jones, G. H., Possible distortion of the interplanetary magnetic field by the dust trail of Comet 122P/De Vico, *Astrophys. J.*, **597**, L61, 2003.

Kahler, S. W., Injection profiles of solar energetic particles as functions of coronal mass ejection heights, *Astrophys. J.*, **428**, 837–842, 1994.

Kahler, S. W., The correlation between solar energetic particle peak intensities and the speeds of coronal mass ejections: Effects of ambient particle densities and energy spectra, *J. Geophys. Res.*, **106**, 20,947, 2001.

Kahler, S. W., and D. V. Reames, Solar energetic particle production by coronal mass ejection-driven shocks in solar fast-wind regions, *Astrophys. J.*, **584**, 1063, 2003.

Kissel, J., and F. R. Krueger, The organic component in dust from Comet Halley as measured by the PUMA mass spectrometer on board VEGA 1, *Nature*, **326**, 755, 1987.

Kohl, J. L., et al., UVCS/SOHO empirical determinations of the anisotropic velocity distributions in the solar corona, *Astrophys. J.*, **501**, L127, 1998.

Krucker, S., and R. P. Lin, Two classes of solar proton events derived from onset time analysis, *Astrophys. J.*, **542**, L61–L64, 2000.

Krucker, S., et al., Hard x-ray microflares down to 3 keV, *Solar Phys.*, **210**, 445, 2002.

Leamon, R. J., et al., Contribution of cyclotron-resonant damping to kinetic dissipation of interplanetary Turbulence, *Astrophys. J.*, **507**, L181, 1998.

Le Roux, J. A., G. P. Zank, and W. H. Matthaeus, Pickup ion acceleration by turbulent field-aligned electric fields in the slow low-latitude solar wind, *J. Geophys. Res.*, **107**, SSH 9-1, DOI 10.1029/2001JA000285, 2002.

Li, X., et al., The effect of temperature anisotropy on observations of Doppler dimming and pumping in the inner corona, *Astrophys. J.*, **501**, L133, 1998.

Li, G., and G. P. Zank, Mixed particle acceleration at CME-driven shocks and flares, *Geophys. Res. Lett.*, **32**, L02101, 2005.

Longcope, D. W., D. S. Brown, and E. R. Priest, On the distribution of magnetic null points above the solar photosphere, *Phys. Plasmas,* **10**, 3321, 2003.

Love, S. G., and D. E. Brownlee, A direct measurement of the terrestrial mass accretion rate of cosmic dust, *Science*, **262**, 550, 1993.

Mann, I., and E. Murad, On the existence of silicon nanodust near the Sun, *Astrophys. J.*, **624**, L125–L128, 2005.

Mann, I, A. Krivov, and H. Kimura, Dust cloud near the Sun, *Icarus*, **146**, 568, 2000.

Mann, I., and A. Czechowski, Dust destruction and ion formation in the inner solar system, *Astrophys. J.*, **621**, L73, 2005.

Mann, I., et al., Dust near the Sun, *Space Sci. Rev.*, **110**, 269, 2004.

Marsch, E.; et al., Solar wind protons: Three-dimensional velocity distributions and derived plasma parameters measured between 0.3 and 1 AU, *J. Geophys. Res.*, **87**, 52, 1982.

Marsch, E., and C.-Y. Tu, Heating and acceleration of coronal ions interacting with plasma waves through cyclotron and Landau resonance, *J. Geophys. Res.*, **106**, 227, 2001.

Mason, G. M., et al., Impulsive acceleration and scatter-free transport of ~1 MeV per nucleon ions in ^{3}He-rich solar particle events, *Astrophys. J.*, **339**, 529–544, 1989.

Mason, G. M., et al., ^{3}He enhancements in large solar energetic particle events, *Astrophys. J.*, **525**, L133, 1999.

Mason, G. M., et al., Abundances of heavy and ultraheavy ions in ^{3}He-rich solar flares, *Astrophys. J.*, **606**, 555, 2004.

Matthaeus, W. H., and M. L. Goldstein, Low-frequency 1/f noise in the interplanetary magnetic field, *Phys. Rev. Lett.*, **57**, 495, 1986.

Matthaeus, W. H., and S. L. Lamkin, Turbulent magnetic reconnection, *Phys. Fluids*, **29**, 2513, 1986.

Matthaeus, W. H., et al., Coronal heating by magnetohydrodynamic turbulence driven by reflected low-frequency waves, *Astrophys. J.*, **523**, L93, 1999.

McComas, D. J., et al., The three-dimensional solar wind around solar maximum, *Geophys. Res. Lett.,* **30(10)**, 24-1, DOI 10.1029/2003GL017136, 2003.

McDonnell, J. A. M., HVI phenomena: Applications to space missions, *Int. J. Impact Eng.,* **23**, 597, 1999.

McKenzie, D. E., and D. J. Mullan, Periodic modulation of x-ray intensity from coronal loops: Heating by resonant absorption, *Solar Phys.*, **176**, 127, 1997.

McKibben, R. B., C. Lopate, and M. Zhang, Simultaneous observations of solar energetic particle events by IMP 8 and the Ulysses Cospin High Energy Telescope at high solar latitudes, *Space Sci. Rev.*, **97**, 257, 2001.

Mewaldt, R. A., et al., Heavy ion and electron releases time in solar particle events, in: *Proc., 28th Int. Cosmic Ray Conf.*, eds. T. Kajita et al., p. 3313, 2003.

Meyer-Vernet, N., M. G. Aubie, and B. M. Pedersen, Voyager 2 at Uranus: Grain impacts in the ring plane, *Geophys. Res. Lett.*, **13**, 617, 1986.

Miller, J. A., Particle acceleration in impulsive solar flares, *Space Sci. Rev.*, **86**, 79, 1998.

Misconi, N. Y., The spin of cosmic dust: Rotational bursting of circumsolar dust in the F corona, *J. Geophys. Res.*, **98**, 18,951, 1993.

Morabito, D. M., et al., *The 1998 Mars Global Surveyor Solar Corona Experiment, Telecommunications and Mission Operations Progress Report,* TMO PR 42-142, Aug. 15, 2000.

Morabito, D. M., et al., Ka-Band and X-band observations of the solar corona acquired during superior conjunctions using interplanetary spacecraft, *7th Ka Band Utilization Conf.*, Genoa, Italy, Sept. 26–28, 2001.

Morabito, D. M., et al., The Cassini May 2000 solar conjunction, *IEEE Trans. Antennas Propag.*, **51(2)**, 201, 2003.

Murphy, N., E. J. Smith, and N. A. Schwadron, Strongly underwound magnetic fields in corotating interaction regions: Observations and implications, *Geophys. Res. Lett.*, **29(22)**, 23-1, DOI 10.1029/2002GL015164, 2002.

Neubauer, F. M., et al., Hypervelocity dust particle impacts observed by the Giotto magnetometer and plasma experiments, *Geophys. Res. Lett.*, **17**, 1809, 1990.

Neugebauer, M., The quasi-stationary and transient states of the solar wind, *Science*, **252**, 404, 1991.

Neugebauer, M., et al., Sources of the solar wind at solar activity maximum, *J. Geophys. Res.*, **107(A12)**, SSH-13, DOI 10.1029/2001JA000306, 2002.

Noci, G., et al., First results from UVCS/SOHO, *Adv. Space Res.*, **20**, 2219, 1997.

NASA, *Sun-Solar System Connection: Science and Technology Roadmap 2005-2035*, National Aeronautics and Space Administration, August 2005.

NRC, *Radiation Hazards to Crews of Interplanetary Missions: Biological Issues and Research Strategies*, p. 2, National Academy of Sciences, 1996. (This report uses the acronym SPE, for solar particle event, rather than SEP.)

NRC, *The Sun to the Earth—and Beyond: A Decadal Research Strategy in Solar and Space Physics*, National Academy of Sciences, 2003.

Oberc, P., and W. Parzydlo, Impacts of dust particles $m > 10^{-9}$ g in Halley's coma as seen in the electric field waveforms of VEGA 2, *Icarus*, **98**, 195, 1992.

Ofman, L., V. M. Nakariakov, and C. E. DeForest, Slow magnetosonic waves in coronal plumes, *Astrophys. J.*, **514**, 441, 1999.

Ofman, L., et al., Ultraviolet Coronagraph Spectrometer observations of density fluctuations in the solar wind, *Astrophys. J.*, **491**, L111, 1997.

Ofman, L., et al., UVCS WLC observations of compressional waves in the south polar coronal hole, *Astrophys. J.*, **529**, 592, 2000.

Parker, E. N, Dynamics of the interplanetary gas and magnetic fields, *Astrophys. J.*, **128**, 644, 1958.

Parker, E. N., Nanoflares and the solar x-ray corona, *Astrophys. J.*, **330**, 474, 1988.

Parsons, J. L., and L. W. Townsend, Interplanetary crew dose rates for the August 1972 solar particle event, *Radiation Res.,* **153**, 729, 2000.

Ragot. B. R., and S. W. Kahler, Interactions of dust grains with coronal mass ejections and solar cycle variations of the F-corona brightness, *Astrophys. J.*, **594**, 1049, 2003.

Raymond, J. C., et al., Solar Wind at 6.8 Solar Radii from UVCS Observation of Comet C/1996Y1, *Astrophys. J.*, **508**, 410, 1998.

Reames, D. V., Particle acceleration in the Sun and the heliosphere, *Space Sci. Rev.*, **90**, 413, 1999.

Reames, D. V., and C. K. Ng, Streaming-limited intensities of solar energetic particles, *Astrophys. J.*, **504**, 1002, 1998.

Reames, D. V., and C. K. Ng, Heavy element abundances in solar energetic particle events, *Astrophys. J.*, **610**, 510, 2004.

Sasaki, S. et al., Observation of interplanetary and interstellar dust particles by Mars Dust Counter (MDC) on board NOZOMI, *Adv. Space Res.*, **29**, 1145, 2002.

Schrijver, C., et al., Sustaining the quiet photospheric network: The balance of flux emergence, fragmentation, merging, and cancellation, *Astrophys. J.*, **487**, 424, 1997.

Schwadron, N. A., and D. J. McComas, Solar wind scaling law, *Astrophys. J.*, **599**, 1395, 2003.

Schwadron, N. A., An explanation for strongly underwound magnetic field in co-rotating rarefaction regions and its relationship to footpoint motion on the sun, *Geophys. Res. Lett.*, **29(14)**, DOI 10.1029/2002GL015028, 8-1, 2002.

Scudder, J. D., Ion and electron suprathermal tail strengths in the transition region: Support for the velocity filtration model of the corona, *Astrophys. J.*, **427**, 446, 1994.

Sello, S., Solar cycle activity: a preliminary prediction for cycle #24, *Astron. Astrophys.*, **410**, 691, 2003.

Sheeley, N. R., Jr., et al., Measurements of flow speeds in the corona between 2 and 30 R_S, *Astrophys. J.*, **484**, 472, 1997.

Singh, J., et al., Existence of nanoparticle dust grains in the inner solar corona? *Astrophys. J.*, **608**, L69, 2004.

Sittler, E. C., and M. Guhathakurta, Semiempirical two-dimensional magnetohydrodynamic model of the solar corona and interplanetary medium, *Astrophys. J.*, **523**, 812, 1999.

Sittler, E. C., and M. Guhathakurta, Erratum: "Semiempirical two-dimensional magnetohydrodynamic model of the solar corona and interplanetary medium," *Astrophys. J.*, **564**, 1062, 2002.

Smith, E. J., The heliospheric current sheet, *J. Geophys. Res.*, **106**, 15,819, 2001.

Sokolov, I. V., et al., A new field line advection model for solar particle acceleration, *Astrophys. J.*, **616**, L171, 2004.

Sterling, A. C., Solar spicules: A review of recent models and targets for future observations, *Solar Phys.*, **196**, 79, 2000.

Teriaca, L., et al., The nascent solar wind: Origin and acceleration, *Astrophys. J.*, **688**, 566, 2003.

Thomson, D. J., C. G., Maclennan, and L. J. Lanzerotti, Propagation of solar oscillations through the interplanetary medium, *Nature*, **376**, 139, 1995.

Title, A. M., An innovative imaging package for a near-Sun flyby mission, in: *Solar Probe Instrument Research Results*, ed. J. E. Randolph, NASA Publication JPL D-18137, 1999.

Tsurutani, B. T., et al., Dust impacts at Comet P/Borrelly, *Geophys. Res. Lett.*, **30**, SSC 1-1, 2134, 2003.

Tu, C.-Y., E. Marsch, and Z.-R. Qin, Dependence of the proton beam drift velocity on the proton core plasma beta in the solar wind, *J. Geophys. Res.*, **109**, A05101 DOI 10.1029/2004JA010391, 2004.

Tylka, A. J., et al., Shock geometry, seed populations, and the origin of variable elemental composition at high energies in large gradual solar particle events, *Astrophys. J.*, **625**, 474-495, 2005.

Velli, M., On the propagation of ideal, linear Alfvén waves in radially stratified stellar atmospheres and winds, *Astron. Astrophys.*, **270**, 304, 1993.

v. Steiger, R., et al., Composition of quasi-stationary solar wind flows from Ulysses/Solar Wind Ion Composition Spectrometer, *J. Geophys. Res.*, **105**, 27,217, 2000.

Wang, Y.-M., et al., Solar wind stream interactions and the wind speed-expansion factor relationship, *Astrophys. J.*, **488**, L51, 1997.

Webster, J., *Magellan Spacecraft Performance During Solar Conjunction,* Inter-Office Memorandum no. 3395-94-44, Jet Propulsion Laboratory, Pasadena, CA, Aug. 4, 1994.

Wilhelm, K., et al., The solar corona above polar coronal holes as seen by SUMER on SOHO, *Astrophys. J.*, **500**, 1023, 1998.

Wimmer-Schweingruber, R. F., and P. Bochseler, On the origin of inner-source pickup ions, *Geophys. Res. Lett.*, **30(2)**, 49-1, DOI 10.1029/2002GL015218, 2003.

Withbroe, G. L., and R. W. Noyes, Mass and energy flow in the solar chromosphere and corona, *Ann. Rev. Astron. Astrophys.*, **15**, 363, 1977.

Witt, A. N., K. D. Gordon, and D. G. Furton, Silicon nanoparticles: Source of extended red emission? *Astrophys. J.*, **501**, L111, 1998.

Xapsos, M. A., et al., New techniques for predicting solar proton fluences for radiation effects applications, *IEEE Trans. Nucl. Sci.,* **43(6)**, 2772, 1996.

Yamauchi, Y, et al., The magnetic structure of Hα macrospicules in solar coronal holes, *Astrophys. J.*, **605**, 511, 2004.

Zank, G. P., et al., Particle acceleration and coronal mass ejection driven shocks: A theoretical model, *J. Geophys. Res.,* **105**, 25,079, 2000.

Zubko, V. G., T. L. Smith, and A. N. Witt, Silicon nanoparticles and interstellar extinction, *Astrophys. J.*, **511**, L57, 1999.

Zurbuchen, T. H., et al., The solar wind composition throughout the solar cycle: A continuum of dynamic states, *Geophys. Res. Lett.*, **29(9)**, 66-1, DOI 10.1029/2001GL013946, 2002.

Appendix B: Dust Protection

Methodology

The approach used to asses the risk and to design dust shielding systems for the spacecraft was briefly described in Section 4.14. The flow-diagram in Figure 4-31 of the main text (repeated here for convenience as **Figure B-1**) illustrates the procedure followed to design shielding concepts and/or analyze risk for exposed components. The following is a detailed description of this diagram:

① The first step in the risk assessment process was the characterization of the dust environment, which was discussed in Section 4.3.5.

② Once the dust environment was defined, the next step was to characterize the dust impacts to individual components of the spacecraft. To accomplish this, a software tool was developed to numerically integrate the dust flux over time on individual components of the spacecraft as it orbits the Sun. Components having curved or box shapes were analyzed by discretizing the surface into flat panels. The total cumulative number of impacts was then calculated as the sum of the flux integral on the individual panels. This software tool calculated total cumulative number of impacts as a function of particle mass as well as histograms of relative impact speeds and obliquity angles.

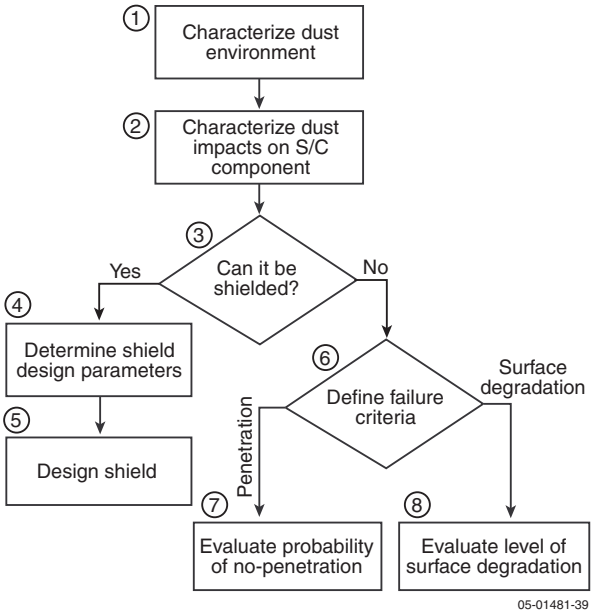

Figure B-1. Methodology employed in the dusk risk/protection study.

③ The next step was to make a distinction between those components that can be protected by some type of shielding system (i.e., instrument boxes, bus, harnessing, etc.) and those that by their functionality can not be protected (i.e., instrument apertures, Thermal Protection System (TPS), radiating surfaces, etc).

④ For those components that can be protected by incorporating a shielding structure, the next step was to define shield design parameters. These parameters are the critical particle size, impact speed, and obliquity angle and are indirectly defined by the selection of an acceptable probability of no-penetration (PNP). This step was done using two different approaches. The first was to select the worst-case speed and obliquity conditions. This approach led to a conservative set of design parameters but allowed us to bound the problem in the critical direction. The second approach was to select the design parameters using a statistical procedure that considers the statistical distribution of mass, speed, and obliquity of dust particles as well as their lethality/damage potential. This approach was less conservative but was based on robust statistical theories and thus should be considered more accurate than the worst-case approach.

For the worst-case approach, the design parameters selected were an impact speed of 500 km/s and an obliquity angle of zero. The particle size for both approaches was selected using a probability of no impact (PNI) of 99% (see equation (2)).

For the second approach, the selection of the design parameters was based on the assumption that the penetration potential of dust particles impacting a shield is directly proportional to the kinetic energy associated with the normal component of their relative velocity vector (*Christiansen,* 1993). Thus, the selection of design parameters reduces to the selection of a critical dust-particle kinetic-energy (K_c) that has a probability of occurrence equal to 1 – PNP (1% was used in this study). The probability of having n impact events of a particle with a kinetic energy equal to K_c or larger is assumed to follow a discrete Poisson's distribution and is defined as

$$P(K_c,n) = \frac{[N_T(K_c)]^n}{n!} e^{-N_T(K_c)}, \qquad (1)$$

where $P(K_c,n)$ is the probability of having n impact events with a kinetic energy equal to K_c or larger, N_T

is the cumulative number of impacts as a function of kinetic energy, and $N_T(K_c)$ is the total cumulative number of impacts of the critical kinetic energy, K_c. The probability for $n = 0$, defined as the probability of no-impact, is defined as

$$\mathrm{PNI}(K_c) = e^{-N_T(K_c)}. \tag{2}$$

Then, the critical dust-particle kinetic-energy K_c is that with a cumulative number of occurrences defined by

$$N_T(K_c) = -\ln(\mathrm{PNP}), \tag{3}$$

where the PNI has been substituted by the desired PNP.

The cumulative number of impacts as a function of kinetic energy N_T was calculated by running a Monte Carlo simulation and sampling pairs of "particle mass" and "normal impact speed" from the cumulative number of impacts and from the histogram of normal impact speeds calculated in step 2. Then, K_c was calculated using equation (3). The next step was to select a pair of critical particle mass (m_c) and critical normal impact speed (V_c) that yielded the desired K_c. First, m_c was defined by using the cumulative number of impacts as a function of mass and selecting a particle mass with a probability of no-impact equal to the PNP. Then, V_c was calculated to yield the critical kinetic energy K_c. It should be noted that the selection of m_c is arbitrary, and any other pair (m_c, V_c) that yields the critical K_c would be acceptable under the assumption that damage potential is proportional to kinetic energy.

⑤ Once the pair (m_c, V_c) was defined, the shield was designed so that a particle with the critical parameters did not penetrate or spall the shield. The design of the shield was based entirely on computer simulations in CTH.

⑥ For those components that cannot be protected by a shielding system, the next step in the risk assessment process was to define a failure criterion. Two types of failure criteria are relevant to Solar Probe: penetration of the components or surface degradation.

⑦ Components for which penetration would constitute failure can be evaluated in terms of their probability of penetration. For Solar Probe the instrument apertures need to be evaluated under this failure criterion, but this is not yet possible, given that there are no detailed instrument designs in this study.

⑧ The TPS is the primary Solar Probe component that was analyzed to determine the degradation of the surface caused by dust particle impacts. The TPS surface degradation was evaluated by running a Monte Carlo simulation of size equal to the total number of impacts and sampling sets of dust particle mass, impact speed, and obliquity angle to calculate the total surface area loss due to penetration and cratering. For each sample point, the diameter of the penetration hole was calculated using the following equation (*McDonnell,* 1999):

$$\frac{d_P}{f} = A\left(\frac{10}{9+\exp[(D_h/(B\cdot f)]}\right) + \frac{D_h}{f}\{1-\exp[-D_h/(B\cdot f)]\}], \tag{4a}$$

$$A = 6.97\left(\frac{V\rho_P}{\sqrt{\sigma_t\rho_t}}\right)^{-0.723}\left(\frac{\sigma_t}{\sigma_{Al}}\right)^{-0.217} f^{-0.053}, \tag{4b}$$

$$B = B_1 + B_2 V, \tag{4c}$$

where d_p is the dust particle diameter, f is the thickness of the C–C shield, D_h is the hole diameter, B_1 and B_2 are material parameters, ρ_p and ρ_t are the mass density of the dust particle and the C–C shield, σ_t and σ_{Al} are the yield stress of the C–C shield and aluminum, and V is the relative impact speed. The equations developed by McDonnell are only applicable to normal impacts. For oblique impacts the major and minor axis of the penetration hole was calculated as follows (*Hill,* 2004):

$$D_h^{\mathrm{maj}} = D_h e^{1.064\theta}, \tag{5a}$$

$$D_h^{\mathrm{min}} = D_h(\cos\theta)^{0.283}, \tag{5b}$$

where θ is the impact obliquity angle. The minimum D_h for every sample was set to 10 times the particle diameter to account for cratering in the cases where no penetration occurs. In addition, the D_h calculated with equations (4) and (5) was multiplied by 1.5 to account for possible cracking of the coating on the TPS beyond the crater or penetration hole.

Comparison of Shield Design Parameters Using Kinetic Energy to Worst-Case Velocity and Obliquity

As described in step 4 of the preceding section, two approaches were followed for the selection of shielding design parameters. **Table B-1** shows a comparison of the 1% kinetic energy case to the worst-case velocity of 500 km/s and obliquity assuming a particle density of 2.5 g/cm^3. The results show a significant level of conservatism for the worst-case velocity against a 1% probability kinetic energy case for all components analyzed. The level of conservatism measured as the ratio of the kinetic energy of the worst case to the 1% kinetic energy case is as high as 16.9 for the power distribution unit (PDU) and the lowest is 5.8 for the spacecraft bus.

Dust Impact Characterization on Bus Panels

As already discussed in Section 4.14.1, it is important to note that since no detailed instrument designs were available as a part of this study, the vulnerability of instrument apertures to impacts was not analyzed. However, to provide instrument designers with a tool to estimate dust impacts on instrument apertures, a characterization of the dust impacts on the bus panels per unit area was conducted. **Figure B-2** shows the cumulative number of impacts per square centimeter for all six panels of the bus as identified in the inset diagram.

These plots can be used by instrument designers to estimate the expected number of impacts and critical particle size for any given instrument aperture depending on surface area and its location on the bus. Panels 1 and 6 are expected to receive the largest number of impacts, while panels 3 and 4 will receive the fewest number of impacts. To complement the cumulative number of impacts plot, the following histogram plots (**Figures B-3 to B-8**) show the distribution of impacts as a function of impact speed and obliquity angle. The vertical axis on these histograms does not represent the actual number of impacts on the panels and thus is intended only to show the distribution and relative comparison of number of impacts between panels. Panels 1, 5, and 6 will receive a large number of impacts over a wide range of impact speeds, but they mostly occur at obliquities larger than 40º. Panel 2 also will receive a large number of impacts but mostly at the low end of the velocity range (10 to 100 km/s) and in the medium obliquity angles (40º to 60º). Panels 3 and 4 will receive a low number of impacts at the low end of the velocity range (10 to 200 km/s) and at high obliquities (>60º).

Table B-1. Comparison of 1% kinetic energy case to worst-case velocity and obliquity assumptions

Component	Critical Particle Diameter (μm)	1% Probability Kinetic Energy		Maximum Velocity		Conservatism (Ratio)
		Impact Speed (km/s)	Kinetic Energy (J)	Impact Speed (km/s)	Kinetic Energy (J)	
Fast Electron Analyzer (FEA)	132	152	34	500	376	11.0
Fast Ion Anayzer (FIA)	132	152	34	500	376	11.0
Ion Composution Analyzer (ICA)	148	178	67	500	530	7.9
Power Distribution Unit (PDU)	266	122	182	500	3,079	16.9
Spacecraft Bus	437	208	2358	500	13,655	5.8

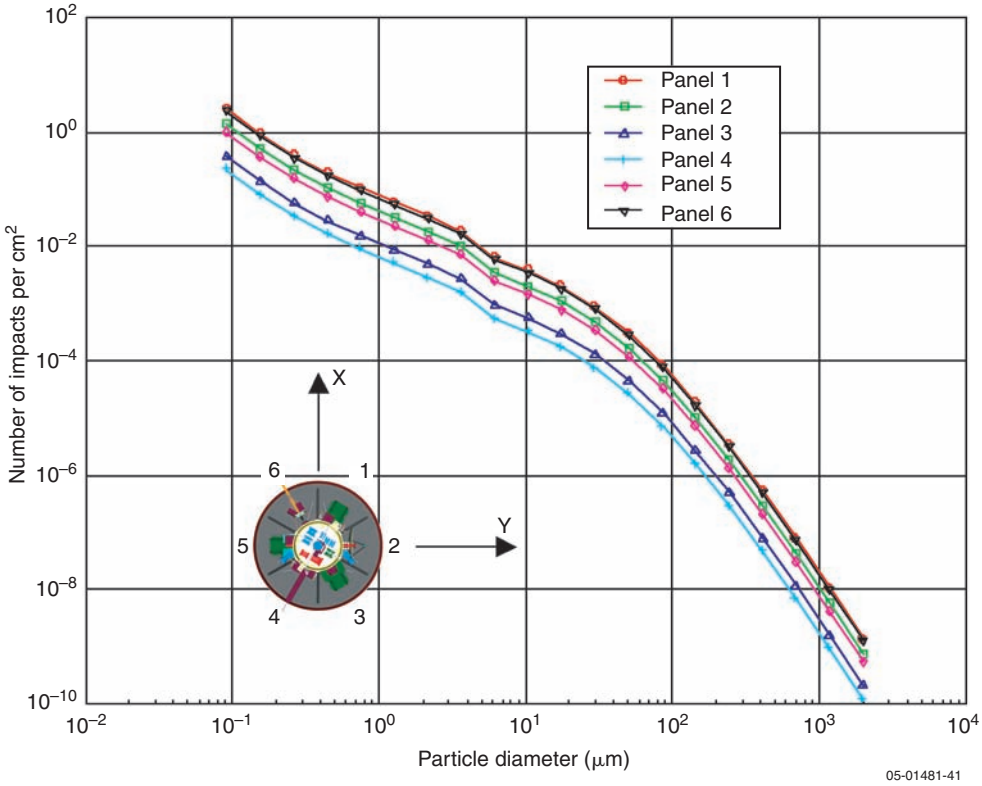

Figure B-2. Cumulative number of impacts per square centimeter on bus panels calculated with dust model without collisions.

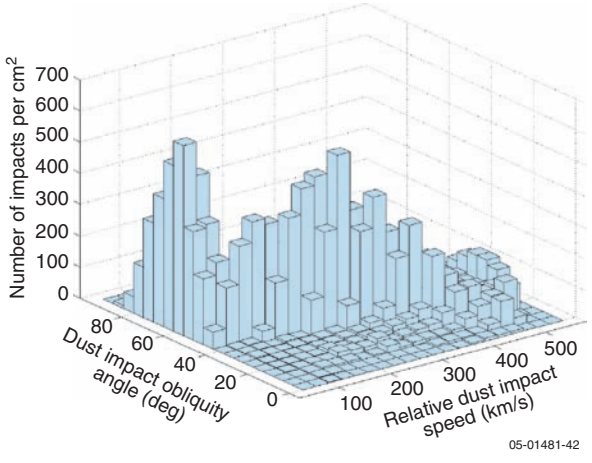

Figure B-3. Histogram of the number of impacts as a function of impact speed and obliquity angle for panel 1.

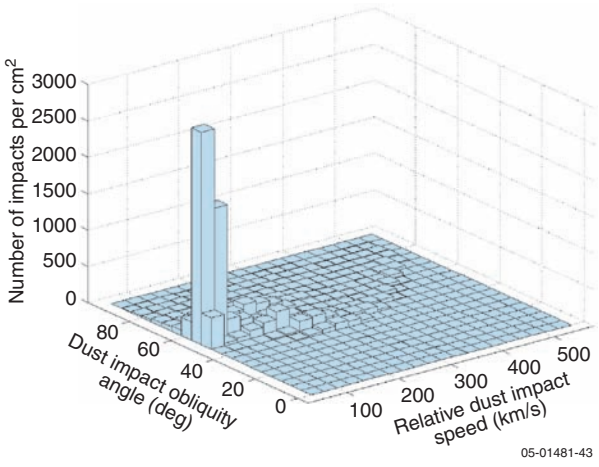

Figure B-4. Histogram of the number of impacts as a function of impact speed and obliquity angle for panel 2.

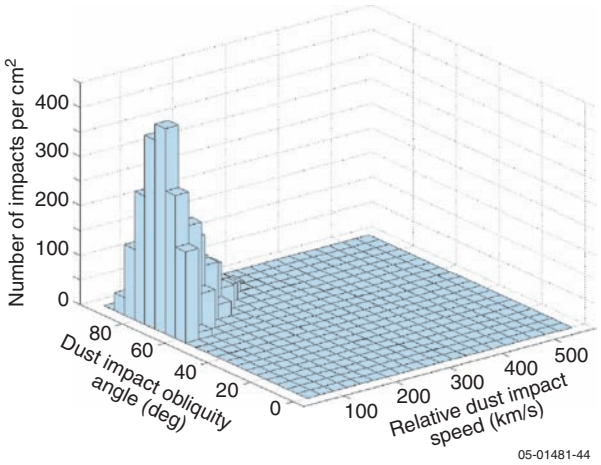

Figure B-5. Histogram of the number of impacts as a function of impact speed and obliquity angle for panel 3.

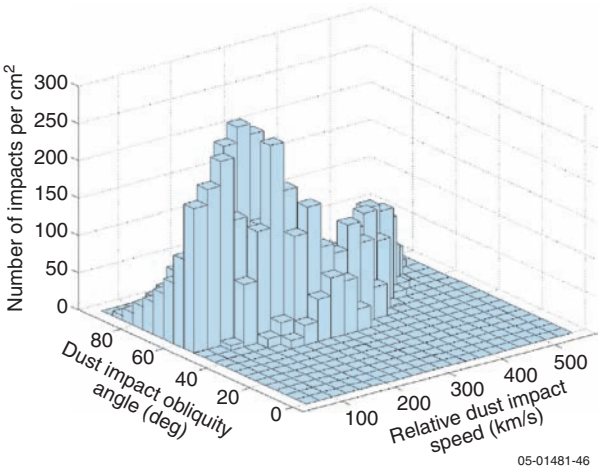

Figure B-7. Histogram of the number of impacts as a function of impact speed and obliquity angle for panel 5.

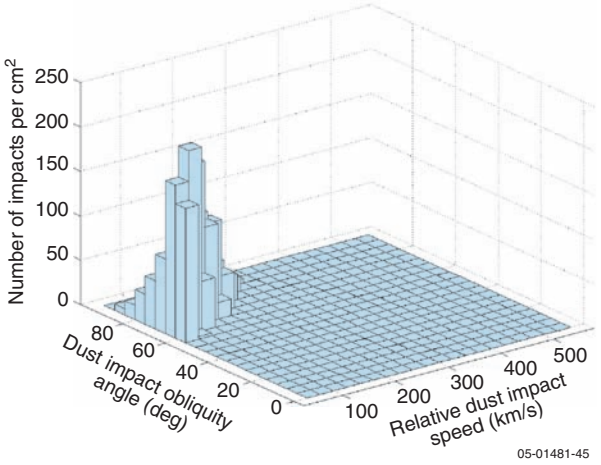

Figure B-6. Histogram of the number of impacts as a function of impact speed and obliquity angle for panel 4.

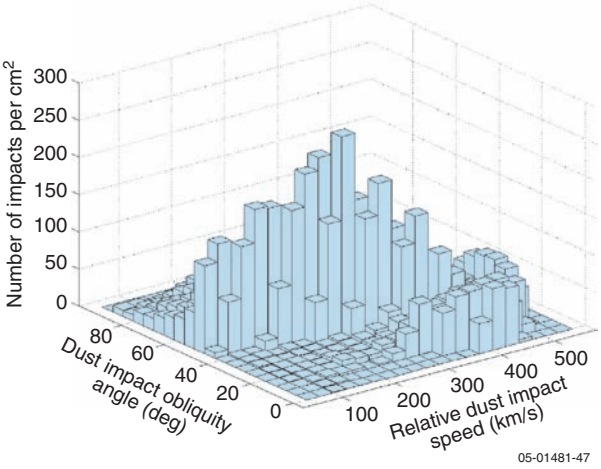

Figure B-8. Histogram of the number of impacts as a function of impact speed and obliquity angle for panel 6.

Blank

Appendix C:

Solar Probe Mass and Power Budgets

Solar Probe Mass Budget (1 of 4)

Name	Qty.	CBE Mass Each (kg)	CBE Mass Total (kg)	Basis for Estimate
Instruments				
Instrument Total			**51.7**	
Hemispheric Imager (HI)	1	1.5	1.5	Provided by STDT
Polar Source Region Imager (PSRI)	1	3.5	3.5	Provided by STDT
Fast Ion Analyzer (FIA)	1	2.8	2.8	Provided by STDT
Fast Electron Analyzer (FEA)	2	2.5	5.0	Provided by STDT
Ion Composition Analyzer (ICA)	1	7.0	7.0	Provided by STDT
Plasma Wave Electronics Box	1	5.0	5.0	Provided by STDT
Plasma Wave Preaamp	3	0.4	1.2	Provided by STDT
Search Coils	3	0.6	1.8	Provided by STDT
Magnetometer (MAG)	1	2.5	2.5	Provided by STDT
Energetic Particle Inst. High Energy (EPI-Hi)	1	2.7	2.7	Provided by STDT
Energetic Particle Inst Low Energy (EPI-Lo)	1	1.4	1.4	Provided by STDT
Neutron & Gamma Rays (NGS)	1	2.0	2.0	Provided by STDT
Coronal Dust Detector (CD)	1	1.5	1.5	Provided by STDT
Common Data Processing Unit (DPU)	1	10.8	10.8	Provided by STDT
Instrument Harnessing	1	3.0	3.0	Conceptual JHU/APL estimate
Spacecraft Provided Instrument Accommodation Harware				
Spacecraft Provided Instrument Accommodation Total			**18.6**	
Fast Plasma Instrument Suite (PWI) Actuator/Arm	1	7.2	7.2	JHU/APL concept estimate
Plasma Wave Antenna, Actuator. and Dep Mech.	3	1.5	4.5	JHU/APL concept estimate
Science Boom (MAG, Search coils)	1	2.0	2.0	Estimate based on Northrup-Grumman Bi-Stem Boom 2.1 m length
PSRI Periscope	1	4.9	4.9	JHU/APL concept estimate
Spacecraft				
Spacecraft Total			**542.5**	
Telecommunications				
Telecommunications Total			**21.6**	
High Gain Antenna (HGA)	1	3.8	3.8	0.8 m antenna. Includes horn feed and dichroic subreflector
HGA Actuator	2	2.0	4.0	Estimate based on Moog Rotary Actuator Type 3, catalog data
High Gain Arms	1	0.7	0.7	JHU/APL structures estimate
HGA Actuator Electronics	1	1.0	1.0	Moog ECU, catalog data

Solar Probe Mass Budget (2 of 4)

Name	Qty.	CBE Mass Each (kg)	CBE Mass Total (kg)	Basis for Estimate
Medium Gain Antenna (MGA)	1	0.4	0.4	JHU/APL RF system estimate. Attaches to HGA assembly
Medium Gain Antenna Bracket	1	0.3	0.3	Structural estimate
K-Band SSPA Module	1	0.9	0.9	All K-Band Hardware. Mounted on HGA assembly
HGA Assembly Separation System	1	2.5	2.5	Based on STEREO heritage
Low Gain Antenna (LGA) Assembly	2	0.7	1.3	STEREO heritage, Includes brackets and hardware
RF Plate	1	0.8	0.8	Estimate from STEREO
RF Plate Components (X-Band)	1	0.7	0.7	Includes all X-band hardware (switches, hybrid, RF controller, etc.)
Ultra Stable Oscillator (USO)	2	1.3	2.6	Estimated from New Horizons (Pluto mission)
Coax/Waveguide	1	2.6	2.6	JHU/APL RF system conceptual estimate
Guidance and Control (G&C)				
		G&C Total	**38.1**	
Inertial Measurement Unit (IMU)	1	6.6	6.6	Litton
Reaction Wheel Assembly (RWA)	4	4.8	19.2	Teldix - STEREO wheels
Reaction Wheel Brackets	4	0.3	1.2	Based on STEREO
RWA Metglass Shielding	4	0.3	1.2	Based on STEREO
Star Tracker	2	3.0	6.0	SODERN, SED-16
Star Tracker Brackets	2	0.5	1.0	Based on NEAR/MESSENGER
Sun Sensor Heads	2	0.3	0.6	Estimate based on Adcole digital solar aspect detectors (DSADs)
Sun Sensor Electronics	1	1.1	1.1	Estimate based on Adcole DSADs
Sun Sensor Head Brackets	2	0.1	0.2	Based on STEREO
Solar Horizon Sensor (SHS)	1	1.0	1.0	JHU/APL conceptual estimate
Power				
		Power Total	**149.1**	
Radioisotope Thermoelectric Generator (RTG)	3	42.0	126.0	Based on January 2005 data from Boeing. Removed cooling tubes 1.5 kg
Shunts	2	0.9	1.8	Based on New Horizons
Power System Electronics (PSE)	1	7.8	7.8	Combined New Horizons SRU reduced cap bank + battery control elect.
Battery	1	2.5	2.5	Based on SAFT V34570 D, 4.6 A-h
Power Distribution Unit (PDU)	1	11.0	11.0	Based on MESSENGER - AIU functionality removed

Solar Probe Mass Budget (3 of 4)

Name	Qty.	CBE Mass Each (kg)	CBE Mass Total (kg)	Basis for Estimate
Thermal Protection System (TPS)				
		TPS Total	**133.8**	
Primary Shield	1	52.7	52.7	2.72 m dia, CC density 1.6, CC thickness 40 mil, coating thick 5 mil, 3.4 dens.
Secondary Shield Thermal Insulation	1	55.9	55.9	20 cm of insulation, 0.05 density
Secondary Shield Structure	2	7.5	15.0	30 mil face sheets of carbon-carbon, 1.6 density
Primary TPS Support Struts	6	0.8	4.8	Structures estimate
Launch TPS Support Struts	6	0.9	5.4	Structures estimate
Thermal Control				
		Thermal Control Total	**15.7**	
Multi Layer Insulation (MLI)	1	10.0	10.0	Conceptual estimate, surface area x 0.2 lb/ft^2 (16000 in^2 area)
Radiators	1	0.3	0.3	Estimated based on previous programs
Heater/Thermistor Harness	1	2.5	2.5	Placeholder, scaled from STEREO
Diode Heat Pipe	1	0.9	0.9	Estimated from MESSENGER
Doublers, Gaskets, etc.	1	2.0	2.0	Estimated based on previous programs
Avionics				
		Avionics Total	**20.4**	
Attitude Interface Unit (AIU)	1	2.2	2.2	APL SEE estimate based on 4-in. slice concept no processor
Integrated Electronics Module (IEM)	2	8.4	16.8	APL SEE conceptual estimate (evolution from current designs)
Temperature Remote Input/Output (TRIO) units	14	0.1	1.4	CONTOUR/MESSENGER/STEREO heritage
Propulsion				
		Propulsion Total	**26.2**	
Hydrazine Tank	1	10.8	10.8	PSI P/N 80409-1, Centaur Upper Stage heritage
Hydrazine Tank Supports	1	3.0	3.0	Propulsion estimate
Propulsion Plumbing	1	2.2	2.2	JHU/APL Propulsion System Estimate/Pluto heritage
Thruster Reaction Engine Modules (REMs)	12	0.6	7.2	Based on STEREO REM estimates
Filter	1	0.2	0.2	Vacco P/N FOD10635, CONTOUR/Pluto heritage
Latch Valves	2	0.3	0.6	Vacco P/N V1E10747, CONTOUR/Pluto heritage
Pressure Transducers	2	0.2	0.4	Paine P/N 213-76-260-02, CONTOUR/Pluto heritage
Electrical Connectors	12	0.0	0.3	JHU/APL propulsion system estimate
Propulsion Harness	1	1.3	1.3	JHU/APL propulsion system estimate
Fill and Drain Valves	2	0.1	0.2	Vacco P/N V1E10433, CONTOUR/Pluto heritage

Solar Probe Mass Budget (4 of 4)

Name	Qty.	CBE Mass Each (kg)	CBE Mass Total (kg)	Basis for Estimate
Mechanical				
Mechanical Total			**108.3**	
Propulsion Deck	1	4.9	4.9	Structures estimate
Equipment Deck	1	6.5	6.5	Structures estimate
Bottom Deck	1	2.1	2.1	Structures estimate
Hexagonal Panels	6	3.1	18.6	Structures estimate
8 Angled Panels	1	11.2	11.2	Structures estimate
Strut Fittings	12	0.4	4.8	Estimated as aluminum 2-in. cube
RTG Support Structure	1	21.4	21.4	From Pro E model
G10 Isolators	2	1.6	3.2	140 in^3, 2 in. thick, 0.055 density 75% hogged out
Miscillaneous Secondary Structure	1	3.0	3.0	Estimate for covers, vents, additional brackets, purge gas manifold
Spacecraft Balance Mass	1	10.0	10.0	Estimate from experience on previous programs
Fasteners	1	4.0	4.0	Estimate from experience on previous programs
Launch Vehicle Adapter Ring	1	11.3	11.3	Structures estimate
Dust Protection Mass Allocation	1	7.3	7.3	Based on New Horizons (MLI spacers)
Harness				
Harness Total			**29.3**	
Main Harness	1	24.0	24.0	5% Spacecraft dry mass minus TPS
1553 Harness	2	0.9	1.8	Based on STEREO
Ord.,Prop.,Flight Test Plugs	1	1.0	1.0	Based on STEREO
TBU, ADU, RFDU, etc	1	2.0	2.0	Based on STEREO
Grounding Straps	1	0.5	0.5	Based on STEREO
Observatory				
Obsrvatory Dry Mass Total			**612.8**	
Propellant				
Propellant Total			**59.4**	
Useable Propellant			57.6	Based on 150 m/s total ΔV includes ACS. 30% dry growth margin
Residual Propellant			1.2	Estimated for Centaur tank
Pressurant			0.6	Estimated for Centaur tank
Observatory Wet Mass Total			**672.2**	
Launch Mass with 30% Growth Margin			**856.0**	
Dry Mass Margin (kg)			**183.8**	

Solar Probe Power Budget

Subsystem/Component	Average EOL Power (W)	During Encounter Duty Cycle	Avg. Power (W)	Peak Power (W)	Basis for Estimate
Instruments	**57.2**		**53.2**	**57.2**	
Hemispheric Imager (HI)	4.0	50%	2.0	4.0	Provided by STDT
PSRI	4.0	50%	2.0	4.0	Provided by STDT
FIA	3.7	100%	3.7	3.7	Provided by STDT
FEA x 2	7.2	100%	7.2	7.2	Provided by STDT
ICA	6.0	100%	6.0	6.0	Provided by STDT
PWI	5.0	100%	5.0	5.0	Provided by STDT
MAG	2.5	100%	2.5	2.5	Provided by STDT
EPI-Lo	2.3	100%	2.3	2.3	Provided by STDT
EPI-Hi	1.7	100%	1.7	1.7	Provided by STDT
NGS	3.0	100%	3.0	3.0	Provided by STDT
CD	3.8	100%	3.8	3.8	Provided by STDT
Common DPU	14.0	100%	14.0	14.0	Provided by STDT
Inst. Accommodation Hardware	**16.0**		**1.6**	**16.0**	
Fast Plasma Arm	5.0	10%	0.5	5.0	Conceptual estimate based on available actuators
PSRI Periscope	5.0	10%	0.5	5.0	Conceptual estimate based on available actuators
PWI Actuators x 3	6.0	10%	0.6	6.0	Conceptual estimate based on available actuators
Spacecraft Total	**229.9**		**176.4**	**229.9**	
Power Subsystem	**13.0**	100%	**13.0**	**13.0**	
PDU	7.0	100%	7.0	7.0	JHU/APL conceptual estimate
PSE	4.0	100%	4.0	4.0	JHU/APL conceptual estimate
Battery Charge	2.0	100%	2.0	2.0	JHU/APL conceptual estimate
G&C Subsystem	**73.8**	91%	**66.8**	**73.8**	
IMU	29.5	100%	29.5	29.5	Based on MESSENGER experience
RWAs (4)	28.0	75%	21.0	28.0	Based on STEREO and MESSENGER experience
Star Trackers (2)	16.0	100%	16.0	16.0	Based on STEREO and MESSENGER experience
SHS	0.3	100%	0.3	0.3	JHU/APL conceptual estimate
Propulsion Subsystem	**46.3**	29%	**13.3**	**46.3**	
Thrusters (4 firing)	33.0	0%	0.0	33.0	Based on MR-111C
Cat Bed Heaters (6 active)	11.5	100%	11.5	11.5	Based on MR-111C
Pressure Transducers (2)	1.8	100%	1.8	1.8	Based on MESSENGER/STEREO experience
RF Subsystem	**38.6**	65%	**25.1**	**38.6**	
Transmitter	20.0	100%	20.0	20.0	JHU/APL conceptual estimate
Ka-Converter	1.1	100%	1.1	1.1	JHU/APL conceptual estimate
HGA Actuators	15.0	10%	1.5	15.0	Based on Moog Type 3 actuator
USOs	2.5	100%	2.5	2.5	Based on New Horizons
Avionics Subsystem	**58.2**	100%	**58.2**	**58.2**	
IEM 1	34.0	100%	34.0	34.0	JHU/APL estimate new layout based on MESSENGER
IEM 2	18.2	100%	18.2	18.2	Reduced to only have necessary functions
AIU	6.0	100%	6.0	6.0	JHU/APL Conceptual Estimate
Thermal Subsystem	**0.0**	100%	**0.0**	**0.0**	Assumes RTG heat used at 5.5 AU
Subtotal	**303.1**		**231.2**	**303.1**	
Harness Losses	**4.5**		**3.5**	**4.5**	
Total	**307.6**		**234.7**	**307.6**	
Available Power 3 MMRTG (BOL)			**375 W**		
Available Power 3 MMRTG (4.1 yr)			**353 W**		
Available Power 3 MMRTG (8.8 yr)			**328 W**		
First Pass					
Margin (W)			118.3	45.4	
Growth Margin (%)			50.4%		
Second Pass					
Power Reserves (W)			93.3	20.4	
Growth Margin (%)			39.8%		

Appendix D:

Solar Probe Spacecraft Dimensions

Blank

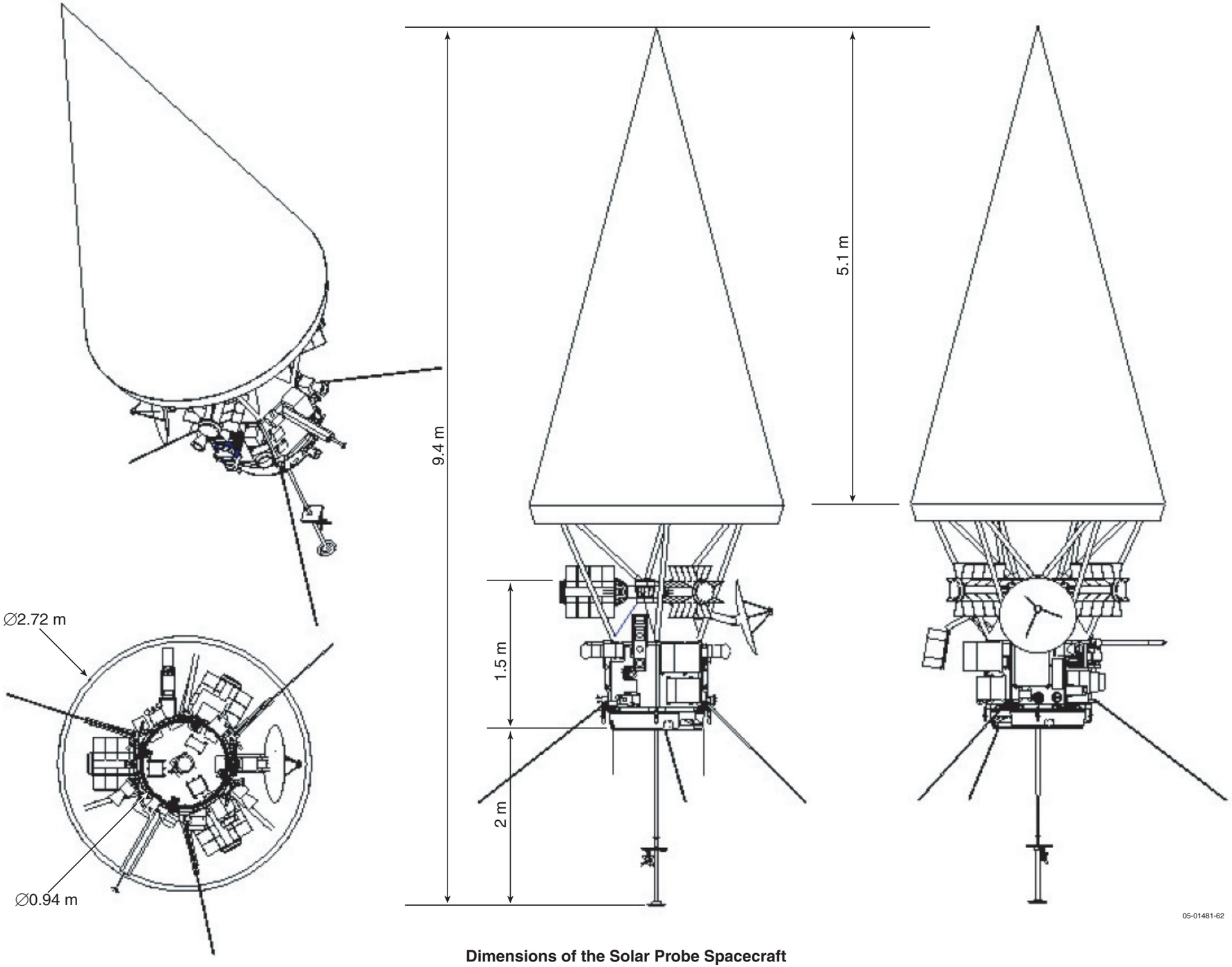

Dimensions of the Solar Probe Spacecraft

Blank
(Back of Foldout)

Appendix E: Optical Surface Technology Overview

Introduction

Research supporting solar exploration has been funded by The Johns Hopkins University Applied Physics Laboratory (APL) over the time period of fiscal years 2003 through 2005. The research has specifically addressed the applicability of high-temperature optical surfaces as a means of providing spacecraft thermal management in the near-solar environment. Structures for solar applications are required to function in the temperature regime ranging from deep space at 77 to 2100 K at 4 R_S. Initial out-gassing experiments performed by JPL indicate that out-gassing thresholds for carbon–carbon materials will be reached for heat shield equilibrium temperatures >2200 K. Such out-gassing could potentially contaminate critical science experiments. However, high-fidelity high-temperature out-gassing measurements are extremely difficult to conduct in a controlled manner, owing to variations in materials, accuracy of measurement devices, and high-temperature oven out-gassing sources. When design and testing uncertainties are applied to the initial out-gassing data, the Solar Probe spacecraft primary heat shield (composed of carbon–carbon material), could exceed desirable heat shield out-gassing limits at temperatures as low as 1900 K. Consequently, a lower-risk design solution was sought by the APL research team, not to only eliminate potential out-gassing issues (by reducing the primary heat shield temperature below 1900 K), but also to provide protection from other temperature-driven environmental effects by reducing the potential for chemical or radiation interactions (resulting material degradation).

While the reduction in contamination sources was a primary driver early in the research, we quickly realized that the ability to significantly reduce spacecraft equilibrium temperature had a substantial impact on the spacecraft design and mission. The APL approach incorporates a white ceramic coating (which is highly reflective in the visible and highly emissive in the IR) applied to the carbon–carbon spacecraft primary heat shield structure. Studies predict that this solution enables a significant reduction in the equilibrium temperatures of critical Thermal Protection System (TPS) components to <1900K. In-turn, higher-fidelity science can be expected as temperature-driven contamination sources are reduced. However, the impacts on the spacecraft design are more noticeable. The reduction in the primary heat shield equilibrium temperature directly impacts prior high-risk components such as the secondary heat shield and the struts that connect the primary heat shield to the bus. In early design studies, the secondary heat shield was proposed to incorporate emerging materials such as aerogels and low-density carbon battes to meet thermal conductivity and mass/volume budgets. However, with lower temperatures, mature insulation systems such as carbon foams can now be incorporated. In addition, the lowered operating temperature reduced the required thickness of the secondary shield and its mass. Also, in the early studies, the struts were configured to be pyrotechnically severed in order to create a thermal short after launch. In addition to increasing risks due to the severance operation, this approach resulted in significant mass penalties (as a result of the severance hardware and provisions for attaching the hardware to the struts). The new strut design, enabled by the reduced thermal load, now incorporates a thin-walled strut geometry that is tailored to produce a minimum conductivity and does not require severing the struts. The result for the mission is anticipated to be a lower-risk spacecraft with significant launch mass (and cost) savings.

The research has been highly integrated with the Solar Probe program in an attempt to make the findings timely and value-added as a means of risk reduction. Material, mission, and science requirements were obtained from the Solar Probe Science and Technology Definition Team (STDT) and APL Space Department personnel. The research has specifically addressed the following technology issues related to the functionality of an optical surface in space:

- Optical properties (a/e) and relationship with predicted primary heat shield equilibrium temperature
  - Optical property degradation at elevated temperature
  - Optical property degradation due to radiation (p^+, e^-, ions, and EUV)
  - High-speed particulate impact damage and effects on equilibrium temperature

- Structural integrity of the coating and substrate
  - Launch vibration loads (representative displacements and durations)
  - Thermal cycling (deep space to near-solar temperatures)
- Material charging due to radiation (p^+, e^-, ions, and EUV)
  - Fundamental material responses (carbon–carbon and ceramics)
  - Impact on integrated spacecraft at critical trajectory points
- Out-gassing and chemical interactions
  - As a function of elevated temperature and vacuum

Three candidate ceramic-based optical surfaces have been investigated from an initial feasibility perspective. These materials include aluminum oxide or alumina (Al_2O_3), pyrolytic boron nitride (PBN), and barium zirconium phosphate ($BaZr_4P_6O_{24}$, herein identified as BaZP). While the all materials have performed well to date, alumina was selected as the baseline coating due to its overall maturity level and supporting historical database. The PBN (second to alumina in maturity and database) and BaZP will remain as backup solutions. Based on time and funding allocations for the research effort, a majority of the investigations were focused on alumina. **Table E-1** shows a summary of the investigations.

Thermal management via C–C substrates with optical surfaces

The conical primary heat shield is designed to present a small view factor to the Sun (and reduce the amount of solar irradiance absorbed) while providing significant surface to radiate to deep space. Combining this design approach with optical surfaces that reflect a large portion of the visible solar irradiance and emit the remaining energy (in the IR band) results in significant reductions of heat shield equilibrium temperature. Such a temperature reduction greatly influences other thermal management and structural components, since radiant thermal energy is directly imparted from the inner surface of the primary heat shield to the interior face of the secondary heat shield. This heat load is then conducted to the opposite face of the secondary heat shield where it can be transmitted to other spacecraft components (such as the instrument bus and its supporting struts). Reducing the temperature of the primary heat shield thus reduces the heat flux (and temperature) experienced by these components.

Coatings which are highly reflective in the visible band while highly emitting in the IR band are desirable characteristics for the optical surface. The maximum predicted temperature of the spacecraft's primary carbon–carbon heat shield (with no reflective coating, i.e., a blackbody) is on the order of 2100 K (assuming a ratio of solar absorptivity to IR emissivity, $\alpha/\varepsilon = 1$) when it approaches to within 4 solar radii of the Sun. (the thermal load from the sun at this distance is notionally 400 W/cm^2). The optical property of α/ε needs to be lower than 1 to provide significant temperature reduction (thus providing a significant decrease in C–C out-gassing from the primary heat shield). Three candidate "white" ceramic coatings that

Table E-1. Summary of optical surface investigations.

Candidate material	Optical						Structural			Out-gassing			Charging				Particulate Impact	
	Baseline	Temperature effects	Radiation effects: EUV	Radiation effects: Electron	Radiation effects: Proton	Predicted PHS temperarure	Thermal cycling	Vibration	Cumulative/residual strengths	Temperature effects	Temperature/vac effects	Chemical interaction	Temperature effects	Radiation effects: Electron	Radiation effects: Proton	Cumulative effects	Impact damage modeling	Effect on PHS performance
Al_2O_3	E,A	E,A	E	E	E	A	E	E	E	E	E	A	A	A	A	A	A	A
PBN	E,A	E,A	E	E	E	A				E		A	A					
BaZP	E,A	E,A	E	E	E	A				E		A						

E = Experiment A = Analysis E = to be completed in risk reduction program 05-01481-63

satisfy these α/ε goals were studied: alumina, PBN, and BaZP. A roadmap summarizing the complexity of the experiments is shown in **Figure E-1.**

To validate the thermal management approach, optical data as a function of temperature and wavelength were collected by APL (at discrete laser wavelengths mapped to the solar irradiance profile as shown in **Figure E-2**) and then incorporated into a spectral-based radiant thermal model. Reflectance was measured at specific wavelengths over a range of temperatures (from room temperature to the predicted equilibrium temperature) and the solar absorptance or IR emittance calculated using Kirchoff's Law:

$$\alpha_\lambda = 1 - \rho_\lambda,$$

which can also be written as

$$\varepsilon_\lambda = 1 - \rho_\lambda,$$

where λ = wavelength.

Optical property testing (up to 1773 K and using an Argon cover gas) was performed on C–C coupons coated with Al_2O_3 and PBN. The α/ε results these coupons[1] are shown in **Figure E-3** as a function of temperature. In addition, Figure E-3

[1]Multiple samples (each using different material vendors) of $A1_2O_3$ and PBN-coated C–C coupons were fabricated and tested. In addition, differnet fabrication methods were also evalulated.

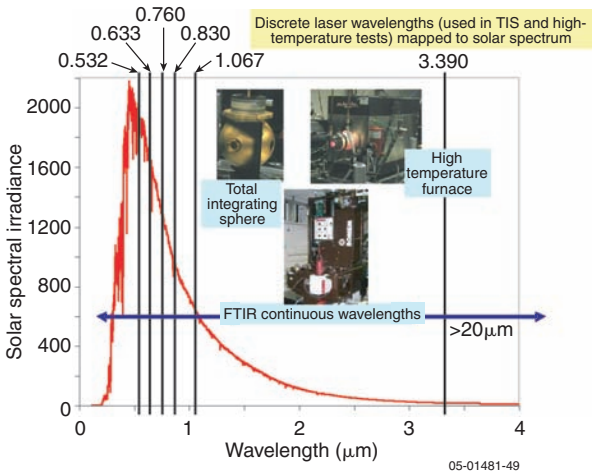

Figure E-2. Map of solar irradiance and optical property measurements.

shows the resulting primary heat shield temperature (at a distance of 4 solar radii from the Sun) as a function of α/ε. The use of optical coatings (all with $\alpha/\varepsilon < 0.6$) is seen to reduce the heat shield temperature to < 1850 K using alumina (to as low as 1400 K in the case of one of the PBN-coated coupons).

Operation of the baseline system (composed of an alumina optical surface on top of the carbon–carbon heat shield) is shown in **Figure E-4**. The bulk (80 to 90%) of the incoming solar radiation is reflected by the coated heat shield. The remaining radiation is absorbed and conducted to the

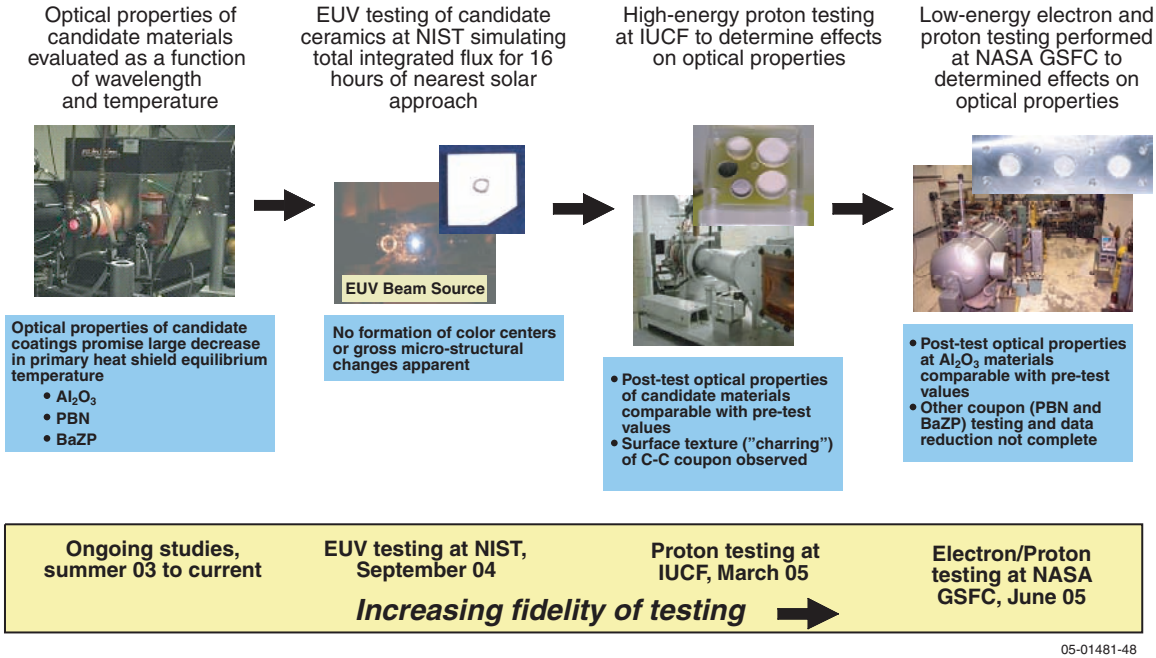

Figure E-1. Summary of experiments investigating optical properties.

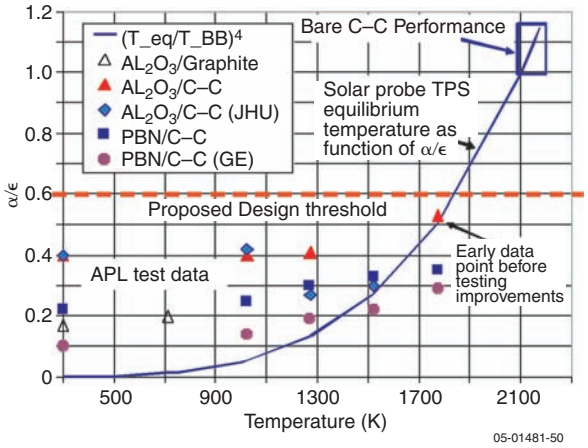

Figure E-3. Optical property data for Al_2O_3 and PBN.

carbon–carbon substrate. This absorbed heat is then re-radiated back to space. The thin alumina coating has a window of transparency between the upper limit of the visible band ($\lambda < 1$ μm) and the mid-IR band ($\lambda > 4$ μm). This spectral-dependent transparency allows energy to be directly radiated from the carbon–carbon substrate (which has an IR emissivity of ~1) to space. As the alumina's transparency decreases, it becomes an effective IR radiation emitter (note the rise in emittance shown in Figure E-4 from $\varepsilon = 0.2$ at $\lambda < 1$ μm to $\varepsilon > 0.9$ at $\lambda > 6$ μm).

Testing was performed at NIST to assess the stability of the alumina and PBN at a total integrated EUV flux of 120 J/mm^2. This flux is greater than the total integrated flux predicted for the 16 hours of closest solar approach (for a notional Solar Probe mission to 4 R_S). These specimens showed no visual or microscopic evidence of color center formation or microstructural damage (see **Figure E-5**). Because of the small size of the beam exposure locations, optical properties could not be verified.

Radiation effects on optical properties were evaluated experimentally by measuring material optical properties before and after exposure to representative radiation environments. Material coupons tested included pyrolitic graphite, bare C–C, and C–C with Al_2O_3, PBN, and BaZP coatings. Radiation doses included very energetic protons (**Table E-2**) and lower energy proton and electron

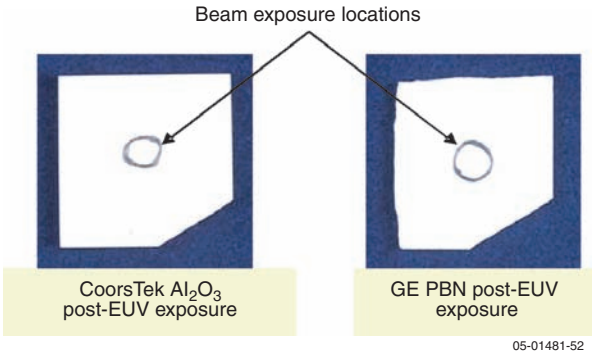

Figure E-5. Coupons post-EUV exposure at NIST.

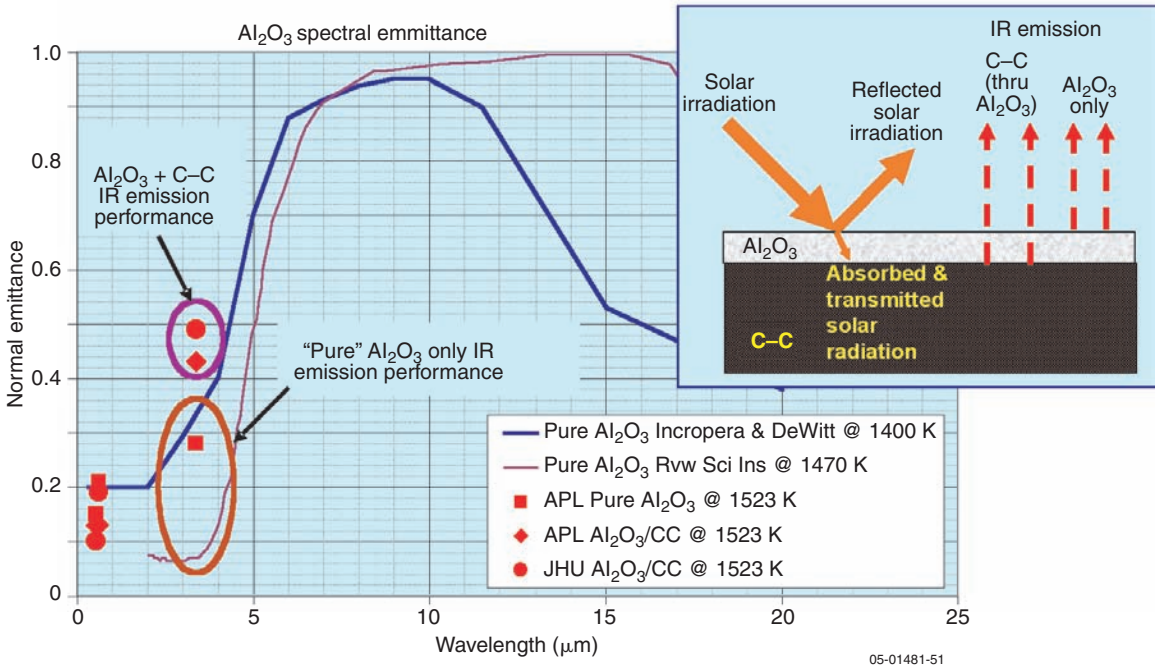

Figure E-4. Operation of baseline primary heat shield system.

exposures (**Table E-3**). Optical measurements were performed before and after radiation exposure and showed no measurable change in optical properties or physical appearance. For reference, test coupons from the single solar event test at IUCF (tray 5) and post run 4 at NASA-GSFC are shown in **Figure E-6**.

System-level trade studies were performed to evaluate the effects of particulate impact (and subsequent degradation of the optical surface) on the primary heat shield equilibrium temperature. A finite element thermal model (**Figure E-7**) of a single impact location was first developed and parametric numerical studies conducted to evaluate the effects of hole diameter, radius of any spall zone around the hole, thermal conductivity of the substrate, and α/ε ratio of the optical coating. The results revealed that any significant temperature increase would be limited to the immediate region of the damage (where the optical surface has been removed and α/ε is that of the underlying carbon–carbon substrate, that is, $\alpha/\varepsilon \sim 1$). Any portion of the primary heat shield interior surface "views" the opposite interior surface and exchanges heat via radiation. Since the (uncoated) carbon–carbon interior surfaces have high IR emissivity and the "view factor" between the surfaces is unity, radiation heat transfer between the damaged and undamaged sides of the heat shield serves to restrict any temperature increase to a small region around the spall area.

After determining that temperature change due to damage was a local phenomenon, the next step in assessing the effect of damage on system thermal performance was to parametrically vary the total

Table E-2. High energy proton exposure conditions tested at IUCF.

Run	Proton Energy (MeV)	Trays	Vacuum (mtorr)	Fluence no./cm^2	Simulation	Substrates Discolored or Damaged
1	54.7	1,4	60	8.50E+10	12 Events	None
2	73.7	2,4	80	3.80E+10		None
3	104.2	3,4	80	2.00E+10		None
4	104.2	5	80	1.84E+13	Single event near Sun (1/r^2)	Possible C–C structural change

Table E-3. Moderate energy proton and electron exposure conditions test at NASA-GSFC.

Run	p+ energy	e$^-$ energy	Tray	Vacuum	Fluence
1	500 keV		4	yes	3.6E12
2	1 MeV		4	yes	1.9E12
3		100 keV	4	yes	2.8E14
4		1 MeV	4	yes	5.5E12

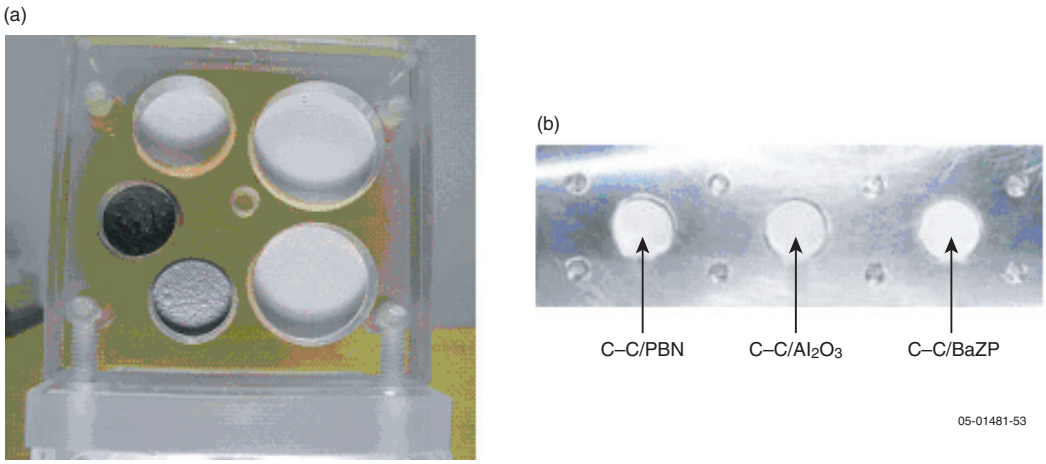

Figure E-6. Post-test "Tray 5" material coupons and holder. (a) Tray 5 "worst-case" proton fluence exposure at IUCF; (b) Tray 4 from IUCF test series post-run 4 at NASA-GSFC.

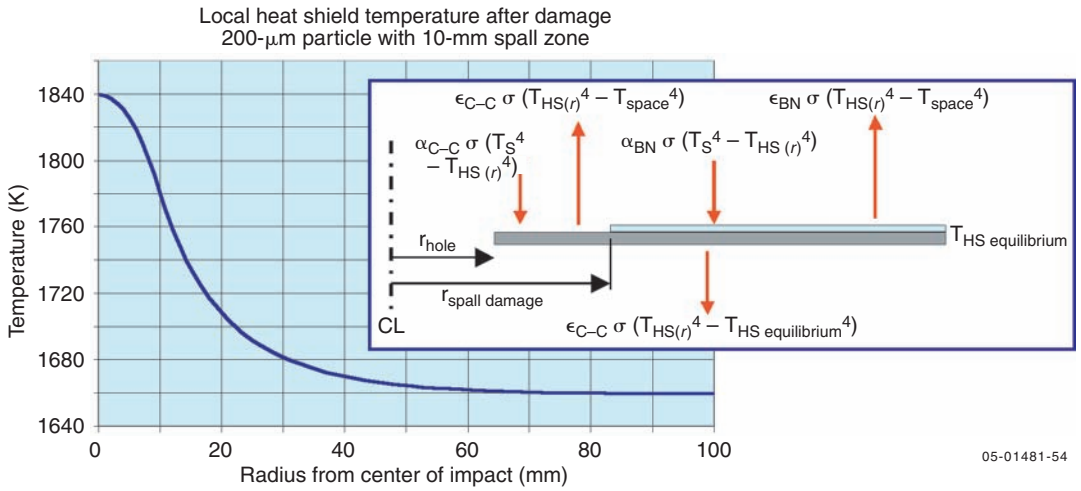

Figure E-7. Typical finite element thermal model of a single impact location (PBN optical coating).

damage to the optical surface and calculate the resulting average temperature of the primary heat shield. Damaged areas were treated as local hot spots (with elevated temperature), while undamaged areas remained cooler. An area-weighted average temperature was then calculated for the heat shield as a function of damaged area. The results, shown in **Figure E-8**, reveal the robustness of the design. Over 20% of the heat shield would need to be damaged to increase the heat shield temperature by 100 K. As documented elsewhere in this report, the predicted primary heat shield damage level is much less than 0.1%, thus indicating that no significant temperature increase is expected.

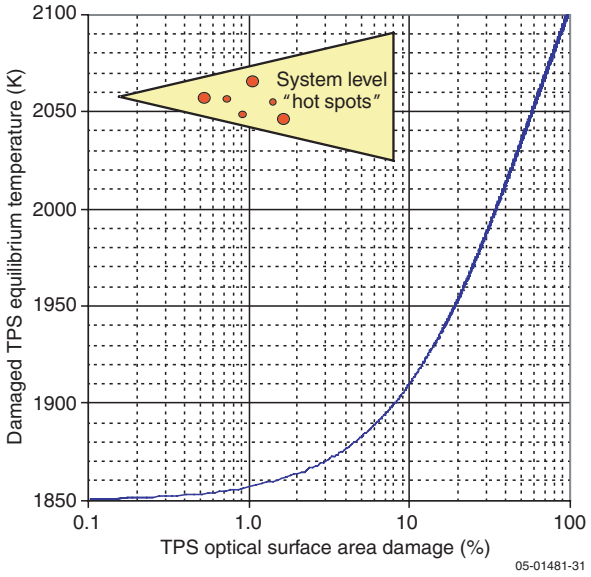

Figure E-8. Primary heat shield equilibrium temperature with damaged Al_2O_3 optical surface.

Structural integrity of coatings and substrate interface

The structural integrity of the optical surface (and substrate interface) was identified as a risk area relative to optical surface performance (and potential impact on equilibrium temperature if the coating was to be removed due to spalling). Three series of experiments were performed in an attempt to identify potential show-stoppers as identified in **Figure E-9**. The first series consisted of thermal cycling tests. These tests were performed using flat circular coupons and were cycled three times from 77 to 1600 K (the limit of the thermal cycling furnace; subsequent optical property testing has taken the coupons to ~1800 K). Critical elements of the coating (and potential coating elements added to improve structural integrity) were evaluated, including graphite with a plasma sprayed Al_2O_3 coating; carbon–carbon coated with SiC; and carbon–carbon coated with SiC followed by plasma-sprayed Al_2O_3 (doped with Zr). No spalling of the coating or coating cracking was observed, as shown in **Figure E-10**.

The next test series consisted of a three-point bend test to determine the structural integrity of the coating and the coating-to-substrate interface after exposure to large displacements (**Figure E-11**). The carbon–carbon coupon (1 in. wide × 9 in. long × 0.050 in. thick) coated with Al_2O_3 was displaced to a total deflection of 0.60 in. with no observable damage. The maximum allowable dis-

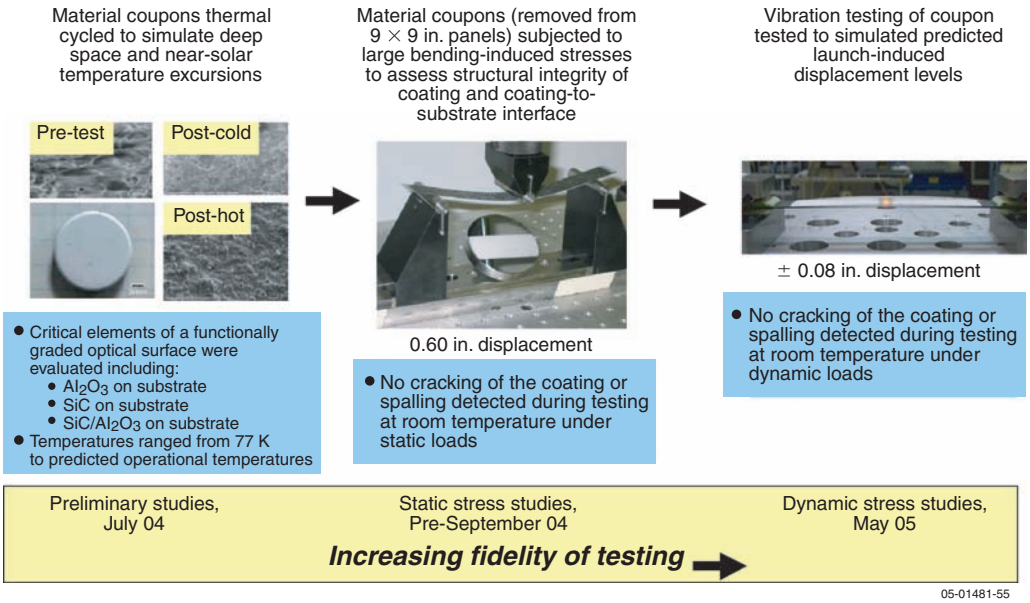

Figure E-9. Progression of structural integrity investigations.

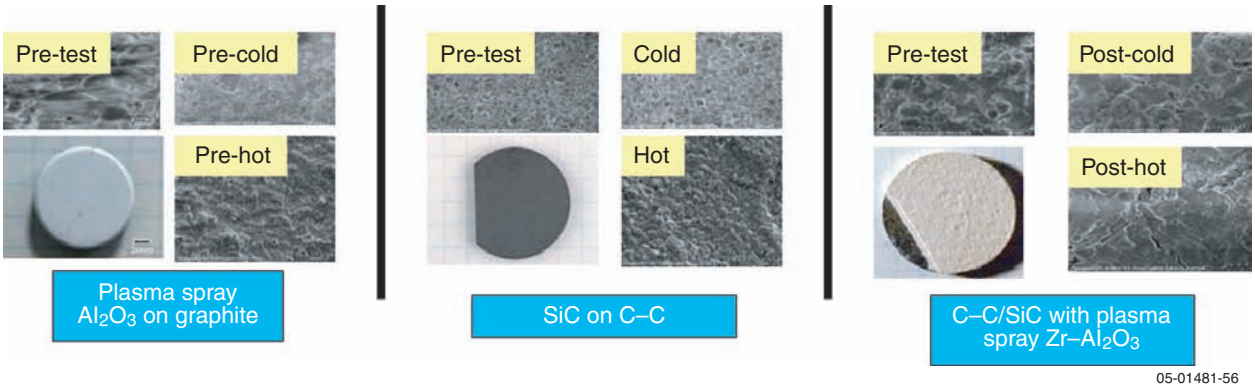

Figure E-10. Results from thermal cycling structural integrity investigation.

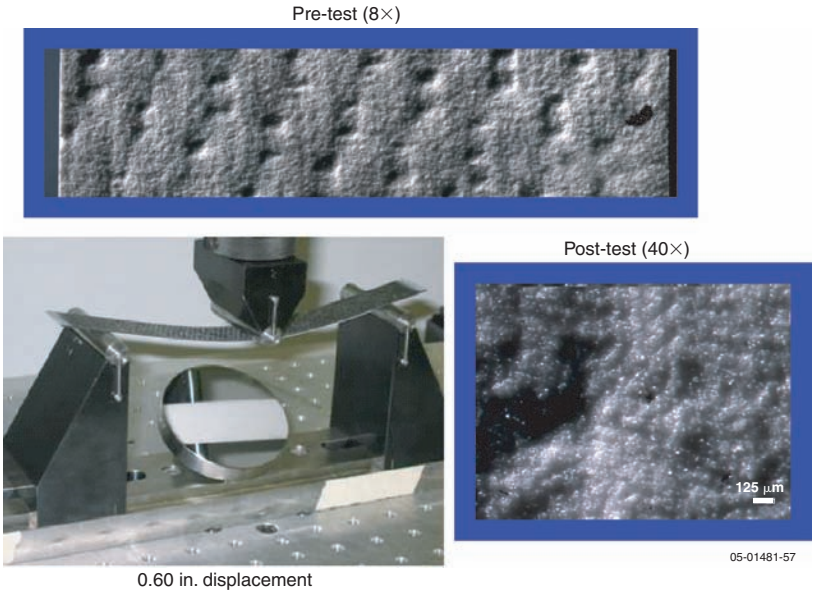

Figure E-11. Static displacement test results.

placement for the spacecraft during launch is anticipated to be << 0.160 in.

The third and final test series was conducted on the shaker table in the vibration laboratory at APL. As shown in **Figure E-12**, test specimens composed of carbon–carbon coated with Al_2O_3 and were removed from the same panel as the displacement test coupon. The coupon was vibrated to simulate launch loads through a match of displacement (under dynamic fatigue conditions). Microscopic evaluations of the coupons revealed no coating cracking or spalling at the substrate interface. The coupon (1 in. wide × 9 in. long × 0.05 in. thick) was subjected to a maximum measured deflection of ±0.08 in. at an acceleration level of 2 g's for 15 minutes. Additional vibration testing to higher displacement levels will be performed in an Independent Research and Development (IRAD) program later this fiscal year.

Out-gassing and chemical interaction

Tests for out-gassing were performed on multiple small samples of alumina, PBN, and BaZP using a thermal gravimetric analysis (TGA) system. These materials (surrounded by a nitrogen cover gas) were taken to elevated temperatures (exceeding their predicted equilibrium temperatures at perihelion) in order to investigate out-gassing as a function of time and temperature. Measurable mass loss occurred for all samples up to 773 K, but this mass loss was attributed to contamination due to collection of organics and water during storage (note that repeated cycles to 773 K showed no additional measurable loss, which would have occurred if the material had been out-gassing). All the materials were subsequently exposed to higher temperatures (up to 1400 K for BaZP and 1773 K for alumina and PBN) and no additional mass loss was detected (that is, any changes in the measured masses were within the TGA measurement resolution, ±0.1% of the sample weight). These results agreed with predictions (based on literature review and analysis) that these white ceramics were stable and posed no significant risk of contamination due to out-gassing. Additional higher-fidelity testing on larger test specimens is planned as part of IRAD in FY 2005.

Thermodynamic stability analyses were performed for candidate coatings and multi-layer coatings using the *NASA-Lewis Chemical Equilibrium Code*. This code assumes pure species and calculates the interface chemical reactions where gas products indicated a potential for delamination-based failure (spalling) of the coating. Models were run up to 2100 K with no gas products generated for carbon–carbon coated with Al_2O_3, carbon–carbon coated with SiC, carbon–carbon coated with SiC followed by Al_2O_3, carbon–carbon coated with PBN, and carbon–carbon coated with Sic followed by PBN. These results indicate stability at high temperatures for all these material combinations.

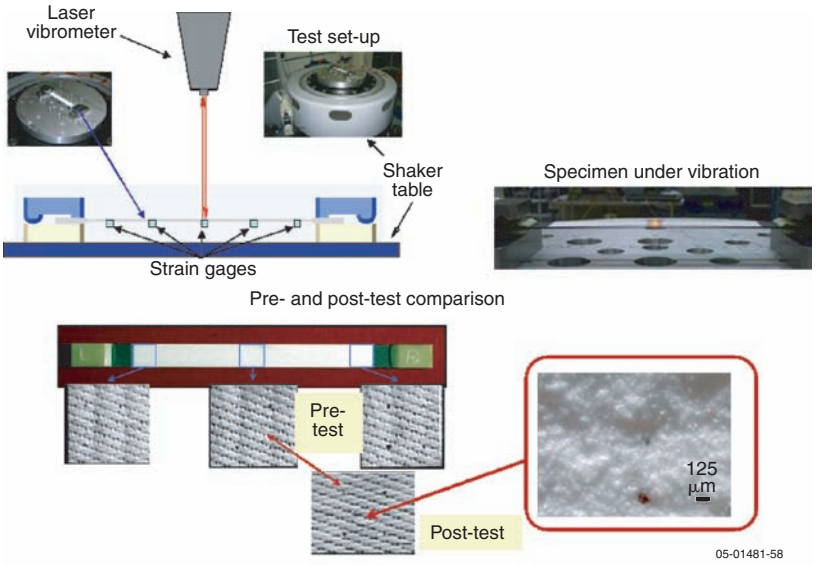

Figure E-12. Vibration test setup and results.

Charging of optical surface materials in radiation environments

The proposed white ceramic coatings have unique charging characteristics, which depend on factors including material resistivity as a function of temperature, dielectric constant, photoelectron emission characteristics, and secondary electron emission. Surface charging is a complex function of these and other parameters, including spacecraft geometry, orientation, sunlight intensity and distribution, and specific radiation environment. The white ceramics, which are typically electrically insulating at room temperature and are traditionally considered as insulators in space, can notionally be problematic for spacecraft, as they can collect charge and/or develop unmanageable voltage potentials (both magnitude and gradients) leading to arcing.

Several methods (see **Figure E-13**) were used to evaluate possible charging of heat shield insulating coatings relative to conductive carbon coatings such as pyrolitic graphite (PG). Several tools were employed, including cursory analysis based on material properties; NASA's *Space Environmental Effects (SEE) Interactive Spacecraft Charging Handbook* (to explore fundamental effects of photoemission and secondary electron emission); and NASCAP-2K, a sophisticated spacecraft-level charging analysis program developed by SAIC (to explore integrated spacecraft effects such as geometry, component interactions, etc.).

Initial analysis was based on evaluation of material properties as a function of temperature. It was determined that insulators naturally become more conductive as temperature increases. Insulator resistivity is inversely proportional to temperature; thus, the conductivity of insulators is proportional to temperature. Near the Sun, specifically within ~0.2 AU, the Al_2O_3 is relatively conductive, such that its resistivity thickness product falls below 2×10^9 for a 4- to 5-mil coating, thus falling within NASA specifications for partially conductive coatings applied over conductive substrates. Temperature-dependent resistivity data for the specific proposed coatings (plasma sprayed, with or without dopants, etc.) is required for precise analysis. Because literature data on temperature-dependent resistivity, dielectric constant, secondary electron emission coefficients, etc., was available for alumina but not for the other materials being considered (PBN and BaZP), all subsequent studies were performed for the case of alumina only. It is not

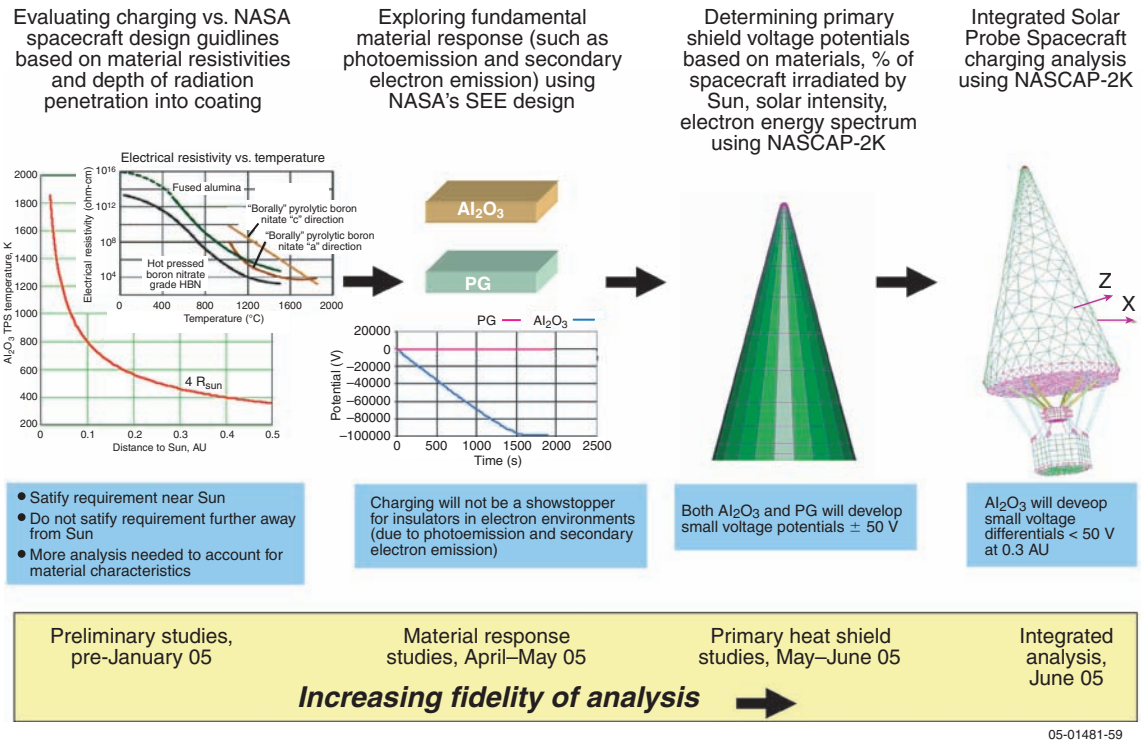

Figure E-13. Vibration test setup and results.

known at this time whether or not all three proposed electrically insulative coatings will respond similarly to the same radiation environment.

Additional charging studies involved using NASA's *SEE Interactive Charging Handbook* for simple charging modeling. SEE was used to model the materials with their complex material properties as a sheet with a monoenergetic beam of electrons of defined energy striking the sheet at normal incidence. This analysis afforded an understanding of how alumina charges relative to PG in various electron environments.

Under the IRAD program, the response of Al_2O_3 in near-solar (0.3 AU), Jovian, and deep space (2.5 AU) radiation environments was investigated to determine the differences in voltage potential between a bare carbon–carbon heat shield and one coated with Al_2O_3. Analytical predictions indicate relatively low differential charging (relative to conductive substrates) < 30 V for the coated heat shield, as shown in **Figure E-14.**

As can be observed from the predictions, there are differences in material response at the near-solar and Jovian/deep-space environments. Most notably, the conductive carbon substrate does not develop a differential charge, even though only one side is in sunlight in the 2.5 AU and Jovian cases. This homogeneous charging is due to the electrical conduction of the conductive carbon, which distributes accumulated charge very quickly. The ceramic does, however, develop a differential potential across the cone when the sunlight illuminates one side (as it does in the 2.5 AU and Jovian cases). Near the Sun, the insulative characteristics of the ceramic decrease (due to temperature effects) to the point of being effectively conductive, thus enabling equilibration of the charge (as is the case for the bare carbon heat shield). In addition, at this point in the trajectory, the spacecraft will be pointed such that sunlight is incident evenly across the cone (i.e., the cone tip is pointed at the Sun).

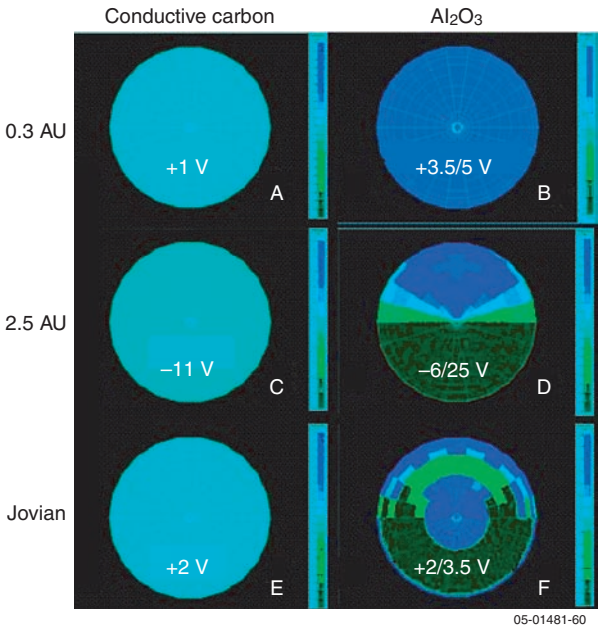

Figure E-14. Cone-end view NASCAP results for conductive carbon and Al_2O_3. The conductive carbon substrate charges homogeneously, whereas the insulating Al_2O_3 substrate charges differentially with the more positive potential in the direction facing the Sun.

Further analysis is required to determine the charging effects for the integrated spacecraft considering material properties as a function of temperature, resistivity between grounded components, radiation environments as a function of trajectory, etc. NASCAP-2K software will be used as an analytical tool to predict differential charging between components for critical radiation environments, such as start of science, the Jovian encounter, and deep space. Analog experiments will be performed to more accurately determine material properties, validate analytical models, and determine material responses. These analyses will enable system engineers to identify and address issues associated with spacecraft electronics, communications, and sensitive science functions. Overall, this charging analysis indicates that both carbon–carbon and ceramic coated carbon-carbon present manageable charging situations.

Appendix F: Solar Probe, a Brief History

The idea of a spacecraft mission to explore the near-Sun environment goes back to the first year of the space age. In October 1958, the month in which NASA was founded, the Physics of Particles and Fields in Space Committee of the National Research Council's Space Studies Board issued an interim report that contained recommendations for future missions that the new agency should include in its long-term planning. Among the missions recommended by the committee, which was chaired by John Simpson (University of Chicago) and co-chaired by James Van Allen (University of Iowa), was one that would send a spacecraft inside the orbit of Mercury (0.387 AU) to measure the particles and fields environment near the Sun.[1]

Past Solar Probe reports and studies.

In 1962, four years after the Simpson Committee presented its recommendations, the Mariner II Venus probe made the first definitive measurements of the solar wind, confirming E. N. Parker's controversial theory of the supersonic expansion of the Sun's corona. During the next dozen years, the properties of the solar wind were measured in different of regions of space by a variety of spacecraft. No probes ventured closer to the Sun than 0.7 AU (the orbit of Venus), however, until the mid-1970s, when the joint German–U.S. Helios project placed two spacecraft into a highly elliptical orbit whose apogee lay at ~0.3 AU, just inside the orbit of Mercury. The data acquired by Helios 1 and 2 were enormously valuable and are still unique as the only in-situ measurements of the inner heliosphere made as close to the Sun as 60 R_S.

Despite the important contributions of the Helios *Sonnensonden*,[2] the heliosphere inside 60 R_S remained unexplored. This is the critical region where the Sun's million-degree corona is accelerated to form the supersonic solar wind. A few technical studies of a mission to explore this region had been carried out, the first in 1963. However, "a new era in the studies began in 1976, when new heat shield technologies became available and higher- performance spacecraft allowed a more diverse scientific payload."[3] Thus in May 1978, 15 months after the launch of Helios 2, a workshop was held at the California Institute of Technology to examine the scientific objectives that could be achieved by a Solar Probe mission that would

[1]This information is drawn from J. E. Naugle's account of the origins of the Space Studies Board and its role in space science planning during the formation of NASA in *First Among Equals: The Selection of NASA Space Science Experiments*, Ch. 3, NASA SP-4215, 1991.

[2]"Sun probes" (German).

[3]Randolph, J. E., NASA Solar Probe mission and system concepts, *Adv. Space. Res.,* **17**, 3–12, 1996. Randolph's article offers a valuable history of the development of the Solar Probe concept from Starprobe to the joint U.S.–Russian Fire and Ice project. It also contains an extensive bibliography of Solar Probe studies and reports, beginning with the 1963 AVCO technical report, *Close Approach Solar Probe.*

fly within 4 R_S of the Sun and directly sample the outer corona and nascent solar wind. The papers presented at the workshop were published later that year in a thick volume titled *A Closeup of the Sun*.

The Caltech workshop was followed by a number of technical studies to address the engineering and mission design challenges inherent in a Solar Probe mission. Further studies of the science were performed as well. What emerged during the course of these studies was "Starprobe," an ambitious mission whose science objectives included solar gravitational and general relativity experiments as well as experiments to study coronal heating, solar wind acceleration, and the production of solar energetic particles.

Acknowledging the desirability of the Starprobe science goals but recognizing the reality of limited resources, the NRC's Committee on Solar and Space Physics (CSSP), chaired by Tom Krimigis (Johns Hopkins University Applied Physics Laboratory), recommended a reduced-capability Solar Probe mission in its 1985 report on research priorities in solar and space physics.[4] The primary objective of this mission would be to study the genesis of the solar wind through in-situ measurements of the solar wind plasma, electric and magnetic fields, and energetic particles in the region between 60 and 4 R_S. In 1988 NASA formed a Solar Probe Science Study Team (SST), headed by W. C. Feldman (Los Alamos National Laboratory), to define the science goals and develop a mission concept for a Solar Probe mission that would make only in-situ measurements, as recommended by the CSSP. In parallel with the SST's efforts, engineering and mission design studies for the Solar Probe mission were carried out at JPL under the direction of J. E. Randolph. The SST's report was published in November 1989. However, the engineering studies continued throughout the 1990s, as spacecraft system and mission design solutions were sought that would reduce the cost of the Solar Probe mission without compromising the science. A notable design change that came out of these studies was the switch from a large conical heat shield to a smaller, parabolic shield that would also serve as the spacecraft's high-gain antenna.[5]

A new scenario for a Solar Probe mission resulted from the Clinton administration's policy toward Russia, which sought to encourage economic and technological cooperation between the two countries in a number of areas, including space research. In 1994, U.S. and Russian scientists began developing concepts for joint space missions, one of which, known as Fire and Ice, would send spacecraft to the Sun and Pluto. The Fire project envisioned two Solar Probes, one U.S. and one Russian, launched together on a Russian Proton launch vehicle. The U.S. spacecraft would be placed into a 4×8 R_S elliptical polar orbit, the Russian probe into a 10×20 R_S polar orbit. Both spacecraft would carry in-situ and imaging instruments. However, after the loss of the Mars 96 probe, Russia curtailed her robotic space flight activities, and the idea of a joint Solar Probe mission was abandoned.

In June 1995, an ad hoc study team chaired by Ian Axford (Max-Planck-Institut/Lindau) was convened to define a "Minimum Solar Mission" as a possible U.S. contribution to the Fire mission and as a less costly alternative to the baseline Solar Probe mission then under consideration. The MSM report was received with some skepticism in the solar and heliospheric physics community, and in 1996 a new science definition team was formed under the direction of George Gloeckler (University of Maryland). The Gloeckler team recommended a scientific payload comprising an in-situ instrument package and a remote-sensing package, each to be developed under the direction of a single principal investigator. The combined mass and power requirements for the two packages were 18.8 kg and 15.5 W (compared with 133.5 kg and 103 W required by the payload described in the 1989 SST report.)

The Gloeckler report was released in February 1999 and defined the Solar Probe science objectives and a strawman payload for a 1999 Announcement of Opportunity, which solicited proposals for the Pluto-Kuiper Express and Europa Orbiter missions as well as for Solar Probe. Solar Probe proposals were submitted in the summer of 2000. Funding for the implementation of a Solar Probe mission was not included in the NASA budget for fiscal year 2002, however, and no selections were made. In 2001, Solar Probe was shifted from the Outer Planets mission line into NASA's new Living With a Star Program. In 2002, the Solar Probe investigations solicited in the 1999 Announcement of Opportunity were

[4]NRC, *An Implementation Plan for Priorities in Solar-System Space Physics*, National Academy Press, Washington D.C., 1985.
[5]Randolph, *op. cit.*, 1996.

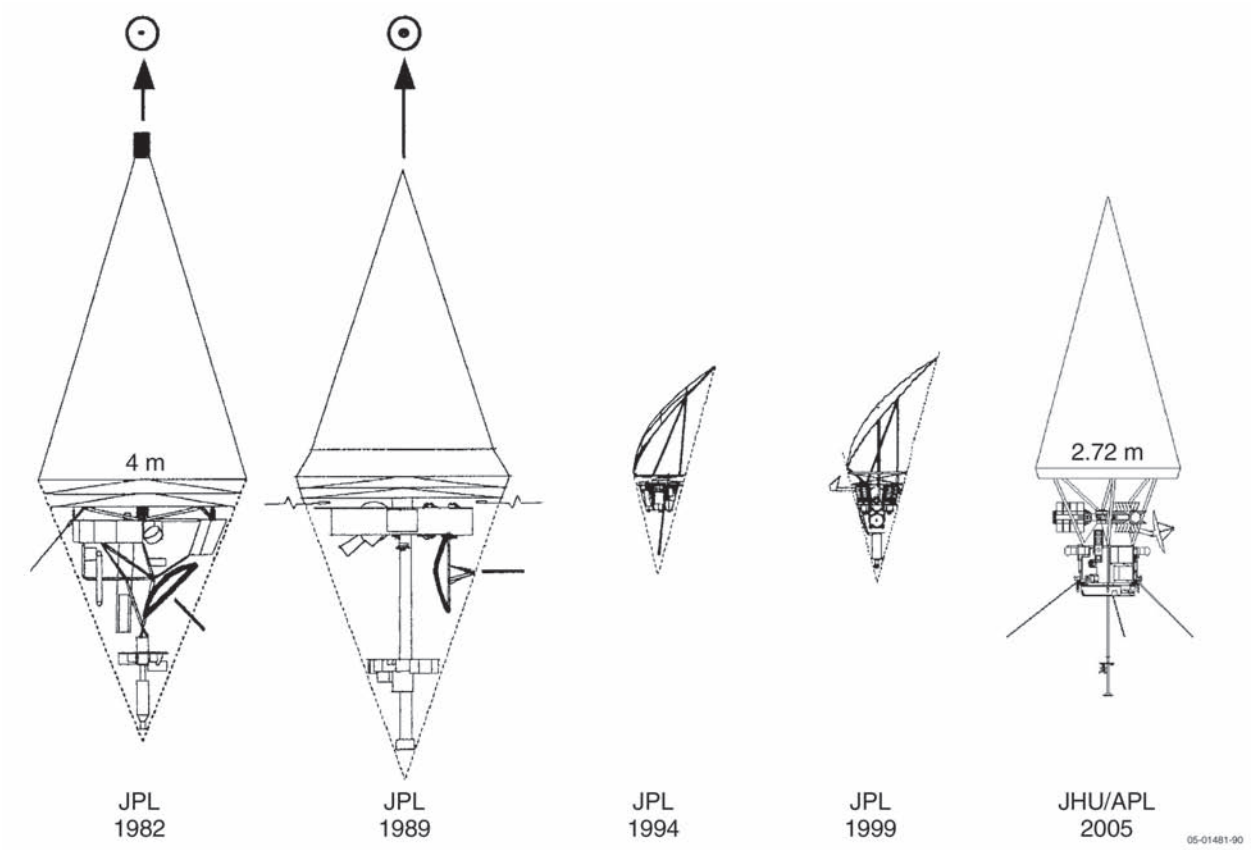

Solar Probe design evolution, 1982–2005.

officially cancelled, and NASA commissioned the John Hopkins University Applied Physics Laboratory to lead a new concept study of the Solar Probe mission and its architecture.

In early 2003, the NRC's decadal survey in solar and space physics was published, which stressed the scientific importance of a Solar Probe mission and recommended "its implementation as soon as possible."[6] In the fall of that year, NASA, noting the NRC's recommendation and the "significant advances" made since the 1999 Solar Probe report "in the areas of science understanding, instrument technology, mission resources, mission environment, and related space missions,"[7] announced plans for a new Solar Probe study and the formation of the present Solar Probe Science and Technology Definition Team.

[6]NRC, *The Sun to the Earth—and Beyond. A Decadal Research Strategy in Solar and Space Physics*, National Academy Press, Washington, DC, 2003.

[7]Letter dated October 6, 2003, from Richard Fisher to the solar and space physics community.

Solar Probe Studies: A Partial Chronological Bibliography

Friedman, L. D., *A Solar Probe Mission—Interim Report*, JPL Internal Document 760-133, October 1975.

Neugebauer, M., and R. Davis, *A Closeup of the Sun*, JPL Publication 82-49, 1978.

Underwood, J. W., and J. E., Randolph, *Starprobe: Scientific Rationale—A Report of the Ad Hoc Working Groups*, JPL Publication 82-49, 1982.

Feldman, W. C., et al., *Solar Probe: Scientific Rationale and Mission Concept. A Report of the 1989 Solar Probe Science Study Team*, JPL Internal Document D-6797, November 1989.

Randolph, J. E. (ed.), *Solar Probe: Mission and System Design Concepts 1989*, JPL Internal Document D-6798, December 1989.

Report of the Joint U.S./Russian Technical Working Groups: Mars Together and FIRE & ICE, JPL Publication 94-29, October 1994.

Randolph, J. E. (ed.), *Solar Probe: Mission and System Design Concepts 1994,* JPL Internal Document D-12396, January 1995.

Axford, W. I., et al., *Close Encounter with the Sun: Report of the Minimum Solar Mission Science Definition Team. Scientific Rationale and Mission Concept*, JPL Internal Document D-12850, August 1995.

Gloeckler, G., et al., *Solar Probe: First Mission to the Nearest Star. Report of the NASA Science Definition Team for the Solar Probe Mission*, The Johns Hopkins University Applied Physics Laboratory, Laurel, MD, February 1999.

Potocki, K. A., et. al., *Solar Probe: An Engineering Study,* Report to the NASA/Living With a Star and Sun-Earth Connection Programs, The Johns Hopkins University Applied Physics Laboratory, Laurel, MD, November, 2002.

Appendix G: Acronyms

AC	Alternating Current
ACE	Advanced Composition Explorer
AIU	Attitude Interface Unit
APL	The Johns Hopkins University Applied Physics Laboratory
AU	Astronomical Unit
BaZP	Barium Zirconium Phosphate
BC	Bus Controller
BOL	Beginning of Life
BOM	Beginning of Mission
bps	Bits per Second
C&DH	Command and Data Handling
C_3	Maximum Required Launch Energy
CBE	Current Best Estimate
C-C	Carbon–Carbon
CCSDS	Consultative Committee for Space Data Systems
CD	Coronal Dust Detector
CDPU	Common Data Processing Unit
CDS	Coronal Diagnostic Spectrometer on SOHO
CFDP	CCSDS File Delivery Protocol
CG	Center of Gravity
CIR	Corotating Interaction Region
CME	Coronal Mass Ejection
CONTOUR	Comet Nucleus Tour
COSPAR	Committee on Space Research
CPU	Central Processing Unit
CSSP	Committee on Solar and Space Physics (NRC)
CTH	Coupled Thermodynamic and Hydrodynamic
DC	Direct Current
DPU	Data Processing Unit
DSAD	Digital Solar Aspect Detector
DSMS	Deep Space Mission System (formerly the Deep Space Network, DSN)
EISCAT	European Incoherent Scatter Radar
EIT	Extreme Ultraviolet Imaging Telescope on SOHO
ENA	Energetic Neutral Atom
EPI	Energetic Particle Instrument
EPI-Hi	Energetic Particle Instrument (High Energy)
EPI-Lo	Energetic Particle Instrument (Low Energy)
ESA	European Space Agency
EUV	Extreme Ultraviolet
FAST	Fast Auroral Snapshot Explorer
FEA	Fast Electron Analyzer
FEM	Finite Element Model
FFT	Fast Fourier Transform
FIA	Fast Ion Analyzer
FIP	First Ionization Potential
FOV	Field of View
FPGA	Field-Programmable Gate Array
FPI	Fast Plasma Instrumentation
G&C	Guidance and Control
GCR	Galactic Cosmic Ray
GPHS	General Purpose Heat Source
GSFC	NASA Goddard Space Flight Center
HET	High-Energy Telescope
HGA	High-Gain Antenna
HGARA	High-Gain Antenna Rotary Actuator
HI	Hemispheric Imager
I&T	Integration and Test
I/O	Input Output
ICA	Ion Composition Analyzer
IEM	Integrated Electronics Module
IFE	Interplanetary Field Enhancement
IFM	Interplanetary Flux Model
IMU	Inertial Measurement Unit
IR	Infrared
IRAD	Independent Research and Development

ISEE	International Sun-Earth Explorer
IUCF	Indiana University Cyclotron Facility
JGA	Jupiter Gravity Assist
JHU/APL	The Johns Hopkins University Applied Physics Laboratory
JPL	Jet Propulsion Laboratory
kbps	Kilobits per Second
KSC	Kennedy Space Center
L	Latch Valve
LASCO	Large Angle and Spectrometric Coronagraph on SOHO
LGA	Low-Gain Antenna
LOS	Line of Sight
LVPS	Low Voltage Power Supply
LWS	Living With a Star
MAG	Magnetometer
MDI	Michelson Doppler Interferometer
MESSENGER	MErcury Surface, Space ENvironment, GEochemistry, and Ranging
MET	Medium-Energy Telescope
MGA	Medium-Gain Antenna
MGS	Mars Global Surveyor
MHD	Magnetohydrodynamic
MIPS	Millions of Instructions per Second
MLI	Multilayer Insulation
MMRTG	Multi-Mission Radioisotope Thermoelectric Generator
MSL	Mars Science Laboratory
MSM	Minimum Solar Mission
N/A	Not Applicable
NASA	National Aeronautics and Space Administration
NEAR	Near Earth Asteroid Rendezvous
NGS	Neutron/Gamma Ray Spectrometer
NIST	National Institute of Standards and Technology
NRC	National Research Council
P	Pressure Transducer
PAF	Payload Attach Fairing
PBN	Pyrolytic Boron Nitride
PCI	Peripheral Component Interconnect
PDU	Power Distribution Unit
PG	Pyrolitic Graphite
PHS	Primary Heat Shield
PNI	Probability of No Impact
PNP	Probability of No Penetration
PSE	Power System Electronics
PSRI	Polar Source Region Imager
PUI	Pickup Ion
PWI	Plasma Wave Instrument
QNS	Quasi-Thermal Noise Spectroscopy
RF	Radio Frequency
RHCP	Right Hand Circular Polarization
RHESSI	Reuven Ramaty High Energy Solar Spectroscopic Imager
R_J	Radius of Jupiter
rpm	Revolutions per Minute
R_S	Solar Radius
RT	Remote Terminal
RTG	Radioisotope Thermoelectric Generator
RWA	Reaction Wheel Assembly
S	Solenoid
S/C	Spacecraft
S/N	Signal-to-Noise Ratio
SAIC	Science Applications International Corporation
SEC	Sun-Earth Connection
SEE	Space Environmental Effects
SEP	Solar Energetic Particle
SHS	Solar Horizon Sensor
SMEI	Solar Mass Ejection Imager
SOHO	Solar and Heliospheric Observatory
SPAS	Solar Probe Affiliated Scientist

SPDT	Single-Pole-Double-Throw
SPE	Solar Particle Event
SRG	Stirling Radioisotope Generator
SSPA	Solid-State Power Amplifier
SSR	Solid-State Recorder
SST	Science Study Team
STDT	Science and Technology Definition Team
STEREO	Solar-Terrestrial Relations Observatory
SUMER	Solar Ultraviolet Measurements of Emitted Radiation on SOHO
SWOOPs	Solar Wind Plasma Experiment on Ulysses
TCM	Trajectory Correction Maneuver
TGA	Thermal Gravimetric Analysis
TIMED	Thermosphere, Ionosphere, Mesosphere Energetics and Dynamics
TOF	Time of Flight
TPS	Thermal Protection System
TRACE	Transition Region and Coronal Explorer
TRIO	Temperature Remote I/O
TSS	Thermal Synthesis System
USO	Ultrastable Oscillator
UVCS	Ultraviolet Coronagraph Spectrometer on SOHO
VLBA	Very Long Baseline Array
XFER	Transfer
α	Absorptivity
ΔV	Velocity Change
ε	Emissivity

REPORT DOCUMENTATION PAGE

Form Approved
OMB No. 0704-0188

1. REPORT DATE *(DD-MM-YYYY)*	2. REPORT TYPE	3. DATES COVERED *(From - To)*
30-09-2005	Technical Memorandum	

4. TITLE AND SUBTITLE

Solar Probe: Report of the Science and Technology Definition Team

5a. CONTRACT NUMBER

5b. GRANT NUMBER

5c. PROGRAM ELEMENT NUMBER

6. AUTHOR(S)

The Solar Probe Science and Technology Definition Team

5d. PROJECT NUMBER

5e. TASK NUMBER

5f. WORK UNIT NUMBER

7. PERFORMING ORGANIZATION NAME(S) AND ADDRESS(ES)

Goddard Space Flight Center
Greenbelt, MD 20771

8. PERFORMING ORGANIZATION REPORT NUMBER

2005-02269-0

9. SPONSORING/MONITORING AGENCY NAME(S) AND ADDRESS(ES)

National Aeronautics and Space Administration
Washington, DC 20546-0001

10. SPONSORING/MONITOR'S ACRONYM(S)

11. SPONSORING/MONITORING REPORT NUMBER

TM–2005–212786

12. DISTRIBUTION/AVAILABILITY STATEMENT

Unclassified-Unlimited, Subject Category: 12, 42
Report available from the NASA Center for Aerospace Information, 7121 Standard Drive, Hanover, MD 21076. (301)621-0390

13. SUPPLEMENTARY NOTES

14. ABSTRACT

The Solar Probe mission of the Living With a Star program will be a historic mission, flying into one of the last unexplored regions of the solar system, the Sun's atmoshpere or corona, for the first time. Approaching as close as 3 Rs above the Sun's surface, Solar Probe will employ a combination of in-situ measurements and imaging to achieve the mission's primary scientific goal: to understand how the Sun's corona is heated and how the solar wind is accelerated. Solar Probe will revolutionize our knowledge of the physics of the origin and evolution of the solar wind. Moreover, by making the only direct, in-situ measurements of the region where some of the deadliest solar energetic particles are energized, Solar Probe will make unique and fundamental contributions to our ability to characterize and forecast the radiation environment in which future space explorers will work and live.

15. SUBJECT TERMS

coronal mass ejections, cosmic dust, solar corona, solar energetic particles

16. SECURITY CLASSIFICATION OF:			17. LIMITATION OF ABSTRACT	18. NUMBER OF PAGES	19b. NAME OF RESPONSIBLE PERSON
a. REPORT	b. ABSTRACT	c. THIS PAGE			Haydee M. Maldonado
Unclassified	Unclassified	Unclassified	Unclassified	96+40Apgs	19b. TELEPHONE NUMBER *(Include area code)* (301) 286-6762

Blank